Title
Structure-Property Relationships in Disordered Complex Oxide Perovskites

Author
Fernandez, Abel

Publication Date
2022

Peer reviewed|Thesis/dissertation

Structure-Property Relationships in Disordered Complex Oxide Perovskites

By

Abel Fernandez

A dissertation submitted in partial satisfaction of the

requirements for the degree of

Doctor of Philosophy

in

Engineering – Materials Science and Engineering

in the

Graduate Division

of the

University of California, Berkeley

Committee in charge:

Professor Lane W. Martin

Professor Ramamoorthy Ramesh

Professor Mike Crommie

Spring 2022

Structure-property relationships in disordered complex-oxide perovskites

Abstract

Structure-property relationships in disordered complex-oxide perovskites

by

Abel Fernandez

Doctor of Philosophy in Materials Science and Engineering

University of California, Berkeley

Professor Lane W. Martin, Chair

This dissertation explores the lattice degree of freedom in several heavily-substituted, highly disordered, and technologically relevant perovskite systems utilizing epitaxial thin-film synthesis and characterization. By creating controlled changes to the boundary conditions imposed on thin films, effecting different surface orientations, strain states, film thicknesses, and elastic stiffness, connections can be drawn between the resulting structural, chemical, and electronic changes that are driven by the film's boundary conditions, and the resulting properties that can be achieved in these films. First, I focus on the impact such changes have on the surface properties of $La_{1-x}Sr_xCo_{1-y}Fe_yO_{3-\delta}$ transition metal perovskites that are being considered for cathodes for oxygen electrocatalysis. There, growth-mediated control of the surface orientation gives rise to distinct evolution of local non-stoichiometry and increased oxygen reactivity in (111)-oriented films. Application of epitaxial strain on the films is then found to impact the electronic structure of these films, modulating the occupancy of transition-metal orbitals at the surface, which ultimately impacts the ability of these materials to perform oxygen exchange. The focus is then changed to relaxor ferroelectrics, and understanding how changes to elastic and electrostatic boundary conditions impact the response of the disordered nanoscale polar structure. In $PbSc_{0.5}Ta_{0.5}O_3$, reducing the thickness of films results in suppression of the polarization response that undergoes a rapid collapse when film thickness is reduced below the polar correlation length. It is then demonstrated that the polarization and piezoelectric response of $0.68PbMg_{1/3}Nb_{2/3}O_3$-$0.32PbTiO_3$ is suppressed by the mechanical clamping of the substrate, and methods for removing films from the substrate allow for enhanced responses. Together, these studies point to the connection between lattice constraints and the achievable responses in perovskites, as well as point to new engineering approaches for enhancing desirable properties across a range of applications.

Acknowledgements:

First, I would like to thank Professor Lane Martin for the opportunity to join this group and conduct interesting, innovative, high-level research. Not only was I provided all the resources I needed to pursue my research, whether it was instrumentation or connections with collaborators, but I was also provided the freedom to pursue interesting questions, and support when I made missteps along the way. With his guidance I learned to be a more productive, more curious, more attentive and more skeptical scientist. On that note, I'd also like to thank Professor Ramesh for asking good questions about my research, and always staying excited about science. I will carry the classic Ramesh quote "Do you believe this?" through to whatever my future endeavors may be. Together Lane and Ramesh have created a group where there is never a lack of excitement about what experiment to do next.

As for others who have helped guide me through my research career to this point, I have to first thank Dr. Chandra Macauley and Professor Carlos G. Levi, who gave me my first taste of what the research world is like as an undergraduate at University of California, Santa Barbara, and I have continued to carry lessons I learned from them through to this day.

I'd like to acknowledge the immense amount of help and advice I received from older members of the group here at Berkeley, including Shishir, Ruijuan, Ran, Sahar, Josh A., Josh M., Arvind, Jieun, Gabe and Eduardo, who really welcomed me to the group and helped get me up and running. In particular, Ran was good company on afternoon coffee breaks and was a great collaborator on the orientation-dependence work, and Jieun who was always ready to take time out of his day to teach me new things about relaxors, research, and keeping things in perspective. I've also learned from younger students in the group: Megha, Yizhe, Zishen, Pravin, Jesse, Djamila, Deokyoung, Leo, and TJ and hope that they continue on successful research paths. I'd also like to acknowledge all the post-doctoral researchers that I got to work with as they have come through the group, particularly Lei, for encouraging me to start work on relaxors, David, for helping me get started with freestanding films, and Jiyeob, for the hard work she put into the synthesis of PMN-PT films.

I was also lucky enough to collaborate with a number of people, particularly in the study of oxygen electrocatalysis. Professor Elif Ertekin and Dr. Tanmoy Chakraborty at the University of Illinois, Urbana-Champaign provided the DFT simulations and provided helpful discussion toward the study of surface-orientation-dependence. Dr. Ethan Crumlin and Dr. Slavomír Nemšák were extremely helpful in initiating and understanding the ambient-pressure experiments at beamline 9.3.2 at ALS. On the same note, Dr. Padraic Shafer and Dr. Christoph Klewe have been extremely helpful, specifically with the dichroism experiments for strain-dependence in LSCF, but also with the other numerous experiments we have performed at beamline 4.0.2.

Getting a PhD would be much harder without friends to celebrate and commiserate with, and I'd like to thank Paul Corbae and Eric Parsonnet for being there to eat lunch, climb rocks, talk science and not talk science.

Finally, thanks to my parents who have been nothing but supportive, regardless of what I choose to do, and my brothers Marcos and Daniel for helping to keep things in perspective and for all the gaming when I need a break from work. And last but not least, I want to thank Ria, for joining me on this journey and putting up with all the hardships that have come her way so she could be here to support me.

Table of Contents

List of Figures:

List of abbreviations and symbols

Abbreviations:

AFM	Atomic force microscopy
AP-XPS	Ambient-pressure X-ray photoemission spectroscopy
AP-XAS	Ambient-pressure X-ray absorption spectroscopy
CERDIP	Ceramic dual in-line package
DFT	Density functional theory
ECR	Electrical conductivity relaxation
EIS	Electrochemical impedance spectroscopy
FWHM	Full-width at half-maximum
HBE	High-binding-energy
HS	High-spin
LBE	Low-binding-energy
LEIS	Low-energy ion-scattering
LS	Low-spin
IS	Intermediate-spin
MD	Molecular dynamics
MIEC	Mixed ionic electronic conductivity
OER	Oxygen evolution reaction
ORR	Oxygen reduction reaction
PLD	Pulsed-laser deposition
PNR	Polar nanoregion
PND	Polar nanodomain
RBS	Rutherford backscattering spectrometry
RSM	Reciprocal-space map
SOFC	Solid oxide fuel cell
SOEC	Solid oxide electrolyzer cell

STEM	Scanning transmission electron microscopy
TEY	Total-electron yield
XPS	X-ray photoemission spectroscopy
XAS	X-ray absorption spectroscopy
XLD	X-ray linear dichroism

Materials:

LSMO	$La_{1-x}Sr_xMnO_3$
LSCF	$La_{0.8}Sr_{0.2}Co_{0.2}Fe_{0.8}O_3$
LSCO	$La_{0.5}Sr_{0.5}CoO_3$
LSGM	$La_{0.9}Sr_{0.1}Ga_{0.95}Mg_{0.05}O_{3-\delta}$
P-E	Polarization-electric field
PDMS	Polydimethyl siloxane
PMN	$PbMg_{1/3}Nb_{2/3}O_3$
PMN-*x*PT	$(1-x)PbMg_{1/3}Nb_{2/3}O_3$-$xPbTiO_3$
PPC	Polypropylene carbonate
PZN-*x*PT	$(1-x)PbZn_{1/3}Nb_{2/3}O_3$-$xPbTiO_3$
PMN-0.32PT	$0.68PbMg_{1/3}Nb_{2/3}O_3$-$0.32PbTiO_3$
PZT	$PbZr_{1-x}Ti_xO_3$
YSZ	Yttria-stabilized zirconia

Symbols:

δ_3	Phase angle of 3rd harmonic
ξ	Polar correlation length
Γ	Half-width at half-maximum
ε_r	Relative permittivity
ε_0	Permittivity of free space
ϵ	Biaxial strain

λ	Wavelength
ω	Frequency
BE	Binding energy
d_{33}	Piezoelectric coefficient
E_a	Activation energy
E	Electric field
f_D	Frequency shift
I_{ab}	Intensity along *a/b* directions
I_c	Intensity along *c* direction
KE	Kinetic energy
k_b	Boltzmann constant
k_s	Surface reaction rate constant
p_{O_2}	Partial pressure of oxygen gas
Q_s	Surface constant-phase element
Q_{ct}	Charge-transfer constant-phase element
R_t	Resistance at time *t*
R_s	Surface resistance
R_{ct}	Charge-tranfer resistance
S_{ij}	Elastic compliance tensor components
$Tan\ \delta$	Dielectric loss tangent
T^*	Intermediate critical temperature
T_b	Burns temperature
T_f	Freezing temperature
T_{max}	Temperature of maximum in permittivity
Z	Complex impedance

Chapter 1:
Structure-property relationships in disordered complex-oxide perovskites

This chapter provides the reader an introduction to the perovskite structure and properties. Details of the structure and an overview of perovskite chemistries and properties are provided. Discussion of key structural features of the perovskite crystal structure, and the impact that manipulation of these features may have on properties provides the background for asking the central questions of this thesis: how can manipulation of the boundary conditions of the perovskite lattice be used to understand and engineer the physics and functionalities of perovskite materials? An overview of considerations for studying epitaxial films with controlled surface orientation, epitaxial strain, film thickness, and mechanical clamping is discussed. Finally, an outline for the remainder of the thesis is provided.

Chapter 1: Structure-property relationships in disordered complex-oxide perovskites

1.1. Perovskites: structure and properties

Complex oxides exhibit a wide range of physical phenomena and properties that are not accessible in more traditional materials like elemental metals and group IV or III-V semiconductors. These properties, which include ferroelectricity,[1] high-temperature superconductivity,[2] magnetism and colossal magnetoresistance,[3] electrocatalysis,[4,5] and metal-insulator transitions,[6,7] couple mechanical, electrostatic, electronic, and thermal stimuli and responses.piezo[8–10] More impressive than the range of properties, is the sensitivity of these properties to chemical and structural perturbation, providing researchers and engineers opportunities for developing new, better materials through careful synthesis approaches. From this, one can envision numerous use-cases where complex oxides provide critical functionalities, enabling smaller, faster, or more efficient devices. Yet widespread use of complex-oxide devices is, in part, precluded by the well-established capabilities and understanding of synthesis-structure-property relationships in more traditional metallic and semiconducting materials. Developing that depth of understanding and control of the properties of complex oxides can enable a new paradigm of technologies enabled by the unique sensitivities and functionalities of complex-oxide materials.

The class of complex oxides known as perovskites, with chemical formula ABO_3, exemplify the traits discussed above. The prototypical cubic perovskite structure can be described by a 5-atom unit cell (Figure 1.1), where *A*-site cations (often, but not always, lanthanides or alkaline earth metals) sit at the cube vertices, while *B*-site cations (often, but not always, transition metals) occupy the cube center. Oxygen anions situated in the middle of the cube faces form a network of corner-sharing oxygen octahedra, with each octahedron centered around a *B*-site cation. While this structure provides the framework, the family of perovskites encompasses a host of structures related by structural distortions to the cubic prototype, and includes tetragonal, orthorhombic, rhombohedral, and monoclinic variants (Figure 1.1), often induced by off-centering of cations or ordered-tilting patterns of the oxygen-octahedra network. The oxygen-octahedral network of the perovskite is also found as a building block of other, more complex layered structures, including structures such as that of $YBa_2Cu_3O_{7-\delta}$ and the Ruddlesden-Popper family with chemistry $A_{n+1}B_nO_{3n+1}$. The structural motif of oxygen octahedra plays a central role in the properties of perovskites. The relatively large electronegativity of oxygen contributes significant ionic nature to the metal-oxygen bonding, yet the orbital overlap of the transition metal *d* orbitals with the oxygen 2*p* orbitals gives rise to strong covalency and correlated-electron effects. Together, this sets up a competition between electronic and electrostatic interactions in

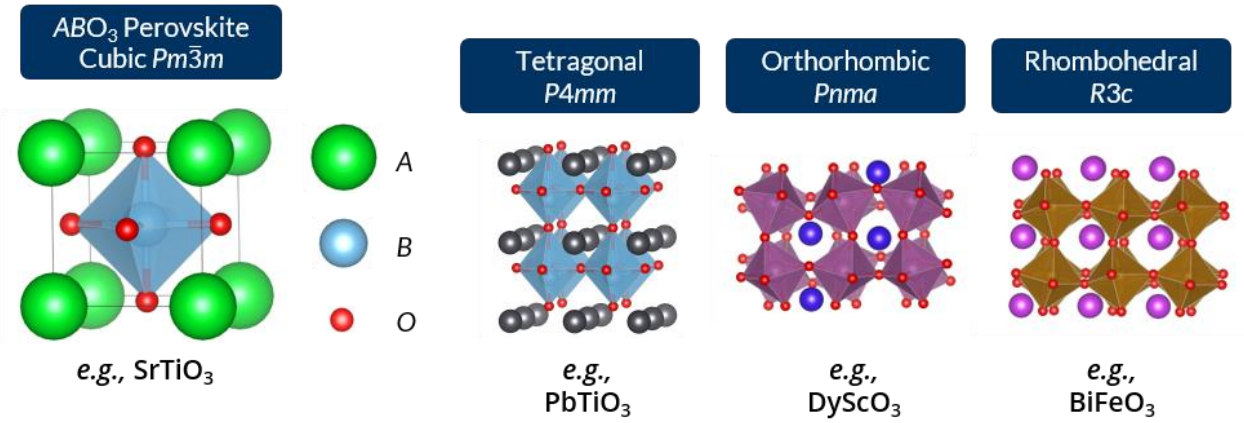

Figure 1.1: The prototypical cubic perovskite depicting the *A*-, *B*-, and *O*-sites. Other common perovskite structures and space groups are shown with distinct symmetries driven by cation displacements or octahedral tilt patterns

perovskites, that results in strong sensitivity to chemical and structural perturbation as chemical identity and structural distortions push and pull the balance of these interactions.

The wide range of physical properties found in perovskites is, in part, due to the chemical flexibility of the perovskite structure. In fact, an overwhelming majority of metallic elements on the periodic table can be found in the perovskite structure in some form.[5] Of particular importance to both the structure and properties is maintaining charge neutrality with the -6 charge/unit cell provided by the three oxygen anions. This requires that the sum of the *A*- and *B*-site cation charges must equal +6, with deviation from this resulting in oxygen nonstoichiometry, typically in the form of oxygen vacancies. Common cation charge distributions are $A^{3+}B^{3+}O_3$, as in the case of $DyScO_3$, an orthorhombic distorted perovskite dielectric (Figure 1.1), and $BiFeO_3$, a rhombohedral multiferroic, exhibiting simultaneous ferroelectricity and antiferromagnetism (Figure 1.1). Another common case is that of $A^{2+}B^{4+}O_3$, as is the case for $SrTiO_3$, a dielectric which possesses a prototypical cubic structure, and $BaTiO_3$, which exists as a cubic paraelectric at high temperatures, and can possess tetragonal, orthorhombic, or rhombohedral ferroelectric distortions at lower temperatures. Alternatives include $A^{1+}B^{5+}O_3$, which can be found in $LiNbO_3$, a rhombohedral ferroelectric, but are less common in oxide perovskites. Already, the range of structures and properties can begin to appear daunting, yet the chemical versatility is even more striking when one takes into account the possibility of forming solid solutions. In many cases, perovskite systems can exhibit complete solubility with three, four, and five cations randomly distributed on either the *A*- or *B*-sites, while maintaining the perovskite structural framework. These complex, multicomponent systems can have equally complex structural phase diagrams, in additions to ferroic and electronic phase diagrams, where ferroelectric, magnetic, or electronic order evolves with both temperature and chemistry. For decades, a primary means of developing the "best" material for a given application involved brute-force, trial-and-error compositional screening and testing, often guided by the chemical intuition of an experienced scientist, to perch materials near such phase boundaries and maximize susceptibilities to external stimuli and increase functionality. A primary example of this is found in the $PbZr_{1-x}Ti_xO_3$ system, in which a structural transition occurs at x = 0.52, and the energetically close structures drive large dielectric and piezoelectric susceptibilities,[11] making this a favored composition for piezoelectric applications. Yet, understanding of the origin of these optimal properties can also become obscured by chemical substitution, convoluted by simultaneous modification of the charge, spin, and orbital degrees of freedom, as well as the lattice degree of freedom through substitution-induced structural distortions.

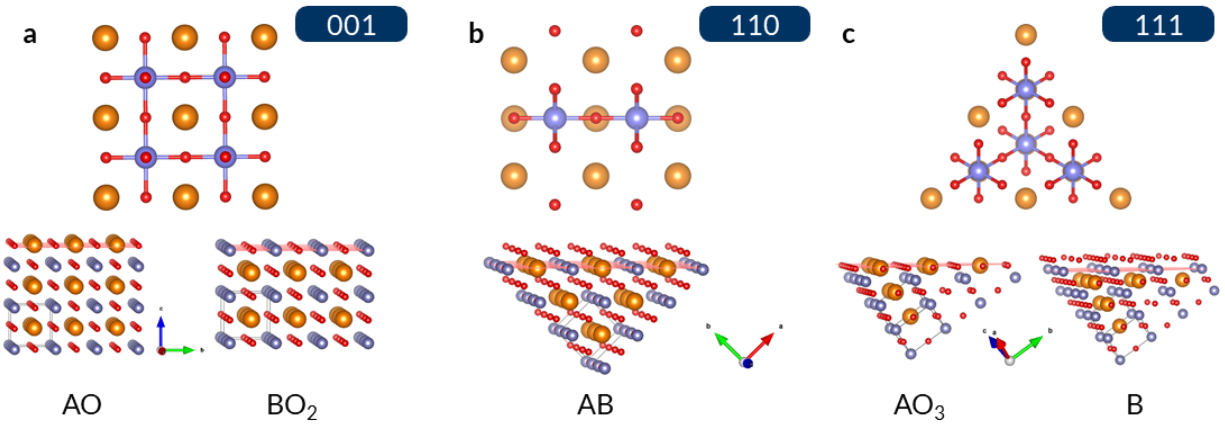

Figure 1.2: Illustration of the symmetry and possible surface terminations of different crystallographic planes of the perovskite structure.

Chapter 1: Structure-property relationships in disordered complex-oxide perovskites

In recent decades, study of the role of the lattice in perovskite oxides has been facilitated by advanced epitaxial thin-film synthesis, allowing for isolation of key structural features.[12–14] Deposition techniques, like pulsed-laser deposition and molecular-beam epitaxy, provide researchers unprecedented capabilities in the synthesis of pristine single-crystalline samples, with the additional freedom of controlling the structural, mechanical, electronic, and electrostatic boundary conditions of the film to deterministically manipulate the crystal lattice without changing the chemical composition. Along with deposition, advanced characterization techniques for studying structure and properties have been developed, spanning from macroscopic to atomic length-scales. With these capabilities, researchers can control and study key structural characteristics from metal-oxygen bond lengths to long-range-ordered rotations of the oxygen octahedra to symmetry changes, all of which impact the electronic and electrostatic interactions between cations and anions. Study of the connection between this lattice degree of freedom, and the charge, spin, and orbital degrees of freedom is of critical importance for understanding structure property relationships in perovskites.[15] This work has proved to be extremely fruitful, particularly in the understanding and manipulation of ferroic materials. The confinement of the thin-film lattice to ultrathin dimensions or unique surface symmetries can set up frustration of ferroic-order parameters, that result in shifting of metal-insulator transition temperatures,[16] suppressed ferroelectric order,[17] novel ferroelectric switching pathways,[18] or changes in electron-orbital order.[19,20] Similarly, the elastic constraints imposed by the substrate can be used to apply strain to films, resulting in novel hierarchical ferroelectric domain structures with enhanced piezoelectric, pyroelectric, and ferroelectric responses.[13] Such studies provide a platform for understanding key electronic, electrostatic, and elastic interactions within these materials, and point toward novel engineering approaches for tuning materials properties.

1.2. The lattice degree of freedom

The sensitivity of the perovskite lattice to structural distortion allows for tuning and manipulation of the properties through structural control afforded by thin-film epitaxy. Whereas the lattice structure in bulk-single crystals and ceramics is largely predetermined by the chemistry, films less than a few hundred nanometers thick are strongly coupled to the elastic boundary conditions of the underlying substrate. The requirement for chemical bonding of coherent thin films to a substrate allows for the independent control of several structural features that can impact electrostatic, electronic, and elastic properties of the film. In this dissertation, we focus on several "knobs" for controlling the boundary conditions imposed on the film, and in turn controlling the perovskite structure: control of surface orientation, epitaxial strain, lattice dimension, and removal from the substrate.

The symmetry of the unit-cell plays a critical role in determining the properties of a crystal, yet in real, finite crystals, this symmetry is broken at the surfaces of the crystal. Many times, the properties at this surface can be entirely distinct from bulk properties due to this symmetry breaking. An interesting question then arises, namely, how are surface properties of the material different when the surface is formed at different crystallographic planes. In a perovskite, for example, slicing the crystal along the (001)-, (110), or (111) results in surfaces that are distinct in symmetry, coordination, and chemistry. As can be seen, (001) surfaces have square symmetry, while (110) and (111) surfaces have rectangular and hexagonal symmetry, respectively. Similarly, focusing on the *B*-site, (001) surfaces have only one dangling bond, while (110) surfaces have two and (111) surfaces have three exposed bonds projecting out of the surface. The exact position of the "slice" also results in multiple possibilities for the chemical termination, that is, which cations

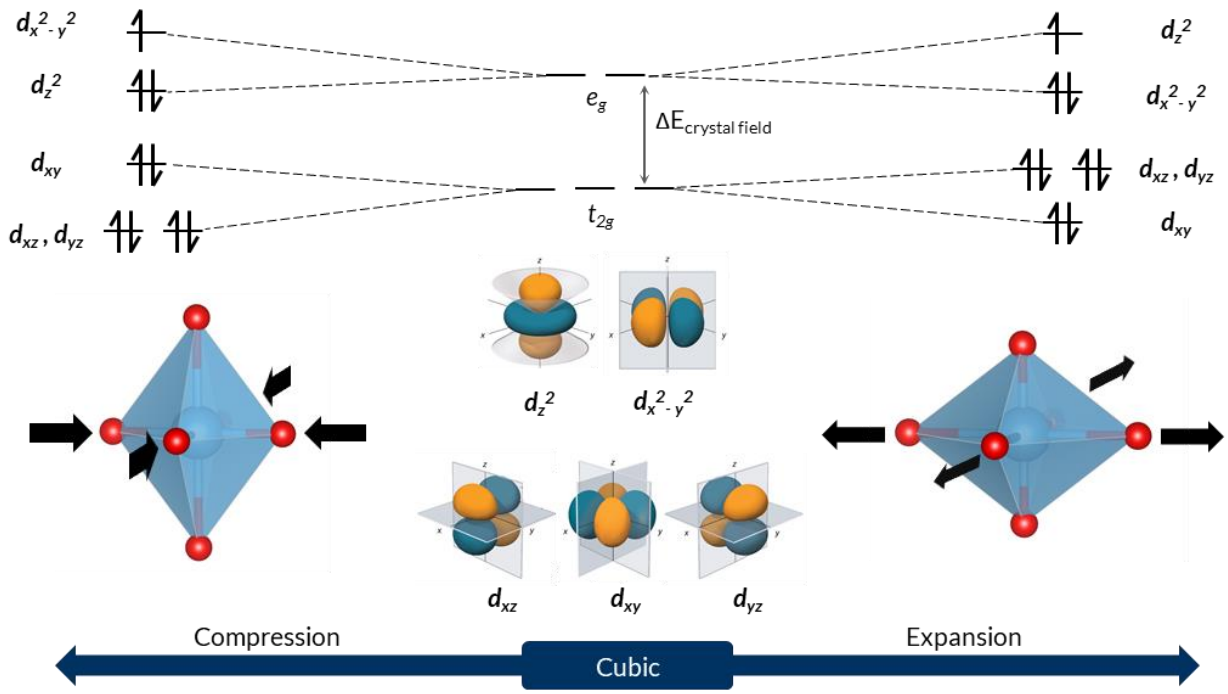

Figure 1.3: Illustration of the expected orbital energy splitting caused by the cubic crystal field of the oxygen octahedra, and the additional degeneracy-breaking associated with compression or expansion of the lattice.

sit at the outermost layer. Two possibilities exist for (001) surfaces, either *A*O, or BO_2, termination. On the other hand, (110) surfaces have only one possibility, *AB*O termination, where all cations sit in the same plane. Finally, (111) can be AO_3-terminated or entirely *B*-terminated. Each of these terminations also impacts the polarity of these surfaces, which depends on the particular cations at the *A* and *B* sites. For example, in the $A^{2+}B^{4+}O_3$-type perovskites, *A*O- and BO_2-terminations both result in a surface with neutral charge, while $A^{3+}B^{3+}O_3$ perovskites produce charged surfaces. On the other hand, all terminations for (110) and (111) surfaces produce charged surfaces. These terminations and their respective polarities become even more complex in the case of chemical doping and, ultimately, the various electronic and electrostatic interactions that occur at a particular surface will be determined by the specific chemical species that occupy those sites.

One of the most fundamental parameters for describing a crystal are the lattice parameters of the unit cell and the resulting unit-cell volume. The equilibrium lattice parameters of a structure are closely connected with the balance of electrostatic and electronic interactions between cations and anions in the structure, and expanding or compressing these lattice parameters through epitaxial strain can push and pull this balance. In transition-metal perovskites, in particular those with unfilled *d*-electron bands, the electronic structure is intimately connected with the symmetry and bonding in the BO_6 octahedra. The *d* orbitals, which are directed along the *B*-O bonds and directly overlap with oxygen 2*p* orbitals, experience crystal-field splitting into lower energy t_{2g} and higher energy e_g orbitals. Expanding or compressing the lattice effectively changes the symmetry of the octahedra, and the *B*-O bond length. A simple picture based on coulombic repulsion (or Pauli exclusion) suggests that increasing the overlap between the *B*-cation *d* and oxygen-2*p* orbitals (by changing the bond length) will increase the energy of electrons in those orbitals. From this, one can see that compression of the lattice along *a* and *b* should increase the energy of orbitals that exist in the *ab* (or *xy*) plane (*e.g.*, the d_{xy}, d_{xz}, d_{yz}, and $d_{x^2-y^2}$ orbitals), while expansion in *a* and *b*, should have the opposite effect. Adding to this is again the surface-symmetry

breaking that occurs at a crystal surface, which may already lift the degeneracy of e_g orbitals near the surface. When chemical disorder is considered, the effects of strain may also depend on the identities and ground-state electronic structures of each cation occupying a particular lattice site.

The finite-size of a crystal can also impact the properties of a crystal compared to a theoretical infinite crystal. A common textbook example of such phenomena is that of quantum confinement in quantum dots, where reducing the size of the lattice to nanometers, where only several hundred atoms are interacting, restricts the electrons wavefunction and creates unique electronic properties.[21] In addition to electronic effects, reducing the lattice dimensions can impact electrostatic and elastic effects in crystals. In ferroelectric materials, which favor long-range correlation of dipoles over many unit cells, reducing the lattice to thicknesses of only a handful of unit cells can shift the energetic balance between correlated polarization and depolarization fields that arise at the crystal's surface. These depolarization fields, which exist to counteract uncompensated surface charge due to the ferroelectric polarization, play an increasingly important role as the crystal is thinned to atomic length scales, where the surfaces become a larger and larger fraction of the crystal volume. Finite-size effects have been extensively studied in traditional ferroelectrics possessing long-range ordered polarization, leading to domain formation and eventually complete suppression of ferroelectric order in the thinnest films. More generally, reducing the lattice dimensions can reduce the length scales over which correlations, whether they are electron correlations or polar correlations, can exist. In the case of materials with chemical disorder, which cannot be easily described by a single 5-atom unit cell but rather are understood from the average properties of many unit cells, a reduction in lattice dimensions also reduces the number of unit cells that can cooperatively interact, and the local chemistry plays an increasingly large role.

Finally, aside from bond-length changes imposed by static epitaxial strain, the stiffness or compliance of metal-oxygen bonds can impact a material's response to dynamic strain processes, like that of electromechanical coupling in a piezoelectric. In piezoelectrics, applied electric fields drive structural deformation in the form of large changes in symmetry and unit-cell volume. Yet, the mechanical coupling of a coherent epitaxial film to its substrate, that allows for the application of epitaxial strain, also implies that the elastic stiffness and compliance of the film is dictated by the substrate. In this case, even in the absence of significant strain, the clamping of the film to the substrate can dramatically impact the ability for the film to deform and respond to applied electric fields compared to an idealized bulk crystal. Removing these constraints, by decoupling and removing the film from its substrate, provides a means to manipulate not just the strain state, but the stiffness of the film, and understand how these elastic parameters impact piezoelectric and ferroelectric responses in thin films.

1.3. Motivation and organization of thesis

Developing new insight and understanding of structure-property relationships in perovskites will provide the foundational knowledge for engineering useful functionalities and ushering in next-generation technologies based on perovskite oxide materials. Whether these materials contribute to electrochemical-energy conversion in a fuel cell or are employed in high-efficiency ultrasonic transducers, fundamental control of the material's structure and properties from synthesis to device integration must be understood. Much of the understanding gleaned from epitaxy-based studies has been focused on relatively simple, prototypical systems, assuming that one day this understanding could be applied to materials used in real applications. Leveraging prior knowledge and tools developed through this prior work on model systems, one can now begin to apply these

approaches to more complex, solid-solution systems which are already employed or considered as primary candidates in new devices. This work can provide new insights into the connection between the lattice, and orbital, charge, and spin order in materials that are highly disorder, while also examining new routes for enhancing properties in systems where enhancement by chemical optimization has already been exhausted. Of particular interest, is how complexity and disorder impacts, and is impacted by, the boundary constraints imposed on the lattice. How does mixed cation and charge disorder manifest along distinct crystal facets, with different surface symmetry, polarity, and bonding arrangement? Similarly, how does the electronic structure at the perovskite surface change under the application of epitaxial strain when multiple transition metals are present? On the other hand, in systems where disorder is critical to functionality, how are those functionalities impacted when the length scale for disorder is reduced to a handful of unit cells? Finally, what impact does the substrate have on materials where disorder is key to the electromechanical response?

In this dissertation, I explore the lattice degree of freedom in several heavily-substituted, highly disordered, and technologically relevant perovskite systems utilizing epitaxial thin-film synthesis and characterization. First, I study the role of the surface orientation and strain in dictating surface properties for oxygen electrocatalysis in the family of $La_{1-x}Sr_xCo_{1-y}Fe_yO_{3-\delta}$ transition metal perovskites. Here, chemical and charge disorder on the *A* site gives rise to disordered, mixed valence of the transition metal *B*-site cations and oxygen non-stoichiometry that allows for oxygen reduction and conduction as a cathode in solid oxide fuel cells. Growth-mediated control of the surface orientation gives rise to distinct evolution of local non-stoichiometry and increased oxygen reactivity in (111)-oriented films. Further the effect of epitaxial strain on the surface electronic structure is studied. It is found that applying epitaxial strain to (001)-oriented films results in a modulation of the electron occupancy of transition metal 3*d* orbitals, impacting the ability for these orbitals to interact with molecular oxygen. We then turn our attention to a class of materials known as relaxor ferroelectrics, and understanding the role of electrostatic and elastic boundary conditions in $PbSc_{0.5}Ta_{0.5}O_3$ and $0.68PbMg_{1/3}Nb_{2/3}O_3$-$0.32PbTiO_3$. In these materials, the *B*-site-cationic disorder gives rise to a complex, nanoscale dipolar structure driven by charge and elastic disorder. Systematic control of film thickness to length-scales below the polar correlation length reveals the limits of relaxor polarization response in epitaxial $PbSc_{0.5}Ta_{0.5}O_3$ films. The impact of the mechanical clamping of the substrate is then examined by producing freestanding nanomembranes from epitaxial thin films of $0.68PbMg_{1/3}Nb_{2/3}O_3$-$0.32PbTiO_3$. Ultimately, the impacts of elastic boundary conditions on the ferroelectric and piezoelectric responses in this system are demonstrated. The remainder of this thesis is organized as follows:

Chapter 2 describes the synthesis and general characterization techniques of perovskite oxide thin films, and the methods and background on manipulation of the perovskite lattice through thin-film epitaxy.

Chapter 3 provides an overview of oxygen electrocatalysis, materials considerations for high-performance oxygen reduction cathodes, and characterization techniques for studying oxygen reduction, local chemistry, and electronic structure at perovskite surfaces.

Chapter 4 details a multi-modal study on the dependence of oxygen electrocatalytic rates on the surface orientation of $La_{0.8}Sr_{0.2}Co_{0.2}Fe_{0.8}O_{3-\delta}$ films. A comprehensive study of high-temperature impedance spectroscopy on all-perovskite half-cell heterostructures in supported by density-

functional calculations, and ambient-pressure X-ray spectroscopy of the perovskite surfaces at high temperatures and in the presence of oxygen gas.

Chapter 5 demonstrates epitaxial strain engineering to control the electron occupancy of transition metal orbitals at the surfaces of $La_{0.8}Sr_{0.2}Co_{0.2}Fe_{0.8}O_{3-\delta}$ and $La_{0.5}Sr_{0.5}CoO_{3-\delta}$ films within the context of electronic descriptors for high-activity oxygen electrocatalysts, and the dependence of spin-structure to epitaxial strain.

Chapter 6 provides an overview of relaxor ferroelectrics, including phase transitions, polarization, and piezoelectric response as well as common characterization techniques for understanding relaxor structures and properties.

Chapter 7 describes the study of finite-size effects in $PbSc_{0.5}Ta_{0.5}O_3$, where reduction of the film thickness below the polar correlation length effectively quenches the typical relaxor response.

Chapter 8 details the synthesis and fabrication of $0.68PbMg_{1/3}Nb_{2/3}O_3$-$0.32PbTiO_3$ freestanding membranes and changes to the electromechanical responses when the mechanical constraint of the substrate is removed.

Chapter 9 provides a summary of the findings in this thesis, as well as discussion of open questions and future work.

Chapter 2:
Manipulating the perovskite lattice through epitaxy

This chapter covers the methods of control of the perovskite lattice through thin-film epitaxy and possible lattice effects that may be observed in various perovskite properties. It includes background on the synthesis of thin films with pulsed-laser deposition, as well as details on processes used in this work. Relevant studies on effects of lattice manipulation via surface-orientation, epitaxial strain, size effects, and freestanding membranes are reviewed.

Chapter 2: Manipulating the perovskite lattice through epitaxy

2.1. What is epitaxy?

Epitaxy refers to the growth of a crystal on a crystalline substrate where the orientations of the two crystals have a specific relationship set by the interface between them.[22] For example, assume one has a cubic substrate cut such that the [100] and [010] are in the plane of the substrate and the surface normal is parallel to the [001]. Upon depositing a film of a similar structure on this surface, one might expect the [100], [010], and [001] of the film to lie parallel to those of the substrate; so-called *cube-on-cube* epitaxy (Figure 2.1a, orange), but depending on the lattice parameters of the deposited layer and the substrate other orientations are possible (Figure 2.1a, green). The result is a distinct relationship between the lattice and lattice parameters of the substrate and the deposited film. The term *homoepitaxy* refers to the deposition of a film with identical composition and structure to the substrate, while *heteroepitaxy* refers to the synthesis of a film with composition or structure that is dissimilar to the underlying substrate.[23] A thin film is said to be *coherently strained* to the substrate when it adopts the same in-plane lattice parameters as the substrate throughout the thickness of the film (Figure 2.1b); one can think of this as applying biaxial strain in the plane of the film. These are general examples, but other forms of epitaxy are possible. Other substrate orientations [*i.e.*, substrates with surface normals parallel to, for example, the (110) or (111)] can be used to control the surface orientation of the film. In cases where the lattice mismatch between the film and substrate is too large, *partially* or *fully relaxed* films (Figure 2.1c) are possible wherein, above some critical thickness, the film adopts the energetically preferred bulk lattice parameters (such relaxation is accomplished by the formation of dislocations at the interface between the film and substrate). In this dissertation, all films are grown with *cube-on-cube* epitaxy, that is, the unit cells of the substrate and films have the same orientation, and the octahedral network is continuous from substrate to film.

2.2. Pulsed-laser deposition

Pulsed-laser deposition (PLD) has become one of the most common methods of depositing epitaxial thin films of complex oxides.[24,25] In general, PLD relies on the interaction of a focused laser beam with a ceramic (or single-crystal) target, vaporizing the target and producing a plasma that is deposited on a substrate (Figure 2.2). The light-matter interactions, however, are complex and involve equilibrium and non-equilibrium processes, and the conversion of electromagnetic

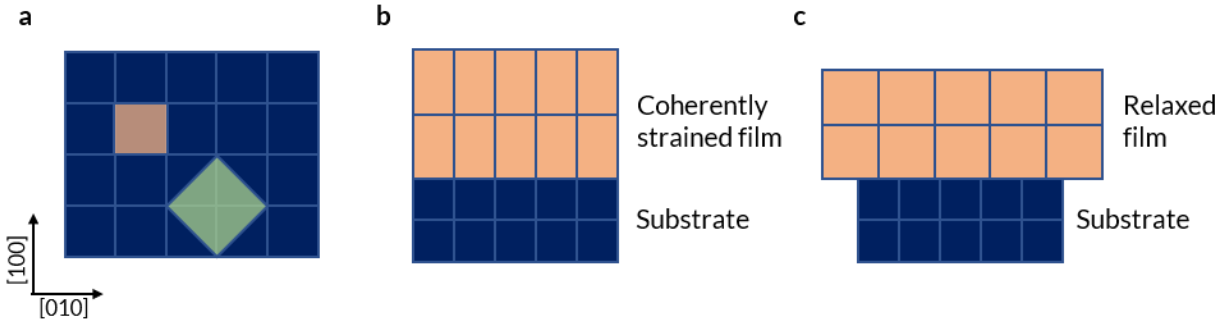

Figure 2.1: Schematic of various epitaxial relationships showing a) a relaxed film with equilibrium lattice paramters different from the substrate, b) a coherently strained film where the film and substrate have the same lattice parameters at the interface and the strain is maintained throughout and c) a depiction of cube-on-cube epitaxy (upper) in contrast to a unit cell that is rotate with respect to the substrate lattice (lower).

energy to thermal, chemical, and mechanical energy.[26–28] The resulting plasma contains a complex distribution of ionized and excited atomic species that interact with an ambient gas (often, but not always, oxygen gas) on the way to the surface of the heated substrate. Early demonstrations of the ability to use this plasma as a source for depositing thin films were reported in the 1960s;[29] however, PLD remained a relatively obscure deposition technique limited to some semiconducting and dielectric films until the synthesis of superconducting $YBa_2Cu_3O_7$ films in 1987 reporting what were, at that time, record high critical temperatures, and were originally attributed to the precise stoichiometry achievable with PLD.[30,31] It has since been shown that PLD can easily result in films with large deviations from the target stoichiometry, and yet, the ability to rapidly synthesize films in a relatively inexpensive, compact chamber has made it an attractive research technique for expanding thin-film studies to a wide range of oxide materials.

Synthesis of high-quality thin films, with appropriate stoichiometry and high crystalline quality, can be achieved through careful optimization of the various growth parameters available to researchers, and significant effort has been expended on understanding how these parameters impact thin-film quality. The pulsed laser used is often an excimer laser, which provides high power and short pulse durations on the order of 10s of nanoseconds. Controllable parameters include the energy, spot size, and repetition rate of the pulsed laser beam. When pulsed onto the target material, the transfer of energy causes rapid melting, vaporization, and ionization of the target material, resulting in ejection of a plume containing neutral atoms, ions, electrons, clusters, and (potentially) particulates and molten droplets. This highly energetic plasma can reach an electron temperature on the order of 10,000 K and adatom kinetic energies can exceed 10-100 eV. Energy and spot size together determine the energy density, or fluence, of the laser incident on the target surface. The laser fluence is a critical parameter in determining the stoichiometry of the plasma plume. Studies have shown, for example, that high fluence promotes deficiency of the heaviest cations, as seen in $SrTiO_3$ and $LaAlO_3$.[32,33] On the other hand, the choice of laser fluence also impacts the kinetic energy of the species in the plume, and those that are landing on the surface

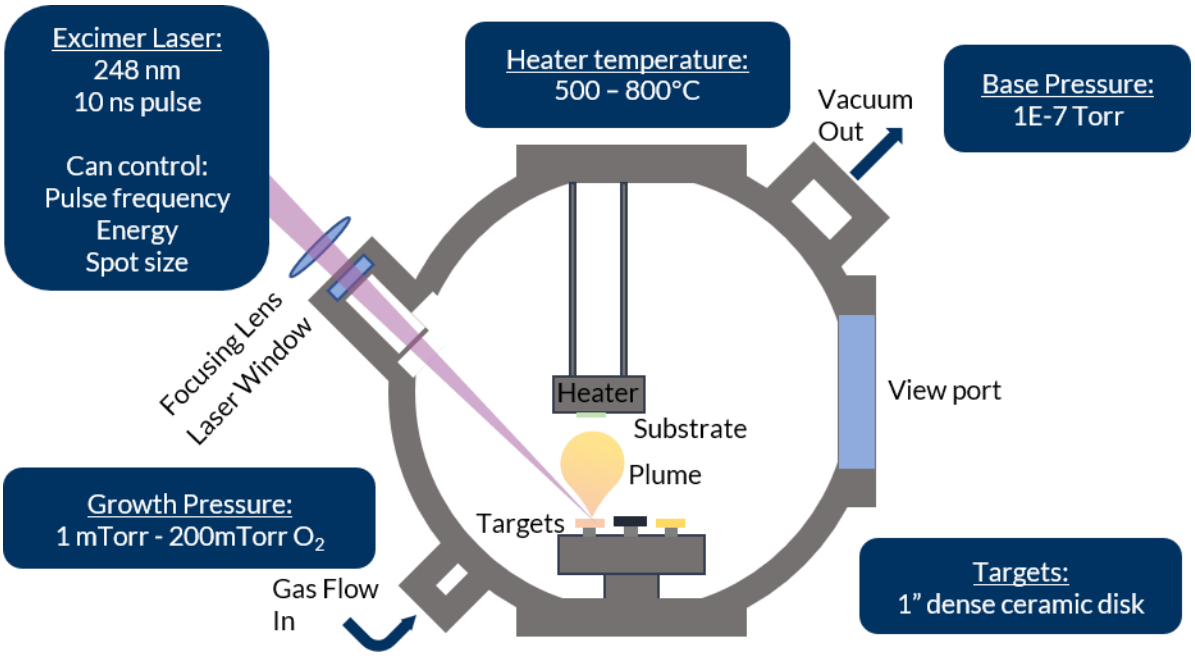

Figure 2.2: Schematic of the pulsed laser deposition chamber used in this work with some relevant parameters

of the substrate, also called adatoms. For example, too high of a fluence can induce crystal defects due to knock-on damage of the deposited film from high-energy incoming adatoms. In ferroelectric $BaTiO_3$ thin films, defects induced from such knock-on damage can dramatically impact the ferroelectric transition temperature and switching kinetics.[34,35] The spot size of the laser determines the fluence, but also the size and dose of the plume, as each pulse ablates a larger volume of material from the target. Controlling the spot size through use of apertures and focusing lenses situated outside the deposition chamber, can effectively increase the deposition rate and hence the growth rate of the film. Laser repetition rate can also determine the growth rate, which can be helpful for reducing the time the film is exposed to high temperatures and reduce volatilization of certain species, as happens in bismuth and lead containing materials such as $BiFeO_3$.[36]

Once ejected from the target, the adatoms in the plasma travel across the chamber toward the substrate, typically through a dynamic, flowing background gas, which is most often oxygen in the case of oxide synthesis. This oxygen pressure, ranging anywhere from 10^{-6} Torr to 100s of mTorr, serves as an oxygen source for the growing thin film, but also serves to scatter and refocus the plume. Deposition in relatively high pressures increases the collisions of adatoms with gas molecules, reducing the kinetic energy of the adatoms, while lower pressures result in wide, less directed plumes with high kinetic energy adatoms. Such control has been used, for example, to induce knock-on damage and create defect-mediated charge traps to reduce leakage in $PbTiO_3$ films.[37] Finally, once the plume reaches the substrate surface, adatoms diffuse along the surface, interacting with the surface potential of the substrate. Each laser pulse deposits only a fraction of the adatoms necessary to form a continuous layer one unit cell thick. With knowledge of the deposition rate, counting pulses becomes sufficient to gain sub-nanometer control of the thickness of the film, while the addition of techniques like reflection high-energy electron diffraction (RHEED) provide *in situ* atomic-level control. With thickness control, and equipment to load and switch between multiple targets, multilayer heterostructures can be constructed *in situ*, to form fully coherent stacks of various materials. This allows for the epitaxial deposition of electrically conducting layers, for example, sandwiching a ferroelectric layer to create epitaxial capacitor structures for later electrical characterization.

The standard procedure for all depositions in this work follows. Prior to deposition the chamber is thoroughly cleaned with isopropanol and the laser window is polished with a colloidal silica soluition (0.05 μm, Ted Pella Inc.). New single-crystal substrates (Crystec, GmbH) are sonicated in acetone and then isopropanol for 5 min. each, rinsing the surface following each sonication. Substrates are fixed to the heater using silver paint (Leitsilber 200 Ag paint, Ted Pella Inc.) and heated at a rate of 10°C/min. to 100°C to cure the silver paint. 1-inch diameter ceramic targets (Praxair, Inc.) are sanded to obtain a fresh surface before each deposition. The chamber is pumped to a base pressure of $< 2x10^{-5}$ Torr (and often into the 10^{-6} Torr range). Once the base pressure is reached, the port to the turbopump is mostly closed, and oxygen is introduced through a variable leak valve to obtain a dynamic pressure between 1-200 mTorr. A KrF excimer laser (LPX 305, Lambda-Physik/Coherent) with a wavelength of 248 nm and pulse duration of 10-30 ns and energies ranging from 80-160 mJ is used first to perform a pre-deposition ablation to clean the surface of the target and then for deposition. During ablation, the target is simultaneously rotated and rastered to evenly ablate the surface. Prior to deposition, the substrate is heated to a deposition temperature ranging from 500-800°C at a rate of 20°C/min. Following deposition, the chamber is filled to an oxygen pressure of 700 Torr and cooled to room temperature at a rate of 10°C/min.

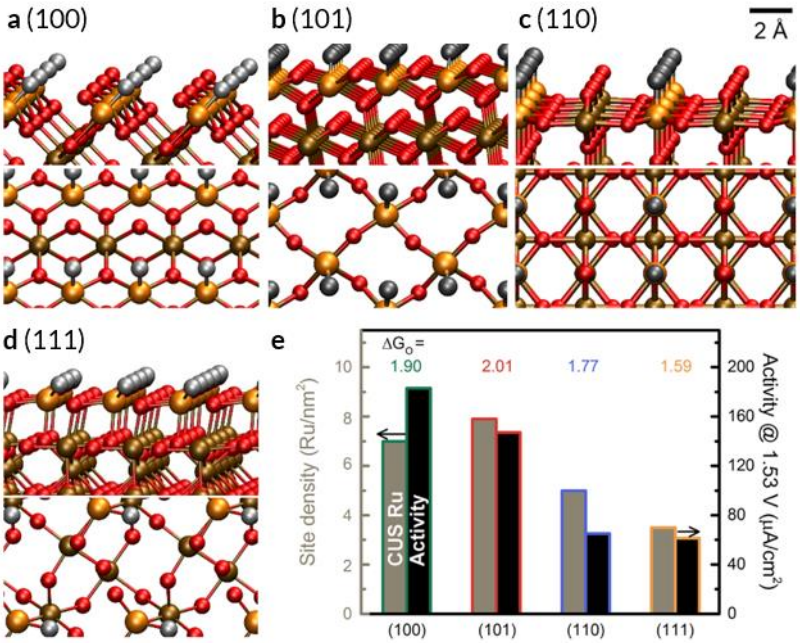

Figure 2.3: Surface-orientation dependence of rutile RuO2 thin films. Reprinted with permission from ref. [*55*] Copyright 2017 American Chemical Society. a-d) Comparison of the coordination of different rutile surfaces. Bulk-like Ru sites are depicted in gold while undercoordinated, active Ru sites are grey. e) The catalytic activity is correlated with the surface density of active Ru sites.

2.3. Controlling surface orientation

The epitaxial relationship between the substrate and deposited film implies that control of the film lattice can be achieved simply through choice of the appropriate substrate. Deposition onto substrates that have been cut along different crystallographic planes of the perovskite crystal allows for synthesis of films with different surface orientations. In ferroic materials, synthesizing films with different surface orientation has been shown to dramatically change the domain structures, polarization, and lattice symmetry of the film, which in turn can impact functional properties such as dielectric permittivity and ferroelectric switching.[38–42]

The control of surface orientation can also have significant impacts on the chemical and electronic structure at the perovskite surface, which are important for perovskite-gas interactions in catalysis. Broken symmetry, dangling bonds, and local defects at oxide surfaces can serve to make the surface more reactive than an idealized "perfect" crystal facet, and even more so in the case of a polar surface.[43,44] A polar surface can be defined as a surface in which there exists a non-zero dipole moment in the repeat unit in the direction perpendicular to the surface. Amongst the various possible terminations for (001), (110), and (111) surfaces in a perovskite, only the (001) surfaces can be non-polar, and only in the case of a composition with A^{2+} and B^{4+} cations. The uncompensated charge at these polar surfaces can be compensated through a number of processes, including formation of local nonstoichiometry, ordering of defects at the surface to create new surface symmetries, or simply by accumulation of charge carriers and a change in band structure near the surface.[43] $SrTiO_3$, (001) surfaces are weakly polar, and some small reconstructions can be observed, particularly in samples that have been vacuum annealed to drive oxygen vacancy formation.[45] $LaAlO_3$ (001) surfaces, which are significantly more polar, exhibit dramatic

reconstructions, and can depend strongly on synthesis conditions.[46] $SrTiO_3$ (110) and (111) surfaces, similarly exhibit a wide variety of surface reconstructions, for example, the formation of (100)/(010) microfacets on (110) surfaces.[47] In addition to structural reconstructions, local nonstoichiometry can be observed at perovskite surfaces. While local *A*-site enrichment of perovskite surfaces is commonly observed,[48] the nonstoichiometry can be so extreme as to result in the formation of distinct phases, as observed in $La_{0.65}Sr_{0.35}MnO_3$ films, which formed an *A*-site-rich Ruddlesden-Popper phase at the surface.[49]

Defects, polarity, and reconstructions of crystal surfaces have significant implications for electrocatalytic properties, and enhanced electrocatalysis at different surfaces of elemental metals and alloys (*e.g*, gold, platinum, and Pt_3Ni) are well established. While reconstructions of perovskites surfaces continue to be studied, there exist only a handful of studies of electrochemical activity at different perovskite surfaces. Various methods have been used to probe the effect of surface orientation, with studies on faceted grains in a bulk ceramic suggesting no orientation dependence,[50] while studies using single crystals of $SrTiO_3$ cut along (001), (110), and (111) surfaces demonstrated large electrochemical differences, with (111) surfaces demonstrating the fastest kinetics.[51] A few thin-film-based studies have been carried out, with a study on $La_{0.8}Sr_{0.2}CoO_3$ reporting fast kinetics on (110)-oriented films,[52] and studies on $La_{0.7}Sr_{0.3}MnO_3$ thin films for found that different surfaces can also possess different activation energies for oxygen exchange.[53] A strong dependence on surface orientation on solution-based electrochemical oxygen exchange was also found in the binary oxide systems, RuO_2 and IrO_2.[54,55] In these systems, thin films with (100) surfaces demonstrated the highest reactivity in alkaline-solution, with density functional theory simulations suggesting the effect was driven by a higher density of undercoordinated ruthenium- and iridium-sites on those surfaces (Figure 2.3).[55] With these studies suggesting a strong dependence of electrochemical activity on surface orientation, there remains a need to carry out systematic investigation of the connection between surface orientation, local nonstoichiometry, reconstructions, and electrochemical activity in perovskite systems to begin to understand important factors for oxygen exchange, and develop surface engineering approaches for enhancing reactivity at oxide surfaces.

2.4. Strain engineering

The ability to epitaxially strain thin films has become one of the most fruitful pathways for engineering perovskite functionalities through structural manipulation. A difference in lattice parameters between a deposited film and its substrate, called the *lattice mismatch* is given by:

$$\frac{a_{film} - a_{substrate}}{a_{film}} \times 100 \qquad (2.1)$$

and serves to describe the strain imposed on the film. For comparison, achieving 1% strain in a typical bulk ceramic or single crystal of $SrTiO_3$ is equivalent to applying 39 GPa of pressure. In thin films, however, lattice strains of 1-3% can regularly be achieved. At the film-substrate interface, the film is forced to adopt the lattice parameters of the semi-infinite and rigid substrate. The film thickness that this coherent strain can be maintained, however, depends on the materials and the magnitude of the strain. Above some critical thickness, the strain energy may become larger than the energy for dislocation formation and the film may begin to relax back to its bulk lattice parameters. A film is said to be *partially relaxed*, if some portion of the film above the critical thickness has relaxed, while in the case of very high lattice mismatch, the critical thickness

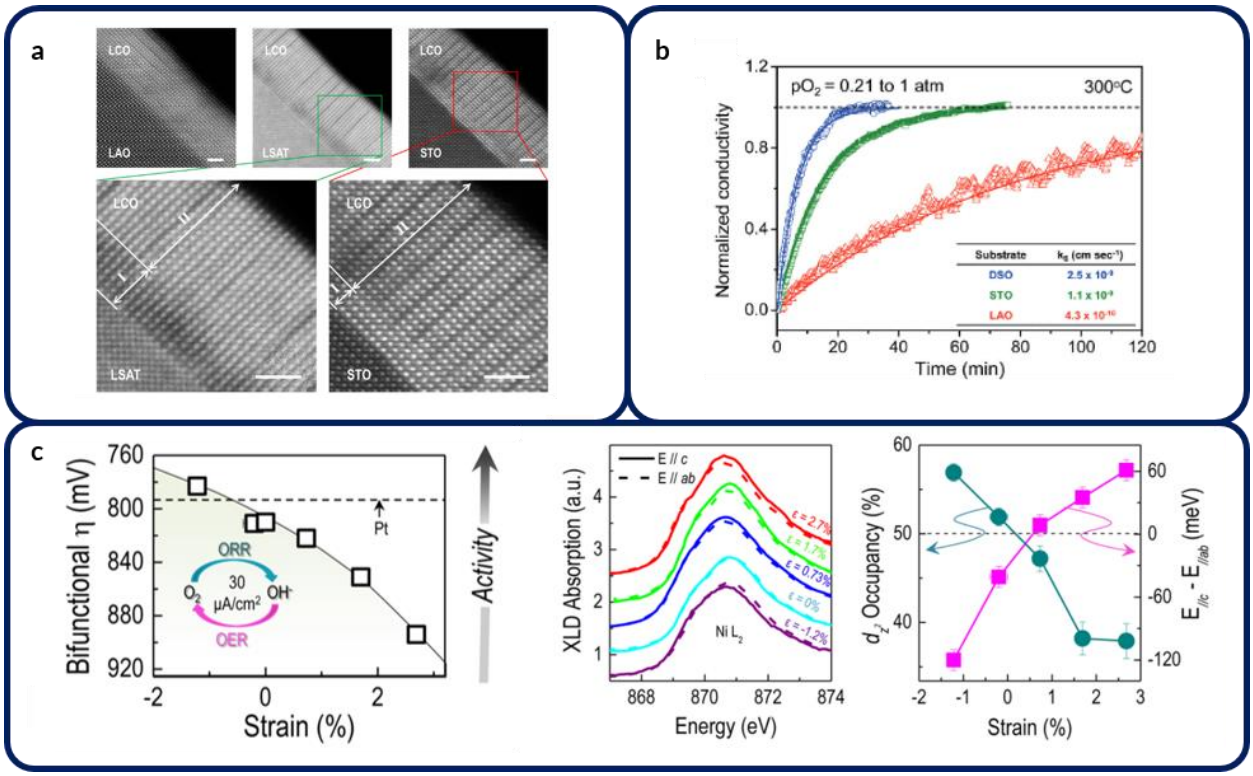

Figure 2.4: Strain dependence of oxygen reactivity in perovskite thin films. a) TEM images illustrate nanoscale ordering of oxygen vacancies (dark stripes) which change ordering period and direction with epitaxial strain. Reprinted with permission from ref. [*77*]. Copyright 2012 American Chemical Society. b) Electrical conductivity relaxation measurements of $SrTi_{0.5}Fe_{0.5}O_3$ show fast reaction kinetics on films under tensile strain (on $DyScO_3$ substrates). Reprinted with permission from ref. [*82*]. Copyright 2007, Royal Society of Chemistry. c) Bifunctional electrocatalysis of $LaNiO_3$ results in a monotonic increase in activity with compressive strain, explained by changing orbital occupation probed by XLD measurements. Reprinted with permission from ref. [*83*] Copyright 2016 American Chemical Society.

can be reduced to only a few unit cells and nearly the entire film can become *fully relaxed* and adopt bulk-like lattice parameters. The application of epitaxial strain shifts the material away from bulk-like structure, and in turn impacts the properties.

The ability to synthesize pristine, single-crystalline materials with lattice parameters that strongly deviate from thermodynamic equilibrium values allows for new dimension of studying and tuning perovskite properties. Ferroelectrics serve as an excellent example of the power of epitaxial strain in dictating properties of thin films.[56] Prototypical tetragonal $PbTiO_3$ can be synthesized in a number of different domain structures with complex hierarchical ordering depending on strain state.[57] Applying large epitaxial strain has also been shown to induce novel ferroelectric phases in $BiFeO_3$,[58] as well as stabilize ferroelectricity in dielectric $SrTiO_3$.[59] The large elastic energies associated with epitaxially strained films can also stabilized complex mixed-phase structures, like that seen in mixed phase T-/R-$BiFeO_3$ domain structures, which are perched near a phase transition such that small applied stimuli are enough to tip the balance and produce large electromechanical responses.[60]

One of the key effects of epitaxial strain in perovskites is the bonding and orbital overlap of the transition metal cations and oxygen anions. As discussed in the previous chapter, changing the bond length can impact the balance of electronic and electrostatic interactions that give rise to perovskite properties. Numerous studies report large strain-induced changes to electronic

conductivity, magnetic properties, and orbital structure in perovskite oxides.[14] In $La_{0.67}Sr_{0.33}MnO_3$, epitaxial strain has been shown to increase resistivity and suppress the ferromagnetic transition under large tensile strains,[61] while films under large compressive strain become insulators.[61,62] Strain can also impact the magnetic properties, changing the magnetic easy axis from in-plane to out-of-plane with increasing compressive strain,[61] and drive complex magnetic stripe domain ordering.[63] In perovskite nickelates (*e.g.*, $LaNiO_3$, $NdNiO_3$) epitaxial strain can shift the temperature of metal-to-insulator transitions,[64,65] while cobaltates (*e.g.* $LaCoO_3$) may undergo a complex evolution of their spin states, giving rise to low-, intermediate-, and high-spin configurations that impact the magnetic order.[66,67] X-ray absorption spectroscopy has become essential in understanding the response of electronic and orbital structure to strain, and such studies of manganites and ferrites have explicitly demonstrated the changing symmetry of the transition metal *d*-orbital occupation as a function of epitaxial strain.[19,68–70] As such, it is now relatively well understood that connections between epitaxial strain, lattice symmetry, and electronic structure are driven by strong coupling between orbital and lattice degrees of freedom, particularly in these systems with partially filled *d* orbitals.

The manipulation of perovskite electronic structure through epitaxial strain suggests strain-control of orbital structure can be used to impact a wide variety of properties beyond charge transport and magnetic structure. Researchers have begun to examine the impact of epitaxial strain on oxygen electrocatalysis, using thin films as model systems to study well-defined perovskite surfaces. In $La_{1-x}Sr_xCoO_{3-\delta}$, it turns out that strain-induced changes to magnetic order are tied to strain-induced changes in oxygen stoichiometry,[71–73] with tensile strain tending to lower the formation energy and increase the concentration of oxygen vacancies. Strain-induced nanoscale ordering of oxygen vacancies has also been observed, forming oxygen-deficient stripes, with the ordering direction changing from out-of-plane under compressive strain to in-plane under tensile strain (Figure 2.4a). [74–77] The strain-dependence of the oxygen vacancy formation energy, and the associated oxygen 2*p*-band center, has been proposed as the driving force for enhanced reactivity of $La_{0.6}Sr_{0.4}CoO_{3-\delta}$ [78] and $SrCoO_x$[79] thin films under tensile strain. In fact, enhanced reactivity under tensile strain in cobalt-based perovskites has been reported using several approaches, including impedance spectroscopy,[78] solution-based electrochemical cells,[80] and oxygen-isotope exchange.[81] Faster kinetics for films under tensile strain were also reported for iron-based materials, including $SrTi_{0.5}Fe_{0.5}O_{3-\delta}$ through high-temperature electrical-conductivity-relaxation measurements (Figure 2.4b).[82] On the other hand, studies of $LaNiO_3$[83] and $NdNiO_3$[84] films have reported slower reaction kinetics under tensile strain, with increased kinetics for films under compressive strain (Figure 2.4c). Only in these latter studies has the electronic structure been directly probed and correlated with electrochemical activity, yet those explanations do not explain the opposite trends observed in cobalt- and iron-based materials, and further studies connecting epitaxial strain, electrochemical reactivity, and surface electronic structure stand to shed new light on strain-dependent reactivities.

2.5. Finite-size effects

Whereas the structures and properties of crystals are often discussed in the context of a semi-infinite lattice with a well-defined unit cell, it is well understood that a material's properties can depend on the size of the crystal, particularly when the size is reduced to nanometer length-scales. Reducing the size of the crystal limits the number of atoms that interact and can dramatically impact the electronic-band structure, and can also shift the balance between surface energy and bulk energy of the crystal volume. For example, the entire field of two-dimensional van der Waals

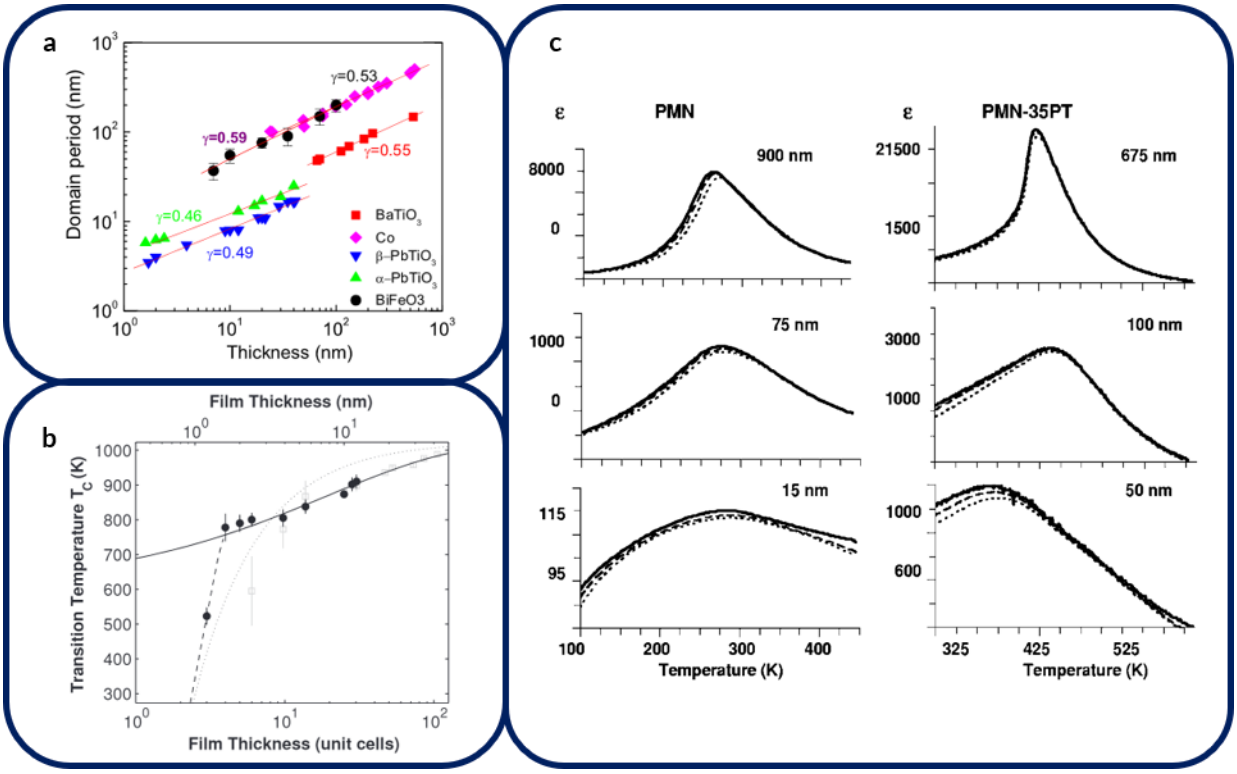

Figure 2.5: Size effects in ferroelectric materials. a) Scaling of ferroelectric domain period with film thickness for various ferroelectric compositions illustrating a power law scaling with exponent ~0.5. Reprinted with permission from ref. [*90*]. Copyright 2008, American Physical Society. b) Scaling of the ferroelectric transition temperature with film thickness shows a suppression of ferroelectric order below 3 unit cells. Reprinted from ref [*17*] with permission from AAAS. c) Size-induced broadening of diffuse phase transitions in relaxor-ferroelectric bulk ceramics show as grain size is decreased from several hundred nanometers. Reprinted with permission from ref [*96*]. Copyright 2005, American Physical Society.

materials, like graphene, hexagonal boron nitride, and the transition-metal dichalcogenides, is predicated on the concept that a single atomic layer of these materials has dramatically different electronic properties than its bulk crystal counterpart.[85] In transition-metal perovskite oxides, numerous studies have demonstrated transitions from metallic (conducting) phases to insulating phases upon reducing the film thickness beyond a critical value.[16,86–88]

The question of finite-size effects, that is, the changes in a material's properties solely from changing the size of the crystal, has also been heavily studied in ferroelectrics. Driven in part by a desire to integrate ferroelectric materials in nanoscale electronic devices, such studies have found size-induced changes to ferroelectric polarization,[89] transition temperature,[17] and domain configuration[90] as film thicknesses are reduced to nanometer length-scales. In brief, the elastic and electrostatic boundary conditions of a ferroelectric crystal are critical in determining the nature of ferroelectric order and reducing a film's thickness down to nanometer length-scales increases the impact of these boundary conditions. In general, ferroelectric domain size follows a power-law scaling with film thickness from several hundred nanometers down to a few nanometers, seen in many ferroelectric systems (Figure 2.5a).[90] At even smaller thicknesses, ferroelectric order can be completely suppressed. X-ray diffraction was used to confirm ferroelectric order in $PbTiO_3$ down to just 3 unit cells, accompanied by the formation of ordered 180° stripe domains, but below 3 unit cells, no ferroelectric transition could be observed (Figure 2.5b).[17] A relatively simple mechanism invoked reconstructions in the outermost unit cells at each of the film's interfaces, leaving a single,

middle unit-cell which can maintain a polar distortion. Yet, while the polar distortion exists in these ultrathin films, maintaining a stable remnant polarization has an even stricter requirement of interfaces which can appropriately screen the polarization. First-principles and experimental studies have both demonstrated that using typical oxide electrodes, remnant polarization becomes unstable below ~5 nm.[91] On the other hand, reports of ferroelectricity in ultrathin, strain-free $SrTiO_3$ films challenge the notion that ferroelectricity is inherently destabilized at reduced dimensions.[92] Studies continue to understand the impact surfaces and interfaces have on ferroelectric remnant polarization, coercive fields, and switching speeds.

These studies examining the thickness scaling and limitations to ferroelectric stability have primarily focused on prototypical materials such as $PbTiO_3$ and $BaTiO_3$, which have well-defined unit cells and long-range order, and still a variety of effects are observed in ultrathin films. Even less clear is how finite-size effects impact a film where chemical disorder is critical for the material's bulk properties. Chemical disorder in relaxor ferroelectrics drives formation of locally correlated nanoscale clusters of polarization that produce large pyroelectric and piezoelectric responses.[93–95] It remains an open question as to what impact restricting the thickness of a relaxor-ferroelectric film, or in other words, limiting the number of atoms that can contribute to disorder and polar correlations, has on the pyro-, piezo- and ferroelectric properties. For example, one might imagine that reducing the film thickness to a length-scale comparable to the size of polar nanodomains might serve to stabilize normal ferroelectric order, as polar correlations could extend the full thickness of the film. Several studies have attempted to broach this question utilizing controlled grain size and microstructure of bulk ceramics.[96–98] In general, reducing grain size reduces the magnitude of the dielectric permittivity, but these studies also produced somewhat contradictory conclusions regarding the temperature of the permittivity maximum. In $PbMg_{1/3}Nb_{2/3}O_3$, one study reported very little shift in temperature is observed upon decreasing grain size from 6 μm to 300 nm,[98] while another suggested an increase in transition temperature upon reducing the grain size from as large as 3 μm (Figure 2.5c).[96] In $0.65PbMg_{1/3}Nb_{2/3}O_3$-$0.35PbTiO_3$, the transition temperature was dramatically reduced only at grain sizes below approximately 100 nm (Figure 2.5c).[96] One problem plaguing studies on polycrystalline ceramics is the lack of control of grain size, which inevitably results in a distribution of grain sizes, and other extrinsic factors like density of the ceramic, morphology of the grains, grain boundary density, and the different processing parameters that need to be changed to control the grain size.[99] All of these can contribute to extenuating factors which cloud interpretation of the true impact of crystal size. On the other hand, thin-film based studies allow for precise thickness control to atomic length-scales in a single crystalline sample, removing extrinsic contributions.

2.6. Freestanding membranes

Thin-film epitaxy has enabled numerous scientific advances in perovskite-oxide research, much of which has been made possible by the fine degree of control over boundary conditions and atomic precision afforded by such techniques. Yet, the necessary requirement of a large rigid substrate supporting the thin film can have strong impact on a materials elastic response. For piezoelectric films, in particular, clamping of the film to the substrate has long been invoked as the reason for surprisingly low piezoelectric coefficients in thin films as compared to their single crystalline counterparts. For example, in single crystals of relaxor ferroelectric solid solutions such as $0.70PbMg_{1/3}Nb_{2/3}O_3$-$0.3PbTiO_3$ ultrahigh piezoelectric coefficients (d_{33} > 2500 pC/N) have been reported, yet the coefficients for thin films of identical compositions can be more than an order of magnitude lower.[100] A variety of methods of releasing this clamping have been attempted,

including fabricating cantilevers,[101] where a freestanding bar of piezoelectric materials is made by undercutting the film with various etchant processes, or by fabricating islands to reduce clamping from inactive regions of the piezoelectric itself.[102,103] Meanwhile, in just the last few years, interest in the properties of freestanding membranes of perovskite oxide thin films has steadily increased. Inspired by progress in two-dimensional materials synthesis and processing, researchers have developed sacrificial layers which allow for epitaxial deposition of a large number of perovskite oxide films, which can subsequently be released by selective chemical etching of the sacrificial layer, and transfer of the freestanding oxide membrane to an arbitrary substrate.[104,105] Here, a suitable sacrificial layer is chosen such that the desired film can be synthesized as a coherent heterostructure on a substrate buffered with the sacrificial layer. After deposition, the sacrificial

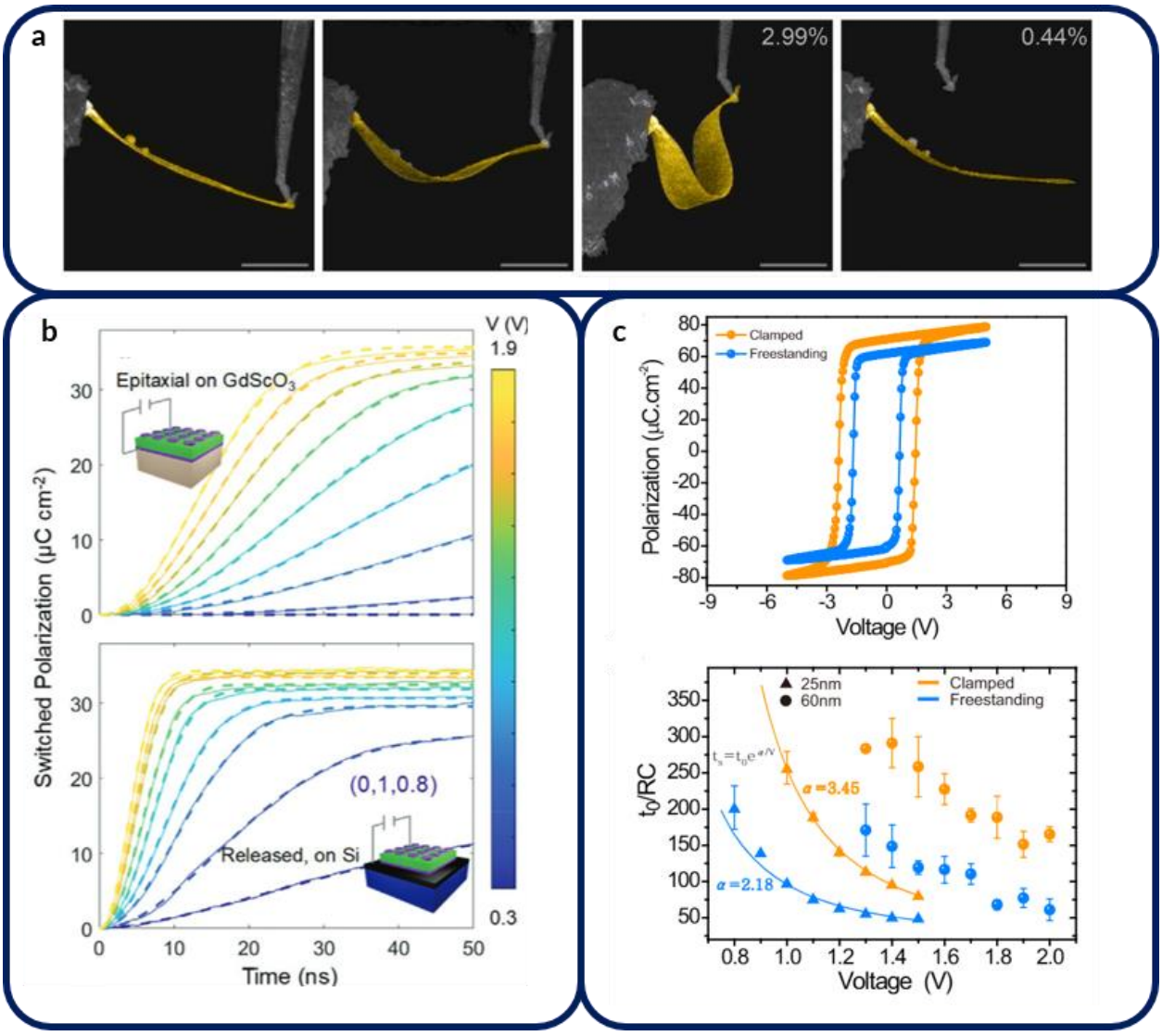

Figure 2.6: Freestanding ferroelectric membranes. a) $BiFeO_3$ nanoribbons demonstrate usually large elasticity. Reprinted from ref [*107*] under Creative Commons 2020, b) $BaTiO_3$ capacitor heterostructures transferred to Si demonstrate faster switching speeds than clamped films on $GdScO_3$ substrates. Reprinted with permission from ref [*104*], Copyright 2020, Wiley VCH. c) Freestanding $BiFeO_3$ capacitor heterostructures exhibit reduced coercive field and reducing switching speeds compared to clamped counterparts. Reprinted from ref [*109*], under Creative Commons, 2021.

layer is chemically etched, breaking the bonds between the film and substrate, and the freestanding membrane can then be transferred to alternative substrates.

The results from this work have demonstrated significant changes to the properties of freestanding perovskite membranes compared to their clamped counterparts. Studies have demonstrated enhanced elasticity of freestanding membranes, including biaxial stretching of $La_{0.7}Ca_{0.3}MnO_3$ films transferred to a stretchable polymer, where strains up to 8% could be sustained, a feat unachievable even with the aid of epitaxy.[106] Freestanding nanoribbons of $BiFeO_3$ films were observed to undergo large bending strains approaching 6%, facilitated by a reversible ferroelastic phase transformation,[107] while $SrTiO_3$ films probed with an atomic force microscopy tip were demonstrated to have an increase in Young's Modulus at reduced thickness, attributed to enhanced contributions from strain-gradient elasticity at thicknesses below 31 nm.[108] Outside of purely elastic effects, researchers have only just begun to explore the impact of releasing the mechanical constraint of the substrate on ferroelectric and piezoelectric properties. Studies on freestanding $PbZr_{0.2}Ti_{0.8}O_3$ membranes transferred to silicon reported more disordered switching and slower domain-wall dynamics, measured by scanning probe microscopy, due to pinning by flexoelectric fields originating from broken-bonds and disordered interfaces in the transferred films. Contrary to this, studies on freestanding epitaxial capacitor structures of $BaTiO_3$ and $BiFeO_3$ reported lower coercive fields and faster switching speeds compared to their substrate-supported counterparts.[104,109] In $BaTiO_3$, this effect was suggested to originate from a lower energy barrier for ferroelastic switching, allowing for two-step 90° switching, which is prevented by the elastic constraint in the clamped film. Phase-field simulations of freestanding $BiFeO_3$ membranes similarly suggested that a dynamic clamping arising from simultaneous clamping of the lattice strain, and octahedral rotations, both of which are coupled to the polarization, limits the switching speed in clamped films. These studies, which have been performed only in the last few years, are just the beginning of understanding elastic and ferroelectric effects originating from substrate clamping. As such, open questions remain as to the role of substrate clamping in limiting the piezoelectric response, both in magnitude and dynamics, of relaxor-ferroelectric compositions, and a detailed studied of ferroelectric and piezoelectric responses in freestanding relaxor-ferroelectric compositions can illuminate such effects.

The background provided here lays the foundation for asking intriguing questions regarding the effect of thin film boundary conditions and manipulation of the perovskite lattice on a variety of important properties. Using pulsed laser deposition, coupled with optimized growth parameters for a variety of materials, and the appropriate single crystalline substrate, model systems can be synthesized to study the effect of surface orientation and epitaxial strain on oxygen electrocatalysis at perovskite surfaces, as well as the dielectric, ferroelectric, and piezoelectric properties of relaxor films at reduced thicknesses or after release from the substrate.

Chapter 3:
High-temperature oxygen electrocatalysis

This chapter provides background on the operating principles and materials considerations for perovskites for solid oxide fuel cell cathodes, as well as characterization techniques for probing electrocatalytic properties in perovskite thin films. First, the basic motivation for studying fuel cell cathodes is provided along with general operating principles. The desired properties for high-performance cathodes and commonly studied compositions are discussed to provide context for the choice of $La_{1-x}Sr_xFe_{1-y}Co_yO_{3-\delta}$ compositions studied in this dissertation. Finally, techniques for characterizing electrochemical properties of thin films, as well as relevant surface chemistry and electronic structures are presented.

Chapter 3: High-temperature oxygen electrocatalysis

3.1. Solid oxide fuel cells and the oxygen-reduction reaction

It has becoming increasingly clear that a rapid shift away from the currently ubiquitous combustion engine as a source of electrical-energy generation will be necessary to mitigate the impact of climate change in the coming decades. Solid oxide fuel cells (SOFCs) provide a means for direct electrochemical-energy conversion without combustion of the fuel, promising cleaner, more efficient generation of electrical energy.[110] Moreover, the fuel requirements are very flexible, allowing for use with either hydrocarbons or hydrogen, making SOFCs an important transitional technology for moving away from a carbon-based economy. The operating principles of such electrochemical cells have long been known, yet advances in materials understanding has only recently pushed them to the brink of widespread commercial adoption. Several companies are in the process of developing fuel cells for both large-scale commercial generation, and home-scale use.

In general, a fuel cell combines two electrochemical reactions to create a flow of electrical current (Figure 3.1). While there are many types of fuel cells, using a variety of electrolytes that conduct charge via protons, carbonates, hydroxides, molten salts, *etc.*, SOFCs are based on electrolytes that conduct oxygen anions.[111] This electrolyte separates the cathode which is fed molecular oxygen, typically in the form of air, while fuel is fed to the anode. The cathode catalyzes the oxygen-reduction reaction (ORR):

$$O_2 + 4e^- \rightarrow 2O^{2-} \tag{3.1}$$

producing oxygen anions (O^{2-}) which diffuse through the electrolyte to the anode, where they are used in the oxidation of a fuel, for example hydrogen, that is catalyzed at the anode:

$$2H_2 + 2O^{2-} \rightarrow 2H_2O + 4e^- \tag{3.2}$$

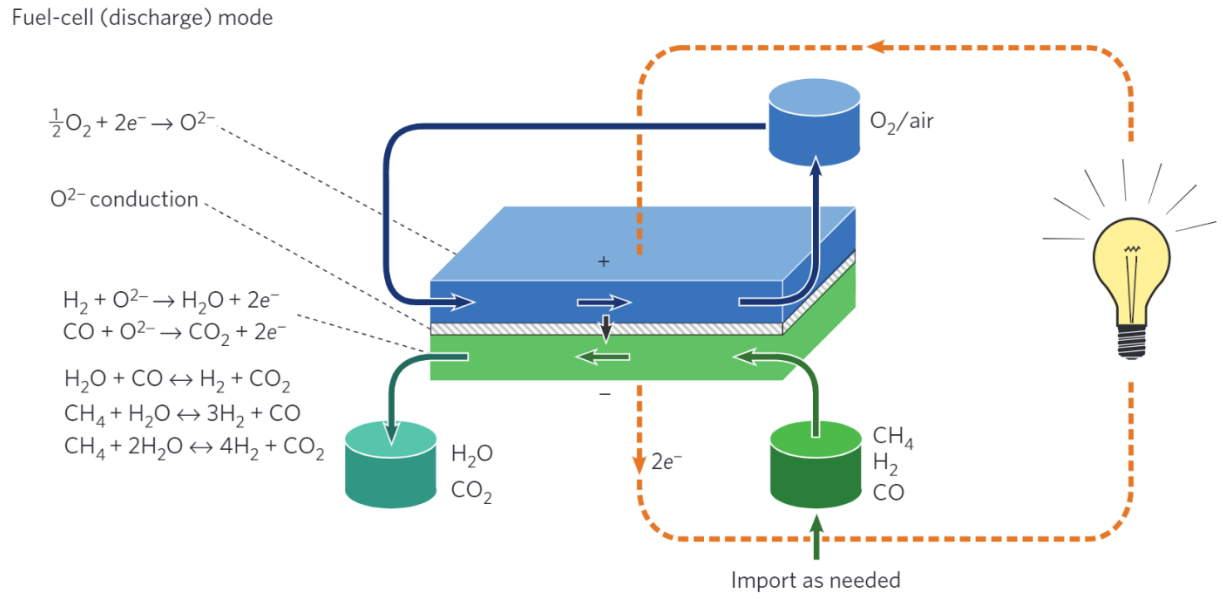

Figure 3.1: Schematic of a solid oxide fuel cell. The cathode (blue) catalyzes the oxygen reduction reaction while the anode (green) catalyzes the oxidation of fuel. Oxygen vacancies are transported from cathode to anode through the anion conducting electrolyte (striped). Reprinted with permission from ref [*113*], Copyright 2014, Springer Nature.

The combined reactions generate an electrical current, allowing fuel cells to be used to convert chemical energy to electrical energy. All three components should have relatively high oxygen-anion conductivity, and the cathode and anode should possess good electrical conductivity, while the electrolyte should be electrically insulating to avoid leakage current. Running these reactions in reverse, the same stack can be used as an electrolyzer cell, where electrical energy is consumed to produce hydrogen and oxygen gases from water in a solid oxide electrolyzer cell (SOEC). The remainder of the discussion is limited to SOFCs, but many of the same materials considerations and benchmarks apply to both SOFC and SOEC designs, and in some cases the same cell can provide reversible operation.[112,113] Current SOFCs are operated at high temperatures (800-1000°C) to promote high ionic conductivities, and increase reaction rates, yet high temperature operation also leads to degradation of component oxides via interdiffusion, demands expensive high-temperature-stable metallic interconnects, and reduces efficiency of the fuel cell.[111] To address these issues, there is a concerted research effort to lower the operating temperature of SOFCs to so-called intermediate temperatures in the range of 500-700°C, allowing for cheaper fabrication, longer lifetimes, and quicker start-up times.[110,114,115]

As the operating temperature is lowered, however, the large activation energy (E_a) of the ORR results in large polarization resistances at the cathode, which become the major limiting factor to high cell efficiencies at intermediate temperatures.[116,117] In this dissertation, we focus our attention on materials of interest for fuel-cell cathodes and the kinetics of the ORR. New approaches for engineering ORR catalysts require understanding of the atomistic processes involved in the ORR, and how these processes are influenced by the cathode's atomic, chemical, and electronic structure, particularly at the surface. The electrochemical reduction of molecular oxygen at an oxide surface involves several steps.[118–120] Broadly, the reaction involves adsorption of an oxygen molecule, two electron reduction of the oxygen molecule, incorporation of the reduced oxygen anions, and

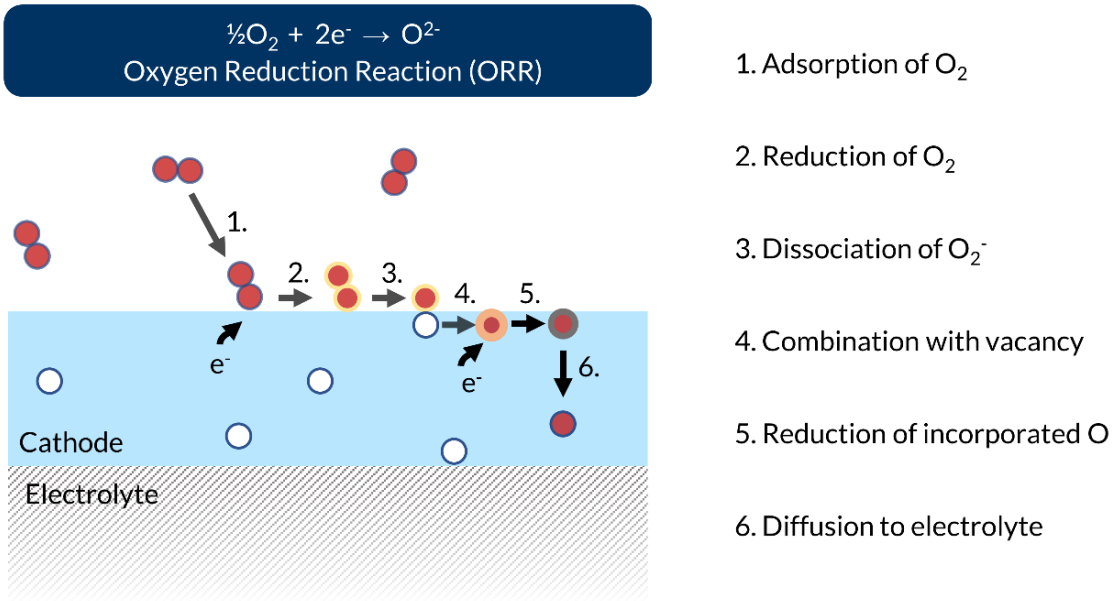

Figure 3.2: Schematic of one possible reaction pathway for oxygen reduction on a perovskite surface exhibiting adsorption, charge transfer, dissociation and diffusion processes.

diffusion of the oxygen to the electrolyte, but the order of these steps is not known *a priori.* One possible pathway is presented (Figure 3.2). First, an oxygen molecule is adsorbed on the surface, which subsequently accepts and electron from the cathode. This partially reduced oxygen then dissociates into oxygen atoms which can be reduced again to oxide anions via another reduction. Oxide anions are then incorporated through recombination with oxygen vacancies on the surface, and finally diffuse through the lattice to the electrolyte. Density functional theory (DFT) calculations have examined this process on perovskite surfaces,[121,122] suggesting that adsorption of oxygen occurs at surface oxygen vacancy sites through interaction with the transition metal d_z^2 orbital and subsequent one-electron reduction of the oxygen molecule to the superoxo state (O_2^-) serves to facilitate oxygen dissociation.

3.2. Material considerations for the study of electrochemical activity in perovskites

What materials are "good" cathodes for SOFCs? A SOFC cathode must provide high reactivity for the ORR, as well as possess both high electronic conductivity and ionic conductivity. In addition, the cathode must be both thermochemically and thermomechanically compatible with the other components of a fuel cell such that thermal expansion mismatch and interdiffusion of the cathode with the electrolyte and metallic interconnects are reduced. The chemical and structural flexibility of perovskites, as well as their relative abundance and low-cost compared to noble metal-based catalysts has made them an important class of materials for catalysis.[4] Chemical optimization has long been the prevailing method for finding high-performance compositions, and numerous perovskite compositions, as well as related phases with ordered double perovskite, Ruddlesden-Popper, or even the vacancy-ordered perovskite Brownmillerite structures, are under study for ORR reactivity.[114,123] Transition metal *B*-sites with partially filled *d* orbitals, most often cobalt, iron, manganese, and nickel, form the basis for providing catalytic reactivity, while the *A*-site is typically trivalent lanthanum (La^{3+}). Such La*M*O_3 (*M* = Co, Fe, Mn) compositions, however, are typically poor electronic conductors with predominantly p-type conduction,[124] as well as poor ionic conductors. To achieve desirable levels of mixed ionic and electronic conductivity (MIEC), heterovalent substitution with Ca^{2+} or Ba^{2+}, but most often Sr^{2+} is used. Substitution of La^{3+} with Sr^{2+} requires charge compensation to maintain charge neutrality,[125] which can be achieved by formation of positively charged electron holes (*i.e.*, removal of electrons), increasing the concentration of the majority charge carrier, increasing electronic conductivity:

$$2\mathrm{SrO} + \frac{1}{2}\mathrm{O}_2 \rightarrow 2Sr'_{La} + 3\mathrm{O}_\mathrm{O}^\times + h^\cdot, \tag{3.3}$$

or formation of positively charged oxygen vacancies, increasing ionic conductivity:

$$2\mathrm{SrO} \rightarrow 2Sr'_{La} + 2\mathrm{O}_\mathrm{O}^\times + 2V_O^{\cdot\cdot}. \tag{3.4}$$

This results in an equilibrium between oxygen vacancies and electron holes that depends on the partial pressure of oxygen:

$$\mathrm{O}_\mathrm{O}^\times + 2h^\cdot \rightleftharpoons V_O^{\cdot\cdot} + \frac{1}{2}\mathrm{O}_{2(\mathrm{g})}. \tag{3.5}$$

As such, strontium substitution results in both increased electronic and ionic conductivities. While important for achieving desirable electrochemical properties, strontium substitution also results in an additional degradation mechanism, namely the segregation of strontium atoms to the surface of the cathode, ultimately blocking catalytically active transition-metal sites and reducing performance. Understanding and mitigating strontium segregation is an important factor in benchmarking cathode performance.

Historically, the choice of perovskite compositions for use in fuel cells has evolved as operating conditions and materials understanding has developed. Compositions in the $La_{1-x}Sr_xMnO_3$ (LSMO) system have been the cathode of choice for fuel cells operating at high temperatures (800-1000°C), due to good thermal stability, high electrochemical activity and chemical compatibility with common electrolytes such as yttria-stabilized zirconia and the perovskite ionic conductor $La_{0.8}Sr_{0.2}Ga_{0.8}Mg_{0.2}O_{3-\delta}$ (LSGM).[114,126–128] Yet, at lower operating temperatures, the activity of LSMO drops off dramatically.[127] Using cobalt-based compositions resulted in significantly higher reactivity for cathodes measured at 600°C.[117,129] Despite these promising results, however, it was found that compositions in the $La_{1-x}Sr_xCoO_3$ (LSCO) system tend to both be thermally incompatible, due to a high thermal expansion coefficient, and chemically incompatible with common electrolyte materials.[117,130] These problems have been mitigated to some extent by substitution with iron, which serves to stabilize the cathode, but also results in lower reactivity.[131] As such, materials in the $La_{1-x}Sr_xCo_{1-y}Fe_yO_{3-\delta}$ (LSCF) are now widely studied, providing a good compromise between electrochemical activity and thermomechanical and thermochemical stability.[117,125,132,133]

There is now a concerted effort to understand the electronic characteristics that give rise to the difference in reactivity between catalysts with different transition metal sites, with the ultimate goal of developing electronic descriptors that can be used in the rational design of new catalysts without the need for extensive compositional screening and testing.[4,134–136] Due to the complexity of the ORR on perovskite surfaces, involving adsorption, dissociation and diffusion of oxygen molecules, adatoms, and surface vacancies, several electronic descriptors have been put forth. On one hand, the formation energy of surface oxygen vacancies has been shown to be important, as vacancy sites are necessary for adsorption of molecular oxygen.[121,137] At the same time, the relative position of the oxygen 2*p* band center with respect to the

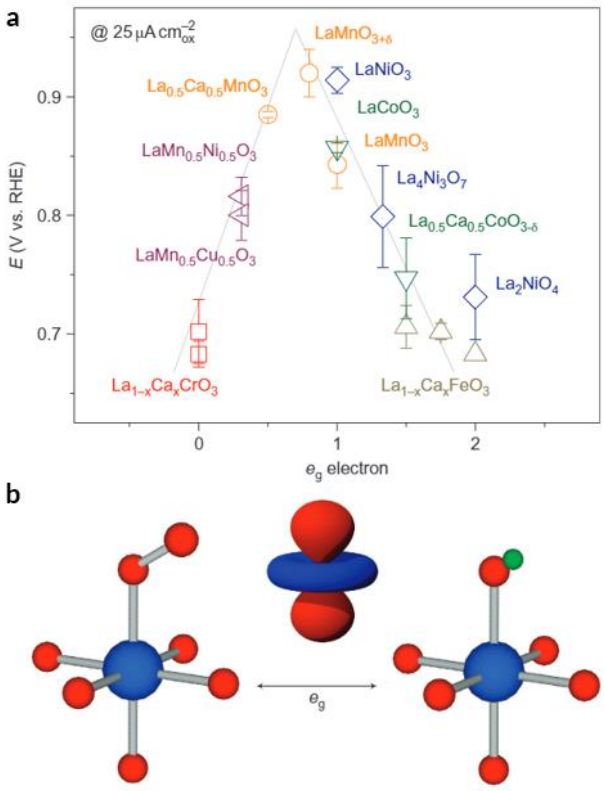

Figure 3.3: a) Volcano plot of various perovskites with different transition metals exhibiting that there is a dependence on the number of electrons in the e_g orbitals of the transition metal site. b) Schematic of the BO_6 octahedra illustrating the geometry of molecular oxygen binding at the transition metal site. Reprinted with permission from ref [*136*], Copyright 2011, Springer Nature.

Fermi level was demonstrated to be directly correlated with both experimentally determined surface-reaction rates, as well as simulated energy barriers for surface-oxygen diffusion, and oxygen dissociation, with a lower energy oxygen 2*p* band center resulting in lower reaction rates.[134,137–139] The structure of the transition metal *d* bands has also been long known as a descriptor for elemental metal catalysts,[140,141] and an analogous structure has been proposed for transition-metal perovskites that takes into account orbital hybridization and crystal-field effects, namely, the filling of the transition metal e_g orbitals. In this case, it has been proposed that an e_g filling of 1.2 electrons results in the fastest kinetics,[136] visualized as a so-called volcano plot. With these descriptors in mind, we can turn now from the impact of chemistry, to the impact of lattice structure on both the electronic structures and the catalytic reactivities of perovskites.

Choosing a composition to serve as a model system for the study of lattice effects requires several considerations. The LSCF system, as described above, is widely studied, used as a cathode in fuel-cell systems, and a promising candidate for intermediate-temperature fuel cells. Moreover, the compromise between reactivity and stability is important for performing extensive high-temperature measurement without degradation issues. Narrowing the precise composition under study also requires examination of practical experimental considerations. Specifically, the specific *x* and *y* values for strontium and iron substitution impact the lattice parameter, which is always an important consideration for synthesizing high quality epitaxial thin films. With the goal of studying the relationship between electrochemical activity and both the surface orientation and epitaxial strain, the composition $La_{0.8}Sr_{0.2}Co_{0.2}Fe_{0.8}O_3$ (a = 3.906 Å)[142] was chosen due to the small lattice mismatch (-0.02%) with the widely used and commercially available perovskite substrate $SrTiO_3$. In the case of the study of surface orientation, not only are $SrTiO_3$ substrates that are cut along different crystallographic planes widely available, but high-quality $La_{0.8}Sr_{0.2}Co_{0.2}Fe_{0.8}O_3$ thin films can be synthesized with nearly bulk-like lattice parameters, isolating the impact of surface orientation from the influence of changing lattice symmetry or epitaxial strain. On the other hand, the small lattice mismatch also provides a good control sample for the study of epitaxial strain, and substrates with ±1% lattice mismatch with $La_{0.8}Sr_{0.2}Co_{0.2}Fe_{0.8}O_3$ are also widely available, making synthesis of epitaxial films under a variety of epitaxial strain states readily achievable.

3.3. Electrical characterization of thin-film cathodes

A number of methods for characterizing the electrochemical properties of epitaxial thin films exist, utilizing half-cell devices or single-layer thin films, and can probe either gas-phase or solution-based reactions. In addition, understanding the impact of lattice manipulation on electrochemical reactivity should include examination of the lattice-induced changes to electronic and chemical changes to perovskite surfaces. *In situ* measurement of the various electrochemical, electronic, and chemical changes in environments resembling the operating conditions of real fuel cells serves to provide more realistic and direct evidence of the impact of lattice manipulation on perovskite cathode properties. In this dissertation, electrical characterization of both single-layer films and novel all-perovskite half-cells was used to investigate the impact of surface orientation and strain on electrochemical properties, while surface-sensitive spectroscopic techniques were used to draw connections between electronic and chemical surface structures to the electrocatalysis in perovskite thin films.

3.3.1. Charge transport

The electronic conductivity of these cathode materials depends strongly on the partial pressure of oxygen, as outlined in the previous section, allowing for the use of charge transport measurements as a probe of oxygen nonstoichiometry. Measurement of the charge carriers in electrically conductive films can be carried out by a simple four-point current-voltage (I-V) measurement (Keithley 2400, Tektronix, Inc.), where current (voltage) is applied to two electrodes on the film and voltage (current) is measured across two separate electrodes. The use of a four-point measurement allows for separation of the contact resistance from the actual charge transport inside the material. Different geometries are also possible, including the standard collinear measurement, where current is applied to two outer contacts and voltage measured across two inner contacts. A van der Pauw geometry can also be used, which involves applying a current across one edge of the sample, and measuring voltage across the other edge. Performing this measurement with different permutations of the driving and measuring edges provides a sheet resistance value, and requires a regular rectangular-shaped sample, while the collinear measurement can be performed on any shape of sample.

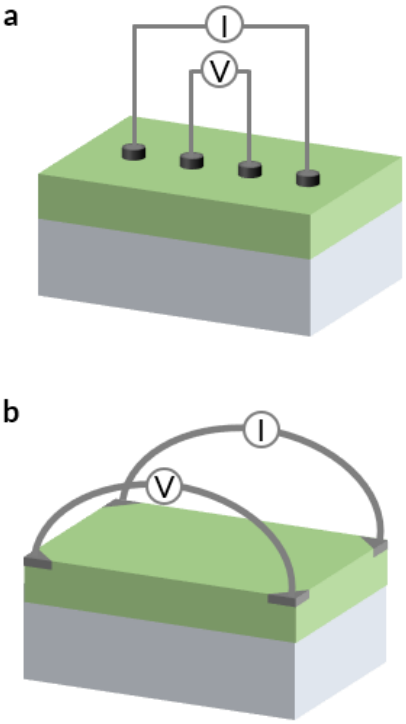

Figure 3.4: Possible geometries for four-point resistivity measurements a) collinear contacts or b) van der Pauw geometry.

Performing charge-transport measurements in different sample environments (*e.g.*, different temperatures and partial pressures of ambient gases) can provide additional information regarding the nature of charge carriers in the material. In this dissertation, temperature- and pressure-dependent transport measurements were carried out in a tube furnace with a home-built measurement apparatus which allowed for electrical contacting of a sample inside a sealed alumina tube (2-inch diameter) with temperature, total pressure, gas flow, and gas concentration control. The alumina tube used a custom-built flange which combined electrical BNC and gas feedthroughs with an internal alumina support bar on which the sample was mounted. Samples are mounted to a CERDIP chip carrier package with silver paint, and sample contacts are wired-bonded to the chip carrier. The leads of the chip carrier were connected to the BNC feedthroughs which can be connected to external current-voltage source meters and potentiostats to conduct various electrical characterization. A separate feedthrough is used to insert a K-type thermocouple adjacent to the sample mount to monitor the actual temperature of the sample during experiments. The opposite end of the alumina tube is connected to a vacuum pump to evacuate the tube, and a pressure gauge is used to monitor the total pressure.

In addition to quasi-static charge transport at fixed temperature and pressure, probing dynamic changes to charge transport while the sample undergoes an environmental change can provide information regarding the surface electrochemical interaction with the ambient gas. Specifically, electrochemical characterization of single-layer perovskite films were measured using a technique known as electrical-conductivity relaxation, which leverages the balance between charge carriers and atmospheric oxygen described by the defect equilibria above (section 3.2). Here, the resistivity (or conductivity) of the sample is measured as a function of time

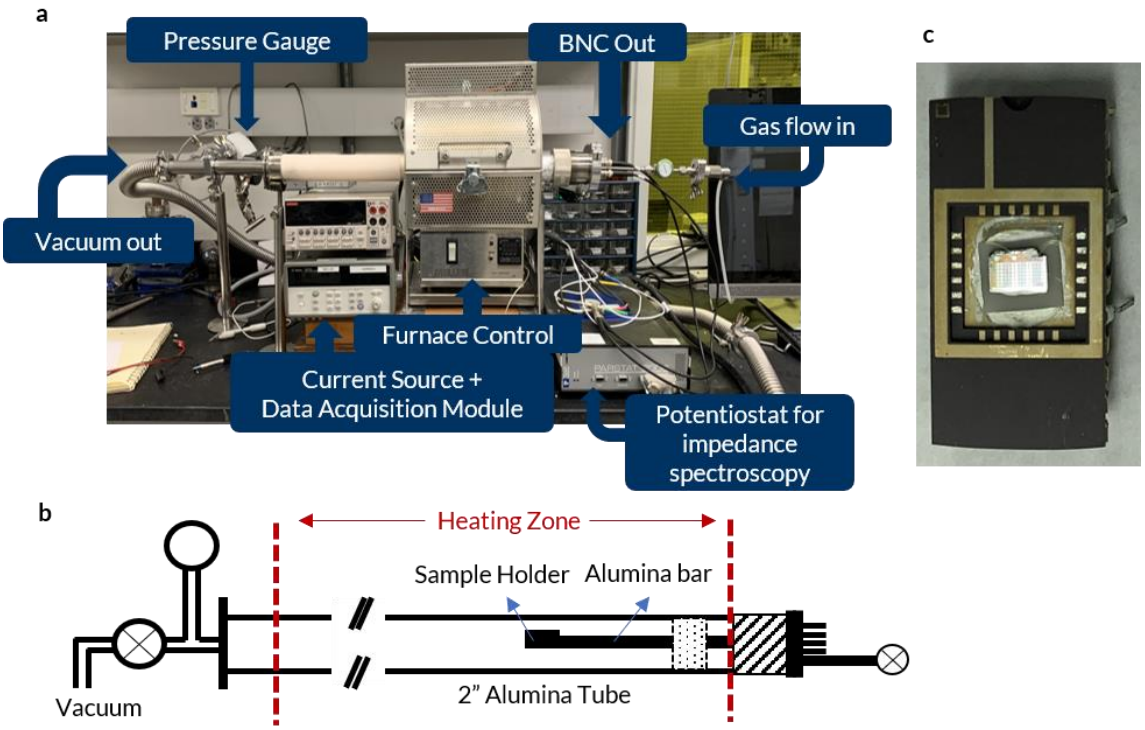

Figure 3.5: Tube furnace-based measurement setup for temperature- and pressure-controlled transport and impedance measurements. a) A photograph of the home-built furnace setup used in this work. b) A schematic of the inside of the alumina tube depicting sample support bar inside the heating zone of the furnace. c) A photograph of a sample wire-bonded to a chip carrier for measurement.

following a step-change in the partial pressure of oxygen gas in the tube at high-temperature.[125,143] Two external mass flow controllers were used to maintain a constant gas flow rate into the tube. At time t = 0, one mass flow controller was switched from flowing pure oxygen to pure nitrogen (or vice versa) to create a sudden change in oxygen-partial pressure. The resulting change to the thin film's resistivity provides a means of measuring the rate of oxygen exchange, as the oxygen vacancy concentration in the film equilibrates with the new gas atmosphere.

3.3.2. Electrochemical-Impedance Spectroscopy

Another common measurement technique for assessing electrochemical activity is electrochemical-impedance spectroscopy (EIS) on half-cell structures. Here, an electrochemical cell is created, where the material under study acts as one active electrode and is separated from a counter electrode by an electrolyte. A potentiostat (PARSTAT 3000, Princeton Applied Research) is used to apply a small AC voltage (5 mV_{rms} in this work) across the two electrodes, and the current response of the half-cell is measured as a function of excitation frequency (in this dissertation several millihertz to several hundred kilohertz). The impedance, $Z(t)$, can be calculated as:

$$Z(t) = \frac{V(t)}{I(t)} \frac{V_0 \sin(\omega t)}{I_0 \sin(\omega t + \varphi)}, \tag{3.6}$$

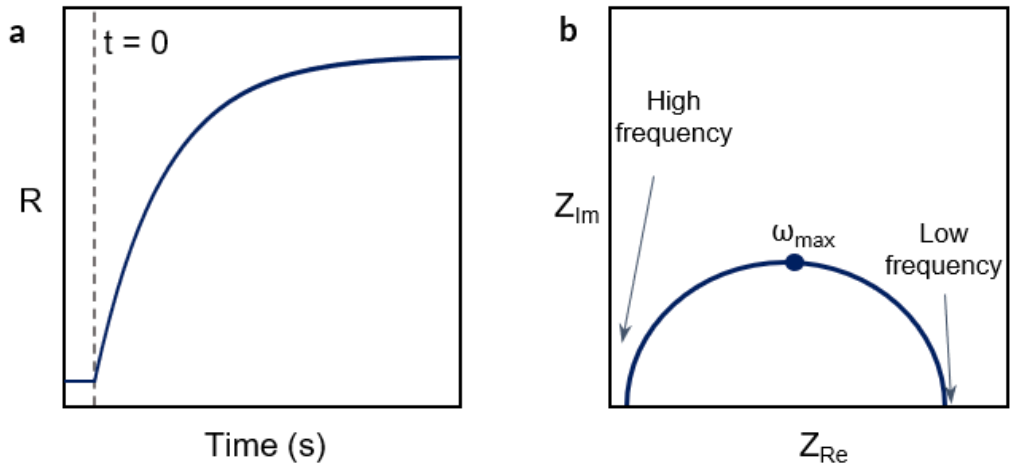

Figure 3.6: Schematic representation of a) electrical conductivity relaxation measurements and b) Nyquist plot of complex impedance plane.

where the AC current response, $I(t)$, is phase-shifted from the AC applied voltage, $V(t)$, by some phase angle, φ. This phase shift indicates that the impedance is a complex value:

$$Z = Z(Re) + Z(Im) = Z_0(\cos\varphi + j\sin\varphi). \tag{3.7}$$

Typical impedance response of the half-cell as a function of frequency is visualized in a Nyquist plot, which is a parametric plot of Z_{re} vs. Z_{im}, with each point measured at a different frequency. The Nyquist plot is then fit using equivalent-circuit analysis, in which the response of a circuit that accounts for the various possible electrochemical and charge transport processes occurring in the half-cell as standard circuit elements is simulated.[144,145] For example, a simple RC circuit produces a Nyquist plot with a single semi-circle, with the max Z_{im} occurring when the measurement frequency matches the RC time of the circuit:

$$RC = \frac{1}{\omega_{max}}. \tag{3.8}$$

Observation of multiple semi-circles suggests multiple sub-circuits with different frequency responses, and other deviations from this behavior may be accounted for with more complex circuit elements. Fitting the equivalent circuit to the real data provides information on the impedance contributions from various electrochemical processes. Performing the electrochemical impedance spectroscopy measurements across a range of temperatures and gas environments can provide additional information, including activation energies and rate-limiting steps, of the half-cell.[146]

3.4. X-ray spectroscopy

X-ray spectroscopy is a powerful tool for studying chemical and electronic structure of material surfaces. In these measurements, an incident X-ray beam is absorbed by the film, exciting electrons from various energy shells, and in the case of the measurements described here, the excited electrons are measured to provide information on atomic structure. In this dissertation, the bulk of the spectroscopy measurements were performed using the synchrotron at the Advanced Light Source of Lawrence Berkeley National Laboratory. In this approach, the synchrotron accelerates

electrons to energies of 1.9 GeV which circulate around a storage ring. Bending magnets are used to direct the electrons around the ring, and the change in acceleration of the electrons results in emission of X-rays. Additional magnets, for example and elliptically polarized undulator (EPU) can be used to control the energy and polarization of the X-rays, which is typically unachievable with standard anode-based X-ray sources. In this dissertation, X-ray photoemission spectroscopy measurements were performed at beamline 9.3.2 and X-ray absorption and dichroism experiments were performed at beamline 4.0.2 of the Advanced Light Source.

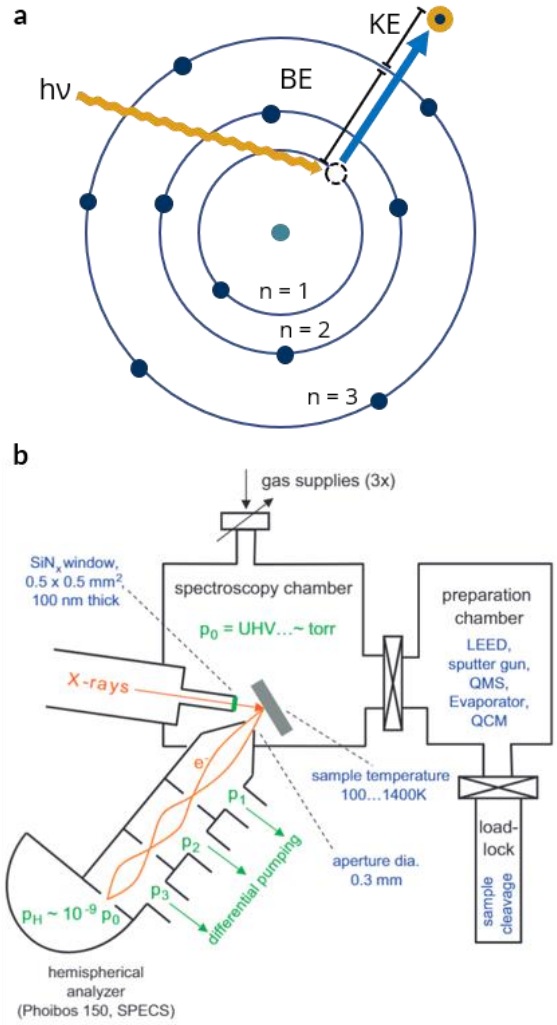

Figure 3.7: Schematic depiction of x-ray photoemission spectroscopy. a) The excitation of electrons from core-level atomic orbital is used to measure the binding energy of the electron. b) A schematic depiction of the ambient-pressure chamber at beamline 9.3.2 of the Advanced Light Source illustrating the separation of the electron analyzer under ultrahigh vacuum and the sample chamber. Reprinted with permission from ref. [*147*], Copyright 2009, Elsevier.

3.4.1. X-ray photoemission spectroscopy

X-ray photoemission spectroscopy (XPS), in particular, is a technique used to acquire surface sensitive information regarding the chemical species, bonding environment, and electronic structure of the surface of thin films. The photoelectric effect, where excited electrons are emitted from a material under incident electromagnetic radiation, provides a means to measuring the binding energies of electrons in materials. In XPS, X-rays with a known wavelength are used to excite core-level electrons at the surface of the material. The emitted electrons then pass through a series of electron lenses and into a hemispherical energy analyzer, which separates the electrons based on kinetic energy, and ultimately to a detector. With a known incident energy, and a measured kinetic energy, the binding energy (BE) of the electron, that is the energy difference between the core-level and valence band, can be calculated as:

$$\mathrm{BE} = \mathrm{h}\nu - \mathrm{KE} - \Phi, \qquad (3.9)$$

where h is Planck's constant, ν is the X-ray wavelength, and Φ is the work function. Typical lab-based XPS instruments often use magnesium K_α (1253.6 eV) or aluminum K_α (1486.7 eV) as the x-ray source and measure binding energies ranging from 0 eV (valence band) to 1200-1400 eV. As the core-level binding energy is dependent on the identity of the atom as well as the local bonding environment of the atom, XPS can provide both quantitative compositional information as well as information regarding the bonding of the atom the electron originated from,

allowing for distinguishing, for example, of the oxygen atoms in hydroxides or carbonates, or atoms that make up the terminating layer of the perovskite and are under-bonded, as in the case of surface-segregated strontium atoms. The requirement for electrons to escape the material into vacuum also makes this technique highly surface sensitive, as electrons from deeper in the film undergo inelastic collisions, recombination, and trapping before they are able to exit the material surface. Practically, a single monochromatic wavelength is used to excite electrons in the film, and the detector measures a range of kinetic energies of the photoemitted electrons.

Photoelectrons, however, are relatively low energy and have a small mean-free path, and can be easily absorbed by atmospheric molecules, requiring that typical XPS experiments be performed in ultrahigh vacuum (typically < 10^{-9} Torr). To study materials in ambient atmospheres, in conditions more closely resembling those experienced in real applications, for example, novel instrumentation has been developed to keep the hemispherical analyzer in ultrahigh vacuum while the sample can be exposed to higher pressures.[147] To achieve this, a series of differential pumping stages is used to rapidly reduce the pressure between the electron aperture and hemispherical analyzer, while the sample is brought in close to the aperture to reduce the distance electrons must travel in the high-pressure regime. This allows for XPS measurements to be performed in pressures up to approximately 1 Torr, and in a variety of gas environments, as well as high-temperatures.

3.4.2. X-ray absorption spectroscopy

The electronic structure of materials can also be probed through X-ray absorption spectroscopy (XAS) experiments, which probe the number of empty electron states in a material. In contrast to XPS, which uses a fixed incident wavelength and measures the energies of the electrons, in XAS experiments the incident X-ray energy is swept, and the quantity of absorbed electrons is measured at each energy. Practically, this makes use of the continuously tunable X-ray wavelength available at synchrotron facilities, while the electron count can be measured in a number of ways. One possibility is measuring the total quantity (rather than energy) of photoelectrons emitted from the sample into an XPS analyzer, allowing for measurement in ambient-pressure chambers like the one described above. Another common method is the total electron yield (TEY) method, where the surface of a thin film is electrically contacted to a copper rod which acts as an electron sink. As the electrons are excited into the valence band, they flow off the

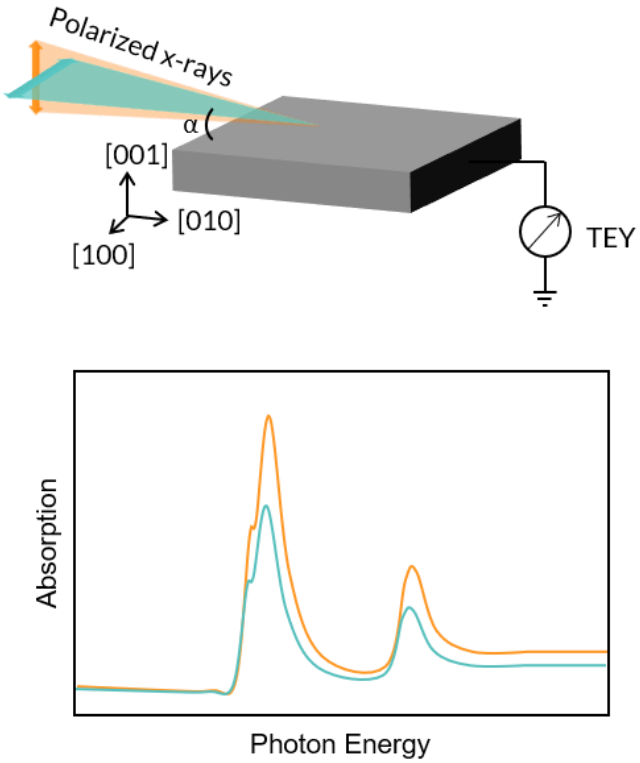

Figure 3.8: Schematic depiction of the grazing incidence geometry used to probe x-ray linear dichroism at beamline 4.0.2 of the Advanced Light Source, along with a schematic depiction of x-ray absorption spectra obtained with different x-ray polarizations, illustrating strong linear dichroism.

sample surface to the copper rod, where the current generated by the flowing electrons can be measured. Since electrons must be excited to the valence band to measure, the range of energies of the incident light allows for probing of different electron transitions, also called absorption edges, with higher energies (hard X-rays, ~1 KeV to 100 KeV) providing information from core-level shells, and lower energies (soft X-rays, ~1 eV to ~ 1 KeV) providing information on valence bands. In this dissertation, the primary focus of absorption experiments are the transition metal *L* edges, which in the case of the 3*d* transition metals studied here, come from $2p \rightarrow 3d$ transitions, and the oxygen *K* edge, which comes from $1s \rightarrow 2p$ transitions. The spectra acquired from XAS experiments can be used for identifying valence state, spin state, and degree of metal-oxygen hybridization. Performing such experiments in an ambient-pressure chamber, for example, can illustrate the evolution of oxidation state as the material is exposed to different environments.

In addition to the energy of incident X-rays on the sample, the polarization of incident X-rays can also impact X-ray absorption, and provide another dimension to XAS experiments. In particular, the absorption cross-section of an electron becomes much larger if the polarization of the incident light has the same symmetry as the orbital the electron occupies. This means that performing XAS experiments with controlled light polarization can provide information not just about the total valence structure, but also the orbital structure of a material. XAS measurements that use linearly polarized X-rays can then be used to probe the number of states in specific transition metal *d* orbitals of a single crystal (see section 1.3). Comparing absorption of linearly polarized X-rays along different crystallographic directions, called X-ray linear dichroism (XLD), provides information on the symmetry of the empty states. The angle of incidence of the X-ray beam on the sample surface can be controlled to probe orbitals along different crystallographic directions, with normal incidence ($\alpha = 90°$) probing orbitals along [100] and [010], and grazing incidence ($\alpha \approx 20°$) providing information from [001] as well as an in-plane direction. Moreover, the escape depth of electrons, particularly in TEY detection mode, is on the order of a few nanometers, making this a highly surface sensitive measurement technique.

3.5. Conclusions

Equipped with these characterization techniques, and an understanding of electrochemical processes on perovskite surfaces, questions regarding the impact of lattice structure on important materials characteristics can now be asked. First, the impact of surface orientation on catalytic reactivity will be probed using a combination of high-temperature charge transport and impedance spectroscopy measurements. In the latter case, epitaxial half-cells will be developed to apply the appropriate equivalent circuit analysis. These results will be correlated with ambient-pressure X-ray photoemission and absorption spectroscopy measurements, and with the help of collaborators, the simulated surface structures and relevant formation energies for specific steps of the ORR will provide insight as to the impact of the surface orientation. Then the impact of epitaxial strain will be probed again using high-temperature charge transport and X-ray absorption spectroscopies to correlate surface electronic symmetries and catalytic reactivity, keeping in mind the proposed descriptors for ORR reactivity in transition-metal perovskites.

Chapter 4:
Surface-orientation-dependent oxygen electrocatalysis

In this chapter, epitaxial thin-films of $La_{0.8}Sr_{0.2}Co_{0.2}Fe_{0.8}O_{3-\delta}$ (LSCF) on $SrTiO_3$ substrates are studied as a model system to probe electrochemical differences between different crystallographic surfaces. Preliminary studies based on electrical-conductivity relaxation establish that (111) surfaces have the fastest reaction rates, while (001) surfaces are slowest, and (110) surfaces have an intermediate reaction rate. To obtain mechanistic insight, all-perovskite, epitaxial thin-film half-cells are produced via microfabrication of the top working electrode (LSCF) into well-defined circular electrodes. Electrochemical-impedance spectroscopy reveals that, at 350°C, the (111) surfaces are more than 3- and 2-times more reactive than the (001) and (110) surfaces, respectively. Oxygen partial pressure ($\boldsymbol{p_{O_2}}$) dependent electrochemical-impedance spectroscopy of the half-cells suggests that the rate-limiting step of the surface reaction is the charge-transfer process to adsorbed oxygen adatoms (for $\boldsymbol{p_{O_2} > 1}$ Torr) and the absorbance of oxygen molecules (for $\boldsymbol{p_{O_2} < 1}$ Torr) for all three surface orientations. This indicates that while similar surface reactions occur on all three orientations, the (111) surfaces contain more active reaction sites to account for the differences. Density-functional theory (DFT) calculations reveal that the different surfaces have different stability with respect to the process of vacancy formation and oxygen adsorption, which stabilizes different surface chemistries. This is corroborated by ambient-pressure X-ray photoelectron (AP-XPS) and absorption spectroscopy (AP-XAS), which reveal the presence of different surface chemistries, with the (111) surfaces containing more oxygen vacancies, less surface-strontium segregation, and more near-surface *B*-site cations. This study reveals the importance of surface versus bulk chemistry and the role that vacancy-formation energy plays in stabilizing surface chemistries that promote oxygen exchange.

Chapter 4: Surface-orientation-dependent oxygen electrocatalysis

4.1. Introduction

Strong interactions with gas molecules at the solid-gas interface have made perovskite ABO_3 oxides promising electrode candidates for intermediate-temperature solid-oxide fuel cells and electrolyzers.[114,126,130] Nevertheless, the rate of oxygen electrocatalysis at the electrode surface remains one of the major factors that limits device efficiency. Extensive work has been performed to understand the surface-gas kinetics of perovskite electrodes and its correlation with specific properties such that better electrodes can be designed. Compositional screening has identified important electronic factors, such as the occupancy of the *B*-site cation e_g orbitals[136,148] or the relative position of the oxygen 2*p* band center,[149] both of which can act as descriptors for predicting high electrochemical activity. As such, controlling the electronic structure of perovskite electrodes *via* chemical-doping has been the prevailing route to optimize gas-exchange kinetics.

Beyond chemistry control, advances in thin-film synthesis now enable researchers to study surface reactions on an oriented single-crystal facet where extrinsic factors of bulk ceramics can be eliminated, and new methods of structural control can be realized. For instance, thin-film-based studies have focused on the relative importance of both surface-termination and sub-surface chemistry of (001)-oriented perovskite surfaces in dictating electrochemical reaction rates[138,150–152] Perovskite electrodes with different exposed crystallographic orientations have also been reported to have different electrochemical reaction rates.[51–53] Attempts to study surface-orientation effects on the gas-exchange kinetics of perovskite electrodes have been accomplished by growing single-layer-perovskite electrodes on perovskite substrates, typically employing techniques such as isotope-tracer diffusion, electrical-conductivity relaxation and solution-based electrochemical cells.[50–55,153] Generally, such studies point to faster kinetics on (111) surfaces and slow kinetics on (001) surfaces, whereas (110) surfaces have provided somewhat contradictory results.[50–53] Nevertheless, there remains a need for detailed mechanistic insights on orientation dependence.

On the other hand, construction of well-defined electrode surfaces and measurement via electrochemical-impedance spectroscopy (EIS) is a common method for examining mechanisms governing oxygen reactivity. Previous EIS studies on electrochemical cells composed of yttria-stabilized zirconia (YSZ) or other fluorite-based electrolytes with perovskite micro-electrodes have been carried out to study surface-gas reactions on perovskite surfaces.[154–156] The structural mismatch, however, between the electrode and electrolyte results in the creation of polycrystalline electrodes and/or the formation of defective heterointerfaces. Such defects can complicate the interpretation of results and limit control of the perovskite-electrode structure (*e.g.,* varying the surface orientations, and/or altering the strain). As such new approaches to microelectrode epitaxy and fabrication can provide a route towards measurement of single-crystalline thin film cathodes and study the impact of surface orientation and other lattice effects.

4.2. Control of surface orientation

Synthesis of single-layer LSCF films on $SrTiO_3$ (001), (110), and (111) substrates (Crystec, GmBH) was carried out using pulsed-laser deposition (see Chapter 2.2) at a heater temperature of

700°C in a dynamic p_{O_2} of 150 mTorr with a laser fluence of 1.6 J/cm^2 and repetition rate of 5 Hz. Following deposition, the films and heterostructures were cooled in a static p_{O_2} of 700 Torr at 10°C/min. X-ray diffraction line scans (Appendix A) reveal single-phase, high-quality, epitaxial films wherein the growth orientation is set by the substrate. The LSCF composition used in this study is closely lattice-matched to $SrTiO_3$ [142] (see Chapter 3.2), eliminating possible contributions from epitaxial strain and providing a way to closely approximate "bulk-like" LSCF. This lattice-matching is evidenced by the main diffraction conditions from the LSCF thin-films overlapping with the substrate diffraction and only the Laue thickness fringes are visible in the line scan (Figure 4.1a). In addition to X-ray diffraction studies, low-energy ion-scattering (LEIS) measurements

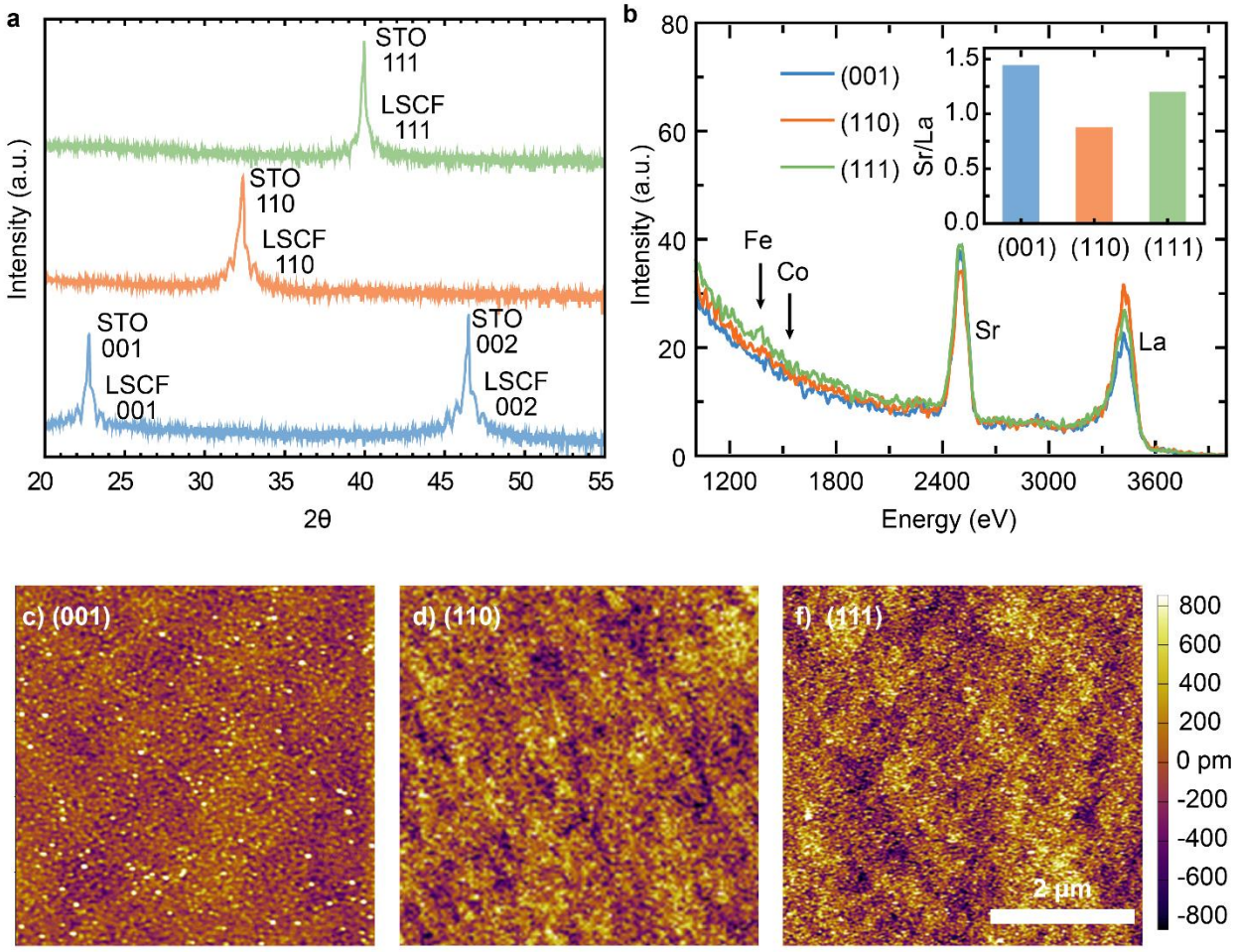

Figure 4.1: a) X-ray diffraction line-scans reveal high-quality epitaxial $La_{0.8}Sr_{0.2}Co_{0.2}Fe_{0.8}O_3$ (LSCF) on (001)-, (110)-, and (111)-oriented $SrTiO_3$ substrates. b) LEIS studies were undertaken to compare the as-grown surface chemistries of the different LSCF surface orientations. All three orientations were found to have A-site-rich terminations, with only the (111) surfaces showing any evidence of surface B-site cations, Inset shows the calculated ration of surface strontium to lanthanum ratio and reveals that all surfaces are non-stoichiometric and have high levels of surface strontium. Surface topography scans of c) (001)-, d) (110)-, and e) (111)-oriented LSCF thin films show smooth surfaces for all three surface orientations with no evidence of secondary phases or faceting, and comparable root-mean-square roughness.

were performed to understand the surface-termination of the as-grown LSCF films (Figure 4.1b). The films are predominantly *A*-site terminated for all three surface variants, with only the (111)-terminated film shows evidence of a small concentration of surface *B*-site cations. This is consistent with previous studies which suggest that the outermost layer is primarily *A*-site cations, and *B*-site cations are present only in sub-surface layers [48,157–159]. Thus, the (001) surface should be (La,Sr)O-terminated and the (111) surfaces should be (La,Sr)O_3-terminated. The resulting strontium-to-lanthanum peak intensity ratios extracted from the LEIS data are 1.44 and 1.20 for the (001) and (111) surfaces, respectively, both of which are larger than the ideal ratio of 0.25. For the (110) surfaces, although the expected termination is (La,Sr)(Co,Fe)O, no detectable *B*-site cations are present, suggesting that some surface reconstruction has taken place, completely masking the *B*-sites with *A*-site cations. Therefore, while the strontium-to-lanthanum peak intensity ratio for the (110) surface is 0.87, lower than those extracted for (111) or (001), the absence of any *B*-site on the outermost layer of the (110) surface suggests an even larger deviation from the expected surface stoichiometry. This suggests that despite identical growth conditions and strain states, the different crystallographic surfaces stabilize different surface chemistries, which deviate from the expected bulk stoichiometry. Atomic force microscopy was used to examine the surface topography of the films with different surface orientations, illustrating the different surface orientations have smooth surfaces with similar root-mean-squared roughness (Figure 4.1c-e). Despite the deviations in surface stoichiometry observed via LEIS, no extrinsic contributions from differences in surface roughness, secondary phases, or faceting are expected to influence the results of the electrochemical measurements.

4.3. Orientation-dependent oxygen-exchange rates

As a first probe of the electrochemical activity of these surfaces, electrical-conductivity-relaxation (ECR) experiments were performed on the three surface variants, whereby the resistance of the films was measured as a function of time following a step-change in the oxygen-partial pressure.

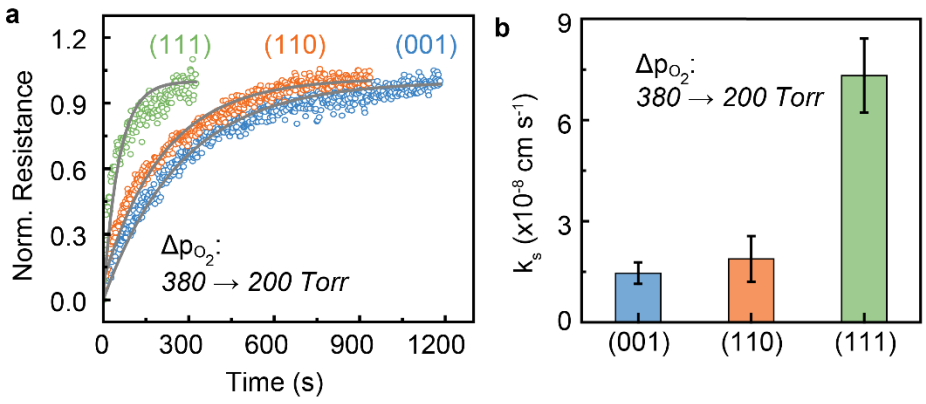

Figure 4.2: a) Electrical-resistivity-relaxation measurements on single-layer LSCF films demonstrate fast kinetics on (111) surfaces. b) Rate constants extracted from fitting of relaxation measurements indicates the same performance trend as half-cell studies, with the fastest exchange happening on (111) surfaces.

As described in Chapter 3, the defect equilibria of these materials dictate that upon decreasing (increasing) the partial pressure of oxygen (p_{O_2}) surrounding the films, the lattice will release (incorporate) oxygen to the environment (film), ultimately reducing (increasing) the conductivity of the films until it reaches a new equilibrium.[143] The ECR measurement is a commonly used technique for determining the oxygen-exchange and bulk-diffusion coefficients[51,53,82,143,160,161] In thin films, however, the small sample dimensions mean that the changes to conductivity are dominated by the surface reaction, allowing for direct comparison of the oxygen-exchange rates of the perovskite surfaces. Previous studies have shown different strontium-segregation rates for different perovskite surfaces, and that high levels of segregation can override the intrinsic differences in reactivity of the different crystal surfaces. As such, electrochemical measurements were carried out at 350°C to slow the strontium-segregation kinetics. Measuring the relaxation of normalized resistance from the LSCF layers following a step-change in pressure from 380 Torr to 200 Torr resulted in the fastest response for (111)-oriented films, with the (001)-oriented films demonstrating the slowest response (Figure 4.2a). Fitting the rate of change of the normalized resistance to the following expression provides for extraction of a surface-reaction rate constant,[162]

$$\frac{R_t - R_0}{R_\infty - R_0} = 1 - Exp\left(\frac{k_s}{d} * t\right), \tag{4.1}$$

where t is the time measured after the pressure change, d is the film thickness, and R_0, R_t, and R_∞ are the measured resistances before the pressure change, at time t, and after the film has equilibrated to a new value, respectively. Fitting each curve to this equation, the surface-reaction rate constant, k_s, can be calculated. The extracted k_s rate constants,[82,162] show that (111) surfaces are nearly 5 times as reactive as (110)- and (001) surfaces (Figure 4.2b). The observation of fast kinetics on (111)-oriented surfaces agrees with studies on related perovskite systems[51,53] and the magnitude of k_s is comparable to studies on LSC-based electrodes measured at similar temperatures.[51,53,163] These measurements provide evidence that (111) surfaces produce faster reaction kinetics, but further information regarding mechanistic differences require more in-depth measurement.

4.4. Epitaxial all-perovskite half-cells with controlled surface orientation

To probe mechanistic differences governing the oxygen exchange on the different surface variants, half-cell-based EIS measurements can be carried out (see Chapter 3.3). Maintaining epitaxial, single-crystalline electrodes in a half-cell structure, however, required development of a micro-fabricated, epitaxial, all-perovskite heterostructure. Based on prior experience with synthesis of epitaxial films of the perovskite ionic conductor, $La_{0.9}Sr_{0.1}Ga_{0.95}Mg_{0.05}O_{3-\delta}$ (LSGM),[164] epitaxial heterostructures that combine the active cathode, an electrolyte and a counter electrode, could be synthesized and fabricated into half-cells.

Fabrication of half-cell structures with form 30 nm LSCF/150 nm LSGM/20 nm $SrRuO_3/SrTiO_3$ (001), (110), and (111) was carried out via a series of pulsed-laser deposition and

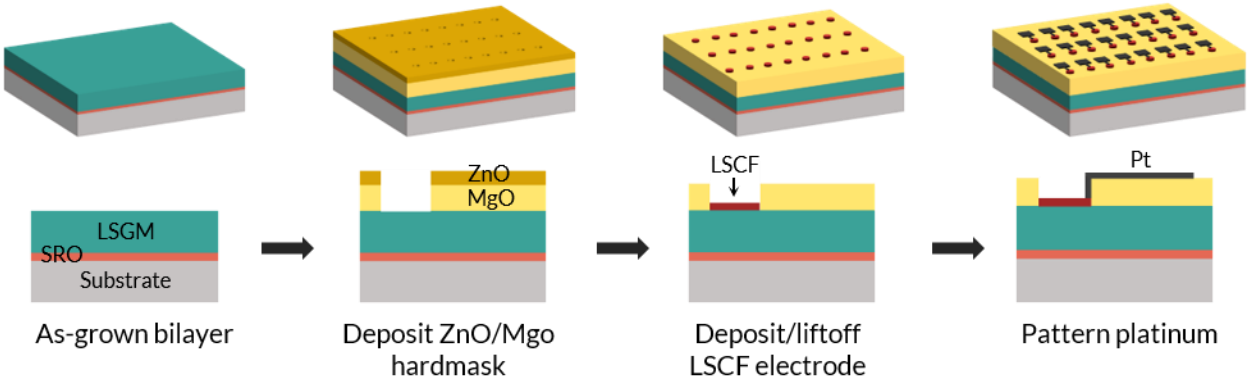

Figure 4.3: Schematic of the half-cell fabrication process utilizing a bilayer hardmask to define LSCF electrodes.

photolithography steps (Figure 4.3). Initially, a bilayer consisting of the $SrRuO_3$ counter-electrode layer and the LSGM electrolyte are synthesized *in situ*. The $SrRuO_3$ bottom electrode layers were deposited from a ceramic target (Praxair) of the same chemistry deposited at a heater temperature of 700°C in a dynamic p_{O_2} of 100 mTorr with a laser fluence of 1.3 J/cm^2 and a repetition rate of 15 Hz. Following the growth of the $SrRuO_3$, the LSGM layers were deposited from a ceramic target of the same chemistry ($La_{0.9}Sr_{0.1}Ga_{0.95}Mg_{0.05}O_3$) at a heater temperature of 800°C in a dynamic p_{O_2} of 40 mTorr with a laser fluence of 1.7 J/cm^2 and repetition rate of 5 Hz. The resulting heterostructures are removed from the deposition chamber and photolithographically patterned to define an amorphous ZnO/MgO insulating layer. The patterned sample is then returned to the pulsed-laser deposition chamber, and a room-temperature deposition of 80 nm of MgO followed by 30 nm of ZnO is deposited using a laser fluence of 2.0 J/cm^2 at a repetition rate of 15 Hz and a pressure of 5 mTorr in both cases. Following ZnO/MgO deposition, the photoresist is removed with acetone and isopropanol rinses, leaving a hard mask to define the LSCF electrodes.[165] The bilayer with patterned hard mask is reinserted into the pulsed-laser-deposition chamber and subsequent high-temperature deposition is used to grow the LSCF top electrode, using the same conditions as those used for synthesis of single layer films described above. The excess and unwanted LSCF (*i.e.*, that not in the circular capacitor areas) is removed via liftoff of the ZnO layer through a NaOH etch which selectively dissolves the ZnO, leaving behind the MgO-insulating layer, and the circular electrodes of LSCF. A final photolithography step is performed to define the platinum pads which are used for wire-bonded electrical connection to the LSCF electrode. Lift-off of the excess photoresist and platinum leaves the completed half-cell structures.

X-ray diffraction line scans reveal that all heterostructures are composed of single-phase, high-quality, epitaxially grown layers wherein the growth orientation is set by the substrate (Figure 4.4a-c). Reciprocal-space mapping (RSM) (Appendix A) studies were carried out to verify that all the layers are epitaxially strained to the $SrTiO_3$ substrates (Figure 4.4d-f), eliminating possible contributions from varying strain state to the observed differences in electrochemical reactivity. Owing to the different surface orientations, distinct diffraction conditions were probed to obtain information about the in-plane configuration of the heterostructures. These epitaxial half-cells provide a unique platform for studying the LSCF electrode *via* electrochemical impedance

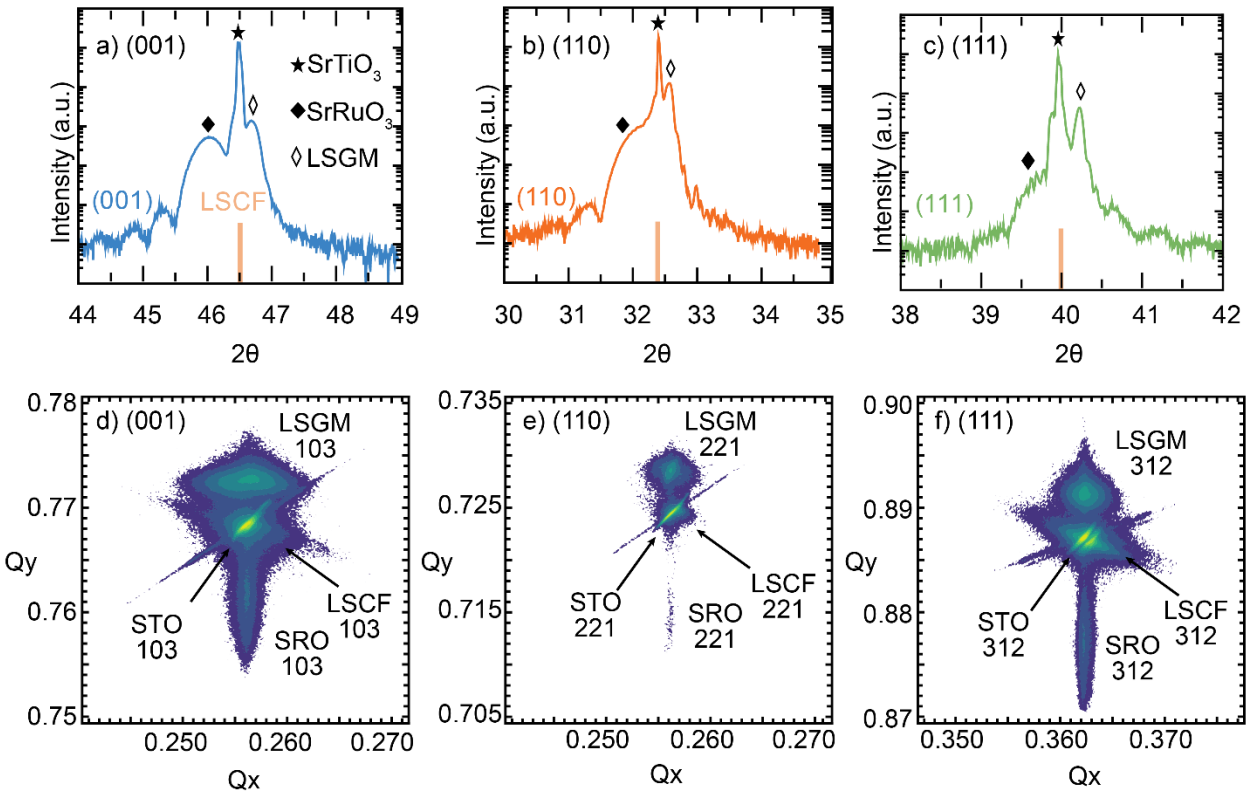

Figure 4.4: X-ray diffraction line-scans reveal high-quality epitaxial $La_{0.8}Sr_{0.2}Co_{0.2}Fe_{0.8}O_3$ (LSCF)/$La_{0.9}Sr_{0.1}Ga_{0.95}Mg_{0.05}O_3$ (LSGM)/$SrRuO_3$ trilayer structures grown on a) (001)-, b) (110)-, and c) (111)-oriented $SrTiO_3$ substrates. Reciprocal-space maps about off-axis diffraction peaks reveal epitaxial relationship and fully strained LSGM electrolyte and $SrRuO_3$ counter-electrode layers for d) (001)-, e) (110)-, and f) (111)-oriented heterostructures.

spectroscopy, maintaining the high-quality, single-crystal nature of the LSCF thin films, and creating pristine interfaces between the electrodes and electrolyte, eliminating the convoluting effects of grain boundaries and defective interfaces without sacrificing control of the surface orientation.

Half-cell structures were synthesized and fabricated for each of the surface orientations to perform electrochemical impedance spectroscopy. To analyze the impedance response, a lumped-element equivalent circuit is employed, consistent with work elsewhere.[166,167] The top part of the circuit is given by parallel elements including a surface resistance R_s and a constant-phase element Q_s, which together describe the surface-reaction process at the electrode-gas interface. Using circular electrodes with 200 µm diameter makes the electrochemical R_s (> 10 kΩ) much larger than the ionic-transport impedance across the 150 nm electrolyte with same cross-section (<10 Ω based on the ionic conductivity for single-crystalline LSGM[164,168] and LSCF[125]); this allows us to lump the ionic transmission line into a simple resistor given by the ionic-transport impedance R_{ion}. The bottom part of the circuit is the charge-transfer impedance at the LSGM-$SrRuO_3$ interface which is described by a parallel resistance R_{ct} and a constant-phase element Q_{ct}. Owing to the fact

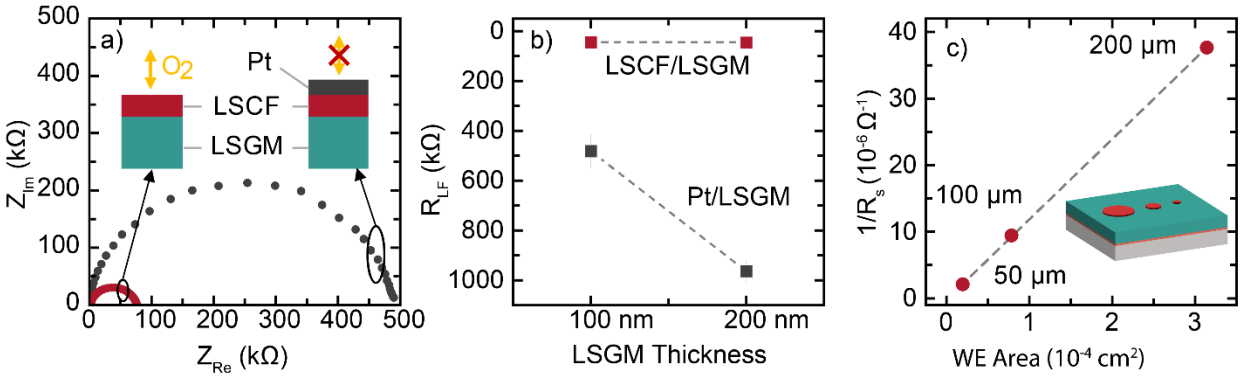

Figure 4.5: Validation of the epitaxial half-cell heterostructures. a) Comparison of an impedance measurement of the half-cell and one where the LSCF has been covered by a thin, platinum blocking layer reveals a large increase in the surface impedance when the LSCF surface is isolated from the gas environments, confirming that the LSCF is redox active. b) Comparison of the low-frequency intercept of the Nyquist plot (R_{LF}) between a half-cell device under study and one where platinum replaces the LSCF layer. The high-frequency intercept in a Nyquist-plot is related to the ohmic drop across the entire device. The large change in the Pt/LSGM impedance with increased LSGM thickness is expected when the majority of the ohmic drop is across the electrolyte layer. The half-cells under investigation show little to no change when the LSGM thickness is increased, confirming that most of the potential drop occurs across the LSCF-gas interface rather than the LSGM thickness, and the ionic diffusion in the LSGM is not contributing to the measured impedance. c) Area dependence of R_s is used to understand the contribution from the triple-phase boundaries in these devices. The linear increase in R_s with increasing working electrode area shows that the measured reaction rate is a property of the surface and not the LSCF/LSGM/gas triple-phase boundary.

that the $SrRuO_3$ is metallic and the electrolyte is thin, under small electrical perturbations, the ionic charges at the LSGM-$SrRuO_3$ interface are expected to be mainly compensated by the stoichiometric change of the LSGM electrolyte. Qualitatively, one can assume that such stoichiometry change in the thin LSGM electrolyte is limited by diffusion at dilute concentration, and that the charge-transfer process is expected to show up at much higher frequencies in the impedance spectra compared to the surface-reaction process owing to small R_{ion}.

While previous studies have described the validity of microelectrode designs,[145,155,156] several verification measurements using the as-described measurement setup were performed to ensure that the chosen geometry allows for isolation of the surface-reaction impedance. First, it must be confirmed that the surface impedance, R_s, extracted is truly related to the oxygen reaction at the surface of the LSCF electrodes. In this case, covering the surface of the LSCF with an oxygen impermeable layer should serve to dramatically increase the surface-reaction impedance, by preventing interaction of the LSCF with the oxygen environment. Using a platinum blocking layer over the surface of the LSCF electrode, an increase in R_s by almost an order of magnitude was observed, indicating that the LSCF surface is indeed redox active (Figure 4.5a). Additionally, most of the potential drop across the half-cell should occur at the LSCF-gas interface, and the measured impedance directly reflects this polarization resistance rather than diffusion processes in the LSGM electrolyte. The total electrical resistance of the half-cell device was directly related to the high-frequency intercept in a Nyquist plot. In the case of diffusion in the electrolyte contributing significantly to the measured impedance, a strong dependence of the high-frequency intercept on the LSGM thickness is expected, as is the case for a platinum electrode on the LSGM (Figure

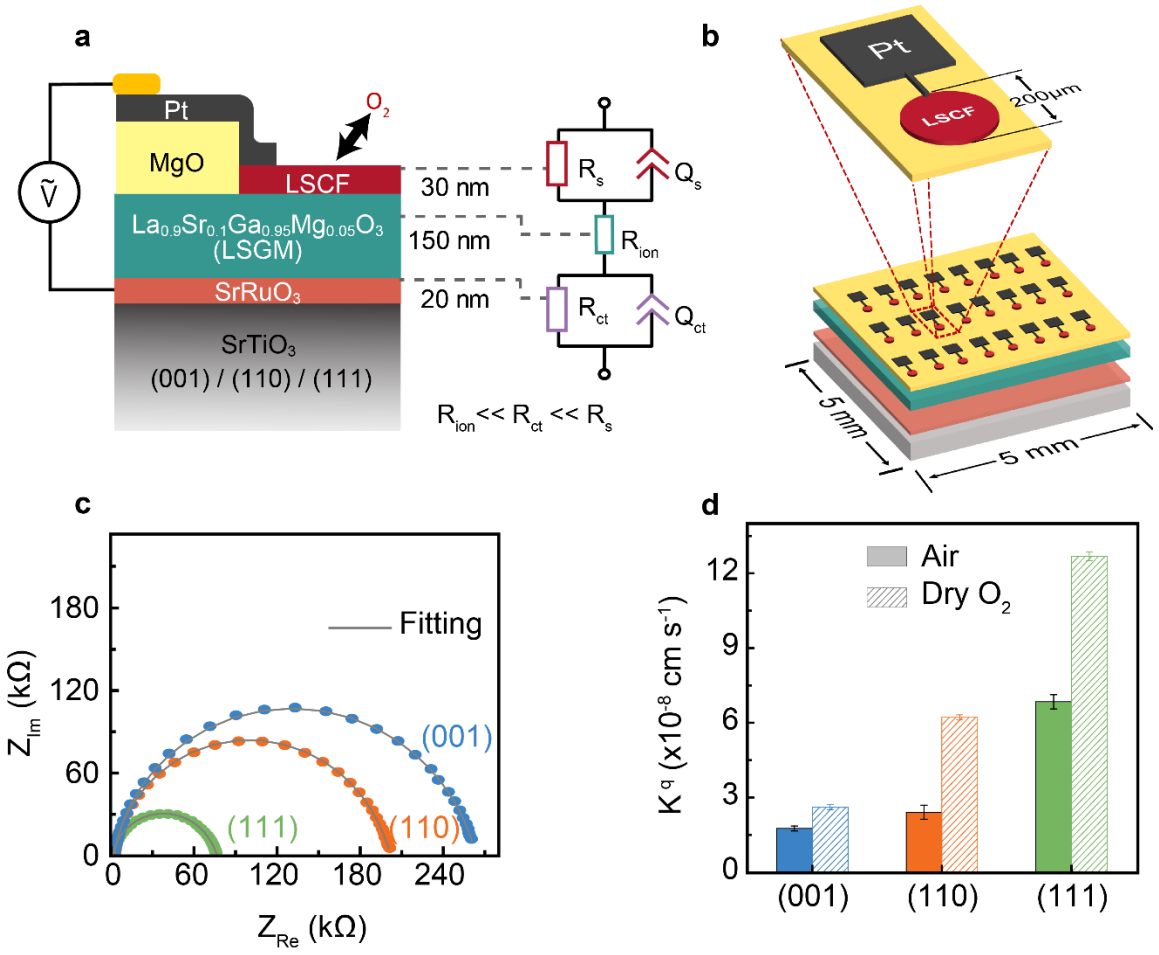

Figure 4.6: a) A cross-section of the heterostructure and the corresponding equivalent circuit used for analysis of the half-cell. b) Microfabrication provides many devices to be patterned on a 5 x 5 mm substrate, allowing for statistical analysis of many devices. c) Representative Nyquist plots from electrochemical-impedance-spectroscopy studies measure on the different surface variants in a dry O_2 environment. d) Rate constants calculated from the extracted R_s values illustrate the large difference in rate constant.

4.5b). With an exposed LSCF electrode, however, no dependence on LSGM thickness was observed, indicating that the surface-reaction is the limiting impedance in the half-cell, and that these devices adequately isolate the surface reaction for further study. Finally, it is well known that the electrode-electrolyte-atmosphere triple-phase boundary serves as the main reaction site for many cell geometries owing to enhanced ionic diffusion of reduced species. With good mixed-ionic-electronic conductors, in a thin-film geometry, the diffusion of oxygen anions no longer is a limiting factor and the reaction truly occurs at the electrode surface. This can be seen in the area dependence of the impedance R_s. A linear scaling of R_s with electrode area is observed, indicating the active sites for oxygen reaction occur on the exposed LSCF surface and triple-phase boundaries provide negligible contribution to the measured impedance (Figure 4.5c).

4.5. Pressure-dependent impedance spectroscopy

The resulting devices provide a means to perform electrochemical-impedance spectroscopy with a well-defined electrode surface and applicable equivalent circuit (Figure 4.6a) on a large number of devices fabricated onto a single 5 mm x 5 mm substrate (Figure 4.6b). EIS measurements of the half-cells with different surface orientations was initially performed at 350°C in both air and dry oxygen. Representative spectra for the three half-cell orientations reveal that all half-cell variants show a single, well-defined semicircle (Figure 4.6c). The low-frequency endpoints reflect the rate of the surface-gas reaction. Fitting the spectra to the equivalent circuit yields R_s which can be further converted into a surface-gas reaction rate constant:

$$k_q = \frac{k_b T}{4e^2(R_s \cdot A)c_o}, \tag{4.2}$$

where A is the electrode area and c_o is the concentration of oxygen species calculated based on reported values.[169] The rate constants (in air) reveal that the (111) surfaces have reaction rates >3- and 2-times higher than that of the (001) and (110) surfaces, respectively (Figure 4.6c). In dry oxygen, the trend holds the same for the three orientations except for an overall higher reaction rate due to a richer oxygen concentration. The error bars are determined by measuring multiple devices each on two different sets of half-cell heterostructures; the small deviation indicates good consistency and repeatability.[170] The results from impedance spectroscopy exhibit the same trend and similar relative magnitudes of k_q compared to k_s extracted from electrical-conductivity-relaxation measurements. These two measurements point to the same performance trend: (111) surfaces have gas-reaction-rate constants at least 3- and 2-times higher than the (001) and (110) surfaces. Although the surface-gas reaction can be decomposed into several elementary steps (*e.g.*, adsorption of oxygen molecules, reduction of adsorbed species, ion incorporation, etc.), it is assumed that at one step will be rate-limiting and dictate the p_{O_2}-dependence of the reaction.[116,146,171] The resulting surface-reaction impedance will be related to p_{O_2} according to:

$$1/R_s \propto (p_{O_2})^m, \tag{4.3}$$

where m depends on the nature of the rate-limiting step. To understand the reaction mechanisms, p_{O_2}-dependent EIS (from 0.08-760 Torr) was performed. Nyquist plots obtained for such p_{O_2}-dependent measurements on the three surface variants demonstrate the increasing R_s with decreasing p_{O_2}, observed in the progressively increasing low-frequency intercept (Figure 4.7a-c). For a given pressure, the (111) surface produces significantly smaller R_s values at all pressures studied. It can be seen that the high-frequency intercept remains constant for all measurements except for the very lowest pressures measured where a small shoulder appears. The origin of this shoulder was not studied in-depth here, but maybe related to the decreasing oxygen conductivity

of the electrode at reduced oxygen pressures, adding an additional contribution to the half-cell impedance.

All three surface variants were found to exhibit essentially the same p_{O_2} dependence (Figure 4.7d-f), differing only in magnitude of R_s. At low pressures ($p_{O_2} < 1$ Torr), $m \approx 1$ corresponding to a reaction that involves diatomic oxygen. In this case, the reaction may be limited simply by the surface coverage of adsorbed oxygen molecules:

$$O_{2,\,gas} \rightarrow O_{2,\,ad} \tag{4.4}$$

or by charge-transfer to the adsorbed oxygen: [146]

$$O_{2,ad} \rightarrow O_{2,ad}^{-} + h^{+} \tag{4.5}$$

$$O_{2,ad}^{-} \rightarrow O_{2,ad}^{2-} + h^{+} \tag{4.6}$$

At high pressures ($p_{O_2} > 1$ Torr), $m \approx 0.25$ and likely corresponds with a charge-transfer-limited reaction. Here the species involved can be either dissociated, adsorbed oxygen atoms (O_{ad}) or diatomic oxygen in one of three charge states: neutral $O_{2,ad}$, superoxo $O_{2,ad}^{-}$, or peroxo $O_{2,ad}^{2-}$. In the case of O_{ad}-reduction, this implies a change in the rate-limiting-step from adsorption to charge transfer as p_{O_2} increases, whereas in the latter case, one rate-limiting, charge-transfer step (*i.e.*, $O_{2,ad}^{-} \rightarrow O_{2,ad}^{2-} + h^{+}$) dominates the entire pressure regime, and the crossover in *m* is driven by a change in the surface coverage and resulting electrostatic interactions of charged-surface species[49]. With all surfaces demonstrating the same crossover, however, it appears there is no mechanistic difference that can explain the differences in reaction rate between the surfaces. In the absence of a clear mechanistic driving force, electronic and chemical differences between the different surface orientations were examined to understand the differences in reactivity.

4.6. Density-functional theory studies of oxygen exchange

To explore possible surface structural and electronic differences that could drive the observed electrochemical differences, DFT calculations were performed to understand the driving forces for oxygen exchange on each surface[52,53]. To begin, the defect-free surfaces for each of the orientations were simulated, using *A*-site terminations enriched with 50% strontium to reflect the LEIS measurements. For (001) and (111) surfaces, this entails *A*O- and AO_3-termination, respectively, while for (110) surfaces, both defect-free *AB*O- and O_2-terminated surfaces were simulated, under the assumption that the two terminations are convertible and coexisting by oxygen adsorption/desorption. Calculating the energies of these surfaces following introduction of a surface-oxygen vacancy and subsequently an adsorbed-oxygen molecule and performing these calculations over sites that have either subsurface cobalt or iron allowed for comparison of the relative energies for oxygen exchange for the different *B*-site species.

The (001), (110), and (111) surfaces were found to exhibit markedly different energy profiles for the hypothesized pathway (Figure 4.8). Focusing first on vacancy formation, the calculations reveal a sizable increase in energy (2-2.5 eV) when an oxygen vacancy is introduced to the (100) surface. On the other hand, vacancy formation on (111) surfaces results in a decrease in energy. This suggests that (111) surfaces are prone to spontaneous vacancy formation, while (100) surfaces limit vacancy formation. For (110) surfaces, the relationship is less clear. In the case of *ABO*-termination, vacancy formation results in an increase in energy (4.5 eV) even greater than that for the (100) surface, while vacancy formation on the O_2-terminated surface results in a significant decrease in energy (0.72-0.9 eV), similar to the (111) surface. In other words, oxygen vacancies on (110) surfaces are unstable in the *ABO* plane but are stable above the cations in the O_2 plane.

These trends are consistent with what would be expected from electrostatic considerations of surface polarity. The net charge of a perovskite surface can be estimated by means of a simplistic picture of the formal charge of all the cations (*e.g.*, La^{3+}, Sr^{2+}, and O^{2-}) in an ideal, defect-free

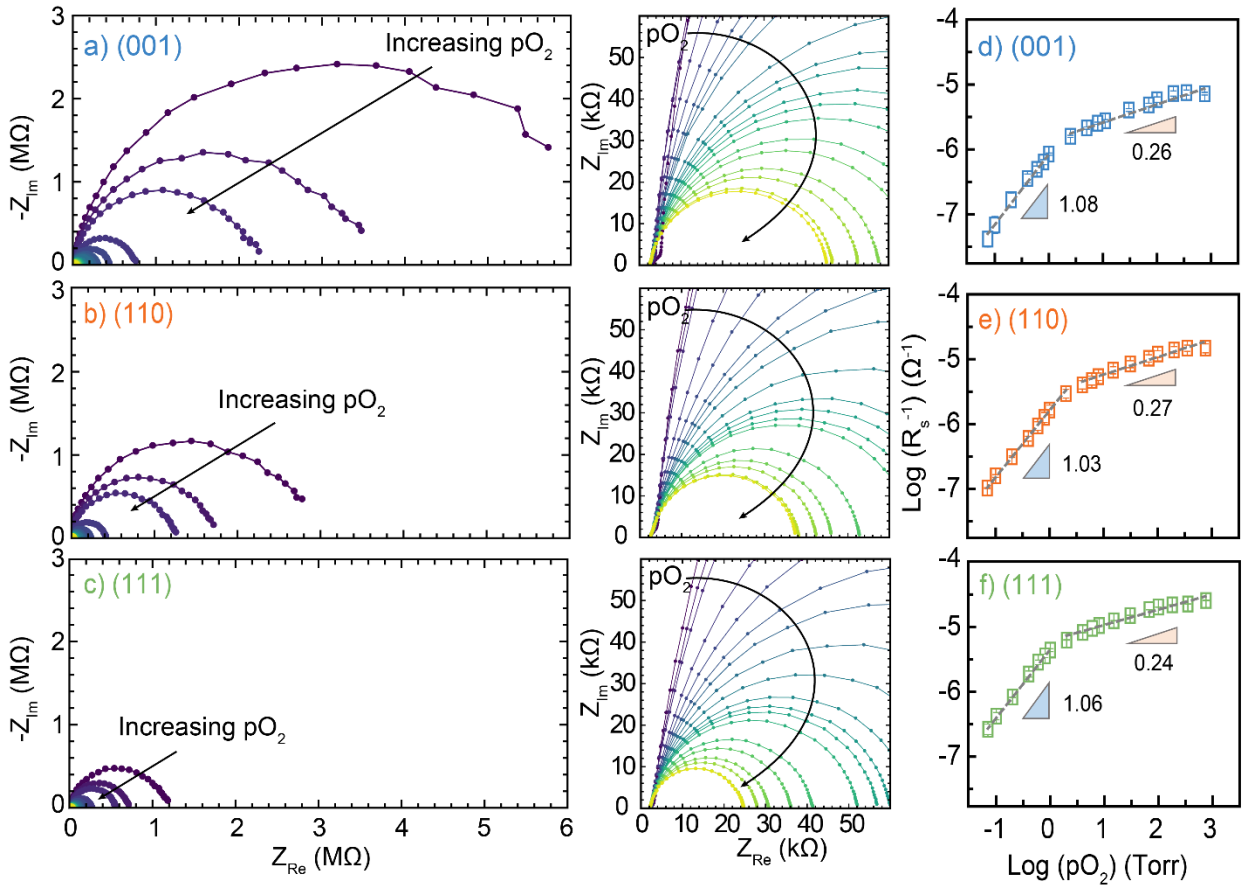

Figure 4.7: Nyquist plots from p_{O_2}-dependent impedance spectroscopy studies. Pressure -dependent studies for a) (001), b) (110), and c) (111) surfaces reveal a decrease in the high-frequency intercept as p_{O_2} is increased. The low-frequency intercept does not change until the lowest pressure, indicating that the half-cell geometry nicely isolates the surface-reaction process at pressure of interest. The right graph shows a zoom-in of the low-frequency range. The electrochemical reaction rate between the different surfaces can be observed to increase from the decreasing high-frequency intercepts from (001) to (110) to (111) surfaces. d-f) The pO_2-dependence of the different orientations demonstrate similar slopes, suggesting the rate-limiting step is consistent across the three orientations.

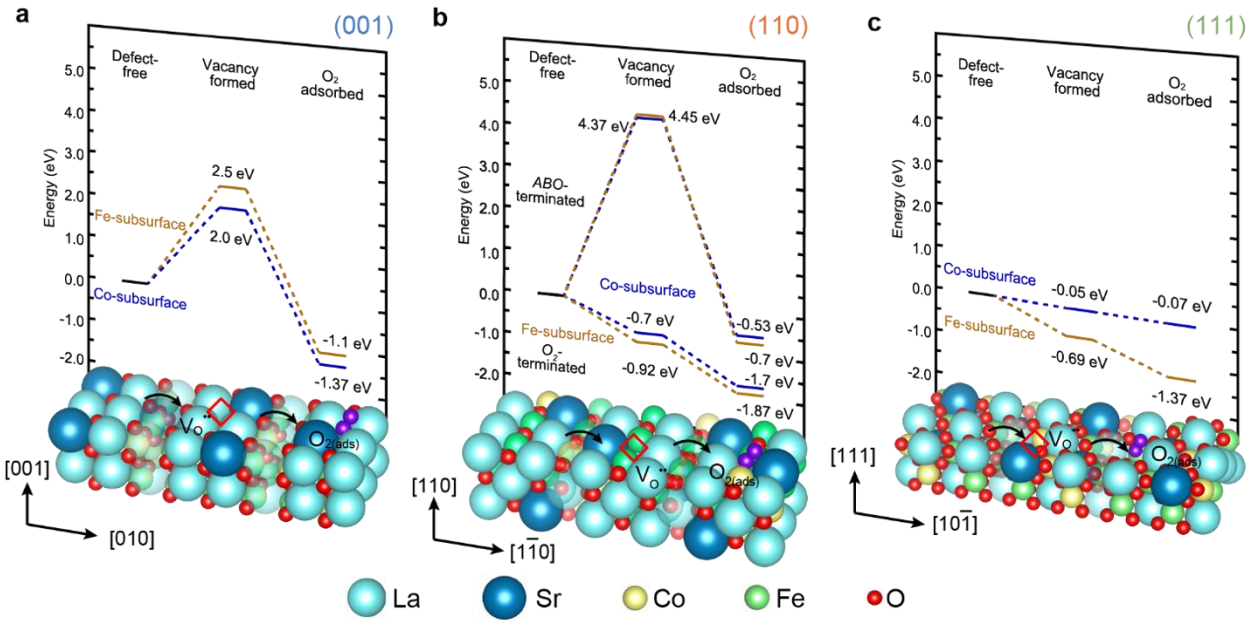

Figure 4.8: First-principles calculations of surface vacancy formation and oxygen adsorption. DFT calculations illustrate the different formation energy for surface vacancies across the a) (001), b) (110) (with both ABO-termination and O_2-termination), and c) (111) surface variants. Vacancy formation is unfavorable on (001) surfaces and ABO-terminated (110) surfaces, whereas (111) and O_2-terminated (110) surfaces have favorable vacancy formation energies.

surface in order to understand the electrostatic driving forces that may drive non-stoichiometry at these surfaces. For the (001) surface, an *A*O-termination with a stoichiometric Sr:La ratio of 1:4 leaves the defect-free surface with a net charge of +0.8 per formula unit. Vacancy formation on this surface would further increase the surface charge, indicating it is unfavorable to form vacancies. Replacing lanthanum with strontium (*i.e.*, strontium segregation) would reduce the net charge thereby electrostatically stabilizing the surface. The stoichiometric *AB*O-terminated (110) surfaces are similarly positively charged, and vacancy formation would worsen the electrostatic stability. Again, strontium segregation serves to reduce the surface charge and stabilize the surface. Applying the same treatment to the AO_3-terminated (111) surfaces, the net charge of the surface is -3.2 per formula unit, and thus formation of positively charged oxygen vacancies serves to stabilize the surface polarity, likely explaining the favorability to form such vacancies observed in DFT. Thus, for both the (001) and (110) surfaces, surface charge hinders vacancy formation, and may provide an additional driving force for strontium segregation, in addition to elastic and chemical driving forces.[172]

Turning to the adsorption of molecular oxygen, the calculations reveal that adsorption at an oxygen-vacancy site results in a lowering of the surface energy in all cases, supporting studies that identify vacancy sites as the primary active site.[121] Additionally, it is notable that the bond-length of the adsorbed-oxygen molecule (~1.35 Å) is increased relative to that of molecular oxygen (1.23 Å), indicative of an activated, superoxo $O_{2,ad}^{-}$ as the stable adsorbed species; lending support to the reaction $O_{2,ad}^{-} \rightarrow O_{2,ad}^{2-} + h^{+}$as the rate-limiting step.[121,146] Interestingly, when the energies of

the different subsurface cations are weighted by their relative concentration, the (100) and (111) surfaces have similar energy reductions upon adsorption of oxygen molecules (~1.1 eV) suggesting that the stabilization of vacancy sites on (111) surfaces is the main driving force for the increased electrochemical performance. The O_2-terminated (110) surface has the most favorable energy of adsorption (~1.8 eV) while the *AB*O-terminated (110) surface has the least favorable adsorption energy (~0.7 eV). Thus, the (110) surface presents a case where the different terminations work in opposition, and the electrochemical results may reflect the competition between the (un)favorable terminations. These results, in conjunction with the absence of surface *B*-site cations in the LEIS data, merit a deeper study of possible surface reconstructions at these polar surfaces, and particularly on (110) surfaces.

4.7. In-situ probes of surface chemistry and electronic structure

Considering the DFT results, a direct probe of electronic structure associated with each surface orientation could shed light on the measured kinetic differences. To do this, AP-XAS and AP-XPS studies were carried out, allowing for the measurement of elemental-specific spectra at high temperatures and in ambient gas environments.[173] Prior to measurement, samples were cleaned in 10 mTorr of gaseous oxygen at 350°C for 15 min. while observing the carbon 1*s* photoemission excitation to ensure carbonaceous contaminants were removed (Figure 4.9). A representative spectrum of the carbon 1*s* peak is presented and shows no carbon 1*s* peak, which appears at >284 eV depending on the type of contaminant (*e.g.* carbonates, adventitious carbon, carbon dioxide, etc.) The only peak observed in this range is a weak peak from the strontium 3*p* 1/2 excitation, confirming samples were appropriately cleaned prior to measurement.

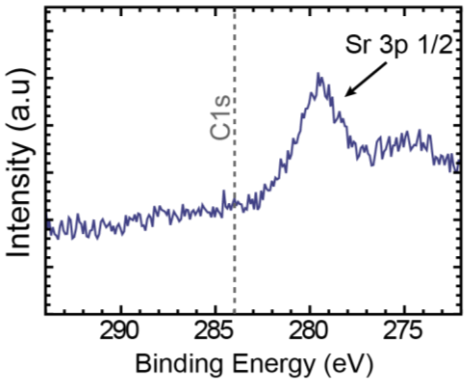

Figure 4.9: XPS measurements after sample cleaning. Measurements in the range of the carbon 1s excitation post-cleaning procedure reveals no adventitious or carbonaceous contamination on the surface of the samples prior to AP-XAS and AP-XPS measurements.

Beginning with X-ray absorption, the cobalt and iron *L* edges and oxygen *K* edges were probed at 350°C in oxygen pressures from 10^{-8} to 0.9 Torr to understand how the electronic structure is influenced by the interaction with molecular oxygen (Figure 4.10). While the AP-XAS results are qualitatively similar across the different surface orientations, their pressure dependence provides insight into the interaction of these surfaces with oxygen molecules. At low $\boldsymbol{p_{O_2}}$, both the iron (Figure 4.10a) and cobalt (Figure 4.10b) *L*-edge spectra suggest that the cations have predominantly 3+ valence.[174–176] As oxygen is introduced the iron *L* edge shows no change, whereas the cobalt *L* edge broadens to higher photon energies, indicating an increase towards 4+ valence. This agrees with studies in bulk ceramics, where changing oxygen stoichiometry results in larger changes to the cobalt valence.[177] It has been shown that the electronic structure of iron

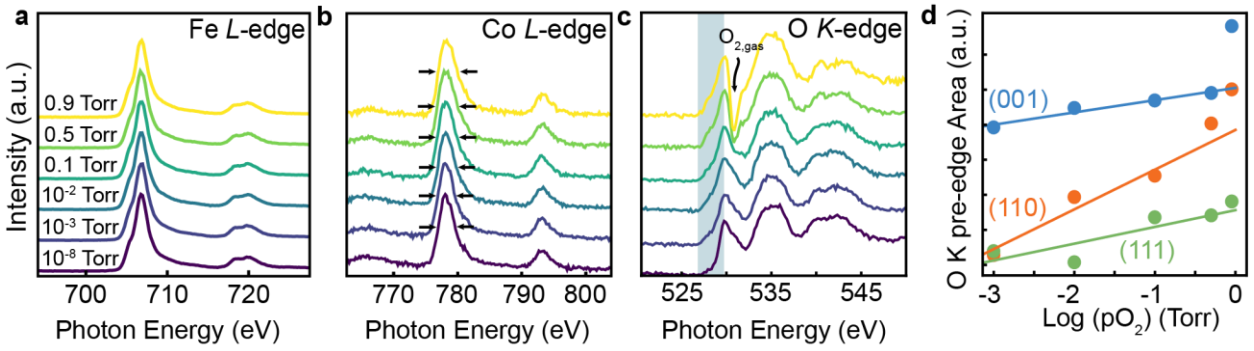

Figure 4.10: Representative X-ray absorption spectra from (110) surfaces as a function of pressure indicate changing surface electronic structure for the a) iron L, b) cobalt L, and c) oxygen K edges. d) Changing pre-peak area (shaded region in c)) of the oxygen K edge is quantified to demonstrate the different propensities for adsorption and charge-transfer on different surfaces, lines are a guide for the eye.

changes from $3d^5$ to $3d^5\underline{L}$, where $\underline{L}$ indicates a ligand hole, with increasing oxidation.[174] As such, changing the oxygen content of the lattice results in hole doping of primarily oxygen 2*p* character, and can be observed in measurements of the oxygen *K* edge. Two broad features at 535 eV and 542 eV are observed, corresponding to lanthanum/strontium 3*d* – oxygen 2*p* hybridized states, and cobalt/iron 3*p* – oxygen 2*p* hybridized states, respectively; however, the most significant changes are observed around a sharp peak at 530 eV, corresponding to excitations involving cobalt/iron 3*d* – oxygen 2*p* hybridized states (Figure 4.10c). At low p_{O_2}, this peak is relatively sharp, and is attributed to excitation into unoccupied $t_{2g}\downarrow$ states. As the pressure is increased, an increase in intensity at 528 eV is observed, suggesting the depopulation of some $e_g\uparrow$ states[178,179] (*i.e.*, hole-doping of the oxygen 2*p* states as electrons are transferred to adsorbed oxygen to form the superoxo $O^-_{2,ad}$ state). This pre-peak area provides a quantitative marker of oxygen adsorption (*i.e.*, $[h^+]$), and comparison of the rate of pre-peak change for different surface orientations reveals a strong preference for hole doping on (110) surfaces as compared to (001) and (111) surfaces (Figure 4.10d). The similarity in driving force for oxygen adsorption provided by DFT for the (001) (-1.1 eV) and (111) (-1.37 eV) surfaces is manifested in the similar rate of pre-peak area increase extracted from XAS. The larger slope for the (110) surfaces may point to adsorption in the O_2-plane rather than the *ABO*-plane considering the larger driving force for oxygen-molecule adsorption (-1.87 eV). Thus, the distinct bonding environments of each surface orientation give rise to distinct electronic interactions with oxygen.

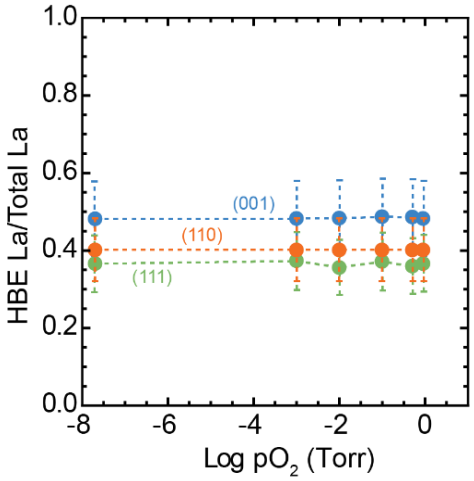

Figure 4.11: Pressure dependence of La 4*d* components shows the relative contributions of the LBE and HBE components of the La 4*d* excitation do not change over the course of the measurement.

The understanding gleaned from the LEIS, DFT, and XAS analysis naturally raises the question if different surface chemistries drive the observed electrochemical differences? To prove this AP-XPS measurement of the oxygen 1*s*, cobalt/iron 3*p*, strontium 3*d*, lanthanum 4*d*,

and valence-band photoelectron excitations was carried out. The probe depth of these measurements, at an excitation energy of 670 eV, is calculated to be ~1.3 nm, using the NIST Inelastic Mean-Free Path Database,[180] indicating these measurements probe just the "near-surface" layers of the film. Beginning with the lanthanum 4*d* photoemission peak, a complex peak shape is observed, which can be decomposed into four components, as typically done with *A*-site cation emission peaks. Spin-orbit splitting introduces a 3/2-5/2 doublet with a branching ratio of 3:2 and a binding energy shift of 2.8 eV,[181] and two doublets, termed low-binding-energy (LBE) and high-binding-energy (HBE), are used to fit the entire peak. Measurement of the lanthanum 4*d* excitation at 350°C in oxygen pressures from 10^{-8} to 0.9 Torr showed no change in the relative magnitude or

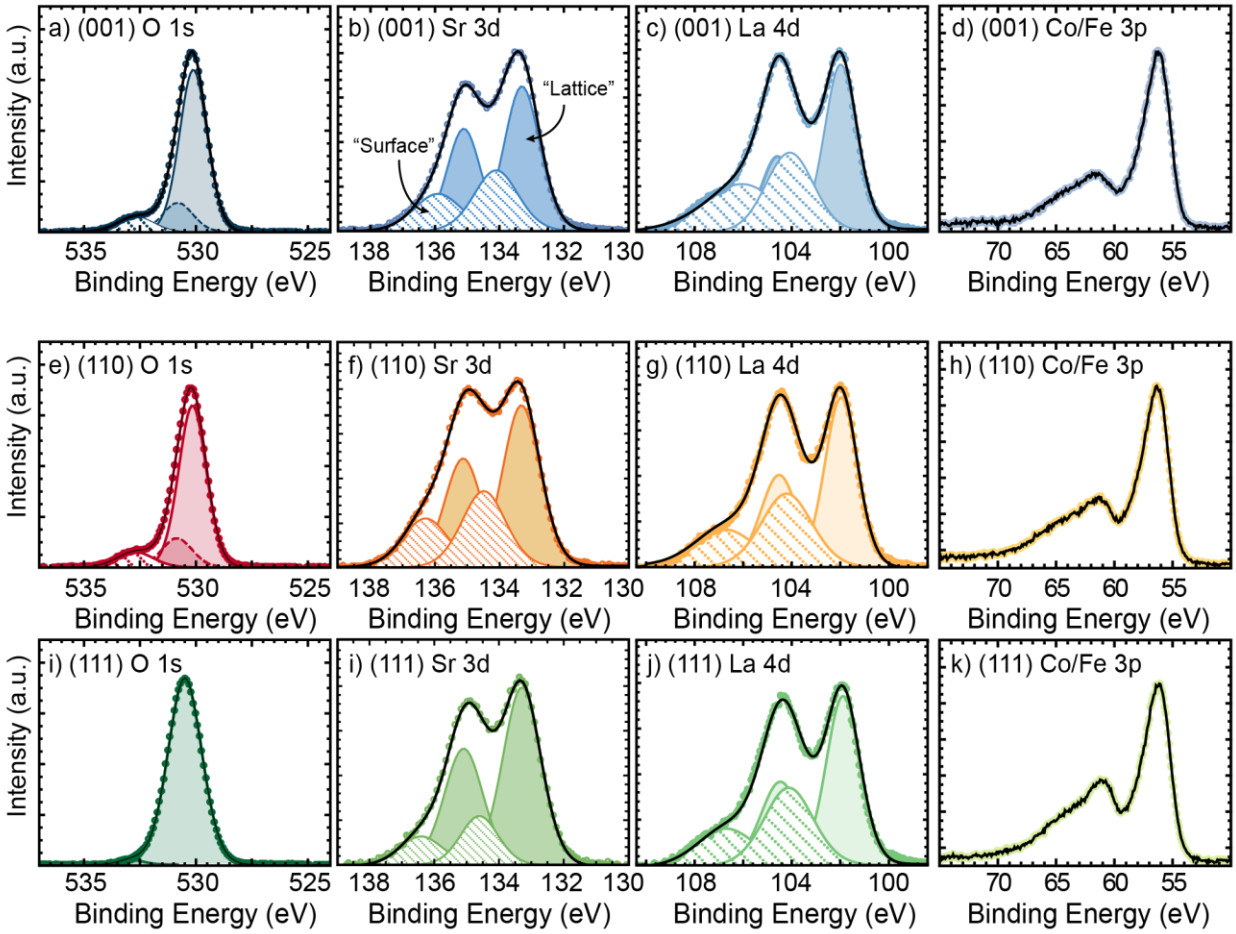

Figure 4.12: Representative spectra of the four main core-level excitations. This study focused on four different core-level excitations for the three surface orientations including the oxygen 1s, strontium 3d, lanthanum 4d, and cobalt/iron 3p levels for (a-d, respectively) (001), (e-h, respectively) (110), and (i-k, respectively) (111) surfaces. All three surfaces show qualitatively similar spectra. The oxygen 1s spectra for all three surfaces were fit using a "surface" and "lattice" component, with the relative intensity corresponding well with the relative intensity of strontium "surface" and "lattice" components. The (001) and (110) oxygen 1s spectra were fit with a third component, occasionally attributed to M-O bond of unknown origin; however, this component was not needed to obtain a good fit for the (111) surface. The complex splitting of transition metal 3p states and the overlapping of the cobalt and iron 3p excitations prevented any meaningful insight to be gained from fitting of components of those states. As such, the integrated area of the entire peak was used to quantify the overall *B*-site cation chemistry at the surface.

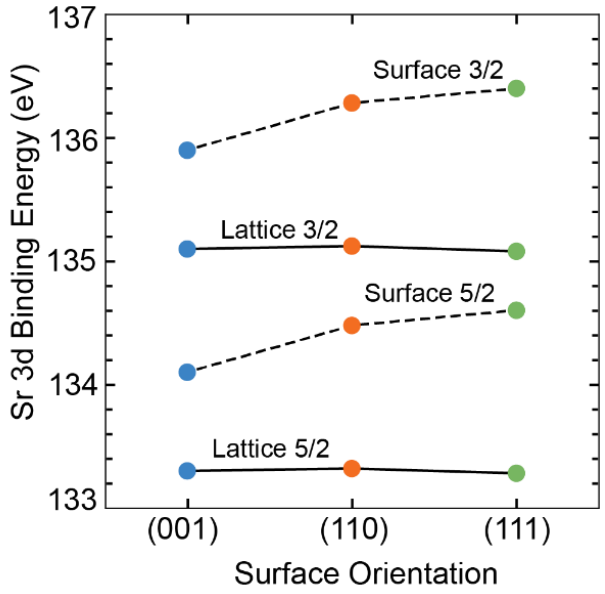

Figure 4.13: The binding energies of the strontium 3d 3/2 and 5/2 excitations are compared across the three surface variants. No change is observed for the "lattice" component, as is expected for the three surface variants which have the same bulk chemistry. The "surface" components have binding energies differing by ~0.5 eV showing that (111) surface strontium have larger effective positive charge than those on the (110) or (001) surfaces.

binding energy of the LBE and HBE doublets (Figure 4.11), indicating the lanthanum 4*d* excitation is insensitive to oxygen pressure. As such, the lanthanum 4*d* excitation could be used as an internal standard[182] and all photoemission spectra were aligned to the LBE peak of the lanthanum 4*d* photoemission peak, resulting in the valence-band edge being located at 0 eV, as is expected for the metallic nature of LSCF at elevated temperatures.

Representative spectra for the four core-level excitations show similar, complex peak shapes for all three orientations (Figure 4.12). The oxygen 1*s* (Figure 4.12a,e,i) emission peak was fit using two or three components, similar to previous studies on perovskite cathodes;[183] however, in this study the cation stoichiometry remained the focus. The strontium 3*d* and lanthanum 4*d* peaks show two doublets, while the cobalt and iron 3*p* excitations are overlapping (Figure 4.12d,h,k). Owing to the well-known deleterious effect of strontium segregation on catalytic reactivity,[169,184] examination of the strontium 3*d* excitation serves as an important first step. For all three orientations, the complex peak shapes typically found for strontium 3*d* peaks are observed (Figure 4.12b,f,j), which, similar to lanthanum 4*d*, are decomposed into LBE and HBE doublets. Components for each strontium 3*d* doublet were fit using a fixed branching ratio of 3:2 and a binding energy shift of the +1.8 eV[170,183] for the 3/2 component relative to the 5/2 component. The HBE doublet has been observed in many different strontium-containing samples, but the precise origin is still under investigation.[170,185] Many reports attribute the HBE doublet to "surface" species, be it surface-terminated strontium, or secondary strontium-based phases that form at surfaces.[183,186,187] In this study, the "surface-like" attribution of the HBE doublet is adopted, owing to the similarity with previous studies, and the changing contributions from the "surface-like" and "lattice-like" species observed during the measurement, as would be expected for strontium-segregation at elevated temperatures.

Differences in the relative magnitude of the "surface-like" component compared to the "lattice-like" component between the different surface orientations can be clearly seen (Figure 4.12b,f,i), suggesting the different orientations inherently possess different degrees of strontium-segregation. It is noted that the binding energy of the "surface" component of strontium is not the same for the three surface orientations, indicating the bonding environment of surface-terminated strontium is

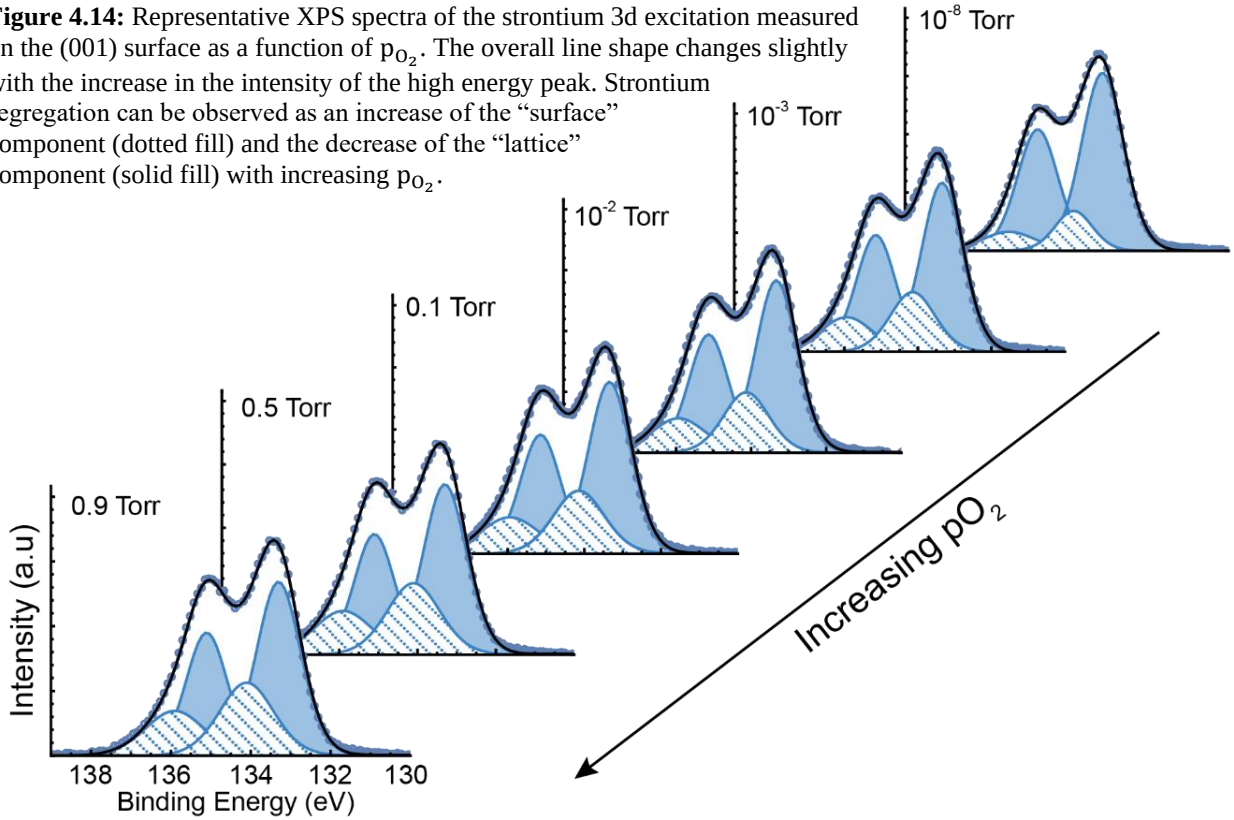

Figure 4.14: Representative XPS spectra of the strontium 3d excitation measured on the (001) surface as a function of p_{O_2}. The overall line shape changes slightly with the increase in the intensity of the high energy peak. Strontium segregation can be observed as an increase of the "surface" component (dotted fill) and the decrease of the "lattice" component (solid fill) with increasing p_{O_2}.

distinct on the different surfaces, which may be expected for surfaces with different terminations (Figure 4.13). Examining the evolution of the strontium excitation with in different p_{O_2}environments can provide information regarding the dynamic evolution of surface strontium species on the different surface. While no shift in the relative binding energies of the LBE and HBE doublet was observed with increasing p_{O_2}, an increase of the "surface-like" LBE contribution relative to the "lattice-like" contribution on (001) surfaces can be clearly seen as p_{O_2} is increased (and the sample is held at 350°C for extended periods), suggesting surface strontium-segregation is actively occurring at measurement conditions (Figure 4.14). To quantify the relative contributions, the total area of the "surface-like" components over the total area of the strontium 3*d* excitation was calculated for each spectrum measured at each pressure. The "surface-like" excitation is observed to increase over the duration of the measurement at 350°C in all samples (Figure 4.15a), suggesting each surface orientation exhibits active strontium segregation; however, the (111) surface maintains the lowest "surface-like" contribution throughout. This supports the notion that the (111) surfaces have an electrostatic driving force originating from the surface polarity that limits strontium segregation compared to the other surfaces, in agreement with previous studies.[188] This strontium-enriched surface can be confirmed without invoking the "surface-like" assignment by comparing the total ratio of strontium to *A*-site species in the near-surface region. Calculating the strontium-to-lanthanum ratio in the near-surface regime, using the total integrated area from the strontium 3*d* and lanthanum 4*d* excitations, normalized by their respective photoionization cross-sections (0.7 and 0.5, respectively), provides an estimation of the

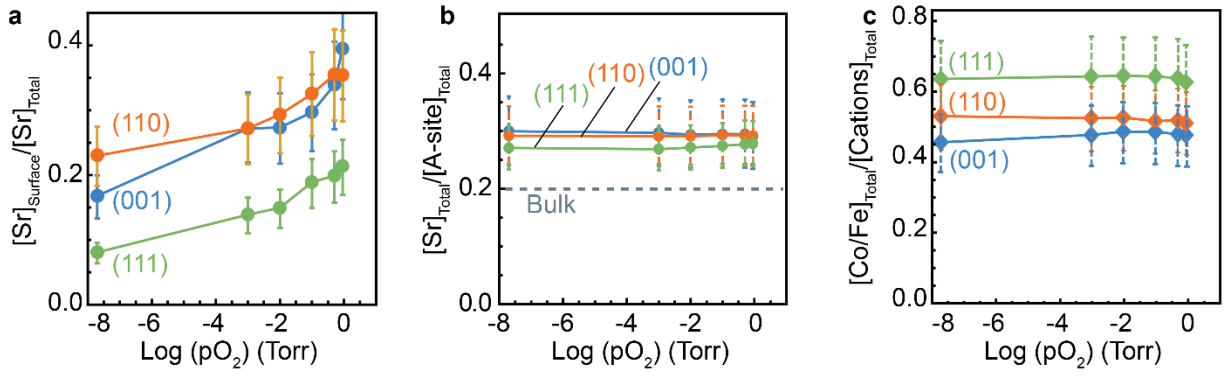

Figure 4.15: a) In situ observation of strontium segregation is quantified using the relative intensities of the "surface" and "lattice" components of the strontium 3d excitation as a function of gas pressure. b) XPS chemical analysis reveals that the different surface orientations have differing quantities of B-site cations in the near-surface region.

A-site stoichiometry in the probed region. The ideal, bulk ratio is expected to be 0.2, and the measured ratio is shown to be ~0.30, indicating good agreement with the expected stoichiometry, and reflecting the increase in the near-surface strontium content by ~50%, and again confirming that the (111) surfaces have the least strontium in the near-surface region (Figure 4.15b). While the LEIS data suggests that the (110) surface has the lowest Sr:La ratio at the outermost atomic layer, the concentration of strontium in top-most 5-6 cationic layers (~1 nm) probed by XPS is higher than that in either the (110) and (111) surfaces. Thus, said another way, while all surface orientations have a higher strontium concentration than the bulk stoichiometry, the (111) surface has the lowest overall concentration of near-surface strontium.

Both the AP-XPS and LEIS point to significant deviations of the surface chemistry from the bulk stoichiometry. How then, do these deviations impact the near-surface *B*-site chemistry, which is expected to impact the available reaction sites? Measurement of the cobalt/iron 3*p* excitation resulted in a complex line shape due to the various possible photoemission peaks and the possible overlapping of the cobalt and iron contributions. Accurately fitting such transition-metal excitations is known to involve many components, which dramatically reduces the confidence in extracting any meaningful insight from individual contributions.[189,190] Owing to the difficulty in assigning precise origins to the various components in the cobalt/iron 3*p* excitation, and the open debate regarding the origin of the LBE/HBE doublets in the lanthanum 4*d* and strontium 3*d* excitations, the total area of the excitations was used to quantify *B*-site stoichiometry. In this study, the total area of the combined cobalt/iron 3*p* peak was used to calculate the relative ratio of *B*-site cations in the near-surface region. For normalization using the photoionization cross-section, the iron and cobalt contributions were separated at 59.5 eV. The peak area integrated above 59.5 eV was normalized using the cobalt photoionization cross-section of 0.17 and the area below 59.5 eV was normalized using the iron photoionization cross-section of 0.15. While there is likely some additional error in the quantification of the *B*-site concentration induced by the potential overlapping of iron and cobalt peaks, as well as differences in the information depth of the cobalt/iron 3*p* excitation compared to the lanthanum 4*d* and strontium 3*d* excitation, this

calculation is expected to provide reliable qualitative differences between the different surface orientations rather than precise measurement of the stoichiometry. The (111) surfaces have the largest fraction of near-surface *B*-site cations, supporting the observation of *B*-site-derived peaks in the LEIS measured only on (111) surfaces (Figure 4.15c). The trends in the fraction of *B*-site cations track closely with the trends in electrochemical response, whereas solely looking at the segregated strontium does not. It is interesting to note that, despite similar surface terminations among the three surfaces, a high degree of near-surface or subsurface *B*-site cations still enhances the catalytic reactivity.[151,152] Ultimately, these differences in surface chemistry explain the lack of mechanistic differences among the three surfaces. With a charge-transfer-limited reaction, surface vacancies and near-surface *B*-site cations are needed for the formation of $O_{2,ad}^{-}$ and subsequent reduction. Stabilizing high oxygen-vacancy concentration and a "large" number of *B*-site cations near the surface and limiting the electrostatic driving force for strontium segregation that quenches these sites results in faster reaction rates for the (111) surfaces.

4.8. Conclusions

This work leveraged epitaxial thin films of a disordered perovskite to provide insight into the chemical and electronic factors that contribute to the catalytic responses of perovskite surfaces. Epitaxial all-perovskite half-cells were developed to serve as a platform for studying the electrochemical response of perovskite cathodes. Such epitaxial control allows for study of the electrochemical response of the different surfaces, revealing large differences in electrochemical activity. While (001), (110), and (111) surfaces exhibit the same rate-limiting step for oxygen exchange, combined DFT and spectroscopic analyses reveal that the local bonding environment at the surface stabilizes distinct (non-bulk-like) surface chemistries. These results highlight the importance of understanding the possible surface reconstructions, and how deviations from bulk stoichiometry at surfaces may hinder otherwise favorable reaction kinetics. Fast reaction kinetics are found at (111) surfaces that exhibit a balance of important factors such as vacancy concentration, favorable adsorption energy, low strontium segregation, and high *B*-site availability. Whereas many studies have pursued performance optimization by tuning the bulk stoichiometry, new avenues for engineering can be envisioned whereby the materials chemistry is engineered to effect favorable surface chemistries and therefore higher catalytic activities.

Chapter 5:
Strain-induced orbital contributions to oxygen electrocatalysis

This chapter details experiments exploring the connection between epitaxial strain-induced structural distortions, transition metal orbital structure, and electrochemical activity in two prototypical catalyst systems. Utilizing epitaxial strain imposed by various substrates in thin films of $La_{0.5}Sr_{0.5}CoO_3$ (LSCO) and $La_{0.8}Sr_{0.2}Co_{0.2}Fe_{0.8}O_3$ (LSCF), high-temperature electrochemical measurements are correlated with the structure of the catalytically active transition-metal sites. In both cases, biaxial tensile strain enhances the reaction rates for oxygen exchange, in agreement with previous studies on similar compositions. Study of the epitaxial strain-induced changes to the electronic structure are carried out using X-ray linear dichroism measurements at the iron- and cobalt-*L* edges. It is shown that the biaxial strain and associated symmetry breaking of the oxygen octahedra shifts the energy levels of the two transition-metal e_g orbitals with respect to one another, ultimately changing the occupancy of the d_z^2 orbital. Together, electrochemical and absorption measurements point to a strong correlation between exchange rates and d_z^2 occupancy, with fast exchange rates found in films with lower d_z^2 occupancy. It is proposed that the d_z^2 orbital is the key orbital involved in oxygen interaction at the perovskite surface and is responsible for strain-induced changes to electrocatalytic activity. These results advance the understanding of the role of the electronic structure in oxygen electrocatalysis, provide a mechanism to enhance chemical activity of oxygen electrocatalysis in thin films, and provide an explanation for several previously reported results regarding epitaxial strain-dependent electrochemical activities.

Chapter 5: Strain-induced orbital contributions to oxygen electrocatalysis

5.1. Introduction

New strategies for enhancing ORR catalysts require understanding of structural, chemical, and electronic characteristics that impact the interaction between the perovskite surface and oxygen gas. As seen in Chapter 4, the electronic structure of a particular surface can drive local nonstoichiometry, but electronic structure itself can also determine the adsorption and charge transfer characteristics of the cathode surface. At the same time, the influence of epitaxial strain on the electronic structure, charge transport, and magnetic order of transition metal perovskite oxides is well-studied (see Chapter 2.4). On the other hand, there has recently been a significant push to develop electronic descriptors for predicting electrochemical activity in perovskite oxides.[134,136,191,192] This work has led to the identification of several electronic descriptors that are closely correlated with high activity for ORR and OER catalysts, including the relative position of the oxygen 2*p* band center,[134] the *B*-O bond covalency,[178] and, in particular, the occupancy of the e_g orbitals.[136,193] For example, e_g orbital occupation has been shown to be strongly correlated with the *B*-site-dependent chemical activity trends, and an "ideal" e_g occupancy of ~1.2 electrons has been used as the justification for high activities in $LaNiO_3$ and $Ba_{0.5}Sr_{0.5}Co_{0.8}Fe_{0.2}O_{3-\delta}$ catalysts.[136,148,193] As such, the development of electronic descriptors has already proved fruitful in identifying compositions with high activities and, in turn, developing synthetic control of materials properties to tune the electronic structure toward these ideal values could unlock a new way to optimize materials.

In parallel to the development of these electronic descriptors, researchers have leveraged thin-film-based studies to understand how manipulation of the lattice structure of these perovskites can affect the electrochemical activity. Several studies have focused on the role of epitaxial strain in perovskite oxides for controlling electrochemical activity.[14,78,80–83,194] Reports have noted enhanced electrochemical activities in cobalt- and iron-based perovskites under biaxial-tensile strain driven by strain-induced changes to surface chemistry[82] or suggested electronic contributions as the driving force for enhanced electrochemical activity under tensile strain.[80,81,195] Meanwhile, strain-induced changes to e_g occupancy have been proposed as the mechanism of enhanced ORR/OER activities in $LaNiO_3$ films under biaxial compressive strain.[83] This discrepancy suggests that strain-induced changes to electronic structure may be dependent on the identity of the *B*-site cation and calls for more direct studies of the effect of strain on electronic structure in these perovskite catalysts.

Drawing from this growing body of work, open questions remain as to how epitaxial strain-induced changes to the electronic structure of perovskite cathodes, particularly at the surface, impact electrochemical activity. Moreover, in heavily substituted cathode compositions, these effects can become more complicated, with different strain-induced contributions from the different transition-metal sites. To begin to address these questions, a series of experiments leveraging thin-film synthesis were used to draw connections between epitaxial strain, high-temperature electrocatalytic reaction rates, and the orbital structure at perovskite surfaces. These experiments shed light on the impact of epitaxial strain on orbital structure, as well as identified key orbital characteristics that correlate to enhanced electrochemical activity. The question of

element-specific effects is further probed by a comparison between the chosen LSCF model system, and a cobalt-rich composition, namely $La_{0.5}Sr_{0.5}CoO_3$ (LSCO), to clarify impacts arising from cobalt and iron sites.

5.2. Synthesis of epitaxially strained cathode films

Two sample variants were examined in this study. First, 20-nm-thick films of LSCO deposited on the $LaAlO_3$ (001), $(LaAlO_3)_{0.3}(Sr_2TaAlO_6)_{0.7}$ (LSAT) (001), and $SrTiO_3$ (001) substrates, corresponding to biaxial strains of -1.22%, 0.87%, and 1.79%, respectively, imposed on the LSCO; henceforth referred to as LSCO/$LaAlO_3$ (-1.22%), LSCO/LSAT (+0.87%) and LSCO/$SrTiO_3$ (+1.79%) heterostructures. Second, we studied 20-nm-thick films of LSCF deposited on LSAT (001), $SrTiO_3$ (001), and $DyScO_3$ (110) substrates, corresponding to biaxial strains of -0.97%, -0.02% and 1.09%, respectively,[142,196] imposed on the LSCF; henceforth referred to as LSCF/LSAT (-0.97%), LSCF/$SrTiO_3$ (-0.02%) and LSCF/$DyScO_3$ (+1.09%) heterostructures. All films were grown via pulsed-laser deposition and films synthesized on different substrates were deposited simultaneously.[196] The LSCO films were deposited from a ceramic target (Praxair) on $LaAlO_3$ (001), LSAT (001), and $SrTiO_3$ (001) substrates (Crystec, GmBH) at a heater temperature of 700°C in a dynamic oxygen pressure of 200 mTorr with a laser fluence of 1.0 J/cm^{-2} at a repetition rate of 10 Hz. The LSCF films were deposited from a ceramic target (Praxair) of the same chemistry on LSAT (001), $SrTiO_3$ (001), and $DyScO_3$ (110) substrates (Crystec, GmBH) at a heater temperature of 650°C and a dynamic oxygen pressure of 200 mTorr using a laser fluence of 0.9 J/cm^{-2} at a repetition rate of 5 Hz. Following deposition, all films were cooled in a static oxygen pressure of 700 Torr. LSCF films were cooled at a rate of 10°C/min following deposition, whereas the LSCO films were cooled at a rate of 5°C/min to avoid cracking the films.

Following film growth, X-ray diffraction studies (Appendix A) were carried out to characterize the resulting structures and strain states (Figure 5.1). The systematic decrease in the out-of-plane *c* lattice parameter with increasing tensile strain is apparent in both the LSCO and LSCF films as a progressive shift of the 002-diffraction condition to higher 2θ angles (Figure 5.1a,b). Additionally, RSM studies about the 103-diffraction condition were performed to examine the in-plane lattice parameters and reveal that all films are coherently strained to the substrate (Figr 5.1c-h). The surfaces of the as-grown films were characterized with atomic force microscopy and it was found that all films exhibit smooth surfaces with root-mean square roughness $\lesssim$ 1 nm (Figure 5.2a,b).

Additionally, considering reports of strain-induced changes to surface strontium segregation, and with the understanding that different surface chemistry can impact reaction rates, the surface chemistry of the LSCF films was studied via XPS. These studies were performed via *ex situ* XPS measurements (XPS, PHI 5600) at a pressure <10^{-9} Torr using an aluminum K_α (1486.6 eV) source. To assess whether strontium segregation rates could impact the measured electrochemical reaction rates, XPS measurements were also performed following annealing treatments of various duration at 350°C in air, allowing for examination of the evolution of strontium segregation over the timescale and under conditions similar to those used for

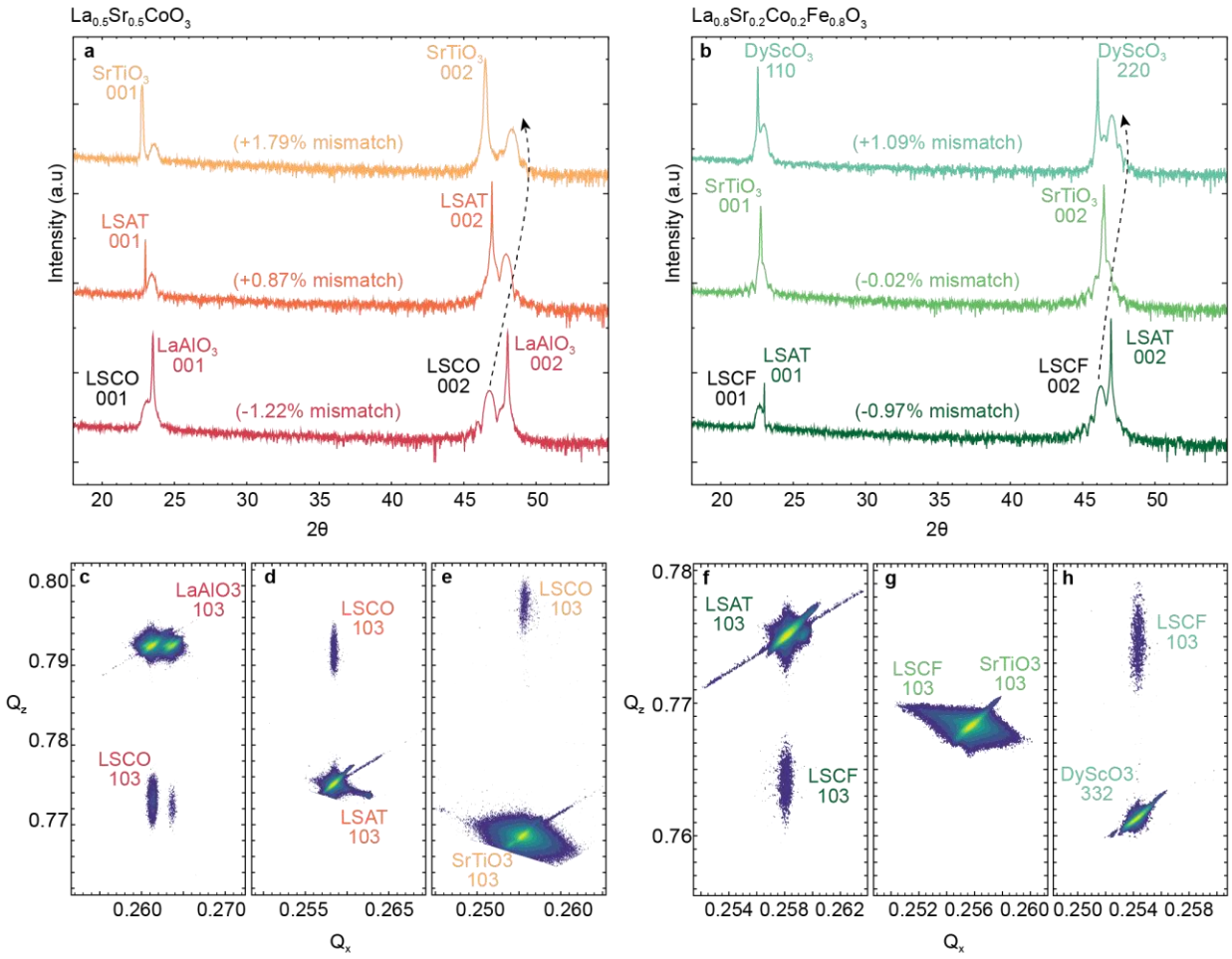

Figure 5.1: Structural characterization of LSCO and LSCF thin films. *θ-2θ* line scans for (a) LSCO and (b) LSCF thin films, on various substrates illustrate the decreasing *c* lattice parameter (increasing *2θ*) for increasing tensile strain in all cases. Reciprocal space maps (RSMs) about the 103-diffraction conditions of (c-e) LSCO and (f-h) LSCF thin films demonstrate the high-quality epitaxial thin films are coherently strained to the substrate in all cases.

electrochemical evaluation. A characteristic spectrum focused about the strontium 3*d* excitation is provided (Figure 5.2c). Adopting the language presented in Chapter 4, the complex peak shape is decomposed into a LBE doublet at 131.5 eV and 133.5 eV corresponding to the strontium 3*d* 5/2 and 3*d* 3/2 excitations from "lattice-like" strontium, and the HBE doublet at 133.5 eV and 135.5 eV corresponding to the "surface-like" strontium excitations.[170,196] The ratio of the areas of these peaks was used to estimate the degree of strontium segregation (Figure 5.2d); however, in this case we also observed some small lead contamination (arising from prior use of the growth chamber of the production of lead-based materials), which is convoluted with the surface strontium peaks. Considering the low intensity of the lead 4*f* peaks identified here, and the large relative sensitivity factor (~22) for lead 4*f* excitations in XPS (compared to ~5 for strontium 3*d* excitations) we can conclude that the lead detected here is a low concentration surface contaminant (again, likely originating in the synthesis chamber which is also used for deposition of lead-containing oxides).[197] Because these lead 4*f* peaks have some overlap with the surface strontium 3*d* peaks we

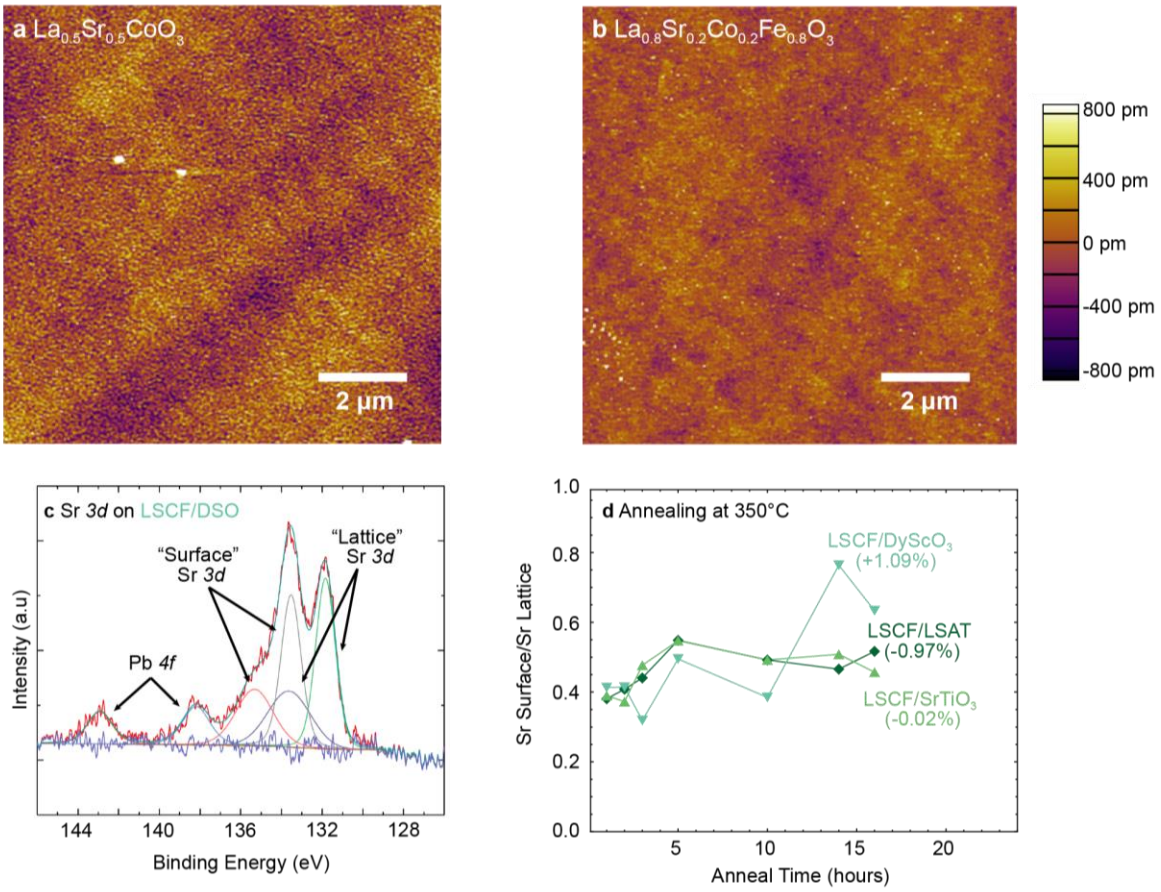

Figure 5.2: Characteristic atomic force microscopy images of a) LSCO and b) LSCF thin films showing smooth surfaces with ~1 nm RMS roughness. c) A characteristic XPS spectrum about the strontium 3*d* peaks taken from an LSCF film deposited on a $DyScO_3$ substrate showing the two doublets corresponding to surface and lattice strontium, along with peaks corresponding to a low concentration of lead surface contaminants. d) The summarized XPS studies following annealing steps shows surface strontium segregation for all strain states, but the difference in overall concentrations for different strain states are low.

do not rely on the XPS studies (alone) for analysis of the electrochemical trends examined. Moreover, the annealing studies demonstrate some strontium segregation, as expected; however, almost no difference between the LSCF/LSAT (-0.97%) heterostructures and LSCF/$SrTiO_3$ (-0.02%) heterostructures after 16 hours of annealing was observed (Figure 5.2d). Finally, the LSCF/$DyScO_3$ (+1.09%) heterostructures appear to exhibit a slightly higher degree of strontium segregation for annealing steps longer than 10 hours, in contrast with more in-depth studies of strain-dependent strontium segregation.[82]

5.3. Strain-dependent oxygen exchange rates

The oxygen exchange rates of the films were measured via the ECR method[143] at 300°C whereby, as described in Chapter 4, the resistance of the films was measured as a function of time following a step-change in the oxygen-partial pressure. ECR curves measured on strained LSCO films show

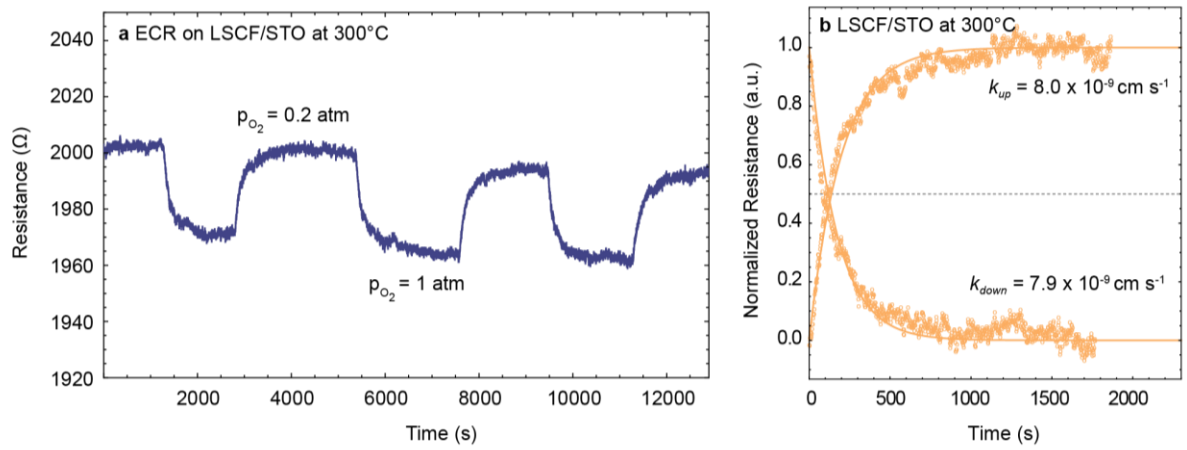

Figure 5.3: a) Raw data is presented for ECR curves from a LSCF film deposited on $SrTiO_3$ (STO) substrate, demonstrating the reversibility of both oxidation and reduction reactions. b) ECR curves for oxidation and reduction produce the same rate constants, demonstrating that the pressure change is small enough to ensure rate constants are being calculated within the linear regime. Solid lines correspond to the exponential fits to each curve.

an increase in resistance following a sudden drop in p_{O2} from 1 atm to 0.2 atm, indicating the defect equilibria of LSCO is similar to that described for LSCF compositions (see Chapter 3.2). Moreover, p_{O_2} for both LSCO and LSCF could be reversibly changed between 1 atm and 0.2 atm with balance nitrogen resulting in reversible changes to the resistance values upon switching the pressure (Figure 5.3a). Measuring the relaxation profiles in both the oxidizing (0.2 atm → 1 atm) and reducing (1 atm → 0.2 atm) directions produces rate constants that are almost identical, demonstrating that the system response is linear (Figure 5.3b). Carrying out measurements on the films under different epitaxial strains resulted in dramatically different reaction rates. The highly compressively strained LSCO/$LaAlO_3$ (-1.22%) heterostructures take the longest to equilibrate (approaching 30 minutes for full equilibration), whereas the tensile strained LSCO/LSAT (+0.87%) and LSCO/$SrTiO_3$ (+1.79%) heterostructures equilibrate in just 3-10 minutes (Figure 5.4a). Fitting the rate of change of the normalized resistance to the following expression provides for extraction of a surface-reaction rate constant,[162]

$$\frac{R_t - R_0}{R_\infty - R_0} = 1 - Exp\left(\frac{k_s}{d} * t\right), \tag{5.1}$$

where t is the time measured after the pressure change, d is the film thickness, and R_0, R_t, and R_∞ are the measured resistances before the pressure change, at time t, and after the film has equilibrated to a new value, respectively. Fitting each curve to this equation, we extract the surface-reaction rate constant, k_s for all strain states. The extracted rate constants for LSCO/$SrTiO_3$ (+1.79%), LSCO/LSAT (+0.87%), and LSCO/$LaAlO_3$ (-1.22%) heterostructures are 2.8x10^{-8}, 1.1x10^{-8}, and 1.5x10^{-9} cm s^{-1}, respectively, demonstrating an order of magnitude enhancement for films under large tensile strain compared to the films under large compressive strain, considerably larger than differences measured for different surface orientations. The measured difference

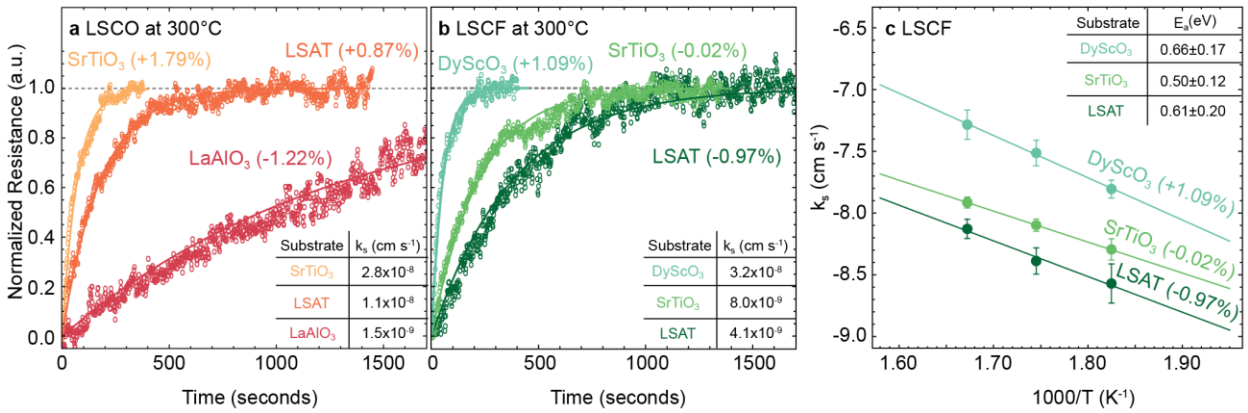

Figure 5.4: Electrochemical testing of (a) LSCO thin films on various substrates at 300°C showing the fastest relaxation kinetics for films deposited on $SrTiO_3$ (001) substrates, corresponding to +1.79% tensile strain. Inset table shows extracted rate constants, k_s, for each strain state. (b) Measurements on LSCF thin films at 300°C showing a similar trend, with films under tensile strain having faster reaction kinetics than the low- or compressively strained films on $SrTiO_3$ and LSAT substrates, respectively. Inset table shows the extracted rate constants, k_s, from each strain state. (c) The strain-dependence of the reactions rates for the LSCF thin films holds over a range of temperatures. Inset shows the extracted slopes of the temperature-dependence and that each strain state gives rise to a comparable activation energy.

between the different strain states is also similar in magnitude to previously reported strain-induced changes for iron-based cathodes.[82] A similar trend for strained LSCF films is observed; namely, close to an order of magnitude increase in rate constant in films under tensile strain (on $DyScO_3$ substrates) as compared to those under compressive strain (on LSAT substrates) (Figure 5.4b). While the poor thermomechanical stability of LSCO prevented more extensive temperature-dependent studies,[114,117] additional measurements were performed on the LSCF heterostructures at 275°C and 325°C (Figure 5.4c). Temperature-dependent ECR was measured for both heating (*i.e.*, measuring first at 275°C and increasing the temperature thereafter) as well as cooling (*i.e.*, measuring first at 325°C and decreasing the temperature thereafter) with no significant difference observed between the routines, suggesting that sample aging did not play an important role in the temperature-dependence observed. LSCF/$DyScO_3$ (+1.09%) heterostructures maintained the fastest surface reaction rate over the temperature range studied, while the LSCF/LSAT (-0.97%) heterostructures remained the slowest. Fitting the temperature-dependence of the rate constants for the LSCF films showed small differences in activation energy E_a, between 0.50-0.66 eV (Figure 5.4c, inset), similar to activation energies reported for other iron-based cathodes[82] and suggesting that any strain-induced difference in E_a is within the error of the measurement and, therefore, does not provide sufficient explanation as to the differences between rate constants. Overall, these results establish that epitaxial strain can induce changes to oxygen-exchange rates. In agreement with previous reports on cobalt- and iron-based cathodes, biaxial-tensile strain is shown to increase reaction rates, while biaxial-compressive strain reduces reaction rates.[78,80–82] Considering these large strain-induced changes to reactivity, and the relatively small difference in surface strontium as probed with XPS, the surface electronic structure of the various films were studied to understand the driving force behind the observed electrochemical trend.

5.4. Probing surface electronic structure

To probe strain-induced changes to the surface electronic structure, X-ray absorption and linear dichroism studies were performed on the epitaxially strained LSCO and LSCF films at beamline 4.0.2 at the Advanced Light Source, Lawrence Berkeley National Laboratory (Experimental Section). An elliptically polarizing undulator allows for control of not only X-ray energy, but also polarization, allowing for measurement of the absorption under differently polarized beams. Rotating the sample in the beam path also provides for alignment of the X-ray polarization with the three primary crystallographic axes, namely [100], [010], and [001]. Grazing incidence measurements performed at an incident angle of 20° with respect to the sample surface provide a comparison of out-of-plane and in-plane directions, while normal incidence scans, performed with an incident angle of 90° with respect to the sample surface, can be used to compare the two in-plane directions. The intensity of the incident X-ray beam and sample drain current were simultaneously measured to normalize the absorption intensity.

Here, the absorption is measured with photons polarized parallel to the plane of the thin film (*E // ab*) as well as nearly perpendicular to the plane of the film (*E // c*) (Figure 5.5a). XLD is defined as the difference between the spectra measured with *E // ab* and *E // c* (*i.e.*, $I_{ab} - I_c$). Larger absorption from *E // ab* (*i.e.*, $I_{ab} - I_c > 0$) indicates more empty in-plane states, whereas larger absorption from *E // c* (*i.e.*, $I_{ab} - I_c < 0$) indicates more empty out-of-plane states. Moreover, absorption is measured *via* a total electron yield (TEY) process (see Chapter 3.4.2), ensuring that the studies are sensitive to only the top few nanometers of the film, thus probing the portion of the film most directly exposed to the environmental gas and involved in oxygen electrocatalysis.

First, the cobalt-*L* edge of strained LSCO heterostructures was examined (Figure 5.5b-d). The relatively broad L_3 and L_2 peaks confirm a mixture of Co^{3+} and Co^{4+} that is caused by the aliovalent doping of Sr^{2+} on the La^{3+} site.[176] Moreover, there has been significant discussion regarding the spin state in Co^{3+}-based perovskites, with competition between high-spin (HS, $t_{2g}^4 e_g^2$), low-spin (LS, $t_{2g}^6 e_g^0$), and intermediate-spin (IS, $t_{2g}^5 e_g^1$) states which are relatively close in energy with each producing unique X-ray absorption and XLD spectra.[176,198,199] In the $La_{1-x}Sr_xCoO_{3-\delta}$ system, spectroscopic studies have proposed that the cobalt exists predominantly as a mixture of HS Co^{3+}, and HS Co^{4+}, with some LS Co^{3+} that decreases in prevalence with increasing Sr^{2+} content.[176] The spectra observed here are consistent with the presence of HS Co^{3+} and Co^{4+} and the relatively high Sr^{2+} content (50%) and suggests that the fraction of LS Co^{3+} is likely to be low in these samples; thus we assume a HS configuration for further analyses. In this case, the significant filling of the t_{2g} orbitals suggests that the majority of the electronic changes observed will originate in the e_g orbitals. Differences in the absorption of in-plane (*E // ab*) and out-of-plane (*E // c*) X-rays are mainly observed on the high-energy side of the L_3 and L_2 edges, suggesting epitaxial strain is primarily modulating the electron occupancy of the e_g orbitals in LSCO. The strain-induced changes are best observed in the linear dichroism. For LSCO/$LaAlO_3$ (-1.22%) heterostructures under biaxial compressive strain (Figure 5.5b), the integrated area is largely positive, indicating more empty in-plane states, whereas for the LSCO/LSAT (+0.87%; Figure 5.5c) and

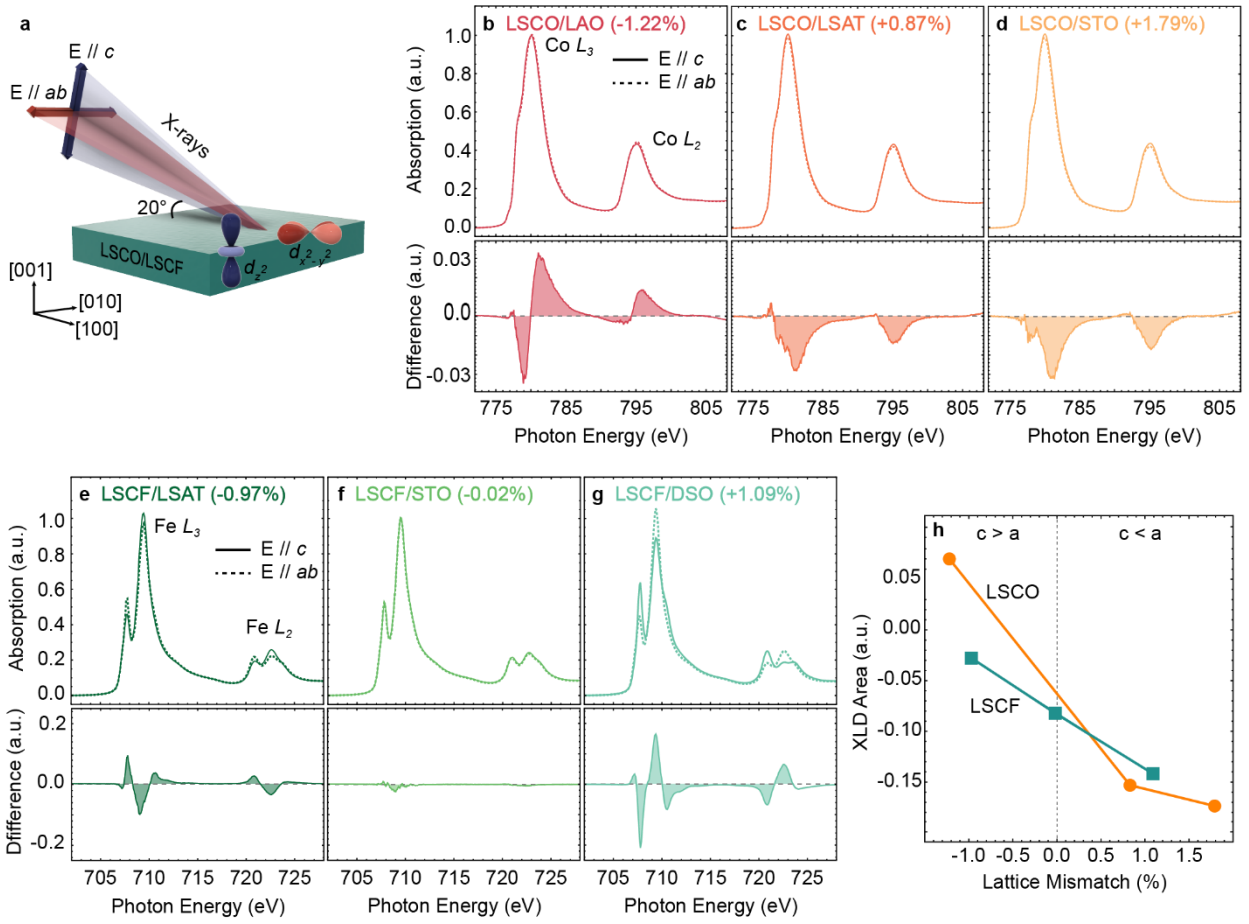

Figure 5.5: XLD measurements of LSCO and LSCF films. (a) The grazing incidence geometry allows for selectively probing the difference between the in-plane $d_{x^2-y^2}$ (red) and out-of-plane d_{z^2} (blue) orbitals. (b-d) Measurements of the cobalt-*L* edge show an inversion of the dichroism moving from compressive strain (LSCO/LAO) to tensile strain (LSCO/LSAT and LSCO/STO). (e-g) XLD at the iron-*L* edge in LSCF films shows a similar inversion of the dichroism between compressive (LSCF/LSAT) and tensile (LSCF/DSO) strain states, while the low-strain, cubic film (LSCF/STO) shows no dichroism. (h) The total integrated XLD area is summarized demonstrating that increasingly tensile strain (decreasing *c*/*a* ratio) results in more negative XLD area, corresponding to more empty states oriented out-of-plane.

$LSCO/SrTiO_3$ (+1.79%; Figure 5.5d) heterostructures under tensile strain we see the inverse, with large negative areas, indicating more empty out-of-plane states.

In the case of the iron-*L* edge in the LSCF films, the spectra generally resemble that of $LaFeO_3$, characterized by doublets in both the L_3 and L_2 edges (Figure 5.5e-g) indicating the iron is primarily in the Fe^{3+} state.[174,178] Examining the L_3 edge, the strongest peaks, centered around 709.5 eV, correspond to the e_g states, while the smaller peak at lower energies corresponds to the t_{2g} states. Beginning with the low-strain $LSCF/SrTiO_3$ (-0.02%) heterostructure, the spectra measured with in- and out-of-plane polarized X-rays are almost identical, exhibiting near-zero dichroism, as expected for a cubic perovskite (Figure 5.5f). Applying strain, however, results in the emergence of more significant dichroism with the LSCF/LSAT (-0.97%; Figure 5.5e) and $LSCF/DyScO_3$ (+1.09%; Figure 5.5g) heterostructures showing inverted dichroism relative to one another. This inversion of the difference curve is an indication of inversion of the preferential occupation of the

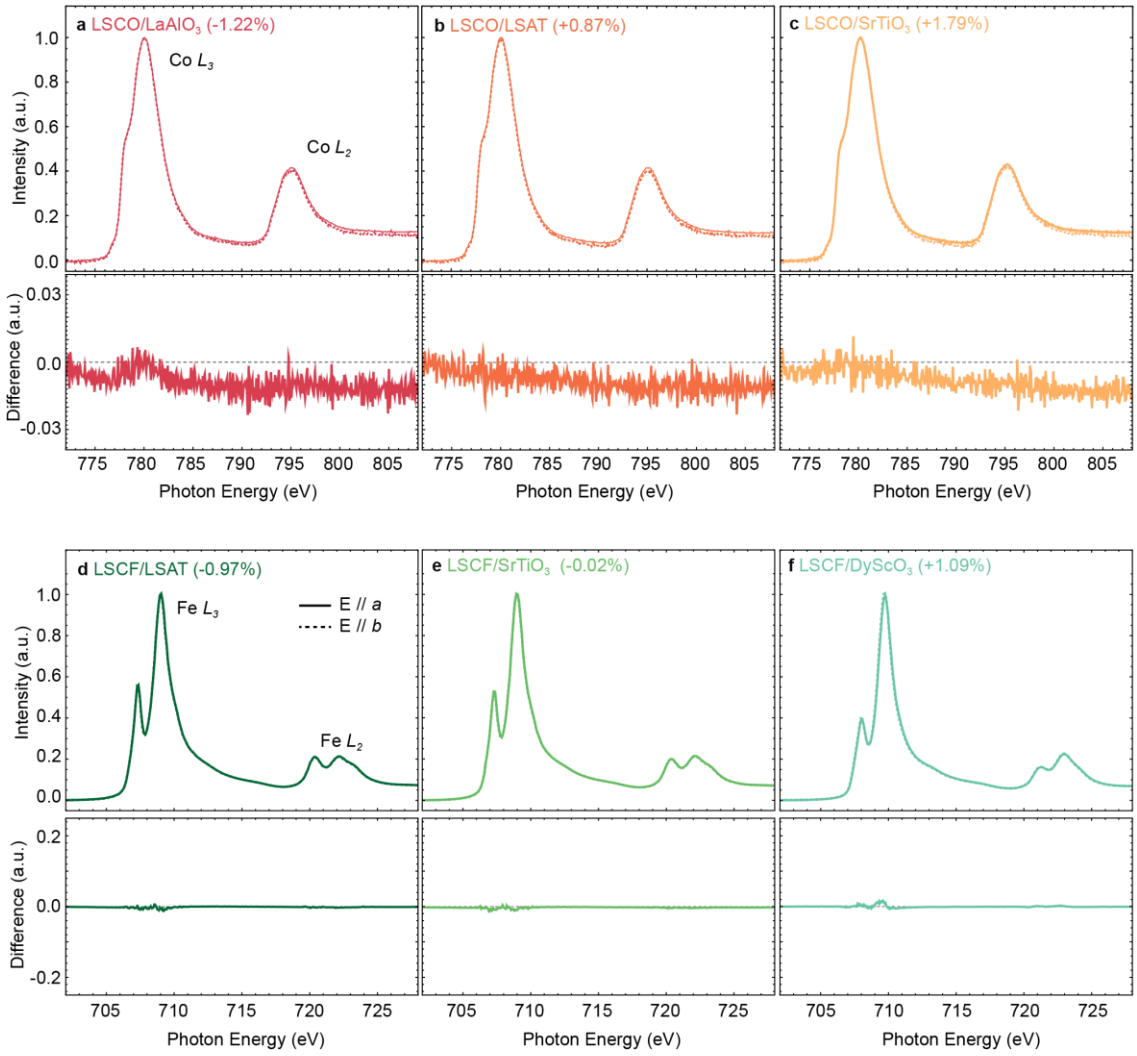

Figure 5.6: XLD measurements at normal incidence for a-c) LSCO films on various substrates and d-f) LSCF films on various substrates show no significant dichroism due to the in-plane symmetry of the a- and b-axes.

orbitals. Thus, the same trend is observed for both LSCO and LSCF films: that the integrated area of the linear dichroism becomes increasingly negative as the films are subjected to increasing tensile strain (Figure 5.5h). This confirms that applying tensile strain results in an increase in the density of available states in the out-of-plane-oriented *d* orbitals for both LSCO and LSCF films.

Strain-induced changes to lattice and orbital symmetry can also be confirmed by examination of other crystallographic axes. Whereas grazing incidence measurements probe out-of-plane and in-plane oriented states, normal incidence measurements can probe electronic differences between two in-plane directions. If the strain-induced changes to the XLD signal measured is due to the broken symmetry of the orbitals under biaxial strain, then no XLD signal is expected for measurements comparing the symmetric in-plane directions. X-ray absorption along the in-plane *a* and *b* axes of LSCO films measured at normal incidence (Figure 5.6a-c) shows no asymmetry between the two in-plane directions, although there was some small systematic offset observed in

the absorption. The noise and lack of structure (*i.e.*, no significant peaks) in the XLD suggests this is just a scan artifact rather than evidence of significant differences in orbital occupation between the in-plane directions. Similarly, normal incidence scans show essentially no XLD signal in LSCF films (Figure 5.6d-f), particularly for LSCF/LSAT (-0.97%) and LSCF/$SrTiO_3$ (-0.02%) heterostructures, which have nominally tetragonal structure and identical *a* and *b* lattice parameters. LSCF/$DyScO_3$ (+1.09%) heterostructures show slightly larger in-plane dichroism, which can be attributed to the anisotropic in-plane lattice parameters of the $DyScO_3$ substrate,[200] which likely induce a small asymmetry in the occupation of in-plane orbitals oriented along $[100]_{pc}$ and $[010]_{pc}$. This confirms that the large dichroism observed in the grazing-incidence measurements is due to the epitaxial strain-induced asymmetry between the *a/b* and *c* lattice parameters, and the associated change in orbital occupation.

5.5. Pushing the limits of strain-induced enhancement and the impact of strain relaxation

Considering the enhanced reactivity of LSCF films under tensile strain on $DyScO_3$ substrates, it is natural to wonder how far this enhancement can be extended. Deposition of LSCF on $TbScO_3$ (110) substrates, which impart a tensile strain of +1.23%, greater than that of $DyScO_3$ (110), was carried out in an attempt to further enhance reaction rates. Pulsed-laser deposition was carried out in the same manner as described above for the other strain states. RSMs about the LSCF 103-diffraction condition (Figure 5.7a), however, exhibited an asymmetric peak shape, with some intensity extending to higher values of Q_x than expected for a completely strained film. Because the majority of the peak falls at the expected strained position, at the same lattice spacing as the $TbScO_3$ 332-diffraction condition, it is expected that a majority of the film is coherently strained, and the observed tail reflects the onset of (some) lattice relaxation near the surface of the film. Despite this, both electrochemical measurements (Figure 5.7b) and XLD measurements (Figure 5.7c) of these films were carried out in the same fashion as the films for the other strain states. Interestingly, slower reaction rates are measured for LSCF/$TbScO_3$ (+1.23%) heterostructures (Figure 5.7b) than those measured for LSCF/$DyScO_3$ (+1.09%) heterostructures, which, at first, may suggest that biaxial tensile strain does not monotonically increase reaction rates. XLD measurements, however, also show reduced dichroism compared with LSCF/$DyScO_3$ (+1.09%) heterostructures (Figure 5.7c), indicating that XLD and reaction rates remain strongly correlated. The effects discussed to this point have correlated two surface sensitive techniques, namely the surface reaction with oxygen, and the XLD signal measured by TEY detection. As described in Chapter 3, the use of the TEY method for measurement of X-ray absorption, that is, measuring the sample drain current that replenishes electrons that are lost by emission of Auger and secondary electrons, limits the sensitivity of the X-ray absorption to the top few nanometers of the films. In the case of the LSCF/$TbScO_3$ (+1.23%) heterostructures, despite evidence that the bulk of the LSCF film is fully strained to the substrate, partial relaxation near the surface can reduce the local lattice symmetry at the surface, where oxygen exchange takes place. Again, due to the difficulty of accurately quantifying the strain state of the very surface of these particular heterostructures, it is difficult to make quantitative comparisons to the fully strained heterostructures discussed above,

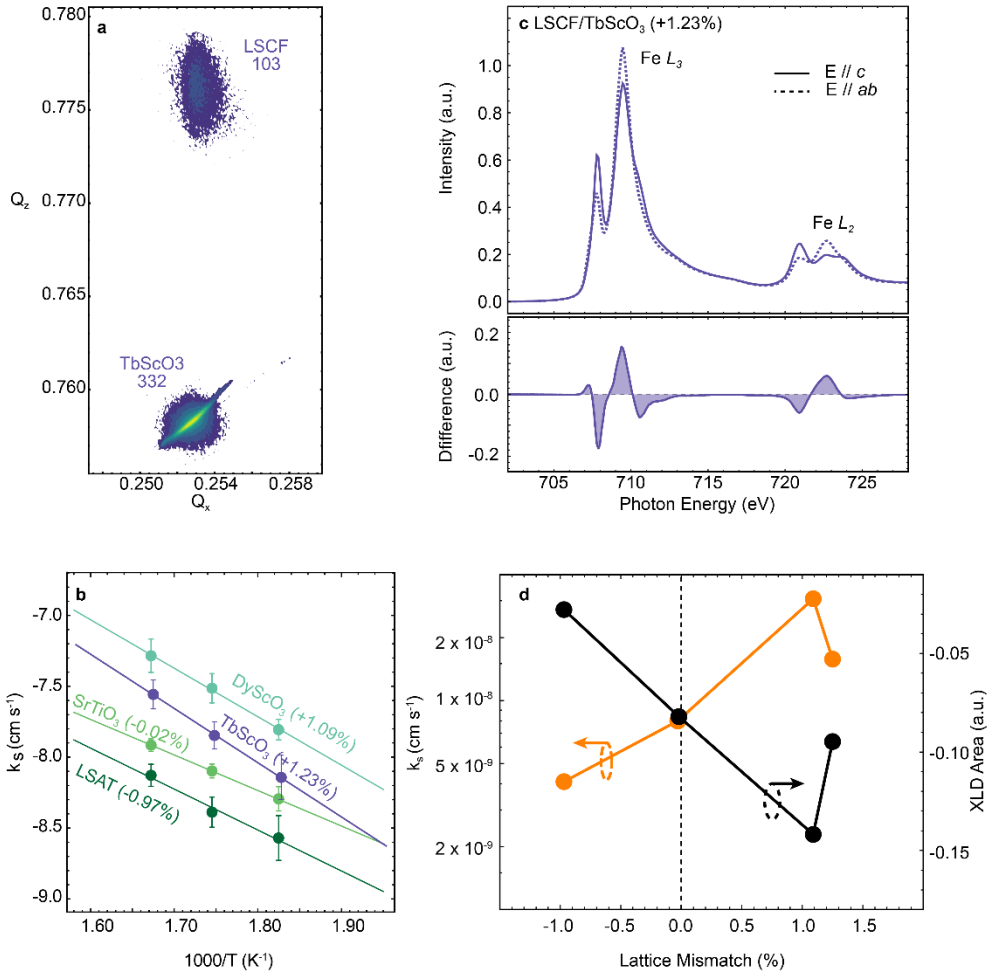

Figure 5.7: a) Reciprocal space maps about the 103-diffraction condition of LSCF suggest the onset of relaxation at the surface of the film. b) XLD measurements demonstrate dichroism similar in nature to that observed for LSCF films on $DyScO_3$, yet smaller in magnitude. c) Temperature-dependent rate constants for LSCF/$TbScO_3$ heterostructures show similar activation energy, but slower kinetics compared to fully-strained LSCF/$DyScO_3$ heterostructures. d) A side-by-side comparison of the trends in dichroism and reaction rate constant shows strong agreement, even for films in which the film is not fully strained.

but this observation further strengthens the correlation between the oxygen surface reaction rates, and the lattice symmetry at the surface of the film. As such, the measured linear dichroism and calculated provides a stronger predictor for reaction rate constants than the epitaxial strain expected from a simple lattice mismatch perspective.

5.6. Quantifying strain-induced changes to orbital structure

With confirmation that the XLD is indeed a result of strain-induced changes to the electronic structure at the films' surface, a more quantitative approach to understanding the energy splitting and electron occupation of the orbitals in question. It is understood that in many transition-metal perovskite oxides the conventional ligand-field model suggests that changing the overlap of the transition metal 3*d* orbitals with the oxygen 2*p* orbitals shifts the energy of the electrons within

these orbitals, with biaxial compressive strain increasing the energy of the $d_{x^2-y^2}$ orbital relative to the d_{z^2} and *vice versa* for biaxial tensile strain.[19] If this is the case, the changing energy of the t_{2g} and e_g states should be readily apparent in oxygen absorption spectra. XLD measurements at the oxygen *K* edge showed no significant dichroism, which may be related to the presence of disordered oxygen vacancies which mask the strain-induced changes to oxygen 2*p* orbital structure. Despite the lack of dichroism, X-ray absorption spectra illustrate changes to the energy splitting in oxygen 2*p* states that are hybridized with the iron 3*d* orbitals (Figure 5.8a). As discussed in Chapter 4, it is well known that in the $La_{1-x}Sr_xFeO_3$ system, aliovalent strontium substitution induces hole doping in the oxygen 2*p* states rather than driving formation of a formal Fe^{4+} state[174]. This is typically observed via the appearance of a pre-edge peak at ~528 eV[178], while peaks at 529 eV and 531 eV reflect the t_{2g} and e_g states, respectively (Figure 5.8b). Fitting each of these peaks

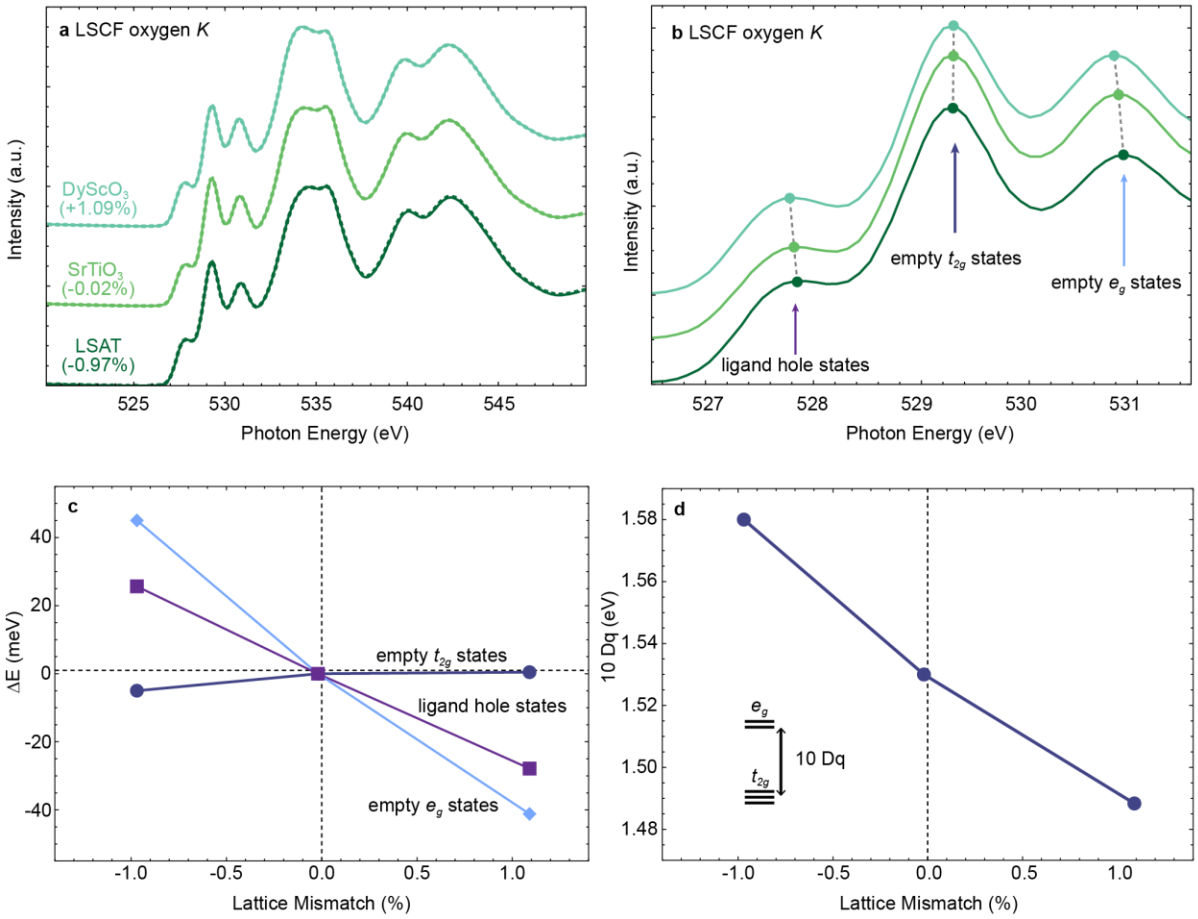

Figure 5.8: a) XLD measurements of the oxygen-*K* edge in LSCF films shows no dichroism for any of the strain states. Both polarization directions are displayed, but no dichroism is observed, and spectra are overlapping. b) A zoom-in of the oxygen-*K* edge in LSCF films showing detailed structure of the iron *3d*-oxygen *2p* hybridized states between 526-532 eV. c) The difference in peak energies extracted from the oxygen *K* spectra show the shifting of e_g states with the application of epitaxial strain. Peak energies are measured with respect to the low-strain LSCF/STO films. d) Crystal field splitting parameter, 10 Dq, extracted from the oxygen-*K* edge shows a progressive decrease in energy-splitting with increasing tensile strain.

to a simple gaussian function allows for extraction of the peak center, and examination of the evolution of peak energies with strain. In order to visualize the strain-induced changes, peak energies extracted from the low-strain film on $SrTiO_3$, which is cubic via X-ray diffraction measurements (Figure 5.1) and shows no dichroism at the iron *L* edge (Figure 5.5f), are used as the zero in energy for each peak (Figure 5.8c). Both the ligand hole states (at 528 eV), arising from strontium substitution and the empty e_g states shift continuously lower in energy with increasing tensile strain, whereas the t_{2g} states remain relatively constant (within 10 meV). This demonstrates that epitaxial strain makes the biggest impact on the higher energy e_g orbitals, rather than the t_{2g} orbitals, and supports the assumption that a majority of the orbital polarization occurs in the e_g orbitals. Finally, the estimated crystal-field splitting (10 Dq), taken as the difference between the t_{2g} and e_g states, shows an approximate 100 meV decrease from the LSCF films compressively strained on LSAT to the LSCF films under tensile strain on $DyScO_3$ (Figure 5.8d). Values of ~1.5 eV are in agreement with previously reported values of 10 Dq for similar systems.[174]

Returning to the transition-metal-*L* edges, the corresponding energy shifts can be observed in the iron and cobalt t_{2g} and e_g states (Figure 5.9a). Comparing the difference in energy of the L_3

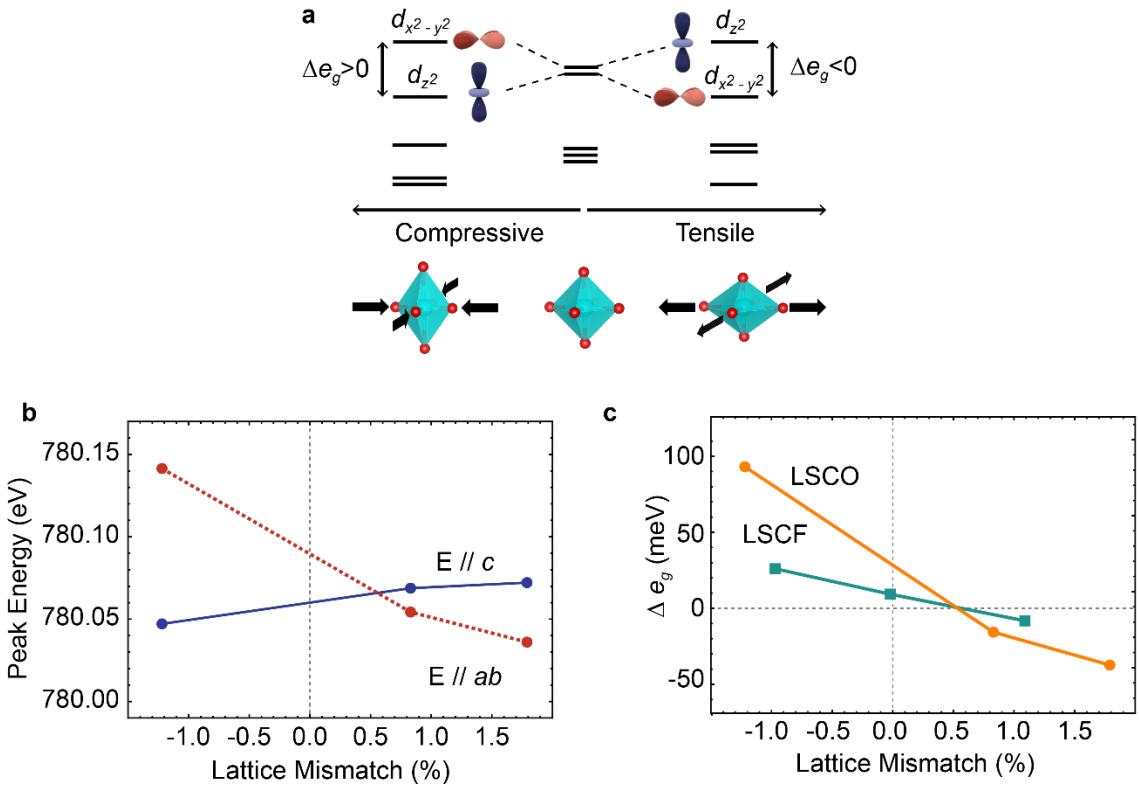

Figure 5.9: a) Schematic illustrating the relationship between epitaxial strain and orbital energies in perovskite oxides showing that applying compressive strain breaks the e_g degeneracy and shifts the $d_{x^2-y^2}$ orbital higher in energy than the d_{z^2} orbital, while for tensile strain the $d_{x^2-y^2}$ orbital is lower in energy. b) Peak energies extracted from the cobalt-*L* edge in LSCO films demonstrate this trend, as the in-plane peak energy, corresponding to the $d_{x^2-y^2}$ orbital shifts lower in energy with tensile strain. c) The difference in orbital energy, Δe_g, changes sign moving from compressive to tensile strain, with LSCO demonstrating a larger strain-induced change in orbital energies than LSCF.

peak for vertically and horizontally polarized light for the cobalt-*L* edge in LSCO can be used to estimate the strain-induced energy splitting of the e_g orbitals (Figure 5.9b). The peak energy of the in-plane polarized light decreases by approximately 100 meV, with increasing tensile strain, whereas the peak energy for the out-of-plane polarized light increases by approximately 25 meV. To quantify the strain-induced energy difference between the e_g orbitals, we define:

$$\Delta e_g \;=\; E_{max}(E//\,ab) \;- E_{max}(E//\,c) \;\approx\; E\left(d_{x^2-y^2}\right) - \;E(d_{z^2}). \tag{5.2}$$

In both LSCO and LSCF, Δe_g goes from positive to negative as we move from compressive to tensile strain (Figure 5.8d). In a cubic crystal field, these two e_g orbitals are energetically degenerate, as evidenced by the smallest Δe_g for the LSCF/$SrTiO_3$ (-0.02%) heterostructures and, thus, electrons are more equally distributed between the two e_g orbitals (Figure 5.9a). When biaxial strain is applied, however, the associated symmetry-breaking removes the energetic degeneracy and we see that under tensile strain $\Delta e_g < 0$ (*i.e.*, the d_z^2 orbital is higher in energy relative to the $d_{x^2-y^2}$ orbital) and under compressive strain $\Delta e_g > 0$ (*i.e.*, the d_z^2 orbital is lower in energy relative to the $d_{x^2-y^2}$ orbital). This breaking of the energetic degeneracy of the e_g orbitals is expected to also break the degeneracy in electron occupancy of the two e_g orbitals.[19,201,202] That is, electrons should preferentially occupy the lower-energy orbital, thereby reducing the occupancy of the higher-energy orbital. In this case, the reduction of the $d_{x^2-y^2}$ orbital energy under tensile strain results in preferential occupation of the lower-energy $d_{x^2-y^2}$ orbital and a reduction of the electron occupancy in the higher-energy d_z^2 orbital.

Using established sum rules for linear dichroism, the strain-induced change in occupancy of the d_z^2 orbital can be calculated for each of the films under study.[70,203,204] These sum rules relate the relative intensities of absorption along the x, y, and z directions as:

$$I_x = \frac{1}{n}\left(\frac{1}{2}n_{xy} + \frac{1}{2}n_{xz} + \frac{1}{6}n_{z^2} + \frac{1}{2}n_{x^2-y^2}\right) \tag{5.3}$$

$$I_y = \frac{1}{n}\left(\frac{1}{2}n_{xy} + \frac{1}{2}n_{yz} + \frac{1}{6}n_{z^2} + \frac{1}{2}n_{x^2-y^2}\right) \tag{5.4}$$

$$I_z = \frac{1}{n}\left(\frac{1}{2}n_{xz} + \frac{1}{2}n_{yz} + \frac{2}{3}n_{z^2}\right) \tag{5.5}$$

where I_j is the integrated normalized intensity along direction j, n_i is the number of holes in orbital i, and n is the total number of holes in the d orbitals. In this work, it is assumed that t_{2g} and e_g orbitals are half filled, corresponding to the high-spin d^5 state. We also assume that the t_{2g} orbitals experience negligible polarization under +/-1% strain, and thus the ratio I_x/I_z reflects the orbital polarization of the e_g orbitals.[70] As such we use:

$$n_{xy} = \; n_{xz} = \; n_{yz} = 1 \tag{5.6}$$

$$n_{x^2-y^2} + \; n_{z^2} = 2. \tag{5.7}$$

The use of the total e_g occupancy to be two electrons is based on previous analyses that report the total occupation of fully oxidized $CaFeO_3$, which has a robust Fe^{4+} state to be approximately 1.85 electrons[70]. Due to the relatively low strontium content in the LSCF films (20% strontium content) used in this study, we assume that the e_g remains closer to the ideal two electrons. Nevertheless, utilizing a value of 1.85, as reported for $CaFeO_3$ does not impact the trends discussed in this study, and only introduces a systematic downward shift of the calculated d_z^2 occupancy by approximately 4%. Finally, we use the ratio of absorbed intensities along the two measured polarization directions to solve for the number of electrons occupying the d_z^2 orbital and divide this by the total possible occupation of 2 for a single d orbital to calculate the d_z^2 orbital occupancy.

Recall that the spin state of $Co^{3+/4+}$ ions in LSCO is a matter of much discussion and such cobalt-based oxides has been found to possess a mixture of spin states along with charge states[176]. In this case, due to the high level of strontium substitution in the LSCO studied here (50% strontium content), we approximate the spin state with a mixture of high-spin d^5 and d^6 states, giving a configuration of $t_{2g}^{3.5}e_g^2$. While that additional 0.5 electron may lay in any of the t_{2g} we found that the trend reported here does not depend strongly on which of the t_{2g} orbitals this electron occupies. The presence of low- and intermediate-spin states may also impact the orbital polarization, in that it additionally changes the total e_g occupation, similar to strontium-induced hole formation in LSCF. As with that case, lower spin states in LSCO will serve to systematically shift the calculated occupancy curves downward by a few percent, but does not dramatically change the trends and their relation to the electrochemical results.

In the case of both sets of films, we see that the reduction in the energy of the $d_{x^2-y^2}$

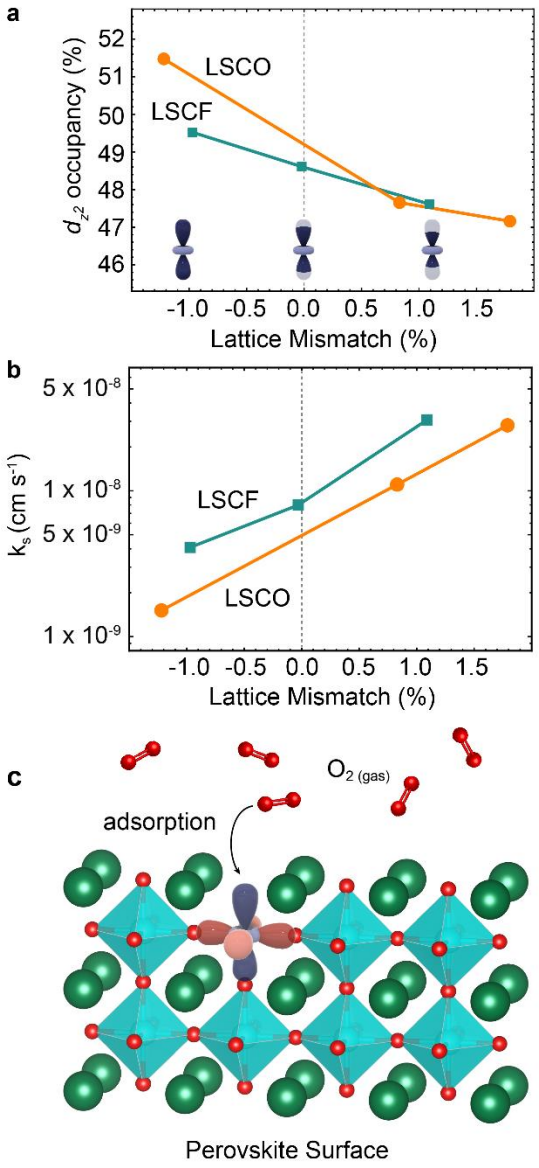

Figure 5.10: a) Calculation of the strain-dependent occupancy of the d_z^2 orbital shows that increasing tensile strain reduces the occupancy towards the proposed optimal value of ~30% and this reduction in occupancy is correlated to the increase in reaction rates with strain summarized in (b). c) Schematic showing that the d_z^2 orbital plays an important role in oxygen electrocatalysis as the primary orbital for interaction oxygen gas molecules adsorbing at the perovskite surface.

orbital under increasing tensile strain results in a reduction of the d_z^2-orbital occupancy as electron density shifts from the $d_{x^2-y^2}$ orbital to the d_z^2 orbital (Figure 5.10a). We note that the trends in orbital occupancy (calculated from the total integrated intensities of each spectrum; Figure 5.10a) and the trends in Δe_g (calculated from peak energies; Figure 5.9c) are in agreement for both compositions, albeit with different magnitudes for LSCO and LSCF, supporting the strain-induced Δe_g splitting as a driving force for changes to d_z^2-orbital occupancy. Overall, this demonstrates that epitaxial strain can be used to modulate the occupancy of the d_z^2 orbitals.

5.7. Chemical trends in strain-induced reactivity

With the correlation between orbital structure and reactivity established, one can now ask: why do the measured changes to transition metal orbital structure result in enhanced reactivity? Recall that the rate constants in both LSCO and LSCF films increased monotonically (in fully strained films) as the strain state was changed from compressive to tensile (Figure 5.10b), or in other words as the *c*/*a* lattice parameter ratio decreased, in agreement with studies on a number of systems reported elsewhere.[78,80–83,194] Corresponding to this change in rate constant with strain, an overall decrease in the electron occupancy of the d_z^2 orbital with increasing tensile strain was observed in both materials (Figure 5.10a). In the context of the proposed electronic descriptors described previously, specifically the e_g filling,[136] this strong correlation between d_z^2-orbital occupancy and rate constant is interesting because the overall e_g filling does not change with strain, only the relative occupation of the two non-degenerate orbitals has changed. The correlation to the occupancy of the d_z^2 orbital can then be understood in that the d_z^2 orbital is the orbital that is projected out of the surface of an [001]-oriented thin film (Figure 5.10c), and would have the most orbital overlap with the oxygen 2*p* orbitals of the incoming oxygen molecule to be adsorbed at the transition metal *B* site; a process which has been shown to be a critical step in the activation and incorporation of molecular oxygen at perovskite surfaces.[121] In this case, the ideal value is no longer an e_g filling of ~1.2 electrons,[136] but instead would be ~0.6 electrons in the d_z^2 orbital, or ~30% occupancy. As observed here, at the cobalt and iron sites in LSCO and LSCF, respectively, the d_z^2-orbital occupancy is near 50% at zero strain, and is decreased toward the optimal value of ~30% with the application of tensile strain. The occupancy trends extracted from both the strained LSCO and LSCF films thus provide additional rationale for the observation of enhanced oxygen electrocatalysis in cobalt- and iron-based perovskites under epitaxial tensile strain reported previously.[78,80–82] Moreover, this insight may also explain the somewhat contradictory report of enhanced bifunctional catalysis of $LaNiO_3$ thin films under compressive strain.[83] Because of the robust low-spin $t_{2g}^6 e_g^1$ electron configuration of the Ni^{3+} in those films, the zero-strain state likely has a d_z^2 orbital occupancy of ~25%, and thus compressive strain increases the d_z^2 orbital occupancy towards the ideal value near ~30%. This sort of chemistry dependence is evident even in the present work, where both the d_z^2-orbital occupancy and rate constant are more dramatically modulated by the application of epitaxial strain in the LSCO films as compared to the LSCF films. The robust, half-filled $t_{2g}^3 e_g^2$ electron configuration of the Fe^{3+} site in LSCF likely prevents more significant orbital polarization in the e_g levels, due to the electron-electron repulsion associated

with trying to increase electron density in the already singly occupied $d_{x^2-y^2}$ orbital, whereas the more complex $Co^{3+/4+}$ system having HS $t_{2g}^4 e_g^2$, LS $t_{2g}^6 e_g^0$, and IS $t_{2g}^5 e_g^1$ states could allow for more flexibility by shifting electron density into the $d_{x^2-y^2}$ orbital since a larger fraction throughout the film may be empty. This dependence on chemistry suggests that the connection between epitaxial strain and oxygen electrocatalysis observed for cobalt- and iron-based perovskites in this and previous studies is not universal but is strongly dependent on the zero-strain electronic configuration.

5.8. Conclusions

In summary, a strong correlation between the orbital structure and oxygen electrocatalysis rates in cobalt- and iron-based perovskite oxides was found through a combination of thin film synthesis, high-temperature electrochemical measurements, and XLD experiments. Electrochemical studies on epitaxially strained LSCO and LSCF thin films confirm an activity trend previously reported by several groups, namely that biaxial tensile strain enhances oxygen reactivity, while biaxial compressive strain suppresses oxygen reactivity. This work illustrates that an important descriptor for this activity trend for the LSCO and LSCF films is the electron occupancy of the d_{z^2} orbital, and not surface strontium segregation or lattice mismatch. The importance of the d_{z^2} orbital can be understood from a geometric perspective, in that it is directly oriented such that it will be involved in the adsorption and subsequent reduction of molecular oxygen on the surface of a [001]-oriented perovskite thin film. Overall, these findings support the claim that an e_g filling of ~1.2 electrons can result in optimal performance and further extend that notion to non-cubic cathodes. This work further provides an explanation for disagreement in the literature regarding the impact of epitaxial on strain, highlighting the importance of the electronic ground state and identity of the transition metal cation in determining the impact of epitaxial strain on orbital structure and electrochemical rates. Finally, this work also demonstrates that epitaxial strain can be used as a synthetic tool to modulate the electron occupancy of this orbital and subsequently enhance the reactivity of these perovskite catalysts.

Chapter 6:
Relaxor ferroelectrics

This chapter provides background on a class of polar material known as relaxor ferroelectrics. The nature of polarization in relaxor ferroelectrics is first explained through comparison to normal ferroelectrics and the phase transitions associated with each. Then, the structural and chemical origins of such behavior is described in the context of the ongoing debate regarding the fundamental polar unit driving relaxor behavior, so-called polar nanoregions or polar nanodomains. The ability of such polar clusters to reorient, and the unit-cell description of this polarization rotation is presented as a fundamental phenomenon that is both technologically useful, and of fundamental physical interest. Finally, specific characterization techniques used in this dissertation to characterize the properties of relaxors are described, including X-ray diffuse-scattering and dielectric and piezoelectric measurements.

6.1. Relaxors

Relaxor ferroelectrics, herein referred to simply as relaxors, are a class of polar materials that are typically characterized by slim polarization-electric field (P-E) hysteresis loops, diffuse phase transitions, and strongly temperature dependent relaxation dynamics.[205–207] In the late 1950s, a search for new lead-based ferroelectric perovskite compositions stumbled upon the relaxor $PbMg_{1/3}Nb_{2/3}O_3$ (PMN).[208] Unlike normal ferroelectrics, the polarization was observed to relax upon removal of the electric field, producing slim P-E hysteresis loops (Figure 6.1). Instead of the sharp peak in permittivity associated with the T_c of ferroelectric phase transitions, the phase transition of PMN was found to exhibit a broad peak with a strong dependence on the measurement frequency (Figure 6.1). Upon cooling to low temperatures, however, P-E loops developed hysteresis and remnant polarization. This behavior was attributed to the structural and chemical disorder in relaxors, giving rise to a complex evolution of disordered polarization that correlate over nanometer length-scales. Such complicated polar structures, which have now been shown to exhibit percolative freezing[209–211] and collective rotations,[212] have parallels in glassy systems, including spin glasses,[213,214] strain glasses,[215] and superparamagnetic systems,[216,217] and for several decades relaxors served as an intriguing class of materials for studying such polar interactions.

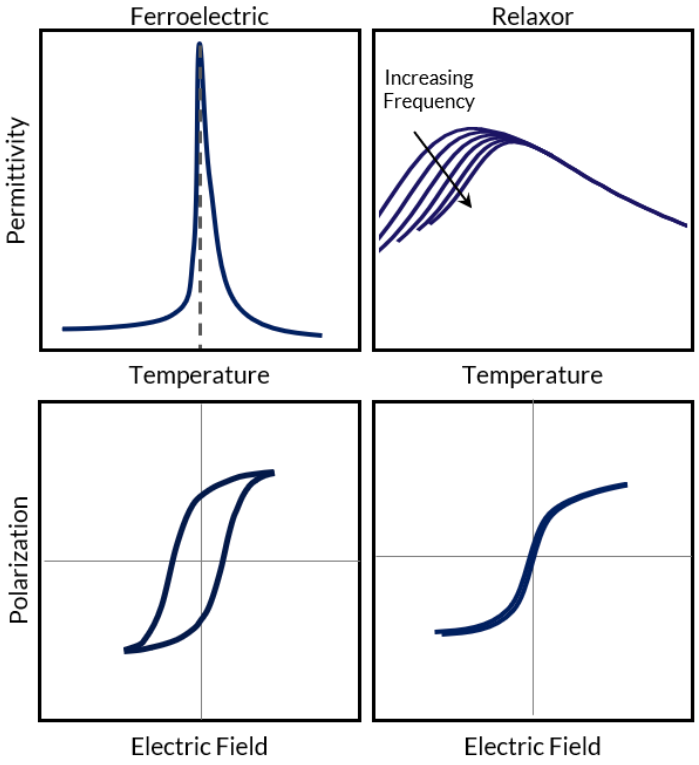

Figure 6.1: Schematic comparison of relaxors to normal ferroelectrics. The sharp phase transition of ferroelectrics is replaced by a diffuse phase transition with strong frequency dispersion. The polarization-electric field loop is slim and exhibits little hysteresis.

In the late 1990s, however, researchers managed to synthesize solid solutions of (1-x)$PbMg_{1/3}Nb_{2/3}O_3$-(*x*)$PbTiO_3$ (PMN-*x*PT) and (1-x)$PbZn_{1/3}Nb_{2/3}O_3$-(*x*)$PbTiO_3$ (PZN-*x*PT),[100] ultimately measuring ultrahigh piezoelectric coefficients, spurring renewed interest in harnessing this strong electromechanical coupling in a new generation of piezoelectric actuators and energy harvesters.[10,218] Even more recently, large energy densities have been reported for both pyroelectric-energy conversion[219] and capacitive-energy storage utilizing relaxor thin films.[220] With such promise across a range of technological applications, there remains growing interest in understanding and engineering relaxor properties. Yet the complexity of the polar interactions across multiple length scales, and the connection between the polar structure and the ferroelectric, pyroelectric and piezoelectric properties has generated heated debate regarding the nature and

origins of relaxor behavior, with articles frequently questioning the established paradigm of relaxors.[221–223] Here, the identifying characteristics, structural origins, and resulting properties of relaxors are briefly covered to provide background for thin film-based studies of the role of the lattice in dictating relaxor properties.

6.2. Phase transitions

One of the defining characteristics of relaxors is found in the diffuse phase transition, characterized by a broad peak in dielectric permittivity. Further, the temperature of maximum permittivity, T_{max}, exhibits strong frequency dispersion, with increasing T_{max} and decreasing ε as the measurement frequency is increased (Figure 6.1). This dispersion was attributed to the presence of a broad distribution of polar relaxation times.[205] Complicating matters further, T_{max}, marks neither the appearance of spontaneous polarization nor a change in macroscopic symmetry, as observed for typical ferroelectrics.

The complex evolution of polar interactions in relaxors has long been attributed to the heterogeneity driven by disordered chemical substitution. Over the years, several important temperatures have been identified as markers of this evolution. Early in the study of relaxors, researchers discovered that despite no macroscopic remnant polarization remains at zero field, a non-zero root-mean-square polarization, $\sqrt{\langle P^2 \rangle} \neq 0$, persists hundreds of degrees above T_{max}.[224] Measurements of the temperature-dependent refractive index for several relaxor systems exhibited a high-temperature anomaly, far from T_{max}, that was ultimately attributed to the formation of local nano-sized regions of polarization that are dynamically correlated and easily perturbed by thermal fluctuations.[225] This temperature, now called the Burns temperature, T_b, marks the first critical temperature in the evolution of polar structure upon cooling from the high temperature paraelectric phase. It was later found that the frequency dispersion of the dielectric maxima followed Vogel-Fulcher freezing,[209–211,213] an empirical law first used to describe the temperature-dependence of relaxation times in silicate glasses. Applied to relaxors, it describes the dependence of T_{max} on measurement frequency (ω):

$$\omega = \omega_0 \, Exp\left[-E_A/(T_{max} - T_f)\right], \tag{6.1}$$

where ω_0, E_A, and T_f are constants. This T_f, now called the *freezing temperature*, is said to describe the low-temperature critical freezing of polar relaxation. More recently, an intermediate critical temperature (T*) was observed between T_m and T_b in a number of relaxor systems.[226] Measurement of the temperature dependence of the dielectric permittivity showed the expected deviation from Curie-Weiss scaling (a linear scaling of ε^{-1} with temperature) that marked the T_b, but observed an additional linear Curie-Weiss regime below T_b. Deviation from this secondary regime, was ultimately labeled T* and attributed to the onset of correlations between local dipoles in the material and marks the onset of the frequency dispersion of the dielectric permittivity. Together, these critical phenomena and associated temperatures can be used to construct a phase diagram for

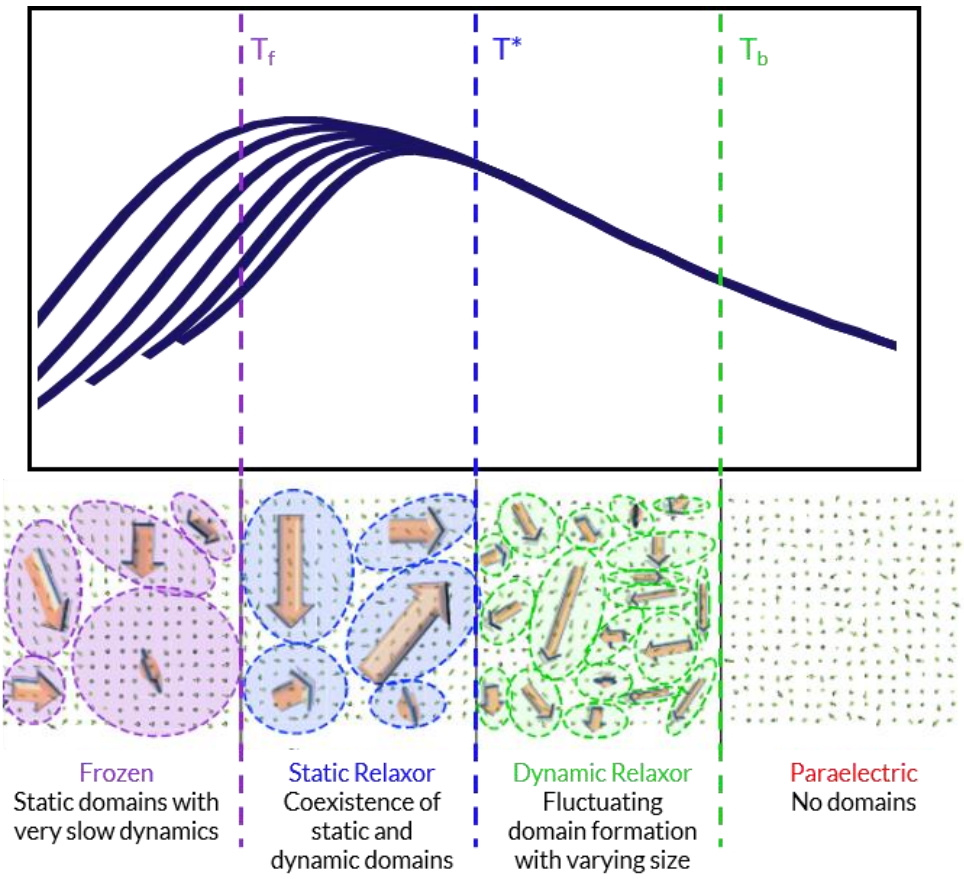

Figure 6.2: Summary of critical temperatures in relaxors relating the measured temperature-dependent permittivity with simulating atomic polar structure. Adapted with permission from ref [*93*], Copyright 2017, Springer Nature.

relaxor behavior.[93,227] At high temperatures above T_b, the material is paraelectric, and forms local polarization that is thermally fluctuating and dynamically correlated. As the material is further cooled below T*, dynamic fluctuations slow and become static, and polar regions become more strongly correlated. Cooling through T_{max} brings about a progressive critical slowing of the relaxation times of polar domains until at T_f the polar domain fluctuations are frozen out. The three critical temperatures, namely, T_b, T*, and T_f have been used to describe the boundaries of 4 phases of relaxors materials: the paraelectric phase ($T > T_b$), the dynamic relaxor phase ($T_b > T > T^*$), the static relaxor phase ($T^* > T > T_f$) and frozen relaxor phase ($T < T_f$) (Figure 6.2).[93]

6.3. What makes a material a relaxor?

While the identifying characteristics of "relaxor-like" behavior are well agreed upon (*i.e.*, a diffuse phase transition with strong frequency dispersion and slim P-E loops), the precise mechanisms, structures, and causes are still the topic of much debate.[222] In general, it is agreed upon that disorder is important for driving relaxor properties, but it seems that different materials systems may have different atomic origins. In lead-based relaxors, where much of the polarization is driven by the lead $6s^2$ lone pair,[228] the most common attribution for the nanoscale polar structure is the charge-

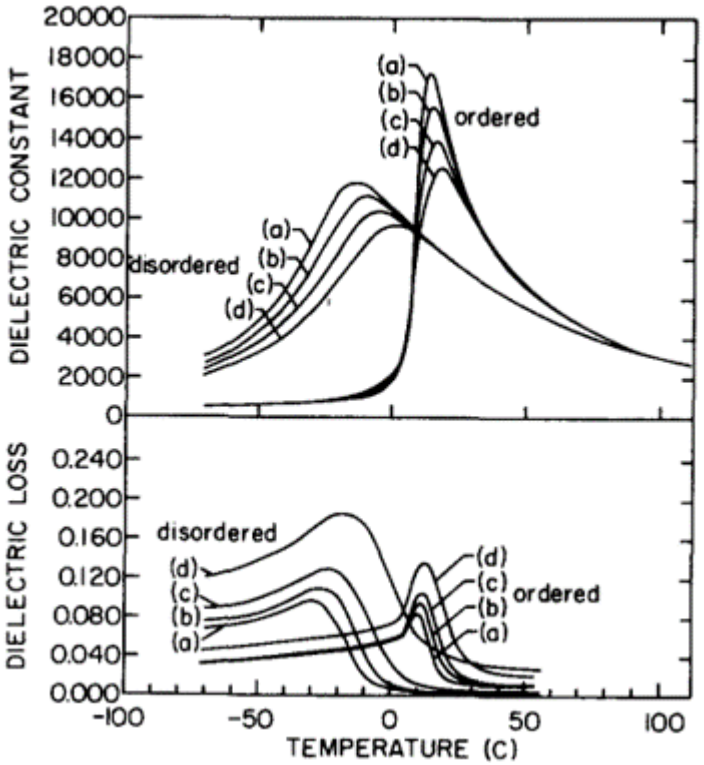

Figure 6.3: Dielectric permittivity and loss as a function of temperature for ordered and disordered $PbSc_{1/2}Ta_{1/2}O_3$ ceramics, illustrating the relaxor-to-ferroelectric transition driven by chemical ordering. Reprinted with permission from ref [*240*], Copyright 1980, AIP Publishing.

and elastic-disorder created by random substitution of *B*-site cations of different size and charge.[229] These random electric and elastic fields break long-range symmetry of the crystal, preventing long-range ordering of polarization, and limit polar correlations to the scale of a few nanometers.[211,230–232] The importance of elastic disorder can be seen in comparison to another relaxor system $BaZr_{1-x}Ti_xO_3$.[233,234] There, one end member of the solid solution, $BaZrO_3$, is a linear dielectric, exhibiting no root-mean-square polarization at zero field. On the other side, is the classical ferroelectric $BaTiO_3$, which has robust, long-range ordered polarization below a T_c of 130°C. A solid solution between the two phases exhibits relaxor behavior, yet the homovalent substitution of Ti^{4+} with Zr^{4+} does not result in charge disorder. Instead, nanoscale polar disorder has been attributed to differences in cation size (0.61 pm and 0.72 pm, respectively), which create random strain fields, as well as differences in polarizability of the two cations, ultimately breaking the long-range symmetry of the $BaTiO_3$ parent phase.[233–235] On the other hand, the importance of charge disorder in lead-based relaxors can be viewed through comparison to another classic ferroelectric system, $PbZr_{1-x}Ti_xO_3$ (PZT), where despite chemical disorder similar to $BaZr_{1-x}Ti_xO_3$, long-range ferroelectric order exists over much of the phase diagram, giving way to antiferroelectric order only at high zirconium concentrations.[236] Many lead-based systems, however, exhibit strong relaxor behavior when the *B*-site is shared by cations with different charge. For example, the first-known relaxor and most prototypical, PMN, has a *B*-site shared by Mg^{2+} and Nb^{5+}, and this charge disorder creates local random electric fields[95] which can drive formation of different local symmetries, but average over the entire crystal to a global cubic symmetry. A large number of lead-based relaxor systems exist, many with a similar 2+/5+ cation distribution, including $PbZn_{1/3}Nb_{2/3}O_3$ and $PbMg_{1/3}Ta_{2/3}O_3$, while other systems possess a 3+/5+ charge distribution, exemplified by systems like $PbSc_{1/2}Ta_{1/2}O_3$ and $PbSc_{1/2}Nb_{1/2}O_3$.[237–241] In these latter systems, long-range ordering of the *B* site can form under appropriate synthetic conditions, owing to the 1:1 ratio of the *B*-site cations. Such long-range ordering drives formation of a ferroelectric state rather than relaxor (Figure. 6.3). These

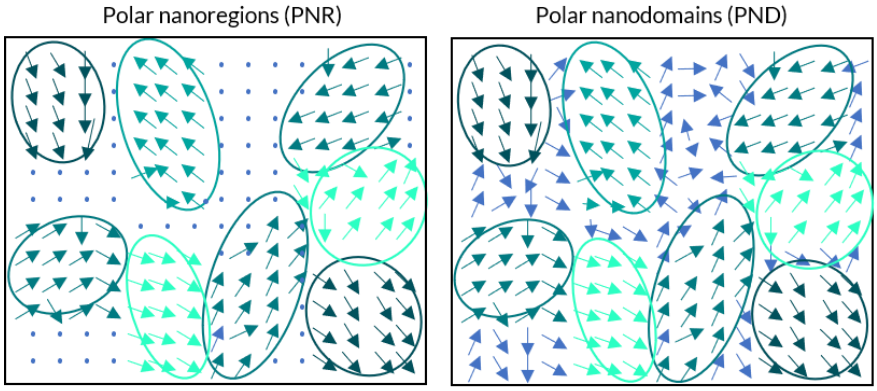

Figure 6.4: Comparison of proposed polar structures in relaxors. Polar nanoregions are separated by a nonpolar matrix, while nandomains are separated by diffuse, low-angle domain walls.

systems again illustrate the importance of charge disorder for relaxor properties, as long-range ordering ultimately drives a long-range correlation of polarization and forms a ferroelectric state.

What then is the actual nanoscale structure of a relaxor? For many years, the dominating paradigm among researchers was that of the polar nanoregion (PNR).[224,225,242] In this model, local nano-sized regions of polarization exist randomly oriented inside a highly polarizable paraelectric matrix (Figure 6.4). On the other hand, there has been a recent shift to recognize that many of the same properties that have been attributed to this PNR model could easily be attributed to a model of polar nanodomains (PNDs) where adjacent polar clusters are separated by disordered, low-angle domain walls rather than a non-polar matrix (Figure 6.4).[93,221] Recent advances in molecular dynamics (MD) simulations[93,230,243] as well as atomically resolved scanning transmission microscopy (STEM) studies on PMN-*x*PT[244,245] have supported this model, illustrating that, unlike normal ferroelectrics which possess relatively sharp domain walls, domain boundaries in relaxors are diffuse and disordered, but still possess local polarization (Figure 6.5). Both models additionally share some traits. First, polar correlations are limited by lattice disorder to nanometer length-scales. Moreover, the small volume of these polar clusters and the lack of strong crystalline

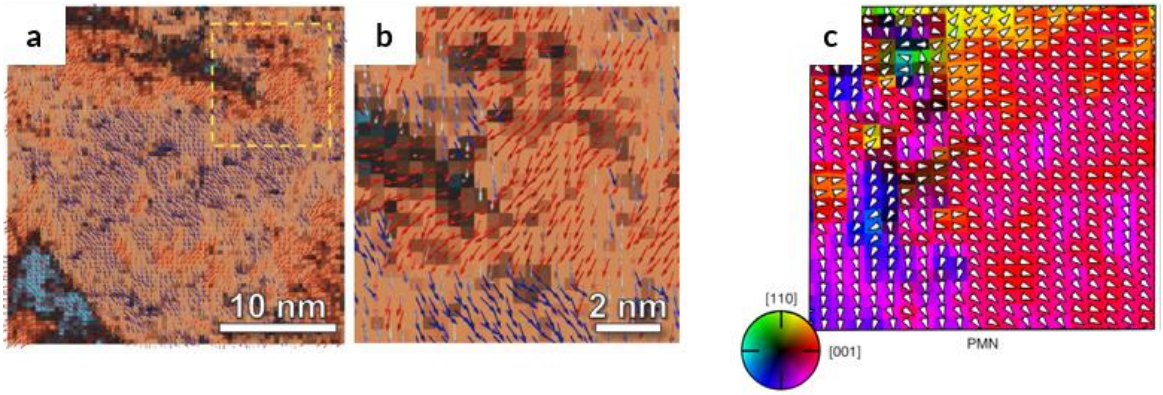

Figure 6.5: a,b) Results of MD simulations on PMN-0.35PT. Reprinted with permission from ref [*243*], Copyright 2017, John Wiley and Sons. c) STEM studies illustrating polar displacements in PMN-0.35PT from with correlated regions separated by low-angle domain walls, and no nonpolar regions, supporting the PND model. Reprinted with permission from ref. [*244*], Copyright 2020, Springer Nature.

anisotropy (typical of normal ferroelectrics) creates a relatively flat energy landscape to determine the orientation of polar clusters, ultimately allowing for a relatively easy reorientation of polar clusters driven by temperature fluctuations, or application of electric field or mechanical force. In fact, some have gone as far as to suggest that the pictures presented by the PNR and PND models are just representative states of the different relaxor phases,[227] with the PNR model being more representative of the high-temperature dynamic state ($T_b > T > T^*$), and PNDs forming in the static relaxor state ($T < T^*$) with a gradual coarsening, correlation and slowing down of the polar clusters as the material is cooled.

6.4. Piezoelectricity and polarization rotation

Research interest in relaxors has been strongly motivated by the discovery of large piezoelectric coefficients in single-crystal relaxor-ferroelectric solid solutions. In the 1990s, polycrystalline ceramics of PZT were the material of choice for high performance piezoelectric actuators, producing larger piezostrains than ceramics of relaxor compositions like PMN-*x*PT.[100] When synthesized as single-crystals, however, PMN-*x*PT and PZN-*x*PT exhibited piezostrains an order of magnitude larger than in polycrystalline ceramic form. Moreover, large piezostrains were strongly dependent on the crystal axis along which they were measured. These crystals, which exhibited a rhombohedral polar axis (*i.e.*, along [111]) produced the largest piezostrains with low hysteresis when poled along [001]. Initially, this observation was somewhat unexpected based on understanding of piezoelectric response in typical ferroelectrics. Ultimately, it was proposed that these large piezoelectric responses originated in a field-induced phase transition between rhombohedral and tetragonal phases, driving large lattice distortions along the tetragonal [001]-axis. One possible explanation put forth was that the reorientation of polar domains drove large lattice deformations, yet this explanation did not explain the observation that the field-induced strain occurred in three distinct stages, characterized by distinct slopes in a strain-electric field diagram (Figure 6.6a).[94,100,246] Simulations examining atomistic origins for the observed three-

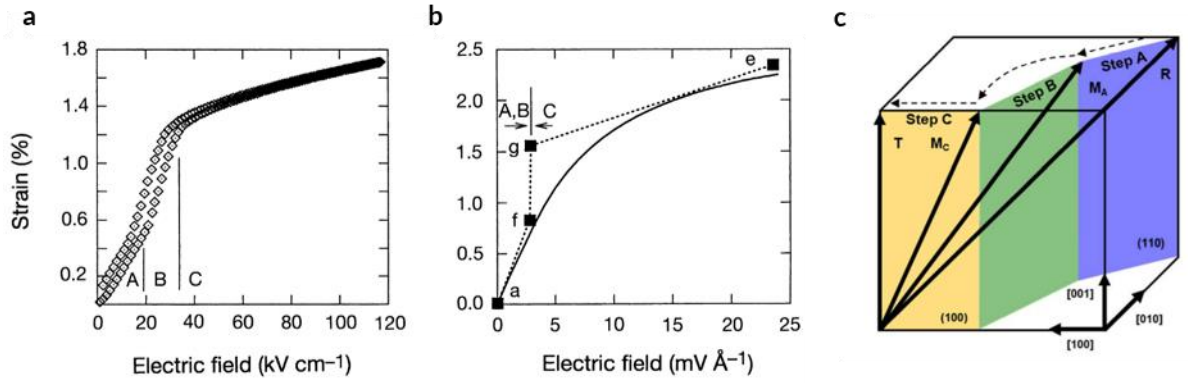

Figure 6.6: Polarization rotation in relaxors. a,b) Real strain-electric field diagrams illustrate three-stages of piezostrain, which are correlated to a simulated unit cell pathway. Reprinted with permission from ref [*94*], Copyright 2000, Springer Nature. c) A schematic of the pathway illustrating the polarization direction at each step of the pathway, from ref [*247*].

stage electromechanical response described a low-energy pathway for transitioning from rhombohedral to tetragonal unit cell symmetries that could explain the observed three-stage response (Figure 6.6b).[94] Subsequent *in situ* studies of the structural transitions under applied field observed this process and confirmed that an additional two monoclinic phases or steps existed and could be observed in the rotation pathway.[222,247] Based on these observations, the rotation pathway is summarized in terms of constituent phases to proceed from R → M_A → M_c → T (Figure 6.6c). Methods for engineering larger piezoelectric coefficients has thus been based off inducing additional structural disorder to lower the energy barrier between these stages of polarization rotation[248–250] or even creating solid-solutions of ferroelectric systems to put different symmetries in competition and engineer relaxor properties.[251,252] On the other hand, studies examining the response of polar nanodomains to applied electric fields have demonstrated that redistribution of these nanodomains does occur.[253,254] As such, both polarization rotation and reorientation of polar domains have been observed and correlated to piezoelectric response, and there remains a need to reconcile these pictures into a unified understanding.[222]

6.5. Thin film-based studies of relaxors

While relaxors have been extensively studied as bulk ceramics and single-crystals, they remain relatively unexplored in thin-film form. The understanding of ferroelectrics, on the other hand, has benefitted immensely from thin film-based studies.[1] Recent studies leveraging epitaxial synthesis of relaxors have already begun to pay dividends in the understanding of the connection between structure and properties,[219,220,235,243,245,255] and further studies stand to expand this understanding to a variety of relaxor systems and properties. For example, epitaxial strain control of thin films of $0.68PbMg_{1/3}Nb_{2/3}O_3$-$0.32PbTiO_3$ (PMN-0.32PT) has illustrated novel nanodomain configurations and the impact of these alternative configurations on dielectric and ferroelectric properties.[243] Another study on films of the same composition aimed to examine the structural evolution of the unit cell structure under applied field. *In situ* X-ray diffraction experiments were able to capture the evolution from R to M_A to M_C as a function of applied field, but also revealed that the M_A → M_c rotation was suppressed at frequencies greater than approximately 20 kHz (Figure 6.7).[245]

These studies illustrate that thin films provide a unique platform for answering important questions regarding the connection between structure and relaxor properties. One fundamental question that remains unanswered is the impact of crystal size on the dielectric and ferroelectric properties of relaxors. As has been illustrated, relaxor properties are driven by disorder and interactions of nanometer-sized polar clusters, but it is difficult to intuit the properties of a relaxor crystal in which the dimensions of the entire crystal are comparable to the polar correlation length. In simpler words, how does a relaxor behave when synthesized as a film only a few nanometers thick. In Chapter 7 this question is explored in the relaxor systems $PbSc_{1/2}Ta_{1/2}O_3$, by completing in-depth electrical and structural characterization of a series of films with decreasing thickness.

The large piezoelectric coefficients reported for relaxor single crystals have long promised a new generation of nanoscale electromechanical actuators, sensors, and energy harvesting devices, where nanoscale relaxors may provide larger displacements at low applied voltages.[10,218] Yet, thin

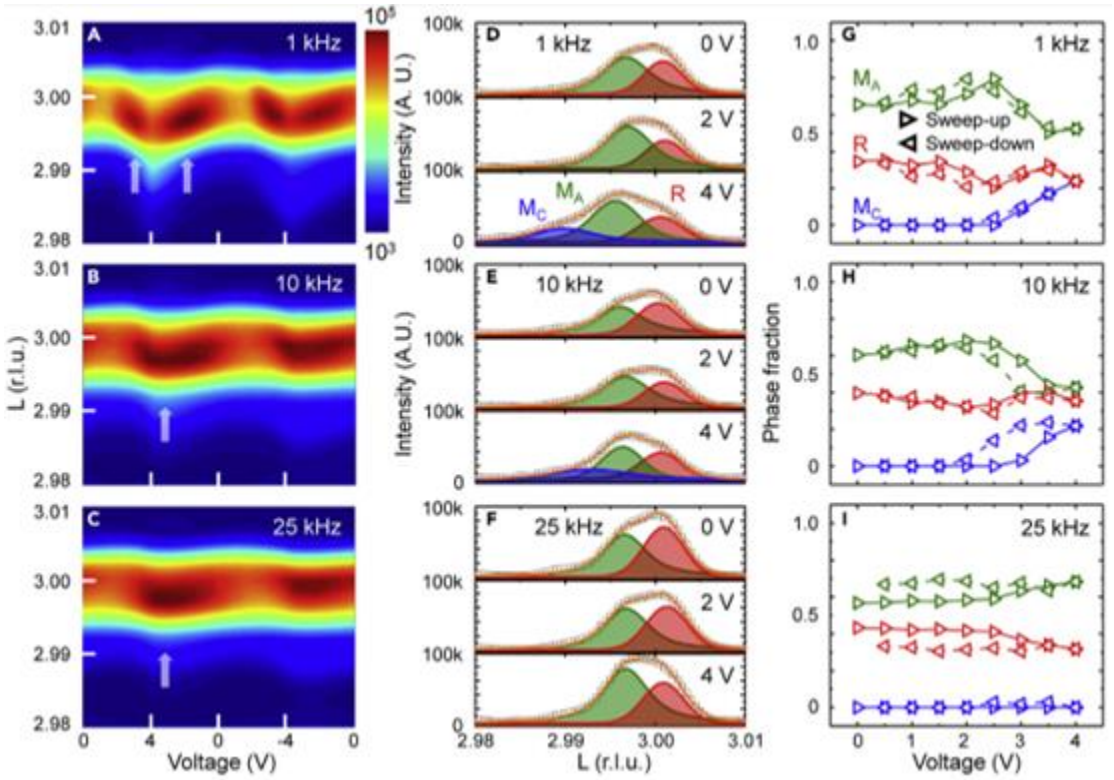

Figure 6.7: a-c) *In-situ* X-ray diffraction experiments show the shifting lattice parameter under applied field, d-f) fits to the 002-diffraction conditions illustrate the presence of R, M_A, and M_C phases. g-i) The phase fraction of each as a function of field shows complete suppression of the MC phase at 25 kHz. Reprinted with permission rom ref [*245*], Copyright 2021, Elsevier.

film relaxors have consistently produced far smaller piezoelectric coefficients than their bulk crystal counterparts. This discrepancy has been attributed to the unique mechanical constraints associated with an epitaxial thin film, and in particular, the bonding of the film to a much larger, stiffer substrate.[101,102,256] This substrate clamping ultimately restricts the distortion of the lattice associated with piezoelectric actuation. In Chapter 8, a means to addressing this challenge is presented in the production of freestanding membranes of PMN-0.32PT which have been removed from the substrate and transferred to a silicon substrate. The properties of such freestanding membranes will be studied and compared to a clamped counterpart.

6.6. Characterization

The remainder of this chapter provides background on the measurement techniques used in this dissertation to characterize the properties of relaxor thin films.

6.6.1. Diffuse scattering

Measurement of the polar structure of relaxors is significantly more limited than that of traditional ferroelectrics. In ferroelectrics, domain structures are often highly ordered, and relatively large scale, allowing for probing via X-ray diffraction as well as a host of scanning probe-based measurements, which allow for the construction of real-space pictures of the polar structure with

relative ease. The disordered, nanoscale polar structure of relaxors, on the other hand, is not detectable with traditional scanning-probe techniques. Even in X-ray diffraction, the signatures of well-ordered ferroelectric domains do not appear. Instead, the nanoscale disorder gives rise to a structured diffuse intensity around the Bragg peaks of the crystal.[232,257] Diffuse intensity surrounding Bragg peaks in X-ray diffraction can arise due to any number of imperfections in the crystal, which cause local displacements of atoms away from the ideal lattice site, disrupting the ideal lattice structure. The symmetry of these local displacements is reflected in the symmetry of the diffuse intensity, with completely random disorder expected to give rise to radially symmetric diffuse intensity. In relaxors, local correlations between off-center lead cations that give rise to the polar clusters results in observation of diffuse intensity with particular symmetry. This diffuse scattering has been studied extensively by both X-ray and neutron diffraction measurements performed on large single crystals of PMN-*x*PT and PZN-*x*PT, revealing a characteristic butterfly-shaped diffuse intensity about the 002-diffraction condition (Figure 6.8).[95,232,243,258,259] Measurement of diffuse scattering in relaxors can then be used to develop a real space picture of the average size and correlation length of polar clusters in the crystal. To perform such measurements, however, samples with high crystallinity such that crystal defects not associated with the polar structure do not overwhelm the diffuse intensity. Moreover, performing such measurement at a synchrotron facility, where the high brightness of the incident beam, and rotation of the sample in three dimensions allows for the construction of 3D RSMs. In this dissertation, diffuse-scattering of relaxor thin films was probed via lab-based 2D reciprocal space mapping studies which were conducted with a high-resolution X-ray diffractometer (X'pert^3 MRD, PANalytical) and 3D RSMs, conducted using a Huber 4-circle diffractometer and Pilatus 100K pixel detector with X-ray energy of 16 keV at beamline 33-BM-C of the Advanced Photon Source, Argonne National Laboratory.

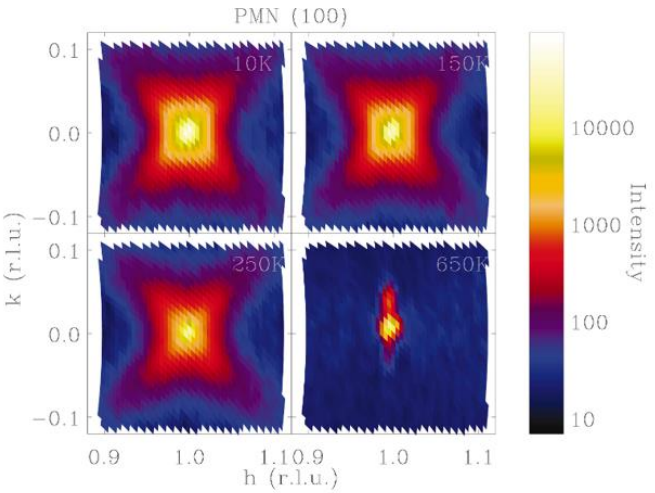

Figure 6.8: Logarithmic plots of diffuse scattering about the PMN 100-diffraction condition illustrating the classic butterfly shape, that disappears at high temperature in the paraelectric phase. Reprinted with permission from ref [*258*], Copyright 2004, American Physical Society.

6.6.2. Dielectric permittivity

Probing the diffuse phase transition of relaxor materials requires measurement of the permittivity of the material as a function of temperature. Measurement of the complex dielectric permittivity of the films is carried out using an impedance analyzer (E4990a, Keysight Technologies), which applies a small sinusoidal voltage excitation (~5 mV), and measures the current response out of

the capacitor. The capacitance, *C*, measured can be related to the relative permittivity, ε_r, of the material through the relationship:

$$\varepsilon_r = \frac{C\,d}{\varepsilon_0\,A}, \tag{6.2}$$

where *A* is the area of the capacitor (area of the photolithographically defined top electrode, see Appendix B), *d* is the electrode spacing (thickness of the film), and ε_0 is the permittivity of free space. The relative permittivity can be separated into real (in-phase) and imaginary (out-of-phase) components:

$$\varepsilon_r = \varepsilon' - i\varepsilon''. \tag{6.3}$$

The ratio of the contributions is reported as the loss tangent:

$$\tan\delta = \frac{\omega\varepsilon''+\sigma}{\omega\varepsilon'}, \tag{6.4}$$

which accounts for the non-zero conductivity, σ, of the material. For ideal capacitor responses the loss tangent is zero, but in real materials conduction of charge carriers (non-zero σ) and relaxation of bound dipoles (non-zero ε'') causes energy dissipation that results in lossy response. The permittivity and $\tan\delta$ can be measured as a function of excitation frequency, amplitude, and under background DC bias field as well as at different temperatures, which, combined, can provide insight into the mechanisms contributing to dielectric permittivity and loss. Measurement of permittivity as a function of frequency provides information regarding the relaxation time of dipolar entities. The degree to which the dielectric permittivity of a material can be suppressed or "tuned" under a background DC field also provides information regarding the ease of dipolar reorientation. Measurement of permittivity as a function of the amplitude of the AC voltage stimulus, often referred to as a Rayleigh measurement,[260,261] provides information regarding the hysteresis of the polarization response and the energy barriers preventing dipolar entities from reorienting under applied fields. Finally, the temperature-dependence of the above measurements can provide information regarding the phase transitions and activation energies of dipolar materials and reorientation processes.

6.6.3. Ferroelectric hysteresis

One of the essential measurements of ferroelectric properties is the P-E field hysteresis loop. A triangular waveform is applied with amplitudes typically ranging from 0.1-20 V (10 kV/cm to 1 MV/cm for a 200 nm film) and frequencies ranging from 0.001 to 50 kHz to the capacitor (for thin-film samples like those studied in this dissertation). The polarization response of the material is measured as the charge that flows through the circuit to compensate the changing polarization inside the capacitor. In this work, a Precision Multiferroic Tester (Radiant Technologies Inc.) was used to perform polarization-electric field hysteresis measurements. Hysteresis loops have several characteristic values which can be used for assessing the polarization response: the saturation polarization achieved at the maximum field, P_s, the remnant polarization when the field is removed, P_r, and the positive and negative coercive fields, E_c.

6.6.4. Nonlinear dynamics and harmonic analysis

The Rayleigh measurements mentioned above have been used to study the hysteresis of domain-wall motion in ferroelectrics for several decades. Typically, such measurements can be used to study the onset of hysteretic motion of domain walls in ferroelectrics. Such studies established the empirical Rayleigh relation for polarization response P(E):

$$P(E) = \left(\varepsilon_{lowfield} + \alpha E_0\right)E + \frac{\alpha}{2}(E_0^2 - E^2) + \cdots, \tag{6.5}$$

where $\varepsilon_{lowfield}$ is the permittivity at zero field, α is the Rayleigh coefficient, and $E = E_0 \sin(\omega t)$ describes the applied electric field. Expanding this into a Fourier series gives:

$$P(E) = \left(\varepsilon_{lowfield} + \alpha E_0\right)E_0 \sin(\omega t) - \frac{4\alpha E_0^2}{3\pi}\cos(\omega t) - \frac{4\alpha E_0^2}{\pi}\left[\frac{1}{15}\cos(3\omega t) - \frac{1}{105}\cos(5\omega t) + \cdots\right]. \tag{6.6}$$

This equation describes the response from higher order harmonics of the polarization response to an applied field, illustrating that odd harmonics contribute to nonlinearity (from the E^2) term, and hysteresis (since they are out of phase with the applied field). As such, measuring higher order harmonics, and in particular the phase angle of higher harmonics, of the polarization response provides additional information regarding the hysteresis of domain walls in ferroelectrics. More recently, these measurements have begun to be applied to relaxors and other systems that display nanopolar order (*e.g.*, $Ba_{0.6}Sr_{0.4}TiO_3$ and $BaTiO_3$ just above T_c) to understand the dynamics of polar clusters. Unsurprisingly, relaxors exhibit distinctly non-Rayleigh-like behavior in regards to the nonlinear permittivity and the phase angle of the 3rd harmonic (δ_3). Whereas hysteretic motion of domain walls in ferroelectrics results in a 3rd harmonic with phase angle ≈ -90°, relaxors exhibit a more complex evolution, evolving from ≈ -180° at low-fields and ultimately increasing to ≈ 0° as the driving field is increased. In this dissertation, harmonic analysis was performed using a lock-in amplifier (SRS 830, Stanford Research Systems) to measure the difference between the 1st and 3rd harmonics of the polarization response while the film was driven with a sinusoidal electric field with either the output of the lock-in amplifier or an external waveform generator (33500B, Keysight).

6.6.5. Piezoelectric surface displacement

Accurate measurement of piezoelectric properties of thin films can be particularly difficult owing to the extremely small piezoelectric strains generated in films hundreds of nanometers thick. To characterize such small displacements, laser-interferometric measurements can be performed. In particular, measurements where a light-based probe of the material's deformation under applied fields is desirable since the voltage-induced changes to the probe (as is the case with a scanning probe cantilever) are avoided. In laser Doppler vibrometry, a laser beam is split into a reference

beam and measurement beam using a beam splitter. The measurement beam is reflected off the sample surface, and the reflected beam is merged back with the reference beam onto a detector inside the interferometer. The displacement of the sample surface induces a frequency shift (f_D) of the reflected beam with respect to the incident beam according to the well-known Doppler effect:

$$f_D = \frac{2v}{\lambda}, \tag{6.7}$$

where v is the velocity of the reflecting surface and λ is the wavelength of incident light. The merging of the reference beam and frequency-shifted measurement beam produces an interference pattern with intensity[262]:

$$I = \frac{1}{2}(I_{max} - I_{min}) + \frac{1}{2}(I_{max} - I_{min}) \sin\left(\frac{4\pi\Delta L}{\lambda}\right), \tag{6.8}$$

where I_{max} and I_{min} are the bright and dark intensities of the interference pattern, respectively, ΔL is the difference in path length between the reference and reflected beams, and λ is the wavelength. The difference in path length arises from the piezoelectric displacement of the sample surface under application of an electric field. Combining a laser Doppler vibrometer with a ferroelectric tester allows for simultaneous measurement of the ferroelectric polarization response and piezoelectric response of the material, allowing for measurement of displacement-electric field curves (Figure 6.9). In this dissertation, a VIO-210 laser Doppler vibrometer (Polytec, Inc.) capable of measuring surface displacement with 0.2 Å resolution over an area of 0.2 µm was coupled with a Precision Multiferroic Tester (Radiant Technologies, Inc.) to measure piezoelectric displacement curves, using the Advanced Piezo task. Measurements of the piezoelectric displacement are measured at a frequency of 10kHz to avoid low frequency vibrational noise, 16 trials are performed for each measurement, and a drift correction is applied to each before the trials are averaged to produce a single displacement-electric field curve.

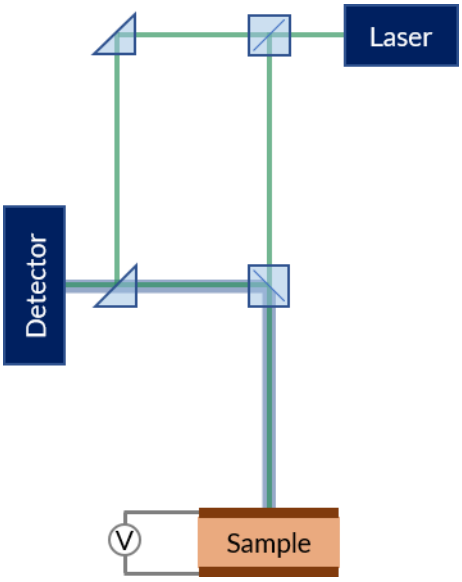

Figure 6.9: Schematic of laser Doppler vibrometer setup illustrating the interferometer used to measure surface displacement from fabricated capacitors.

Chapter 7:
Finite-size effects in lead scandium tantalate thin films

Here, we study the role of finite-size effects on the evolution of relaxor order in epitaxial thin films of $PbSc_{1/2}Ta_{1/2}O_3$. While this composition and other relaxor materials have been extensively studied in the bulk, there is relatively little information on epitaxial-thin films. Utilizing films from 7 to 70 nm thick, temperature- and electric-field-dependent dielectric and polarization studies reveal a general suppression of the polarization and a reduction in the nonlinearity typically associated with relaxor order in the thinnest films. This suppression scales linearly until a thickness of ≈ 30 nm, at which point the suppression accelerates rapidly and by a film thickness of 7 nm the nonlinearity is absent, despite the observation of a broad peak in dielectric permittivity and frequency dispersion. Diffuse-scattering measurements reveal a novel diffuse-scattering symmetry and a polarization correlation length of ≈ 23 nm, suggesting the change in scaling of polarization response is associated with a critical interaction of polar correlations and sample size. All told, rather than fundamentally changing the polar structure, the reduction of film thickness drives a suppression of collective polarization response, limiting polarization response to that of the intrinsic lattice which resembles that of a linear dielectric.

Chapter 7: Finite-size effects in lead scandium tantalate thin films

7.1. Introduction

Of fundamental importance to relaxor properties is the connection between local and long-range polar structure. Whereas the bistable, spontaneous polarization in normal ferroelectrics has its origin in atomic interactions at the unit-cell level,[228] relaxor properties are derived from mesoscopic interactions of an ensemble of polar entities with distinct anisotropies, magnitudes, and relaxation times. Thus, among a range of open questions, there remains a question as to the effect of reducing sample dimensions on the evolution of relaxor properties. While finite-size effects have been studied extensively in ferroelectric thin films (revealing the potential for robust polarization down to the level of just a few unit cells),[17,91] few studies, focusing mostly on grain-size-dependent effects in bulk ceramics, have explored similar concepts in relaxors.[96–98,263,264] Such studies face the additional challenge of having to alter the synthesis process to achieve different grain sizes, thus introducing variations in the degree of chemical order/disorder, grain-boundary density, and porosities, all of which can add to the complexity of studying these complex polar interactions. Only in the last few years have advances in thin-film synthesis and commercially available substrates enabled the high-quality growth of these materials, thus opening up new pathways to study finite-size effects in relaxors.[220,235,243,255]

Important questions regarding the evolution of relaxor properties as the film is thinned center around the impact of the chemical disorder when the lattice is limited to a handful of unit cells, and how the interaction between nanometer-sized polar clusters evolves as the film thickness becomes comparable to the correlation length. A typical ferroelectric like $PbTiO_3$ can be easily conceptualized down to film thickness of a few unit-cells, but creating a similar picture for a relaxor is more difficult. As discussed in Chapter 6, relaxor symmetry remains globally cubic, as the randomized local distortions average out over large crystal volumes. As the size of the crystal is reduced, however, the local symmetry-breaking and correlation between adjacent unit cells becomes more important. One can imagine two potential consequences of this. On one hand, the possibility for a polar cluster to extend the length of the crystal suggests that ferroelectric-like properties could be stabilized in ultrathin films, a mechanism suggested for observed ferroelectricity in ultrathin $SrTiO_3$ films.[92] On the other hand, limiting the extent over which local dipoles can interact may drive destabilization of polar clustering altogether. Moreover, assuming the correlation length remains the same in films of different thicknesses, the number of polar clusters that can interact and cooperatively respond to an applied electric field is reduced, potentially reducing the polarization response of the film. Here, $PbSc_{1/2}Ta_{1/2}O_3$ thin films are used as a model relaxor system to probe such questions and examine the phase transitions, polarization response, and local structure as film thickness is reduced to the nanometer scale.

7.2. Growth-induced chemical ordering

$PbSc_{1/2}Ta_{1/2}O_3$ is known to exhibit a relaxor-to-ferroelectric transition without changing composition, but just by controlling synthesis parameters to achieve chemical ordering of the *B*-site cation.[265–267] In bulk ceramics, this is simply achieved by annealing the sample at temperatures

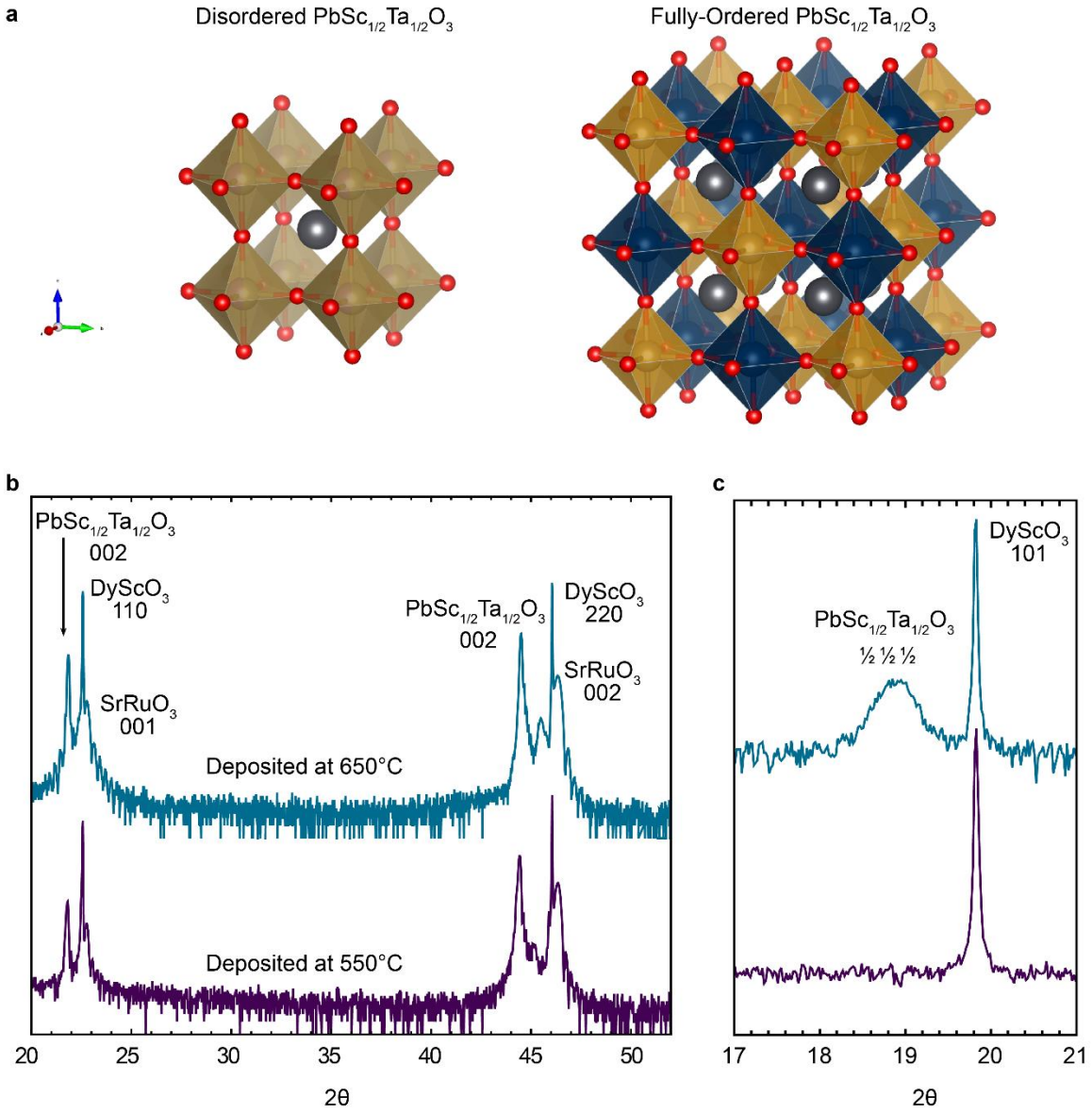

Figure 7.1: a) Schematics of the crystal structure of chemically-disordered and ordered $PbSc_{1/2}Ta_{1/2}O_3$, illustrating the unit cell doubling and 111 ordering-plane. b) X-ray diffraction line scans of $SrRuO_3$ / $PbSc_{1/2}Ta_{1/2}O_3$ / $SrRuO_3$ heterostructures deposited at 550°C and 650°C. c) Scans near the $DyScO_3$ 101-diffraction conditions reveal the appearance of a half-order peak corresponding to $PbSc_{1/2}Ta_{1/2}O_3$ ½, ½, ½ diffraction condition when deposited at 650°C, indicating the presence of chemical ordering.

above 1000°C for long durations.[237–241] PLD is performed at temperatures far lower than this, but the few reports on $PbSc_{1/2}Ta_{1/2}O_3$ thin films have reported a propensity for chemical ordering.[268–274] As such, it was important to confirm that the deposition conditions used for study of finite-size effects resulted in a disordered, relaxor-like composition. During the initial optimization of deposition parameters, many parameters were explored to observe the impact on chemical ordering in the system, with the largest impact by far observed for deposition temperature. Heterostructures of the form 80 nm $SrRuO_3$ / 70 nm $PbSc_{1/2}Ta_{1/2}O_3$ / 30 nm $SrRuO_3$ /$DyScO_3$ (110) were synthesized

via pulsed-laser deposition. The $SrRuO_3$ bottom electrodes were grown at a heater temperature of 690°C in a dynamic oxygen pressure of 100 mTorr with a laser fluence of 1.3 J/cm^2 and a laser repetition rate of 15 Hz from a ceramic target of the same composition (Praxair). The $PbSc_{1/2}Ta_{1/2}O_3$ layers were grown at a heater temperature of 550°C and 630°C in a dynamic oxygen pressure of 200 mTorr with a laser fluence of 1.5 J/cm^2 and a laser repetition rate of 2 Hz from a ceramic target of the same composition with 10% lead excess to compensate for lead loss during growth. The $SrRuO_3$ top electrode layers were grown *in-situ* immediately following $PbSc_{1/2}Ta_{1/2}O_3$ deposition using the same laser and pressure conditions used for the $SrRuO_3$ bottom electrode, at a reduced heater temperature of 550°C, to prevent volatilization of lead from the underlying $PbSc_{1/2}Ta_{1/2}O_3$ layer during growth. Following deposition, the heterostructures were cooled at a rate of 10°C/min in a static oxygen pressure of 700 Torr.

In $PbSc_{1/2}Ta_{1/2}O_3$, chemical ordering of the *B*-site cations occurs in a rock-salt like pattern (that is, every Ta^{5+} site has Sc^{3+} nearest neighbors and vice versa), leading to Sc^{3+} and Ta^{5+} layers that order along the 111 directions (Figure 7.1a),[239] resulting in no changes to lattice parameters, but the appearance of half-order *hhh* peaks. As such, X-ray diffraction line scans along *00l*-direction of the two heterostructures reveal similar diffraction patterns (Figure. 7.1b). To access *hhh*-type diffraction conditions the sample can be rotated, and aligned to the $DyScO_3$ 101-diffraction conditions (equivalent to the 111 pseudocubic diffraction condition). X-ray diffraction lines scans along the *hhh* direction (Figure 7.1c) reveals distinct diffraction patterns for the two films deposited at different temperatures. The film deposited at 630°C exhibits a small peak around 18.7°, corresponding to a half-order ½,½,½ plane that arises due to the ordering of Sc^{3+} and Ta^{5+} cations. The relatively weak intensity, and broad nature of this peak suggests that only partial ordering has occurred. Films deposited at 550°C exhibit no such peak, indicating no detectable ordering. This suggests that both ordered and disordered PST films can be obtained by a careful optimization of deposition parameters.

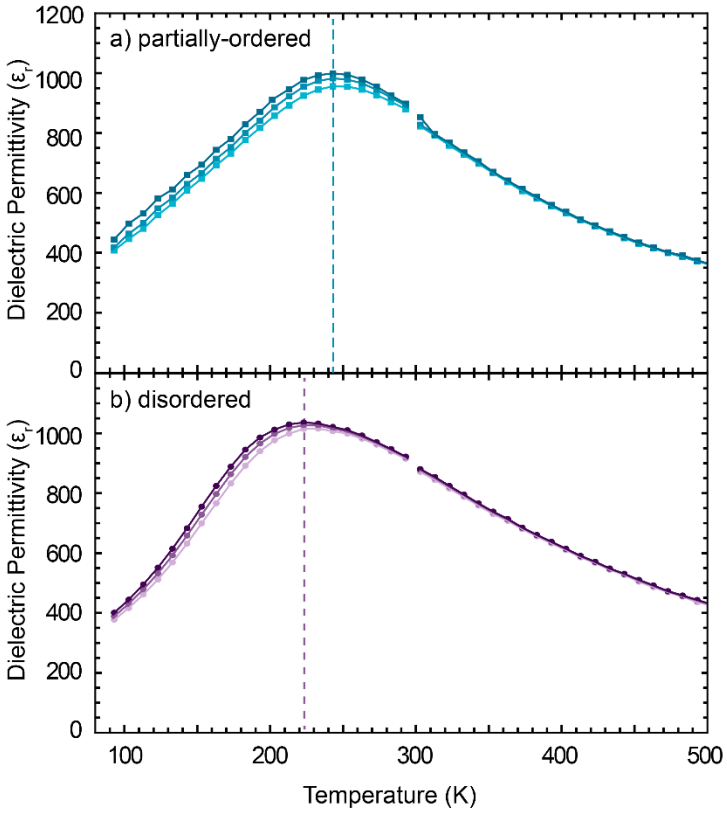

Figure 7.2: Comparison of dielectric permittivity vs. temperature for a) partially-ordered $PbSc_{1/2}Ta_{1/2}O_3$ films deposited at 650°C and b) disordered $PbSc_{1/2}Ta_{1/2}O_3$ films deposited at 550°C.

To assess the impact of this growth-induced ordering on the ferroelectric vs. relaxor nature of the

films, the dielectric permittivity of the films was measured as a function of temperature (Figure 7.2). Both films exhibit relatively broad peaks in permittivity with a maximum in permittivity occurring below room temperature. For the disordered film, the maximum in permittivity measured at 10 kHz occurs approximately 20K lower than that measured for the partially ordered film. Qualitatively, a slightly sharper transition is observed for the partially ordered film, with little change in the dispersion below the maximum temperature, whereas the disordered film exhibits a more asymmetric peak, with a clear opening and closing of the frequency dispersion as temperature decreases. These differences, however, are far smaller than the observed differences for 30% and 80% ordered bulk ceramics. For the remainder of this work, disordered films were synthesized and studied in order to understand the impact of film thickness on relaxor properties.

7.3. Synthesis of lead scandium tantalate films with controlled thickness

Now, having established the relaxor nature of the $PbSc_{1/2}Ta_{1/2}O_3$ thin films, the effect of film thickness on the evolution of relaxor properties can now be studied. Heterostructures of the form 80 nm $SrRuO_3$ / 7, 15, 22, 30, 50, and 70 nm $PbSc_{1/2}Ta_{1/2}O_3$ / 30 nm $SrRuO_3$ /$DyScO_3$ (110) were synthesized via pulsed-laser deposition. All films were deposited using the optimized conditions described above, at a heater temperature of 550°C to obtain the disordered state. The chemical composition of the films was assessed using Rutherford Backscattering Spectrometry (RBS), particularly to confirm the target cation ration of 2:1:1 for Pb:Sc:Ta (Figure 7.3). Owing to the large relative thickness of the substrate compared to the film, a low atomic mass substrate was

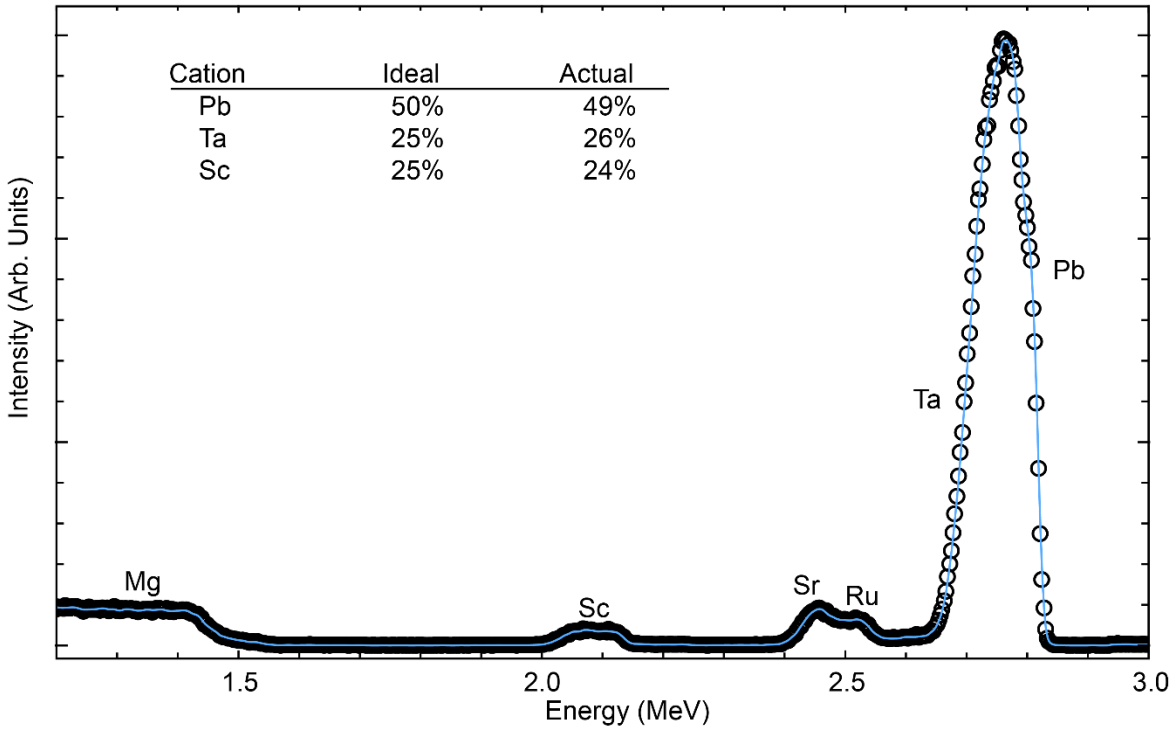

Figure 7.3: Rutherford backscattering spectrometry of 70 nm $PbSc_{1/2}Ta_{1/2}O_3$ / $SrRuO_3$ heterostructures deposited on MgO substrates revealing stoichiometric films.

utilized to allow for adequate resolution of the elemental components of the film. MgO substrates (MTI Corp.) were used to synthesize a 70 nm film at identical conditions to the films under study here. The RBS analysis software, SIMNRA, was used to fit the raw data, and the total simulated spectra (light blue) is presented, showing a good fit to the experimental data. Some interdiffusion of the Mg and film cations is observed, as evidenced by the extended tails on the low energy side of the lead, tantalum and scandium peaks.[36] To account for this compositional gradient, three individual layers were used to simulate the data, with compositions 2:1:1, 2.01:1:1, 1.97:1:1.01, from surface to the substrate interface. Despite this gradient, RBS measurements indicate

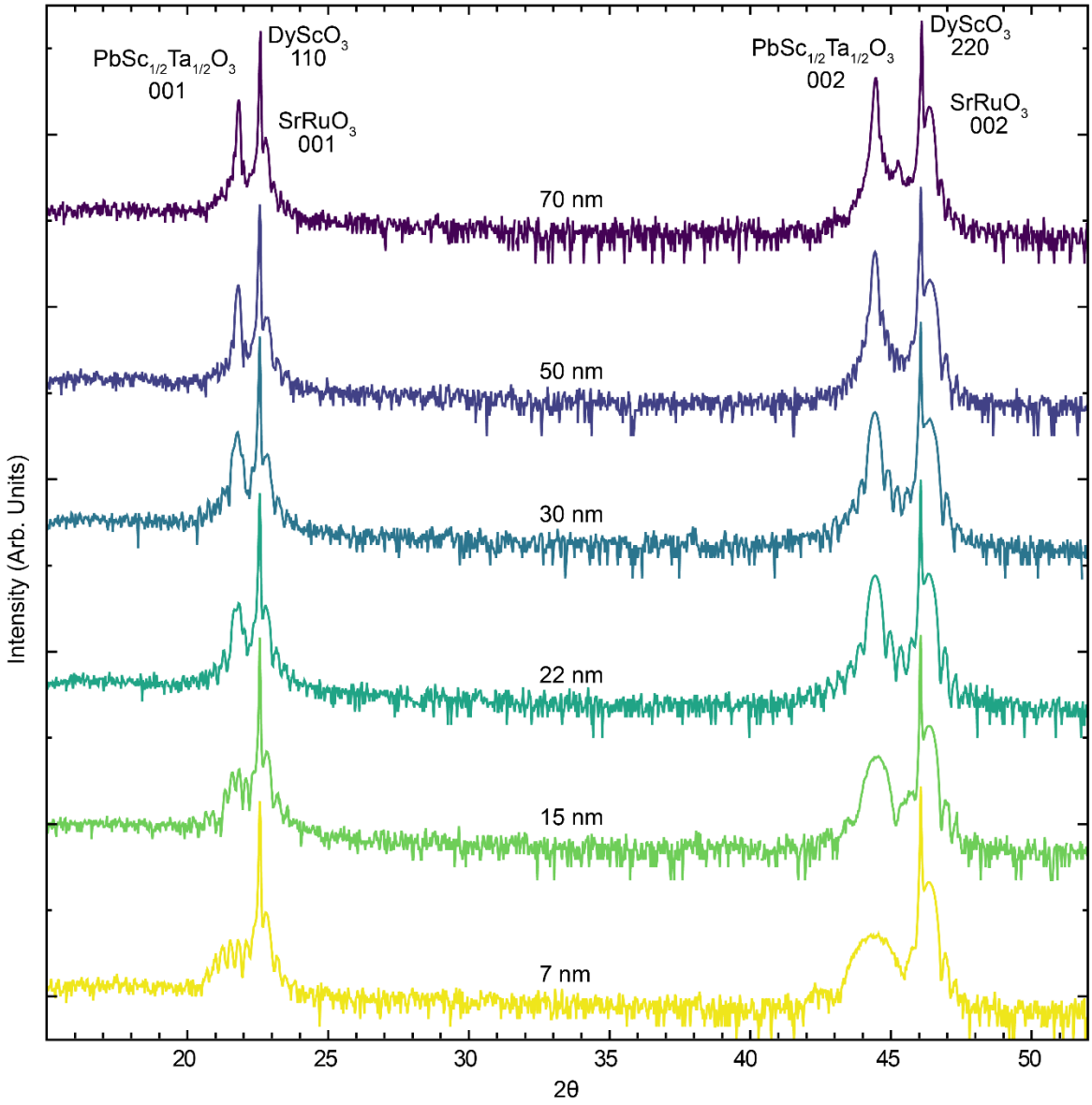

Figure 7.4: X-ray diffraction studies of of $SrRuO_3$ / $PbSc_{1/2}Ta_{1/2}O_3$ / $SrRuO_3$ heterostructures with varying of $PbSc_{1/2}Ta_{1/2}O_3$ thickness, illustrating epitaxial films with a consistent 002 lattice spacing for all films.

stoichiometric $PbSc_{1/2}Ta_{1/2}O_3$ for the top ≈60% (that is, the portion not impacted by diffusion with MgO) of the film ensuring that the films in this study are stoichiometric $PbSc_{1/2}Ta_{1/2}O_3$.

X-ray diffraction studies (Figure 7.4) reveal the production of single-phase, 00*l*-oriented $PbSc_{1/2}Ta_{1/2}O_3$ films, and that the out-of-plane lattice parameter for all films, regardless of thickness, was 4.075±0.03 Å. This agrees with bulk studies[275] and is consistent with the production of fully-relaxed films (as is expected based on the large -3.3% lattice mismatch between the $PbSc_{1/2}Ta_{1/2}O_3$ and $DyScO_3$). Off-axis reciprocal space mapping studies were performed about the 103-diffraction condition of $PbSc_{1/2}Ta_{1/2}O_3$ to study the strain state of the films of different thickness (Figure 7.5). While the $SrRuO_3$ bottom electrode is shown to match the in-plane lattice parameter of the $DyScO_3$ substrate for all heterostructures, the in-plane lattice parameter of the $PbSc_{1/2}Ta_{1/2}O_3$ layer for all thicknesses is shown to be relaxed to the larger, bulk-like lattice parameter (4.075Å). In the thinnest $PbSc_{1/2}Ta_{1/2}O_3$ films, a small portion of the intensity is matched

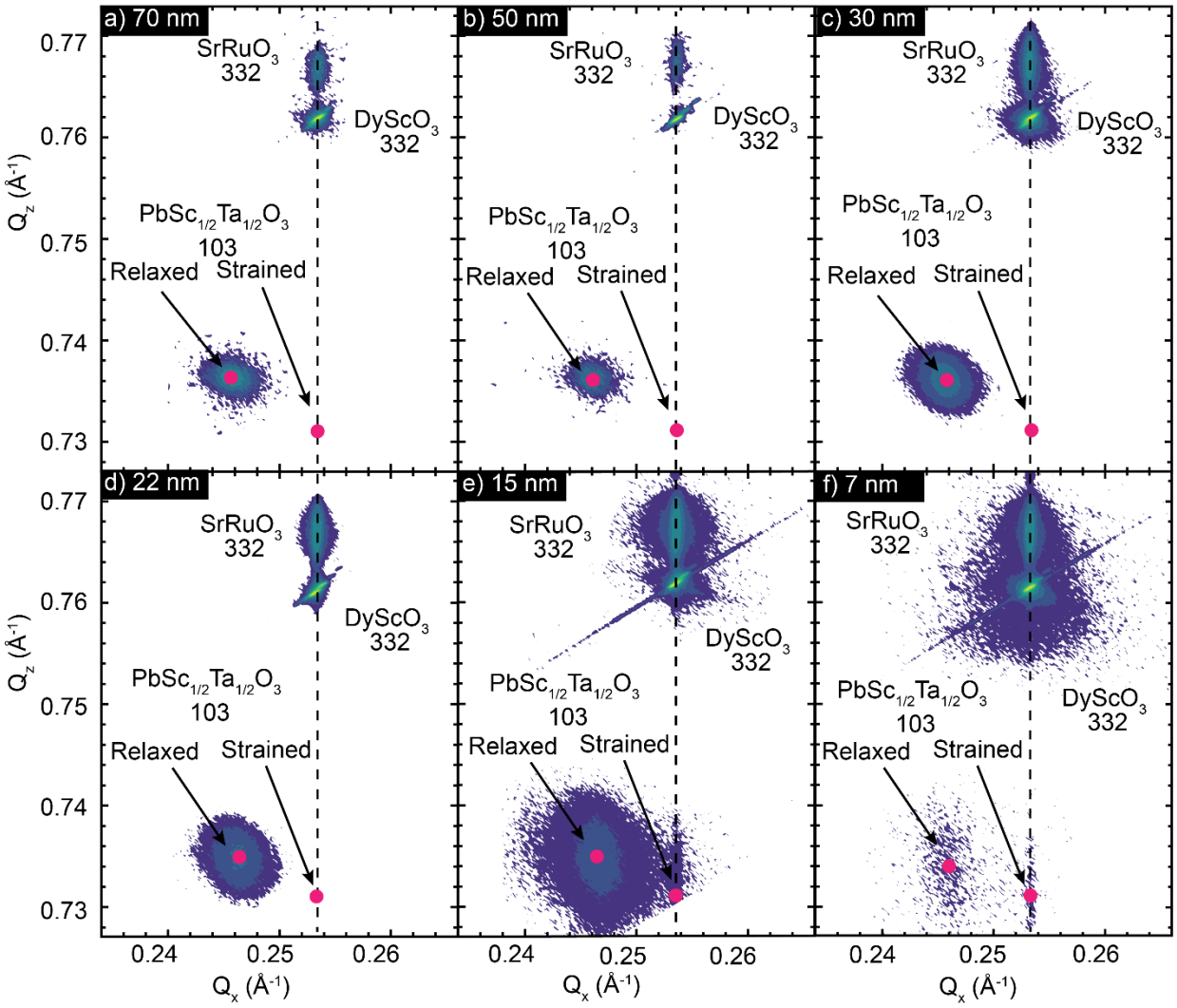

Figure 7.5: Reciprocal-space maps of the 103-diffraction condition of condition of $PbSc_{1/2}Ta_{1/2}O_3$. All thicknesses exhibit a peak at the expected position for a fully relaxed film.

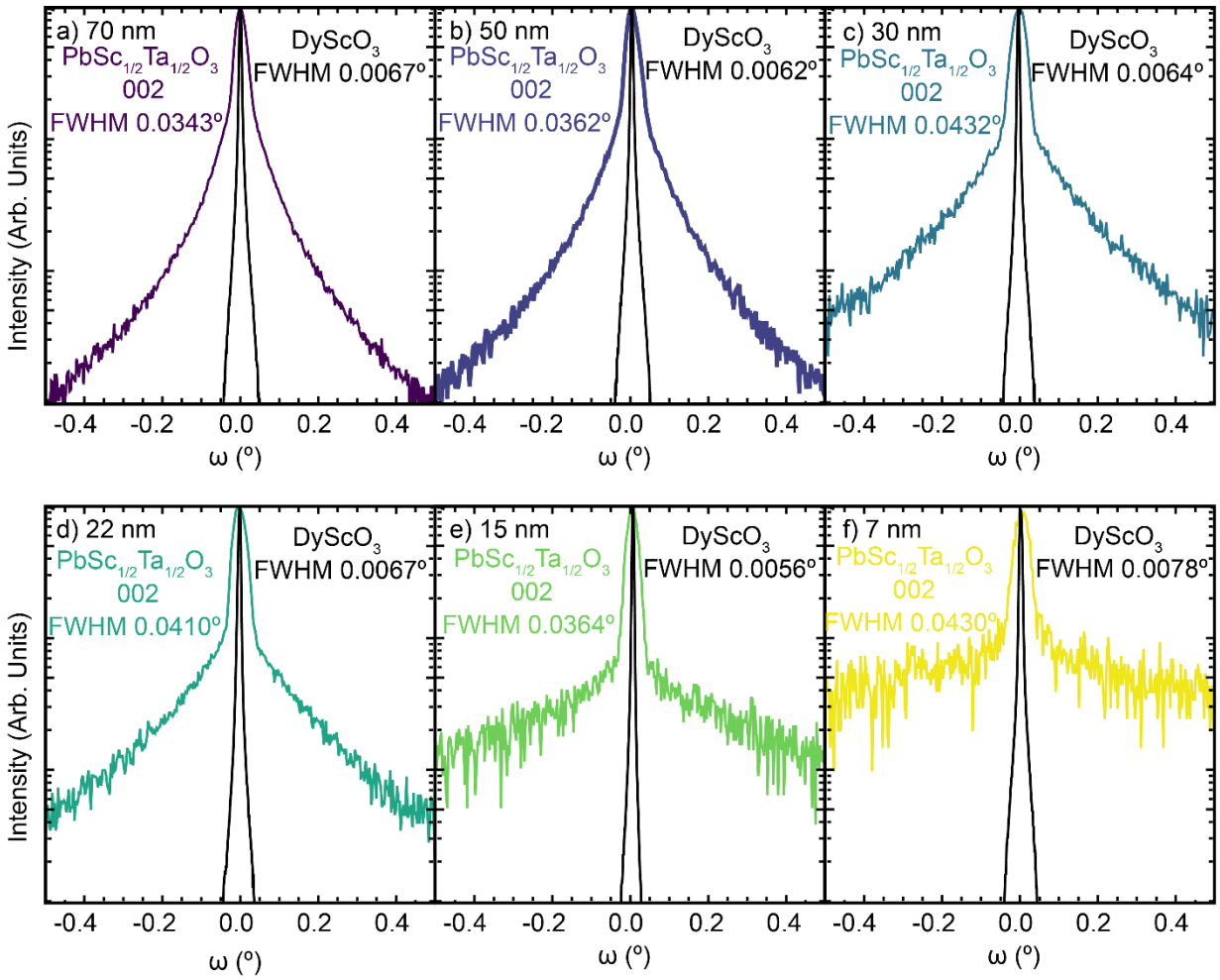

Figure 7.6: Rocking curve measurements about the 002-diffraction condition of $PbSc_{1/2}Ta_{1/2}O_3$. All thicknesses exhibit narrow peaks with FWHM < 0.05°, demonstrating the high degree of crystallinity in all thicknesses.

to the in-plane lattice parameter of the $DyScO_3$ substrate. Heterostructures with large lattice mismatch typically have 2-3 unit cells at the interface that coherently strain to the substrate before relaxation occurs and the remainder of the film adopts the bulk-like lattice parameter.[276] The absence of diffraction intensity between the strained lattice parameter and the bulk-like suggests relaxation happens rapidly, and no large strain gradients are present in the films. Analysis of the X-ray rocking curves (Figure 7.6) reveals that, despite the relaxed nature of the films, a high degree of crystallinity is maintained, as demonstrated by a narrow full-width at half-maximum (FWHM) of ≈0.04° of the 002-diffraction peak of $PbSc_{1/2}Ta_{1/2}O_3$ as compared to that of ≈0.006° for the $DyScO_3$ substrate. This also indicates the strain relaxation has no deleterious effects on the crystalline quality of the films. All told, high-quality, stoichiometric thin films of $PbSc_{1/2}Ta_{1/2}O_3$ were synthesized with thicknesses ranging from 7 nm to 70 nm, with a high degree of crystallinity and bulk-like lattice parameter, providing a controlled system to explore the impact of finite-size effects in on the polar evolution of relaxors.

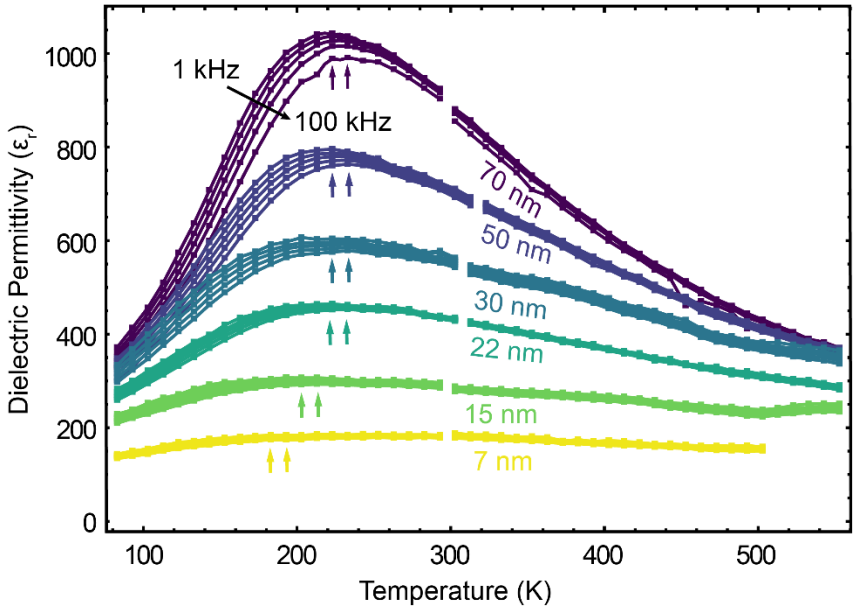

Figure 7.7: Measurements of the dielectric permittivity as a function of temperature reveals the expected diffuse phase transitions in thicker films, with a continuous suppression of the maximum permittivity as thickness is reduced, and a decreasing T_{max}.

7.4. Impact of film thickness on phase transitions

In order to understand the effect of changing thickness on the temperature-evolution of polar order, temperature-dependent, low-field dielectric permittivity and loss studies were completed and used to extract T_b, T_{max}, T*, and T_f (Figure 7.7). The overall magnitude of the dielectric permittivity is found to systematically reduce with decreasing film thickness, with the maximum permittivity changing from ≈ 1000 in the 70-nm-thick films to just ≈200 in the 7-nm-thick films. Despite this change, all films reveal broad temperature evolution and frequency dispersion of the dielectric response (between 1-100 kHz the change in T_{max} is ≈ 10 K) which agrees with bulk data, thus suggesting that the films have a similar degree of relaxor character.[239,240,277] T_{max} is found to be ≈ 40 K lower than typical bulk samples; however, similar shifts have been observed in bulk samples depending on synthesis conditions and in sol-gel derived films.[241,268,270,278]

To ensure the measurement of dielectric permittivity as a function of temperature is not adversely influenced by electronic leakage, the dielectric loss tangent (Tan δ) was measured in tandem (Figure 7.8). Low loss (<0.1) is observed for all films over a large portion of the temperature range studied. Large increases in loss are observed for measurements at 1 kHz (black curves) above 400 K. This loss is associated with increased electronic leakage at elevated temperatures. Additionally, a broad, frequency-dependent peak is observed at low temperatures, that is not expected to be due to electronic leakage, but is more likely associated with the freezing transition at T_f where interaction of polar clusters leads to additional lagging of the capacitive

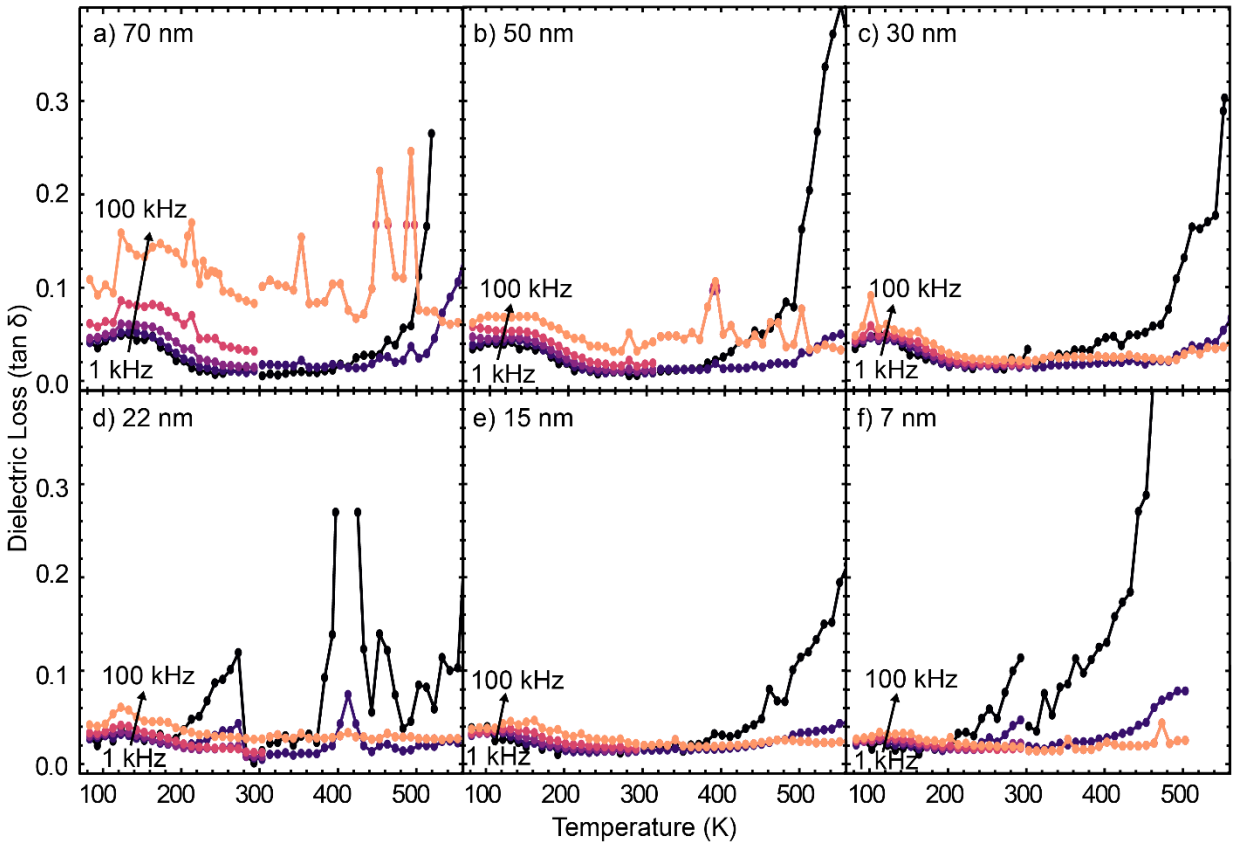

Figure 7.8: Measurement of the dielectric loss as a function of temperature. Low loss is measured for all films until high temperatures, at which point electronic leakage becomes large.

current.[211] All told, loss values are comparable for all films and temperature ranges studied, and confirm that the dielectric permittivity measured for different films have no convoluting effects from leakage current.

To extract the critical temperatures T_b, T*, and T_f, analysis of the dielectric permittivity was undertaken. Measurements of the dielectric permittivity at 10 kHz were chosen for dielectric analysis as these display the lowest loss over the entire temperature range studied. Plotting the inverse of the permittivity (Figure 7.9) shows two linear regions with distinct slopes, with the bounds of these linear regions marking T_b and T*.[224–227] On cooling from the high-temperature paraelectric phase, the inverse of dielectric permittivity (ε^{-1}) follows temperature linearly according to the Curie-Weiss law:

$$\varepsilon^{-1} = \frac{C}{(T-T_0)}. \tag{7.1}$$

The first deviation is observed as a change in the slope, C, indicating T_b. Below T_b, ε^{-1} continues to change linearly with temperature, with a different value of C, until T*, where $\boldsymbol{\varepsilon^{-1}}$ becomes nonlinear, shortly before approaching its minimum value. A linear fit is performed until the value of R^2 for the fit begins to deviate in order to identify different regions of linearity.

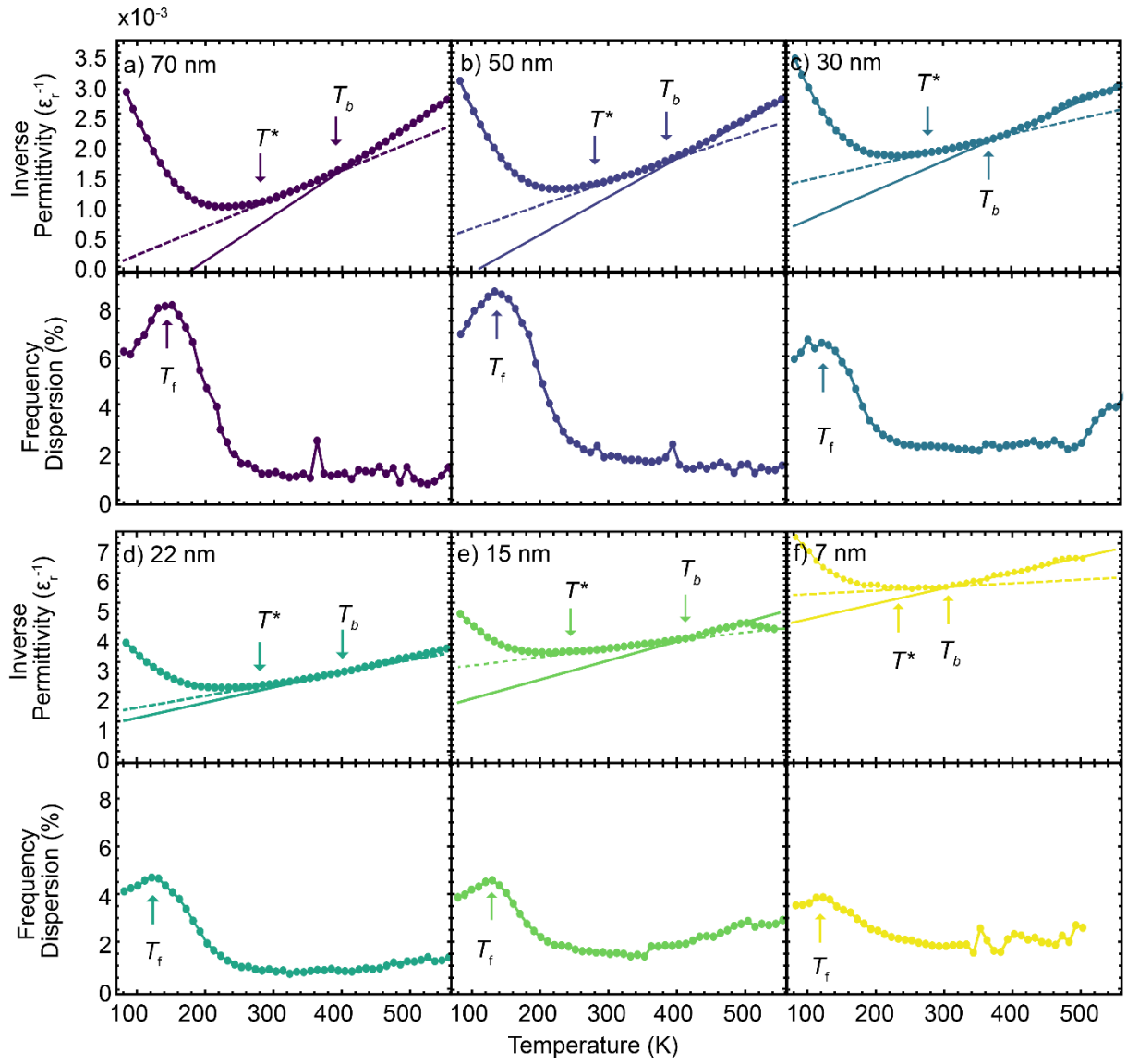

Figure 7.9: Extraction of the T_b, T* via fitting of the inverse permittivity to the Curie-Weiss law, and T_f by examining the peak in the measured frequency dispersion.

Extraction of T_f is typically performed by fitting to the equation describing Vogel-Fulcher freezing:[209,210]

$$\omega = \omega_0 \, Exp\left[-\frac{E_A}{T_{max}-T_f}\right]. \tag{7.2}$$

The Vogel-Fulcher equation describes the dependence of the temperature of the dielectric maximum on frequency with a constant temperature, T_f. A good fit, however, requires measurement of the permittivity with fine temperature step size over several orders of magnitude in frequency,[279] which makes accurate analysis difficult to perform in thin-film samples where the capacitor device structure makes this type of precision prohibitively time-consuming. Here, we use a proxy for the freezing temperature, by measuring the frequency dispersion as a function of

temperature (Figure 7.9). To quantify the frequency dispersion, a percent difference between the permittivity measured at 10 kHz and 100 kHz:

$$\text{Frequency Dispersion (\%)} = \frac{(\varepsilon_{10\ kHz} - \varepsilon_{100\ kHz})}{\varepsilon_{10\ kHz}}. \quad (7.3)$$

Examining the temperature-dependence of the dispersion reveals a large peak in dispersion at temperatures below T_{max}. The frequency dispersion in relaxors is associated with the slowing down of polar clusters with decreasing temperature, influencing the degree to which polar clusters with different relaxation times can contribute to the dielectric permittivity. These relaxation times become progressively slower as the temperature decreases, and eventually diverge to infinity at T_f.[209] When the relaxation time has diverged, that polar cluster can no longer contribute to the permittivity regardless of measurement frequency. The frequency dispersion should then approach zero at very low temperature where the entire spectrum of relaxation times is slower than achievable measurement frequencies. In this case, the frequency dispersion is expected to first increase on cooling until some temperature at which it is maximized, before the polar structure becomes frozen and the dispersion decreases with decreasing temperature. The observed peak in the dispersion therefore is used as a measure of the onset of freezing, *i.e.*, T_f.

A summary of the various critical temperatures, as a function of film thickness, is provided (Figure 7.10). Starting from the thickest films, negligible change is observed for T_b, T_{max}, and T* while T_f decreases slightly as the thickness is reduced to 30 nm. Upon transitioning to thicknesses ≤ 22 nm, however, significant changes in the critical temperatures are seen. First, T_b undergoes negligible changes down to film thicknesses of ≈ 15 nm, at which point a slight increase is observed, before a large decrease occurs in the thinnest (7 nm) films. T_{max} and T* both decrease in the thinnest films, but T_f remains essentially constant at ≈ 120 K in the thin-film regime. The shifting of the various temperatures follows an interesting trend with thickness; whereas T_b changes significantly only at the thinnest films (7 nm and 15 nm), T_f is already decreasing in 50-nm-thick films. Because T_f is associated with the percolative freezing of the largest/slowest polar clusters,[209] it is possible that finite-size effects appear at larger thickness, while T_b is related to the nucleation of highly-local polarization and therefore is only influenced in the thinnest films.[227] The general picture presented by the temperature-evolution is that the polar structures and their temperature-evolution are relatively unaffected by film thickness until the films pass into a thickness regime ≤ 22 nm. Another interesting observation,

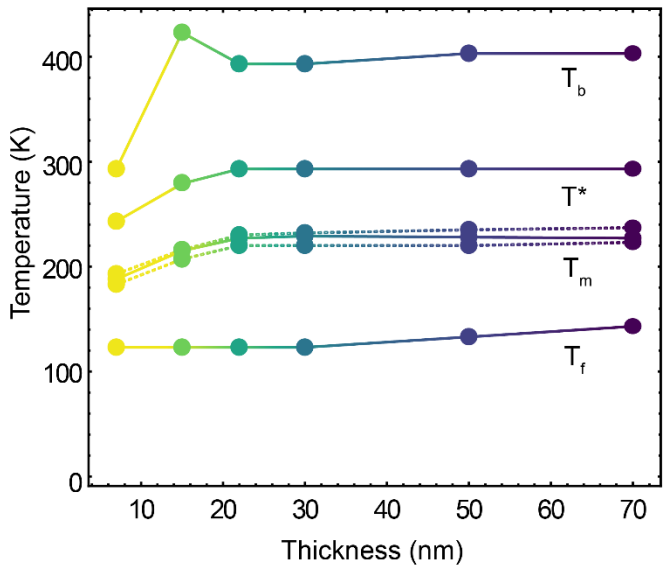

Figure 7.10: Summary of the extracted critical temperatures for decreasing thickness shows little change until thickness is below 20 nm.

however, is that the maximum of the dielectric permittivity has a strong dependence on film thickness even at the largest thicknesses studied, indicating a strong influence of sample size on relaxor response. Note that, at temperatures above T_b and below T_f, where polar clusters are dissolved into a paraelectric phase or frozen and unable to respond, respectively, the dielectric permittivity of the thickest films (≥ 30 nm) approaches the same value of ≈ 300, suggesting the dominant difference between films of different thickness is the extrinsic response and interaction of polar clusters rather than intrinsic lattice response of the material.[249]

7.5. High-field polarization response

To better understand the role of intrinsic and extrinsic polarization response in these films, the dielectric permittivity was measured as a function of DC bias (Figure 7.11a). The effect of the DC bias is to reorient the polar structures, thus suppressing extrinsic contributions and reducing the overall permittivity.[280,281] The characteristic large tunability expected of relaxors is observed in thicker films (*i.e.*, > 30 nm), but the tunability is continually reduced with decreasing thickness until it is completely suppressed in the 7-nm-thick films. At large DC bias fields, the permittivity of all films approaches ≈ 200, supporting the hypothesis that the intrinsic dielectric permittivity of the films is relatively unchanged by the reduced thickness. Instead, the primary difference between the different thicknesses is observed at low DC bias fields, where extrinsic contributions are active. Further insight is garnered from polarization-electric field loops (Figure 7.11b), where a similar trend of reduced polarization response and suppressed nonlinearity with decreasing thickness are observed. In fact, the 7-nm-thick films behave like linear dielectrics, with no nonlinearity even under applied fields of 1 MV/cm. It is also worth noting that, despite reports of stabilization of polar clusters into ferroelectric domains in ultrathin films, no change in remnant polarization is observed with film thickness, suggesting that the stabilization of ferroelectricity at reduced dimensions seems unlikely.[92]

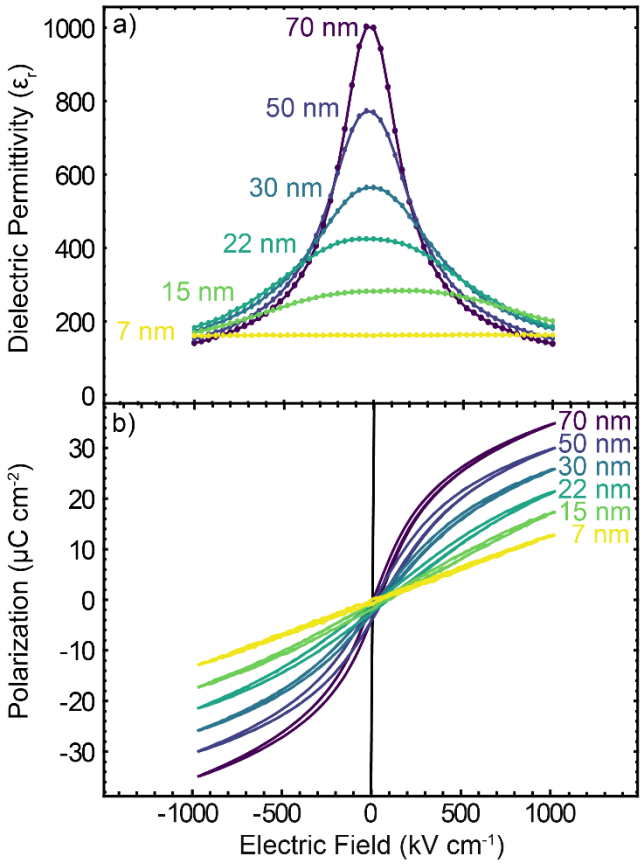

Figure 7.11: a) Dielectric tunability illustrates similar intrinsic (high-field) response for all thicknesses but different extrinsic (low-field) response. Polarization-electric field loops at room temperature reveal decreasing nonlinearity as thickness is reduced.

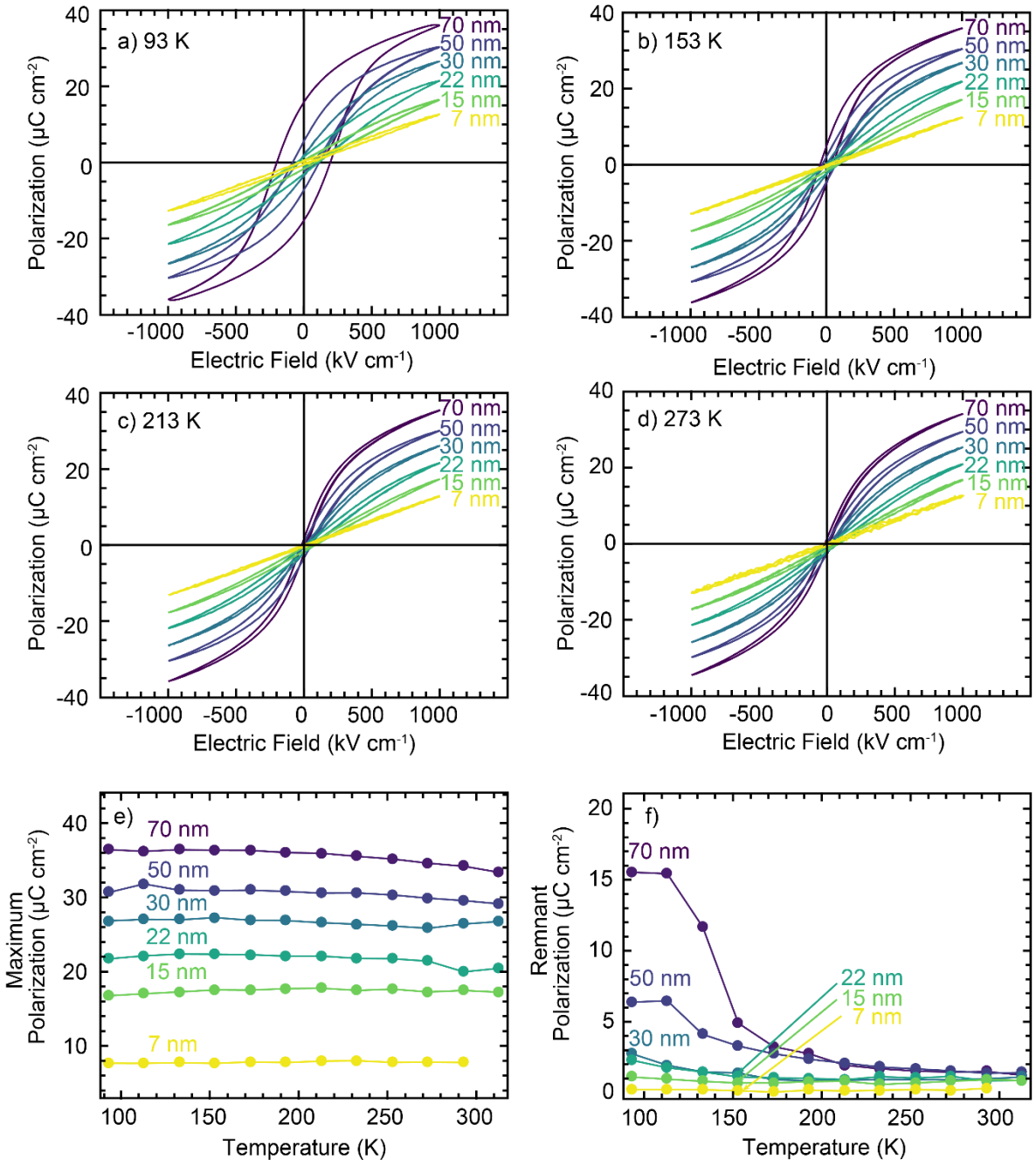

Figure 7.12: Polarization-electric field loops measured at a) 93 K., b) 153 K, c) 213 K, and d) 273 K illustrate the increasing hysteresis in thicker films at low temperatures. A summary of the evolution of e) maximum polarization measured at 1000 kV/cm and f) remnant polarization reveals thinner films possess low maximum and remnant polarization throughout the temperature range studied.

The temperature dependence of relaxor polar structure imparts distinct temperature-dependent behavior in P-E measurements. Measurements were performed at a series of temperatures to study how film thickness influences the development of remnance at low temperatures (Figure 7.12a-d). As expected, remnance is increased with decreasing temperature, while the maximum polarization

is only weakly dependent on temperature (Figure 7.12e). Importantly, the thinnest films have very small remnant polarization even at 93 K, which suggests there is no stabilization of monodomain polarization at reduced thickness (Figure 7.12f). Additionally, the 7 nm films never develop remnance or nonlinearity even at the lowest temperatures measured, significantly below T_m, indicating that the dielectric behavior observed in 7 nm films is not a product of reduced transition temperature, but rather an intrinsic finite-size effect.

Moreover, this behavior is maintained throughout the temperature range studied, with the increase in remnant polarization at low temperatures becoming more pronounced for thicker films, rather than thinner films; again the 7-nm-thick films never develop nonlinearity or hysteresis. In addition to suppressed dielectric permittivity, the curvature of the hysteresis loops at high fields (≈ 400-800 kV/cm), which is associated with the nonlinear response of reorienting polar clusters,[94] is also suppressed with decreasing thickness. Together, these observations suggest that reduction of sample dimensions suppresses the nonlinear, extrinsic contributions from mobile polar clusters, essentially stiffening the relaxor response until only the intrinsic response is observed in 7-nm-thick films. Notably, the suppression of field-induced polarization appears to be linear with decreasing thickness, with a distinct change in slope between 20-30 nm (Figure 7.13).

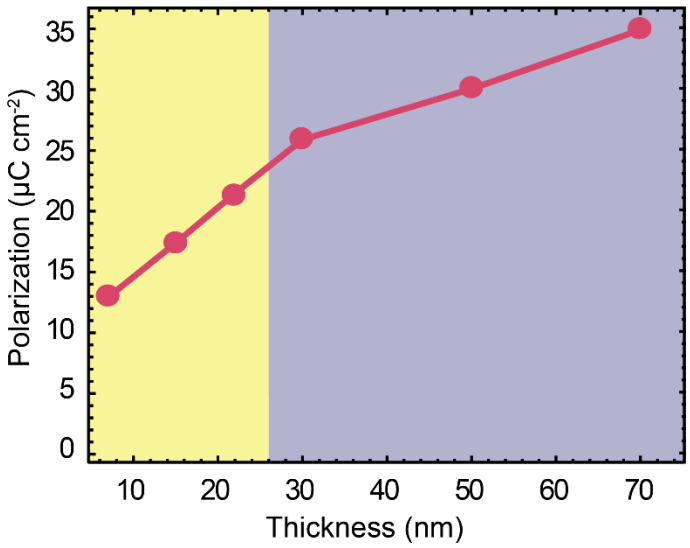

Figure 7.13: Summary of the maximum polarization measured at 1000 kV/cm as thickness is decreased reveals a change in scaling below film thickness of 30 nm.

7.6. Dielectric-harmonic analysis

Considering the observation of suppressed nonlinearity at reduced thickness, additional ways to quantify the changes in nonlinearity and dielectric response were explored. Nonlinearity in ferroelectrics has been studied within the context of Rayleigh-type domain-wall motion in a random distribution of pinning sites, where measurement of the AC-field dependence reveals regimes of reversible and irreversible/hysteretic contributions.[261] Under the application of small AC fields, domain walls oscillate within their potential well, unable to overcome the energy barrier of the local pinning site, and the dielectric response remains flat. As the field is increased, the driving force becomes strong enough to drive domain walls over the energy barrier, allowing them to contribute to the dielectric response. The dielectric permittivity of the $PbSc_{1/2}Ta_{1/2}O_3$ films was measured as a function of applied AC field at 353, 253, 153, and 93 K, revealing a strong dependence of nonlinearity on film thickness and temperature (Figure 7.14 a-d). The data presented has been normalized to the low-field permittivity to better visualize the change in

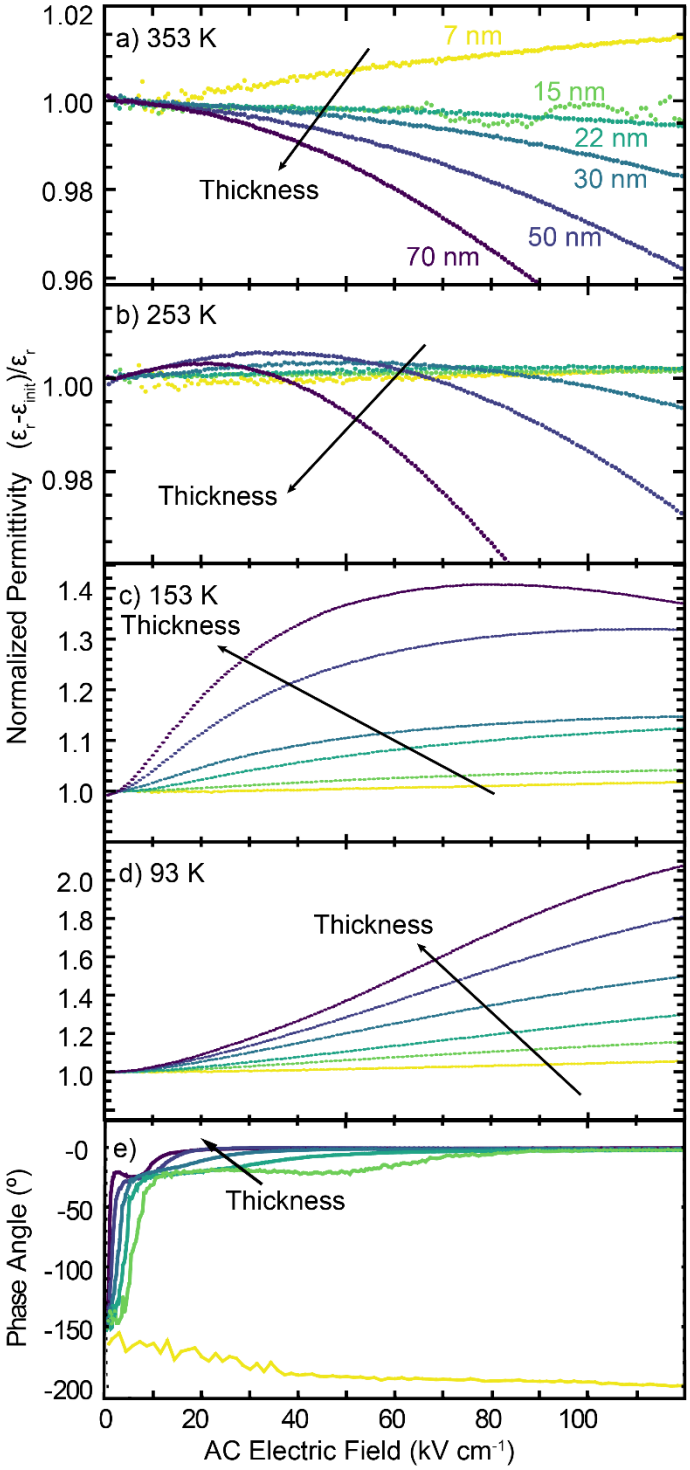

Figure 7.14: Measurement of the dielectric permittivity under increasing AC electric field at a) 353 K, b) 253 K, c) 153 K, and d) 93 K, show suppressed nonlinearity at reduced thickness. A corresponding measurement of the phase angle of the 3rd harmonic at 253 K demonstrates the 7 nm film behaves like a dielectric.

permittivity with increasing applied field. With the exception of the 7-nm-thick films, all thicknesses show qualitatively similar behavior. At 353 K (above T*), the permittivity decreases with increasing field, in agreement with the thermally-activated nature of the fluctuating polar dipoles between T* and T_b. Lowering the temperature below T* brings the appearance of a peak in the permittivity with increasing field, revealing the transition to domain-type dynamics owing to the static off-centering of cations.[282] This static off-centering comes about owing to development of a local potential well, and the increase in permittivity with increasing field appears similar to that expected for normal ferroelectrics. At even larger fields, however, a maximum in the permittivity appears, indicating that the majority of clusters are responding to the applied field. Beyond these AC fields, the permittivity decreases, an effect that has been previously attributed to either reorientation and saturation of polar-cluster response, or tunability of the permittivity, akin to DC bias measurements.[260,283] As the temperature is further lowered, the low-field permittivity is suppressed, but the degree to which increasing field can activate more regions increases from a few percent at 253 K to 40% at 153 K and 10% at 93 K in the 70-nm-thick films. This trend can be understood in the context of the energy landscape for polar displacements in relaxors, where local potential wells become deeper with

decreasing temperature, requiring larger fields to drive dielectric response. In conjunction with DC bias and polarization measurements, measurements of nonlinear dielectric response discussed here indicate that reducing film thickness suppresses the ability of polar structures to respond to applied electric fields, until it is completely quenched in 7 nm films.

At high temperatures the change in permittivity as a function of applied AC field is small for the thinnest films owing to the suppressed nonlinear response. When visualized alongside thicker films, the nonlinear behavior of 15 and 22 nm films becomes difficult to distinguish. Rescaling the plots of nonlinear response, however, reveal that the behavior of 15 and 22 nm films is the same as that of 30-70 nm films. At 353K, the permittivity is clearly decreasing with increasing field for 22 nm films, and despite some noise in the data of 15 nm films, there is no region that indicates an increase in permittivity as is seen at lower temperatures. Similarly, at 253 K a peak appears in the permittivity as a function of applied field, as is observed for thicker films. Additionally, both of these thicknesses behave distinctly from 7 nm films which show no peak or decrease in permittivity at elevated temperatures, which is markedly different from the behavior expected for a relaxor above T_b.

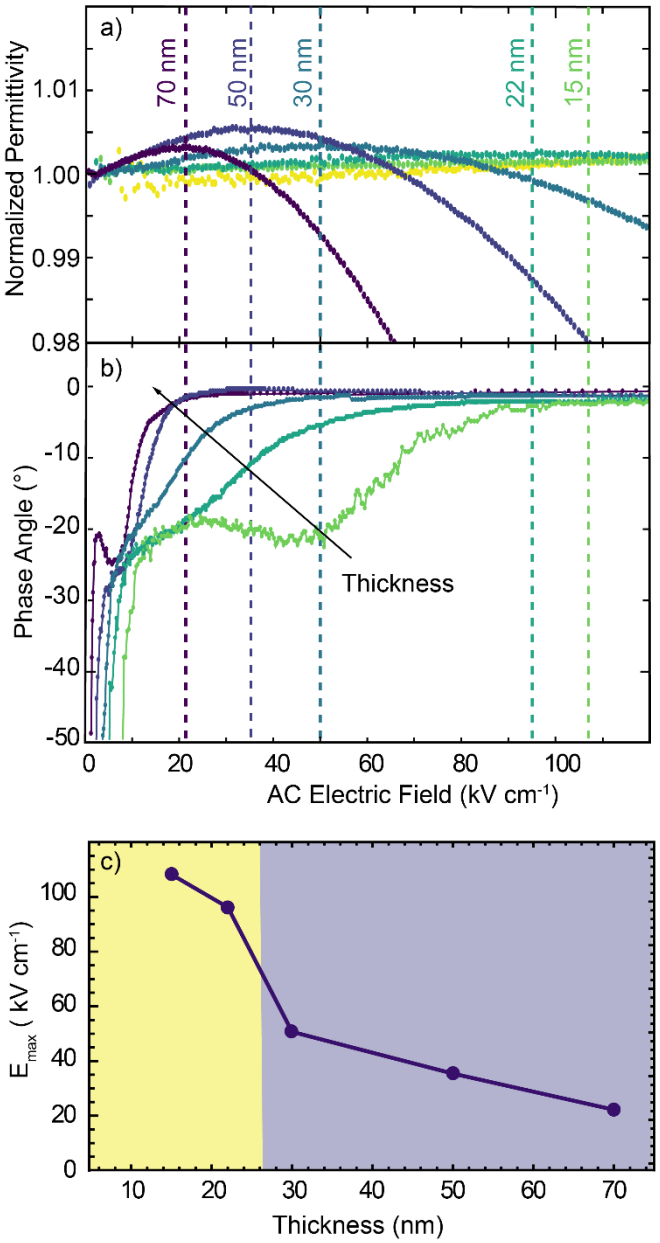

Figure 7.15: Closer examination of the AC electric field studies illustrates the connection between a) the field of maximum permittivity, E_{max}, and b) the field at which $\delta_3 \approx 0°$. c) The scaling of E_{max} with thickness exhibits a change in slope below 30 nm.

In addition to the dielectric permittivity, measurement of higher-order harmonics of the permittivity provides additional insight into the dynamic motion of polarization contributions,[284] and specifically the phase angle (δ_3) between the first and third harmonic has been used to quantify the onset of the hysteretic response of ferroelectric domain-wall motion. In ferroelectrics, the low-field reversible regime is marked by a δ_3 which remains ≈ -180°. At larger fields, depinning of domain walls appears as a rapid increase of δ_3 to ≈ -90° where it plateaus as domain walls are hysteretically moved with the oscillating

field. In contrast, the highly reversible and anhysteretic response of relaxors imparts quantitatively distinct behavior, as shown in PMN ceramics where δ_3 changes from ≈ -180° at low fields to ≈ 0° at higher fields.[260,283] δ_3 was measured at 253 K to understand the origin and thickness dependence of the peak that appears in the permittivity below T* (Figure 7.14e). All films exhibit an increase in δ_3 from ≈ -160° to ≈ 0°; with the exception of the 7-nm-thick films which show minimal changes with field, as expected for a dielectric.[260] The presence of an intermediate plateau $\delta_3 \approx$ -25° also reveals large differences between the films of different thicknesses. While the origin of this intermediate phase angle is not well understood, it may be due to a convolution of contributions from both hysteretic ($\delta_3 \approx$ -90°) and anhysteretic ($\delta_3 \approx$ 0°) motion of polar structures, whose combined polarization response has an intermediate-phase offset. In this case, the proportion of hysteretic contributors appears unchanged by film thickness, as the plateau occurs at the same δ_3 for all films, but decreasing thickness changes the depth of the local wells, necessitating larger fields to drive the maximum dielectric response. By analogy to the effect of reducing temperature, the effect of decreasing film thickness appears to be similar to that of the deepening of local potential wells, suppressing the total polarization response that can be achieved, and increasing the field needed to drive polarization response. The field at which δ_3 reaches ≈ 0° corresponds to the field at which the permittivity is maximized (E_{max}). To visualize the agreement between the measurements, the 3rd harmonic measurements are rescaled and plotted alongside the corresponding permittivity measurements taken at 253 K (Figure 7.15a,b). The 3rd harmonic slowly approaches ≈ 0°, and the field at which it plateaus, typically above ≈ -0.5°, shows good agreement with the peak in permittivity.

Examining E_{max} as a function of thickness, reveals an interesting trend (Figure 7.15c). A linear increase in E_{max} is observed for films from 70 to 30 nm thick; however, a sharp increase in E_{max} occurs below 30 nm, similar to the behavior observed for scaling of the polarization. The linear decrease at large thicknesses indicates a proportional scaling of electrical response with thickness, suggesting the interaction of polar clusters is directly related to the length-scale over which they can interact. This type of behavior has been suggested in efforts to model dipolar interactions in relaxors, where the energy associated with interacting dipoles in high-permittivity crystals was shown to be inversely proportional to the volume of the crystal.[285,286] While this effect may play a relatively minor role in macroscopic samples, reduction of the crystal volume to sizes more comparable to the dipole correlation length may lead to the strong thickness dependence observed here. The change in scaling observed below 30 nm, however, necessitates further study.

7.7. Probing structural origins of thickness scaling

The strong dependence of relaxor behavior on the distribution of polar-cluster size and their interactions suggests the possibility of a fundamental change in properties when the sample size approaches the polar correlation length. As such, understanding of the polar structure and polarization correlation length is necessary to understand the change in scaling at reduced thickness. Diffuse-scattering measurements on PMN, PMN-*x*PT, and PZN-*x*PT, and related relaxor materials have shown correlation lengths between 2-20 nm depending on chemistry and

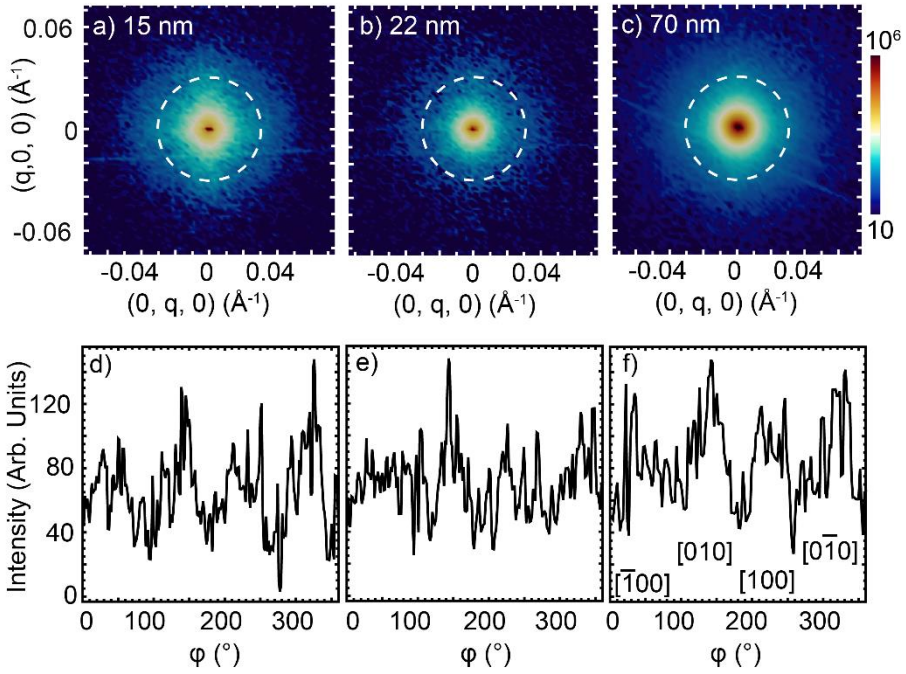

Figure 7.16: Two-dimensional intensity plots of 3D RSM studies performed at 153 K to observe diffuse scattering from polar distortions. (a) The 15-nm, (b) 22-nm, and (c) 70-nm films show a clover-shaped diffuse scattering pattern that is visualized by taking a radial line cut at q = 0.027 Å−1 (white dashed line), showing the intensity variation from the four lobes. (d)–(f) The intensity variation along the radial line cut shows four lobes of intensity with crystallographic directions labeled in (f).

temperature.[231,253,259,287] The strong interplay between cluster size, relaxation time, and the critical temperatures associated with polar evolution in relaxors suggests that the consistency in critical temperatures for films of thicknesses ≥ 30 nm is a result of the polar structure remaining unaffected in this thickness regime. The changes to the response in films thinner than 30 nm, however, indicate a change of polar interactions. To understand the origin of this change, three-dimensional RSM studies were performed at 153 K to study the diffuse scattering from polar structures and determine the polar correlation length (Figure 7.16). Diffuse scattering was studied in 15-, 22-, and 70-nm-thick films, and two-dimensional intensity maps of a slice through the (hk0) of the 002-diffraction condition for the $PbSc_{1/2}Ta_{1/2}O_3$ show a clover-shaped diffuse-scattering pattern in all films studied (Figure 7.16a-c), with diffuse intensity extending along the [100], [$\bar{1}$00], [010], and [0$\bar{1}$0]. The four-fold symmetry of the diffuse intensity is illustrated by a radial line cut (white dashed line in Figure 7.16a-c, plotted in Figure 7.16d-f), showing four broad peaks separated by ≈ 90°.

While diffuse-scattering caused by disordered off-centering of lead cations has been used to study the polar structures of relaxors, a number of other mechanisms can drive the appearance of structured diffuse intensity around an X-ray Bragg peak. The presence of diffuse scattering owing to point defects and defect clusters was first theoretically predicted before experimental verification revealed diffuse scattering from impurity point defects, vacancies and dislocations in various metal alloys.[288,289] More recently this analysis was applied to diffuse scattering from polar

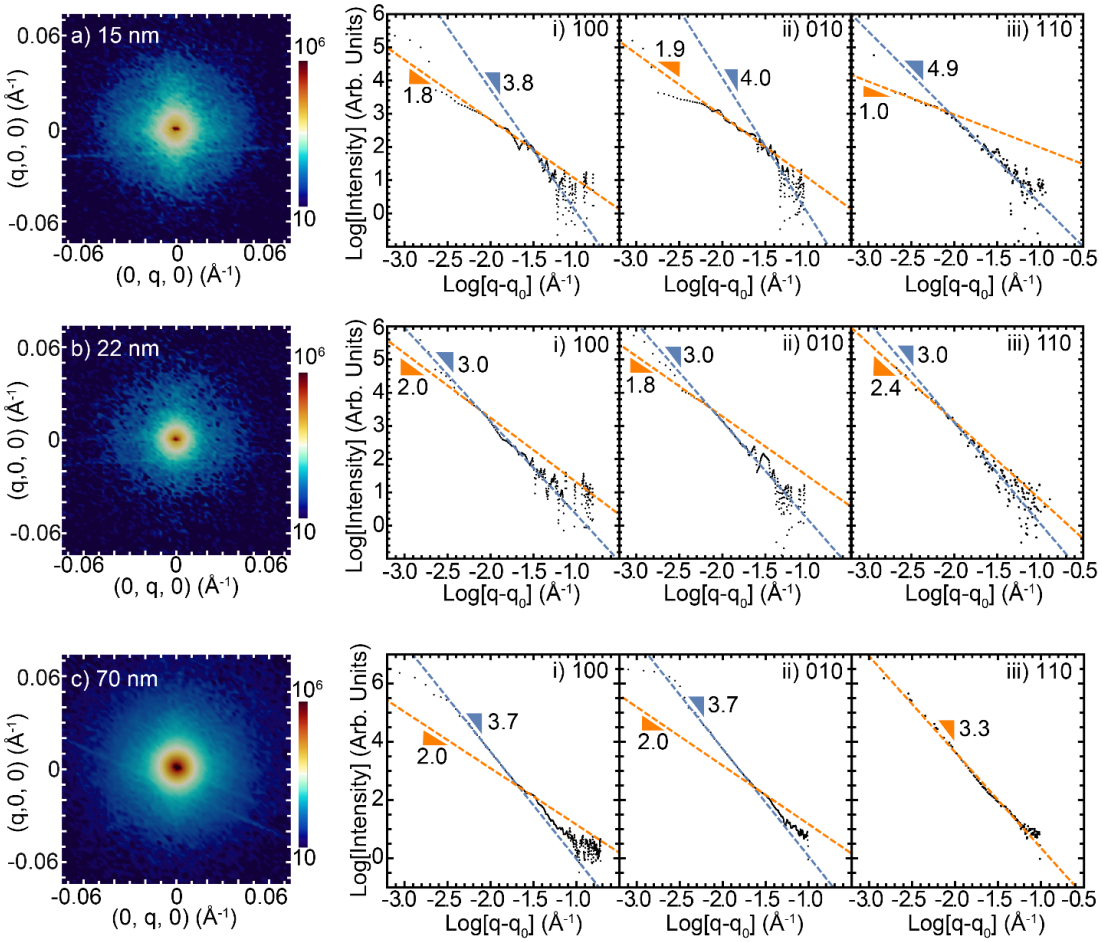

Figure 7.17: Analysis of diffuse-scattering experiments performed at 153 K, with 2D hk0 intensity maps showing a diffuse clover-shape for a) 15 nm, b) 22 nm and c) 70 nm films. The corresponding q dependence along the i) [100], ii) [010], and iii) [110] directions show the transition from Hwang-scattering to Stokes-Wilson scattering. 22 and 70 nm films, however, show a distinct q-dependence, suggesting the presence of additional defect scattering not related to polar distortions.

atomic displacements and has since been used to study shape, orientation, size and response under external stimuli of polar clusters in relaxors.[290] Whereas prototypical relaxors in the PMN-*x*PT and PZN-*x*PT families show a characteristic butterfly shape with diffuse rods extending along [110]-type directions,[231,253,258,259,287] the clover shape with diffuse rods along [100] and [010] directions observed in the 3 films measured suggests either a different polar structure (*i.e.*, shape and orientation of polar clusters) or a different origin all together. Whether this diffuse intensity can be attributed to polar displacements can be answered through examination of the q-dependence (that is, the distance from the Bragg peak center) of the diffuse intensity. Scattering off isolated point defects produces a q^2-dependence of the intensity at small values of q, called Hwang scattering, and at larger values of q, the intensity changes to a q^4-dependence when scattering off defect clusters becomes dominant, called Stokes-Wilson scattering.[288,289] Taking a Log-Log plot of intensity along the [100]- and [010]-directions (*i.e.*, along the clover leaves) as a function of distance from the Bragg peak center ($q-q_0$) and extracting the slope of a linear fit provides further

information (Figure 7.17). In the 15 nm films, the expected slope for polar diffuse-scattering is observed, namely a slope of ≈ 2 and ≈ 4 for small and large q-values, respectively (Figure 7.17a I,ii). Measurement along the 110 direction (*i.e.*, between the clover leaves) results in slopes of ≈ 1 and ≈ 5 at small and large q values, respectively, indicating that the clover shape can be attributed to Hwang and Stokes-Wilson scattering (Figure 7.17aiii). Thicker films, however show distinct q-dependence despite the appearance of a diffuse clover shape. Small regions with a slope of 2 can be seen in both 22 nm and 70 nm films, along the [100]- and [010]-directions, but there appears to be a contribution from scattering off other defects, leading to slopes of ≈ 3 and ≈ 4 at small q-values in 22 nm and 70 nm films, respectively. As mentioned above, point defects not related to polar displacements can also contribute to diffuse scattering, and it is possible that oxygen vacancies or dislocations can cause diffuse scattering that is convoluted with polar diffuse scattering, leading to a different q-dependence despite the appearance of the same diffuse clover shape. This may be seen in the q-dependence along the [110]-directions in the 22 nm and 70 nm films where the slope is ≈ 3, suggesting this additional diffuse intensity, whatever the origin, is radially symmetric.[291,292] As such, the clover shaped diffuse intensity is attributed to polar correlations. The symmetry of the diffuse intensity suggests a preferred direction for polar displacements, although further measurements, including measurements near other diffraction conditions and temperature-dependent measurements are required to fully describe the shape and orientation of polar regions.[243,253,259] While similar diffuse-scattering patterns are observed in all films studied, quantitative analysis of measurements from 22- and 70-nm-thick films is difficult owing to the presence of additional defect-scattering effects that overlaps with the cross-shaped pattern and further analysis is performed on the 15 nm film.

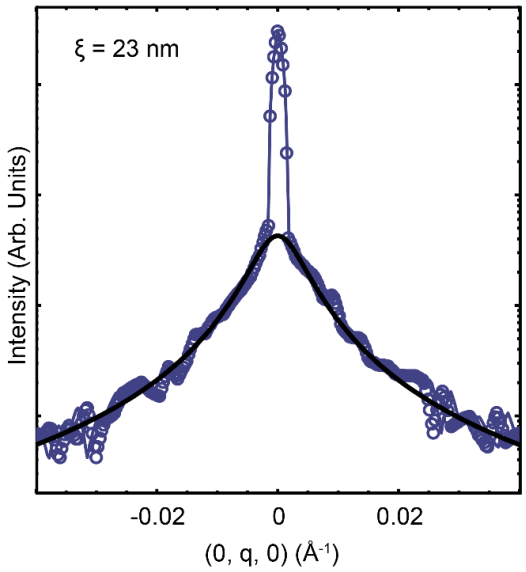

Figure 7.18: Correlation-length analysis is performed on 15-nm films by taking a line cut along the [100] direction and fitting to a Lorentzian distribution, resulting in a polar correlation length of 23 nm.

Using this data, it is possible to perform correlation length analysis on the data from the 15-nm thick films by fitting the diffuse intensity to a Lorentzian profile:[258]

$$I_{diff} = \frac{I_0 \Gamma}{\pi(\Gamma^2 + q^2)}, \qquad (7.4)$$

where Γ is the half-width at half-maximum, q is the distance from the center of the peak, and I_0 is the integrated intensity of the diffuse scattering (Figure 7.18). Taking the reciprocal of $\boldsymbol{\Gamma}$ provides a measure of the correlation length (ξ) of the polar structures; which was found to be ≈ 23 nm for these films. This coincides closely with the length scale at which the polarization scaling abruptly changes (≈ 30 nm), suggesting that this change is associated with an interaction of the thickness of the film with the average correlation length of the polar structures.

In light of this observation, we return to discuss the scaling behavior of the critical temperatures and

polarization response of the films now in the context of this observation. Whereas the linear decrease in polarization response with decreasing thickness may be due to increasing dipolar interaction strength as the crystal volume is reduced, the change in scaling that occurs below 30 nm may be due to a critical interaction of the polar structures with the film interfaces. At the relaxor-electrode interfaces (both top and bottom of the film), weak depolarization fields arising from imperfect screening from the oxide electrodes can create interfacial regions where the small polar clusters are pinned into random orientations to reduce this depolarization field akin to the formation of 180° domains in ultrathin ferroelectrics.[17,91,256] As such, the observation that T_f begins decreasing at the largest thicknesses is likely evidence of the presence of larger clusters that begin interacting with the film thickness even at a film thickness of 50 nm. As thickness is further decreased to the length-scale of polar correlations, it becomes increasingly likely that polar clusters may extend through the thickness of the film. This scenario has been proposed as a driving force for stabilization of ferroelectricity, however, the highly polarizable relaxor polar structures may allow for an internal compensation of depolarizing fields, increasing the interaction between adjacent dipoles in the lattice, and accelerating the suppression of polarization response with decreasing thickness. This may also provide an explanation for the lack of nonlinearity observed in the 7-nm-thick films, despite dielectric measurements showing a peak and frequency-dispersion, since the film has not become purely dielectric, but only the smallest polar clusters and boundaries are still free to move while most of the polarization is locked in strong locally-anisotropic potential wells. Overall, the effect of reducing sample size (or thickness here) appears to be that of reducing the collective response of polar structures, limiting the polarization response to the intrinsic lattice response. The present results indicate that large electrical response in relaxors is highly dependent on the motion of the entire ensemble of polar clusters and is lost when the volume over which clusters can interact and reorient is restricted.

7.8. Conclusions

In summary, high-quality $PbSc_{1/2}Ta_{1/2}O_3$ thin films of varying thickness were synthesized and studied to understand finite-size effects in relaxors. The degree of chemical-ordering was first probed to understand the impact of PLD parameters on the local chemical structure, and the resulting phase transition. A series of $PbSc_{1/2}Ta_{1/2}O_3$ films with thicknesses ranging from 7 – 70 nm were then synthesized and characterized. The temperature-evolution of polar structure in the films is relatively insensitive to finite-size effects, with only small changes apparent below ≈ 22 nm, whereas the magnitude of polarization response is continually suppressed with decreasing thickness. Between 20 nm and 30 nm, a distinct change in scaling is observed that reflects changes in the ability of the material to respond to applied fields. Structural characterization suggests this change in scaling behavior occurs when the film thickness approaches the average correlation length of the polar structures, however, considerably more study of the diffuse-scattering patterns is required. Together, these observations highlight the importance of interactions between polar clusters in producing the well-known nonlinear polarization response of relaxors. Ultimately, these results have important implications for understanding relaxor material response – both in small-grain-size ceramics and thin-film devices.

Chapter 8:
Freestanding $PbMg_{1/3}Nb_{2/3}O_3$-$PbTiO_3$ membranes

This chapter explores the fabrication and properties of $0.68PbMg_{1/3}Nb_{2/3}O_3$-$0.32PbTiO_3$ (PMN-0.32PT) thin films fabricated as freestanding membranes. Details regarding methods for removing thin films from the substrate are presented, along with observations on approaches to avoid high crack densities in released films. Ferroelectric and piezoelectric characterization of freestanding PMN-0.32PT membranes reveals dramatic changes to both the polarization response and piezoelectric surface displacement with reduced coercive field and remnant polarization, as well as larger displacements measured in freestanding films as compared to clamped films. Finally, possible approaches for further enhancing piezoelectric responses of freestanding-relaxor membranes are discussed.

Chapter 8: Freestanding $PbMg_{1/3}Nb_{2/3}O_3$-$PbTiO_3$ membranes

8.1. Introduction

One of the most desirable and well-known characteristics of relaxors is the large piezoelectric coefficients measured for single-crystal samples. Compared to ferroelectric crystals like PZT, which has long served as one of the most common materials used in piezoelectric applications,[10] PMN-*x*PT and PZN-*x*PT crystals exhibit an order of magnitude higher piezoelectric coefficients (d_{33}).[100,222,293,294] Such large piezoelectric coefficients promise lower driving voltage for piezoelectric actuators and higher sensitivity and efficiencies for vibration sensing and energy harvesting applications.[10,101,218,295] Yet, these large effects are specifically found in, and limited to, single-crystal specimens probed along specific crystallographic directions and not polycrystalline ceramics.[100,296–298] While the electric field required to drive large piezostrains may be small, large macroscopic crystals, often with dimensions of the order of millimeters, still necessitate large voltages to achieve the appropriate electric field. This has driven researchers to attempt to create relaxors as thin films, lowering voltage requirements by orders of magnitude and making them amenable to novel micro- and nano-electromechanical systems. Unfortunately, but as expected, measurements of epitaxial thin films have produced far smaller d_{33} and piezostrains in comparison to their bulk crystal counterparts.[299–301] This suppression of the achievable piezostrain has ultimately been attributed to mechanical clamping of the film to the much larger, and mechanically stiff, substrate required for producing high-quality epitaxial thin films.[102,302–304]

Meanwhile in the perovskite oxide community, clamped thin films have been used to develop critical understanding of ferroelectric materials for several decades, with important functionalities enabled by manipulation of epitaxial strain, surface orientation and interface-mediated electrostatic boundary conditions.[1] More recently, epitaxial thin films synthesis, characterization and measurement techniques have begun to be applied to relaxors as a platform for understanding fundamental phenomena related to relaxors.[219,220,235,243,245,255,305,306] For example, thin films have recently been used to study the impact of epitaxial strain on relaxor-phase evolution,[243] as well as performing novel *in situ* structural measurements to probe the evolution of relaxor structure under applied fields.[245] These studies, while insightful, probe the properties of relaxor thin films with a particular set of mechanical boundary conditions, and may not be fully representative of a standalone relaxor crystal. As such, to further understand fundamental physics of relaxors, and achieve long-desired large piezoelectric coefficients in relaxor thin films, new approaches must be envisioned for creating specimens which are free of these mechanical boundary constraints imposed by the substrate.

8.2. Fabricating freestanding membranes

In the last few years, new methods for creating freestanding membranes from epitaxial oxide thin films have been gaining interest.[307] With the discovery of monolayer graphene exfoliated from large graphite single crystals,[308,309] the field of 2D materials has rapidly expanded, and monolayer crystal flakes of a large number of materials have been produced, resulting in the discovery of a range of novel physical phenomena.[310] Such discoveries have prompted oxide researchers to ask

whether oxide thin films could similarly be produced as freestanding membranes with the potential to both induce new physics and enable novel methods of manipulation, particularly for the ferroic oxides. A number of methods have been demonstrated for creating such freestanding membranes of epitaxially deposited perovskite oxides, with the most widespread now employing chemical-etching of an epitaxially deposited sacrificial layer.[105] Such studies have demonstrated novel properties, including increased elasticity in ultrathin films,[107,311] enabled new means of mechanical manipulation to achieve extreme strain states,[106,312,313] and allowed for heterogeneous integration of dissimilar crystal structures.[314,315] It has been reported that the release of ferroelectric heterostructures from their substrates results in large changes to switching dynamics, including reduced coercive fields and faster switching times.[104,109] It has been suggested that reduced coercive fields and faster switching times in freestanding $BaTiO_3$ and $Ba_{1-x}Sr_xTiO_3$ membranes were enabled by a lower energy switching pathway at the unit-cell level involving an intermediate 90° ferroelastic switching contribution.[104] In freestanding $BiFeO_3$ membranes, similar observations were attributed to reduced dynamic strain associated with long-range collective switching of the octahedral-tilt pattern, reducing the energy barrier between polarization states.[109] In both cases, the bonding to the oxide substrate prevents these alternate switching pathways, increasing switching energies and times. Based on these findings, it is worth asking whether the polarization rotation pathway that has been proposed for high performance piezoelectric relaxor systems like PMN-*x*PT could be similarly impacted by release from the substrate.

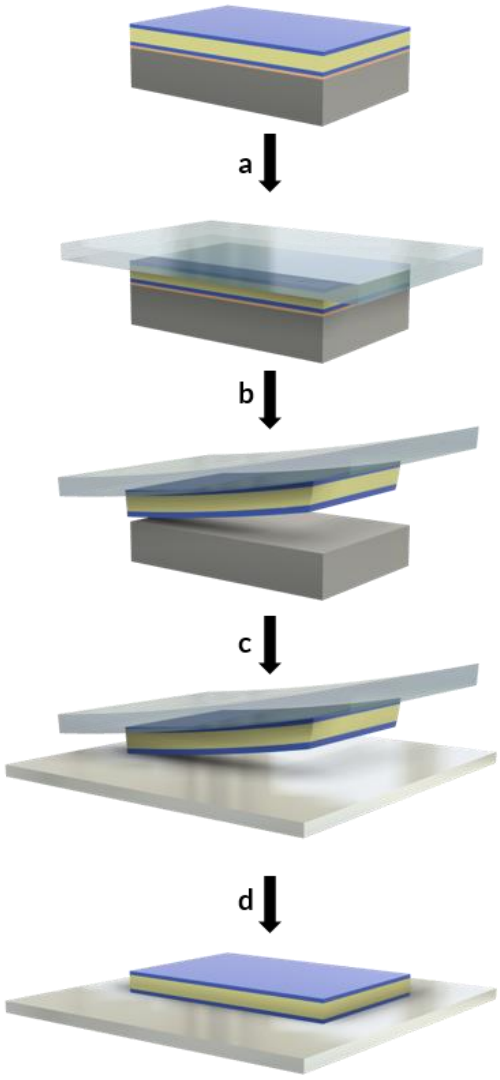

Figure 8.1: Freestanding transfer process. a) The as-grown heterostructure, including sacrificial layer is fixed to a polymer stamp. b) The sacrificial layer is etched, releasing the heterostructure from the substrate. c) The polymer stamp is used to transfer the heterostructure to the receiving substrate. d) The polymer stamp is removed, leaving a freestanding heterostructure.

Freestanding membranes in this dissertation were fabricated using a chemical etchant and an epitaxial sacrificial layer.[104] While the focus will be on freestanding PMN-0.32PT membranes, the lift-off process was first optimized using $PbTiO_3$ films. In general, the desired freestanding

membrane is epitaxially grown on a sacrificial layer of LSMO layer, with the composition chosen to provide low lattice mismatch with both the desired epilayer for lift-off, and the underlying substrate. For release of $PbTiO_3$ films from $SrTiO_3$ substrates, $La_{0.7}Sr_{0.3}MnO_3$ (a =3.868 Å) was used as a sacrificial layer, while for release of PMN-0.32PT films from $NdScO_3$ substrates, the larger lattice parameter $LaMnO_3$ (a_{pc} = 3.935 Å) was used as a sacrificial layer. Once the film is synthesized, the following procedure was used to fabricate freestanding membranes (Figure 8.1). First, the films were ultrasonically cleaned in acetone and isopropanol for 5 min., each before transferring to a hot plate set to 95°C to heat for another 10 min. Following heating, the samples were plasma cleaned for 3 min. In the meantime, a polymer stack is prepared to support the film during etching. The polymer layers are prepared in advance. Briefly, a 1-mm-thick polydimethyl silane (PDMS) layer is synthesized using 10:1 ratio of elastomer base to curing agent (Sylgard 184), degassed, and poured onto a 3-inch silicon wafer. The layer is again degassed before curing at 100°C for 1 hour. A solution of polypropylene carbonate (PPC) is prepared by dissolving 80 g of PPC pellets (Sigma-Aldrich) into 100 mL anisole (Sigma-Aldrich). This solution is then drop casted onto a clean glass slide and baked at 80°C for 10 min. After cooling the PPC has formed a rigid layer with thickness of approximately 100 µm. To assemble the polymer stamp, a square of PDMS (typically 10 x 10 mm) and placed onto a clean, square glass slide (approximately 25 x 25 mm). A square sheet of PPC the same size as the glass slide is cut and placed over the PDMS. The whole stack is heated at 80°C, which softens the PPC, adheres it to the PDMS in the middle, and glass slide around the edges. After 5 min. the stamp is removed from the hot plate and allowed to cool, before the plasma-cleaned films are placed in contact with the PPC. The whole stack is returned to the hot plate at 80°C for another 5 min. to soften the PPC and allow the film to adhere. Finally, the complete stack is allowed to cool to room temperature before being placed in an etchant solution consisting of 1.5 mmol KI in 0.3% HCl. The sacrificial $LaMnO_3$ is slowly etched over the course of several days. To assess the completion of etching, the stack can be lifted out of solution and the substrate will slide off the film, indicating etching has completed. A platinum-coated substrate is cleaned in the same manner as the films, via sonication and plasma cleaning, to prepare for transfer. The receiving substrate is placed on a hot plate, and a drop of deionized water is dropped to wet the surface. The polymer stack supporting the freestanding membrane is inverted to place the membrane in contact with the receiving substrate. The whole stack is then heated at 70°C for 15 min. to dry the film and adhere it to the receiving substrate. The stack is then cooled down, and the PDMS/glass slide are removed leaving a freestanding membrane coated in a PPC layer coating the surface. The PPC is then dissolved by soaking in acetone for 1 hour. After removal from acetone the film is then soaked in isopropanol for 15 min. before drying. This results in a clean, freestanding membrane supported on platinum-coated silicon substrate.

8.3. Observations on cracking

While achieving large, crack-free freestanding membranes with areas on the order of 1-10 mm^2 is achievable with the described procedure, results are highly dependent on the quality of the film synthesized, particularly when attempting to release multilayer structures required for device

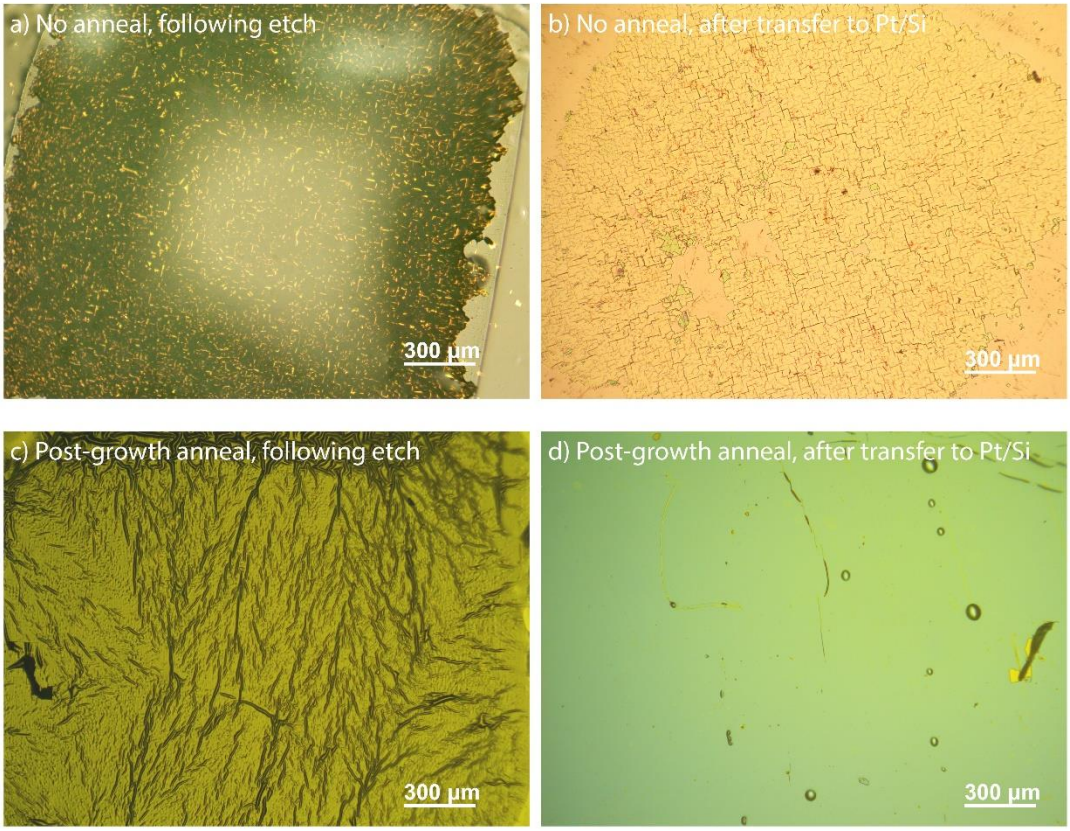

Figure 8.2: Microscope images illustrate the result of wrinkling and cracking during etching on the final transferred film. a,b) $PbTiO_3$ films that were not annealed exhibited extensive wrinkling and cracking during the etch, resulting in a transferred film with a high density of cracks. c,d) A post-growth anneal resulted in a film with distinct surface morphology during etching which could be transferred, leaving a smooth intact, large area membrane.

fabrication and characterization. In this work, it was found that successful release was highly dependent on the as-grown quality of thin films. A few simple experiments were used to probe this behavior. First, single-layer films of typical ferroelectrics produced by PLD, in this case $PbTiO_3$ films, were synthesized. A sacrificial layer of 7 nm $La_{0.7}Sr_{0.3}MnO_3$ was first deposited on $SrTiO_3$ substrate at a heater temperature of 660°C and an oxygen partial pressure of 50 mTorr, using a laser fluence of 1.7 J/cm^2 at a repetition rate of 10 Hz. The $PbTiO_3$ layer was subsequently deposited at a heater temperature of 600°C and oxygen partial pressure of 100 mTorr, using the same laser conditions. Following deposition, films were cooled to room temperature at a rate of 10°C/min. in an oxygen pressure of 30 Torr. Release of such single layer films resulted in intact films 2 mm x 2 mm in area with minimal cracking. To obtain freestanding heterostructures for device fabrication, heterostructures of the form 20 nm $SrRuO_3$ / 50 nm $PbTiO_3$ / 20 nm $SrRuO_3$ / 10 nm $La_{0.7}Sr_{0.3}MnO_3$ were synthesized on $SrTiO_3$ substrates. Following deposition of the $La_{0.7}Sr_{0.3}MnO_3$ layer using the same conditions listed above, an $SrRuO_3$ electrode layer was deposited at a heater temperature of 625°C and oxygen pressure of 50 mTorr, using a laser fluence of 1.7 J/cm^2 and repetition rate of 25 Hz. $PbTiO_3$ was deposited using the same conditions as listed for the single-layer film, followed by deposition of the top $SrRuO_3$ electrode layer at the same

heater temperature and oxygen pressure as the $PbTiO_3$. Following deposition of the top $SrRuO_3$ layer, the films were again immediately cooled to room temperature at a rate of 10°C/min. in an oxygen pressure of 30 Torr. Release of these films resulted in a dense array of wrinkles that formed during etching, while the film is still attached to the polymer (Figure 8.2a). Transfer of this wrinkled film to a Pt/Si substrate results in cracking of the film (Figure 8.2b). The formation of wrinkles during etching suggests that as etching proceeds, and the epitaxial strain of the film is release, the stress associated with this release is enough to drive deformation of the film and subsequent cracking along the wrinkles. Yet, the expected epitaxial strain of a $SrRuO_3$/$PbTiO_3$/$SrRuO_3$ heterostructure on $SrTiO_3$ substrates is relatively low, approximately -0.63% for $SrRuO_3$/$SrTiO_3$ and -1.3% for $PbTiO_3$/$SrTiO_3$. Moreover, release of single-layer $PbTiO_3$ films resulted in crack-free films. It was hypothesized that some additional defects were induced by the synthesis procedure for the trilayer heterostructures, and specifically the oxygen stoichiometry could be impacted by capping the $PbTiO_3$ with $SrRuO_3$ in a high-temperature, low pO_2 environment. To test this hypothesis, synthesis of the trilayer heterostructure was repeated, but instead of immediately cooling the film following deposition of the final $SrRuO_3$ layer, the full heterostructure was kept at the growth temperature of 630°C and an oxygen pressure of 30 Torr for 30 min. before cooling to room temperature at 10°C/min. During release of these films, it was noted that instead of the dense array of rectilinear wrinkles, a relatively smoother film (noted by the lower contrast in the optical microscope image) with dendritic wrinkles was observed (Figure 8.2c). Transfer of this film to a Pt/Si substrate resulted in complete transfer of a large, smooth film, with little to no cracking (Figure 8.2d). This suggests that without the oxygen anneal treatment, the heterostructure likely possesses a great enough oxygen deficiency to cause lattice expansion and the associated strain release during etching drives cracking. With the oxygen anneal, the released strain is smaller and no cracks are formed.

In addition to this observation on the strong dependence growth parameters have on successful membrane release, attempts to release a number of other heterostructures have illustrated important considerations for choosing the appropriate heterostructure. $PbTiO_3$ films were also deposited on $SmScO_3$ substrates in an attempt to release films with a_1/a_2 domain structures;[57] however, most of these films resulted in heavy cracking and disintegration of the film during etching. Here, it was believed that the difference in domain structure between the a_1/a_2 structure of the substrate-supported film, and the zero-strain c/a domain structure imparted high stress concentrations near domain boundaries upon release, driving crack formation. Additionally, PMN-0.32PT films and heterostructures were initially released from $SrTiO_3$ substrates. The large lattice mismatch between PMN-0.32PT and $SrTiO_3$ in those heterostructures (-1.9%) caused some partial strain relaxation in the PMN-PT layer, leading to again to heavy cracking during etching. Similar effects have been demonstrated in other heterostructures, illustrating the detrimental impact of the large strain gradients associated with strain relaxation on release of intact membranes.[316] As such, for release of PMN-0.32PT, heterostructures were deposited on $NdScO_3$ substrates, which provide the lowest lattice mismatch for PMN-0.32PT among the commercially available oxide substrates.[200]

8.4. Freestanding PMN-0.32PT membranes

To study the impact of the mechanical constraint of the substrate on the properties of PMN-0.32PT thin films, freestanding membranes were fabricated. First, heterostructures of the form $Ba_{0.5}Sr_{0.5}RuO_3$ / $0.68PbMg_{1/3}Nb_{2/3}O_3$-$0.32PbTiO_3$ / $Ba_{0.5}Sr_{0.5}RuO_3$ / $LaMnO_{3-\delta}$ / $NdScO_3$ (110) were synthesized via PLD. $LaMnO_3$ layers were deposited at a heater temperature of 800°C in a dynamic oxygen pressure of 10 mTorr, using a laser fluence of 1.6 J/cm^2 and repetition rate of 2 Hz from a stoichiometric target (Praxair). Immediately following deposition of $LaMnO_3$, the pressure was increased to 20 mTorr and $Ba_{0.5}Sr_{0.5}RuO_3$ was deposited at the same temperature and laser conditions from a target of the same composition (Praxair). Following deposition of $Ba_{0.5}Sr_{0.5}RuO_3$, the heater was cooled to a temperature of 600°C and the pressure increased to 200 mTorr to deposit the PMN-0.32PT using a laser fluence of 1.7 J/cm^2 and repetition rate of 2 Hz. Up to four identical ceramic targets, depending on desired film thickness, of the target composition with an additional 10% lead excess were used to maintain stoichiometric films. Each target was used to grow 50 nm of the film, (*i.e.*, four targets for 200-nm-thick films, three targets for 150-nm-thick films, etc.). Following deposition of the $0.68PbMg_{1/3}Nb_{2/3}O_3$-$0.32PbTiO_3$ layers, the chamber was filled with 700 Torr of oxygen and cooled to 550°C. Upon reaching 550°C, the pressure was again reduced to 20 mTorr for deposition of the top $Ba_{0.5}Sr_{0.5}RuO_3$ electrode at the same laser conditions as above. Finally, the chamber was filled to 700 Torr and cooled to room temperature.

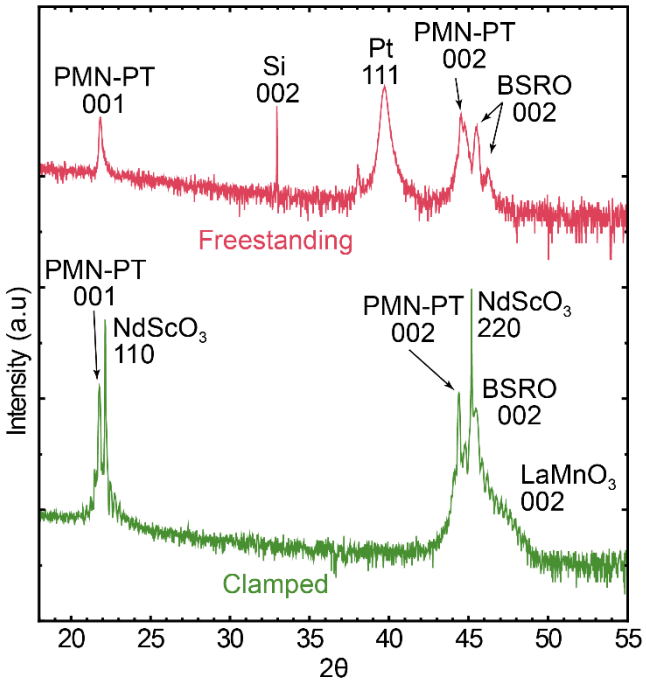

Figure 8.3: X-ray diffraction of clamped heterostructure (green) and freestanding membrane (red) illustrate the similar lattice parameters for PMN-0.32PT and $Ba_{0.5}Sr_{0.5}RuO_3$ layers upon release, due to similar strain conditions.

Following transfer of freestanding PMN-0.32PT membranes to platinum-coated silicon substrates, X-ray diffraction studies were performed to examine any structural changes that may occur upon release from the substrate (Figure 8.3). In the clamped films, the $NdScO_3$ substrate (a_{pc} = 4.01 Å)[200] is expected to impart a biaxial tensile strain on the $Ba_{0.5}Sr_{0.5}RuO_3$ (a_{pc} = 4.00 Å)[317] of 0.25%, and a biaxial compressive strain on the PMN-0.32PT (a = 4.03 Å) of -0.5%. Upon release from the substrate, the entire heterostructure is expected to adopt a new strain state that balances the elastic energy of straining both electrode layers and the PMN-0.32PT layer. This new freestanding strain on the PMN-0.32PT (ϵ_{FE}) can be calculated from[104]:

$$\epsilon_{FE} = \frac{u_{mis}}{1+\frac{t_{FE}\left(s_{11}^{E}+s_{12}^{E}\right)}{2t_{E}\left(s_{11}^{FE}+s_{12}^{FE}\right)}}, \tag{8.1}$$

where u_{mis} is the lattice mismatch between the PMN-0.32PT and $Ba_{0.5}Sr_{0.5}RuO_3$, t_{FE} and t_E are the thicknesses of the PMN-0.32PT and electrode layers, respectively, and S_{ij}^{FE} and S_{ij}^{E} are the in-plane elastic compliances of the PMN-0.32PT and electrode layers respectively. Elastic compliance values for each of the layers can be found in the literature,[318,319] and calculation using t_{FE} = 200 nm and t_E = 30 nm results in a freestanding strain of ϵ_{FE} = -0.7%, only slightly more compressive than the clamped film. X-ray diffraction studies reveal that the PMN-0.32PT out-of-plane *c* axis is slightly expanded relative to the expected -0.5% strain state in the as-grown, clamped films. Upon release, the PMN-0.32PT 002 diffraction condition shifts very slightly to higher angles, suggesting contraction of the out-of-plane lattice parameter, yet it appears at the expected position assuming the -0.7% strain calculated the above equation. This confirms minimal structural change to the PMN-0.32PT film upon release from the substrate, and such samples can be compared to their clamped counterparts.

8.5. Polarization dynamics

To probe the properties of these freestanding films, capacitor structures were fabricated for electrical testing. An array of circular electrodes of varying sizes were photolithographically patterned for subsequent ion-milling. To remove the photoresist, films were soaked for 1 hour in acetone, then 15 min. in isopropanol without sonication, before drying at 95°C for 5 min. Recalling that the reported observation of frequency-dependent suppression of the M_A-to-M_c discussed in Chapter 6 was ultimately correlated to an observed frequency-dependent increase of the coercive field measured in a P-E loop.[245] As such, measuring P-E loops across a broad range of frequencies

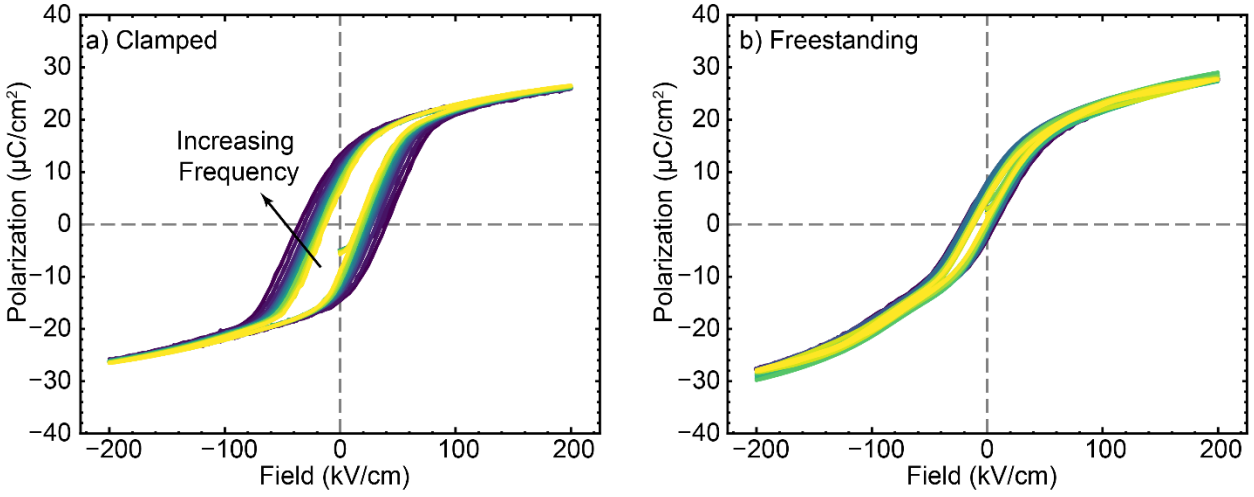

Figure 8.4: Comparison of frequency-dependent P-E loops measured from 5 Hz to 50 kHz for a) clamped films and b) freestanding films. A reduction in both remnant polarization and coercive field is observed for freestanding films, along with an apparent reduction in the frequency-dependence.

in freestanding films may illustrate the impact of substrate clamping on such a polarization rotation pathway. First, P-E loops were measured on 25 μm capacitors as a function of frequency from 5 Hz to 50 kHz for the clamped films, which a relatively slim loop at low frequency, which progressively gets wider as the measurement frequency is increased (Figure 8.4a). Performing the same measurements on the freestanding films shows a dramatically different behavior. At low frequencies, the loop is slimmer than the clamped film, but more striking is that the loop remains slim all the way to measurement frequencies of 50 kHz (Figure 8.4b). This suggests that, similar to reports on freestanding $BaTiO_3$ and $BiFeO_3$,[104,109] removal of the mechanical clamping to the substrate similarly reduced the energy of switching in PMN-0.32PT films, possibly due to a reduction in the elastic energy associated with reorienting polar clusters under applied fields. To directly compare the frequency-dependent polarization behavior of the two films, the remnant polarization, measured where the loop crosses E = 0, and the coercive field, measured where the loop crosses P = 0, is plotted as a function of frequency (Figure 8.5). Clamped films exhibit a continuous increase in both remnant polarization and coercive field with increasing measurement frequency, including a sharp increase in both above ≈ 20 kHz. On the other hand, the freestanding films maintain low coercive field and remnant polarization over the entire frequency range measured, with a minor increase in both as frequency is increased.

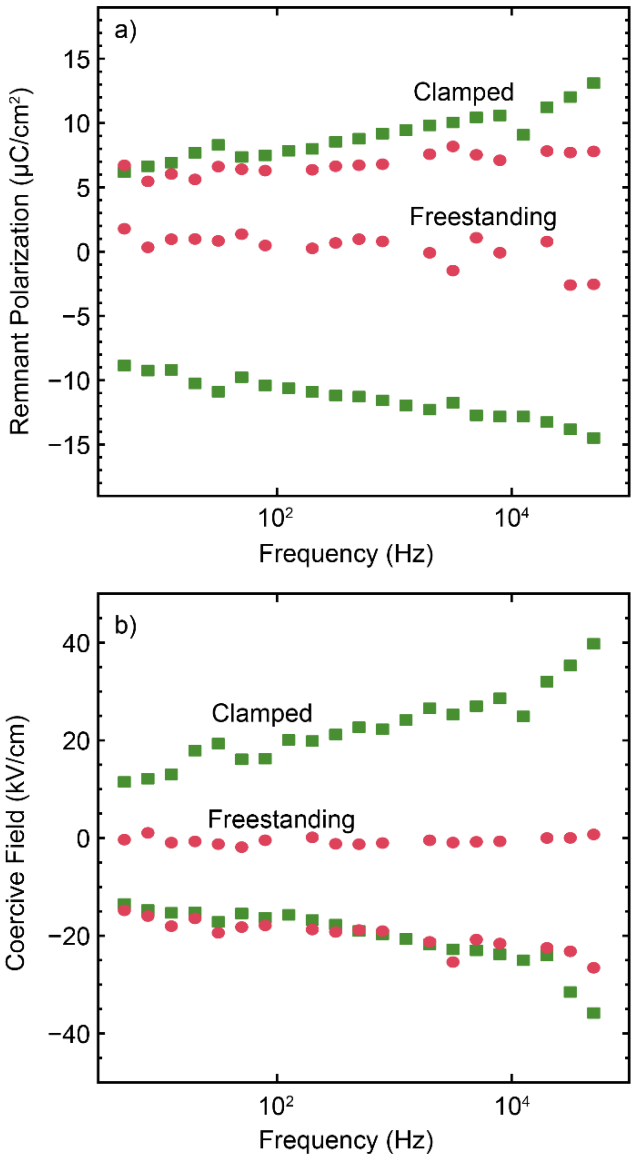

Figure 8.5: Extracted a) remnant polarization and b) coercive field from the frequency-dependent P-E loops on clamped and freestanding films reveals a large decrease in the magnitude of frequency dependence observed in freestanding films.

The absence of frequency-dependent polarization response in freestanding films suggests that the frequency-dependent suppression reported and measured for clamped films, which again has been correlated to polarization rotation pathways via structural measurements, is no longer present in freestanding membranes. Considering the capacitor heterostructures measured for clamped and freestanding films are identical, such frequency-dependent effects cannot be attributed to

frequency-dependent electrode or circuit effects.[320] Instead, such suppression must be caused by mechanical clamping of the substate. On one hand, this may not be so surprising, as the lattice deformation needed to rotate the polarization can be suppressed by mechanical clamping, increasing the energy needed to drive such a rotation. On the other hand, the origin of such a frequency-dependent suppression of polarization rotation, which has not yet been explicitly proposed, is particularly curious due to the relatively slow frequency of 20 kHz. Compare this to the THz frequencies typically associated with soft-phonon modes that mediate polar displacements in both relaxors and typical ferroelectrics,[242,321,322] and the switching speed limits for ferroelectrics on the order of picoseconds that have been proposed in a number of experimental and theoretical works.[320,323–328] Particularly considering the reported picosecond dynamics of polar relaxation in relaxors, and the low-energetic barrier to relaxation often cited as a driver of relaxor behavior, 20 kHz is surprisingly slow.[93,329] Instead, this may be suggestive of a collective mode of associated with reorientation of polar nanodomains that is strongly coupled to the mechanical stiffness of the lattice.[330]

8.6. Piezoelectric response

Having established that releasing relaxor films from the substrate impacts the polarization response, the impact on piezoelectric properties can be probed. It has been proposed that in addition to mechanical clamping from the substrate, another form of clamping can contribute to reduced piezoelectric coefficients that originates from the mechanical constraint of inactive piezoelectric material outside of the capacitor electrode (Figure 8.6).[102,103] Since this material has no field applied, it remains piezoelectrically inactive, yet the expansion or contraction of the crystal underneath the electrode may be restricted by the constraint of this inactive region. To probe the impact of the various mechanical constraints, a series of freestanding membrane capacitor structures were fabricated. In each case, the transferred film is photolithographically patterned with an array of circular capacitor structures of varying size, and structures were defined using ion-milling as described previously. The 4 variants studied here are as follows: one sample was left on the substrate to serve as a clamped control sample, with the standard array of capacitor structures atop a continuous bilayer of relaxor/bottom electrode (Figure 8.7a), the next sample was the same heterostructure released from the substrate and transferred to a Pt/Si substrate (Figure 8.7b), then one sample, instead of ion-milling only the top electrode, the sample was ion-milled to the bottom electrode (Figure 8.7c), removing any relaxor film outside of the active device

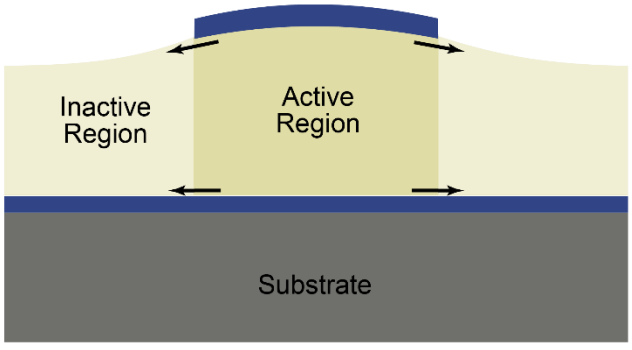

Figure 8.6: Schematic illustrating a cross-section of the measured capacitor structures and the inactive region. Arrows indicate mechanical forces from inactive clamping and substrate clamping.

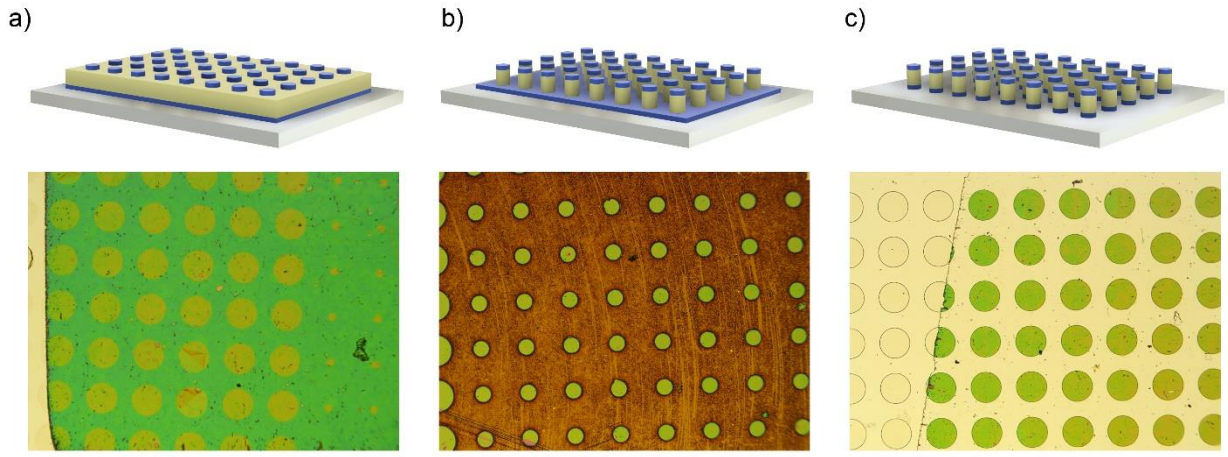

Figure 8.7: Schematic illustrations and microscope images of the three freestanding variants studied. a) A freestanding membrane where only the top electrode is defined, and PMN-PT (green) is left intact. b) A freestanding membrane where only the bottom electrode (brown) is left intact, and c) isolated freestanding cylindrical capacitors where the entire trilayer heterostructure (green).

region, but leaving a continuous bottom electrode layer, and finally one sample was milled all the way to the substrate, and isolated, cylindrical capacitor structures. This set of films presents a series of identical as-grown samples, but fabricated to have varying degrees of mechanical clamping. As a first pass, P-E loops were measured for the series of samples. In general, it is observed that P-E loops become continuously slimmer when the film is released from the substrate, although the largest difference is observed upon removal from the substrate, and release of clamping from inactive regions produces relatively smaller changes.

To probe the piezoelectric response of the four variants, laser-doppler vibrometry was performed on the freestanding films. This technique leverages laser interferometry to perform precise measurements of the surface displacement arising from the piezostrain of the film. A probe tip was used to contact the edge of a top electrode with a diameter of 100 µm, while the bottom electrode was grounded using silver paint to a metallic sample holder. The laser was visually aligned to the center of the top electrode. Polarization and surface displacement were measured for the heterostructures simultaneously while driving the capacitors with an electric field (Figure 8.8). The resulting strain-electric-field plots reveal a large increase in the achievable displacement under the application of 20 V. Interestingly, the piezostrain is largely asymmetric in the clamped films, with positive voltages producing surface displacements of approximately 0.5 nm, and negative voltages producing surface displacements of approximately 0.3 nm. Freestanding films, on the other hand, similarly produce surface displacement of 0.5 nm under positive voltages, but can achieve up to 1 nm displacements under negative voltages, an increase of a factor of 3 compared to clamped films.

While these measurements do not show dramatic differences in surface displacement for freestanding membranes with different degrees of clamping from inactive regions of the PMN-PT, it was questioned whether the entire capacitor produced an even piezoelectric displacement. To understand this, the surface displacement was measured across different points on the electrode.

Chapter 8: Freestanding $PbMg_{1/3}Nb_{2/3}O_3$-$PbTiO_3$ membranes

A freestanding membrane where only the top electrode has been milled, and the PMN-PT film is intact, was used to measure position-dependent piezoelectric displacement loop (Figure 8.9). Examining the loops as a function of position illustrates that negligible displacement is measured

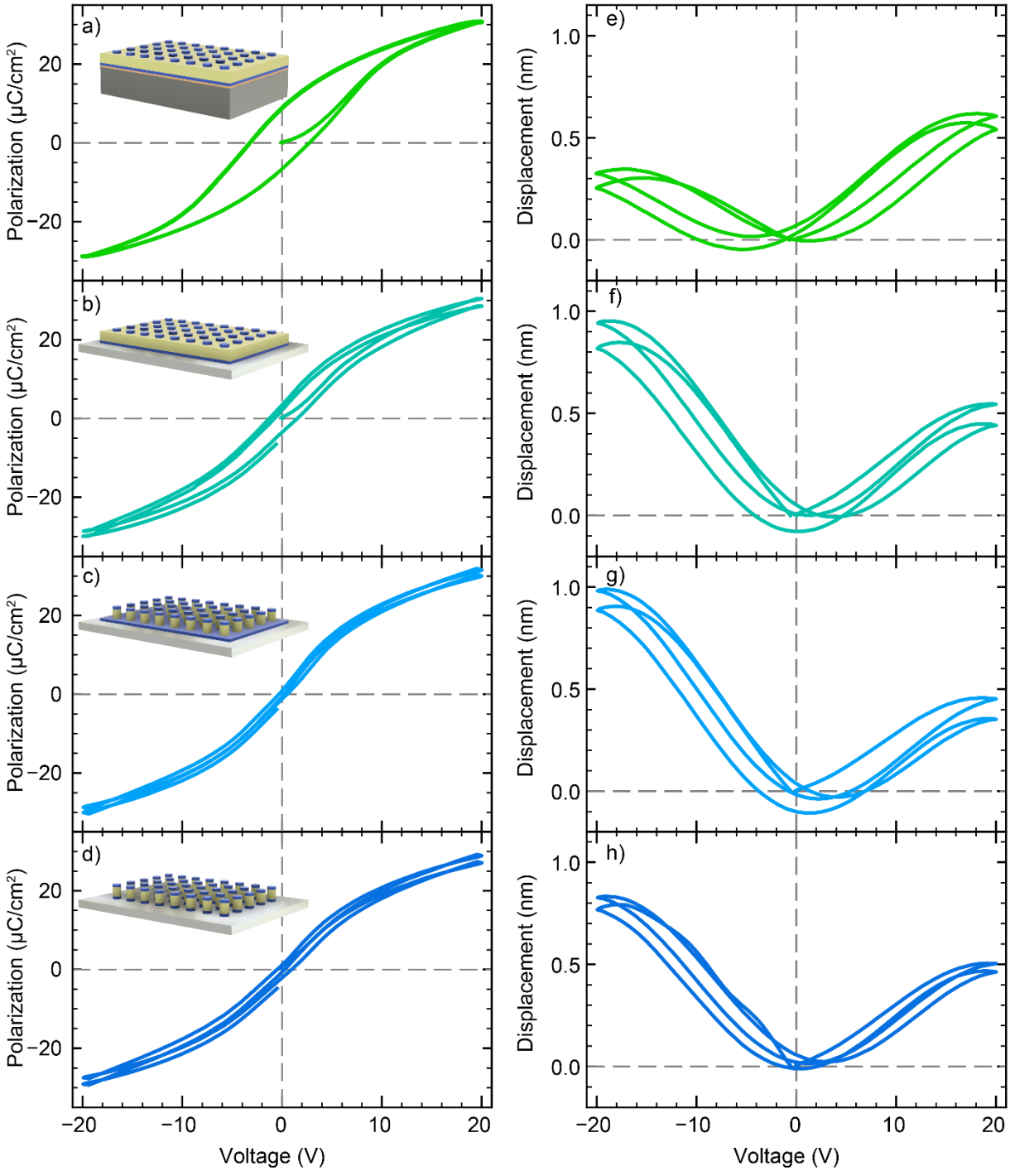

Figure 8.8: a-d) P-E loops measured for the clamped films and three variants of freestanding membrane, illustrating continually reduced coercive field upon reduction of clamping. e-h) Corresponding piezoelectric displacement measured for each of the variants, illustrating increased maximum displacement upon removal from the substrate.

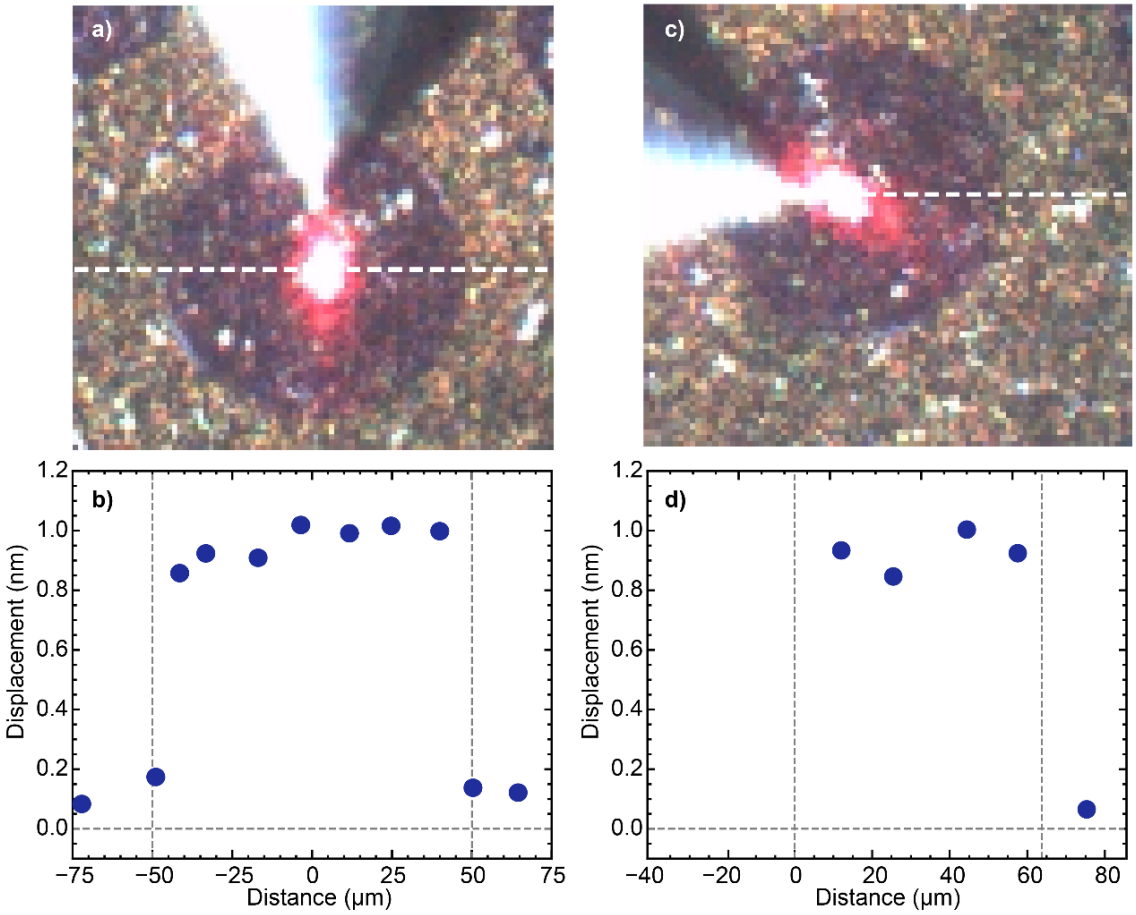

Figure 8.10: Summary of position-dependent measurements. Displacement was measured as a function of distance from the center of the electrode across the white dashed line a,b) across the electrode diameter and c,d) as a function of distance from the probe tip.

outside the capacitor electrode, but almost no change is detectable across the entire electrode diameter. Extracting the total surface displacement, taken by extracting the difference in maximum and minimum displacement, shows well-defined boundaries at the edges of the electrode (Figure 8.10a,b). Additionally, one potentially detrimental impact in the current measurement setup is the use of a micromanipulator-controlled probe tip to make contact to the top electrodes. This contact likely produces an unavoidable force on the piezoelectric, or at the very least restricts the piston motion of the piezoelectric capacitor as the field is applied. To probe the impact of the probe tip, the surface displacement was also measured as a function of distance from the probe tip (Figure 8.10c,d). Again, negligible change in surface displacement is observed until the laser is completely off the electrode, at which point minimal surface displacement is measured. Together, these measurements suggest that the PMN-PT is not asymmetrically strained under application, but instead the entire capacitor produces similar surface displacements within the limits of this measurement. It cannot be excluded, however, that the mechanical force of the probe tip contact restricts the piezoelectric displacement of the entire capacitor to some degree.

The motivating challenge of this work has been to achieve piezostrains in thin-film samples that are comparable with ultrahigh piezostrains measured in bulk-single crystals. Examining the piezostrain of the freestanding and clamped variants, and taking into account the 200 nm thickness, illustrates the enhancement achieved by removing the mechanical clamping of the substrate. Whereas the clamped film achieves a maximum piezostrain of 0.2%, comparable to piezostrains reported for other clamped thin film samples, the freestanding membranes achieve piezostrains of 0.5% (Figure 8.11). This remains lower than the > 1% piezostrains reported for some single crystals, yet there are a few differences that may be responsible for the lower piezostrains measured here. First, large piezoelectric responses are reported in single crystals of compositions close to the MPB in the PMN-0.32PT system. While the target chemistry (32% PT) of these films is close to the MPB, chemical analyses have yet to be performed, and deviation from this target chemistry can readily reduce the piezoelectric response. More importantly, in the heterostructures measured here, more than 20% of the volume of the freestanding heterostructure is $Ba_{0.5}Sr_{0.5}RuO_3$ electrode, and the elastic compliance (stiffness) of these electrode layers is relatively low (high) compared to that of PMN-0.32PT. As such, the mechanical restriction from the stiffer electrode layer may still suppress the piezoelectric response of the PMN-PT layer. Finally, the relatively simple

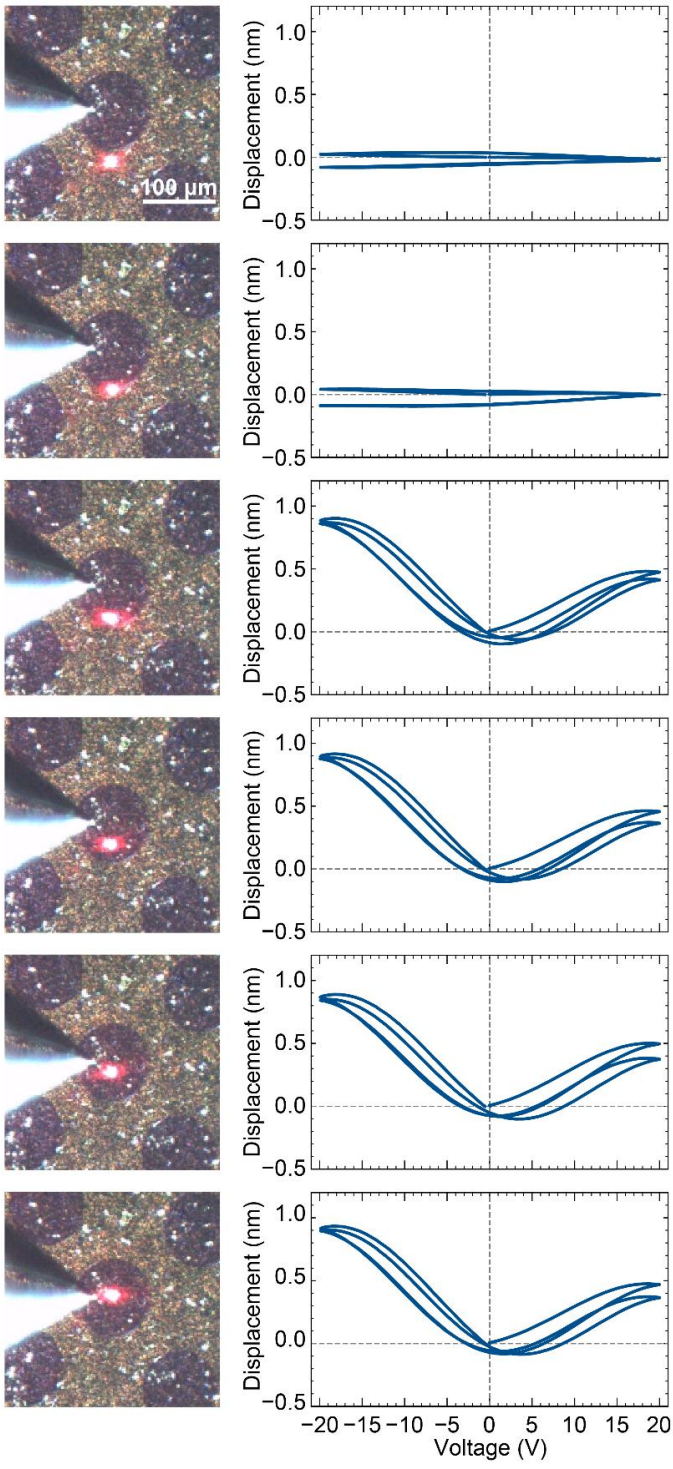

Figure 8.9: Position-dependent piezoelectric displacement loops alongside a microscope image showing the probing laser (red dot) position on the electrode, indicating almost no difference in measured displacement across the capacitor, but no displacement outside of the capacitor.

devices used for this study limited the size of the capacitor structure that could be measured to 100 µm. Considering the PMN-0.32PT is 200 nm thick, this equates to an aspect ratio of 500:1 for the width:height of the active volume of piezoelectric, whereas ultrahigh performance single crystals have aspect ratios of approximately 10:1. The order-of-magnitude large aspect ratio of the samples measured here could result in another form of mechanical constraint and further lower the piezoelectric response.[102,103,331] Lateral scaling of the capacitor area to produce lower aspect ratio devices may allow for larger piezostrains.

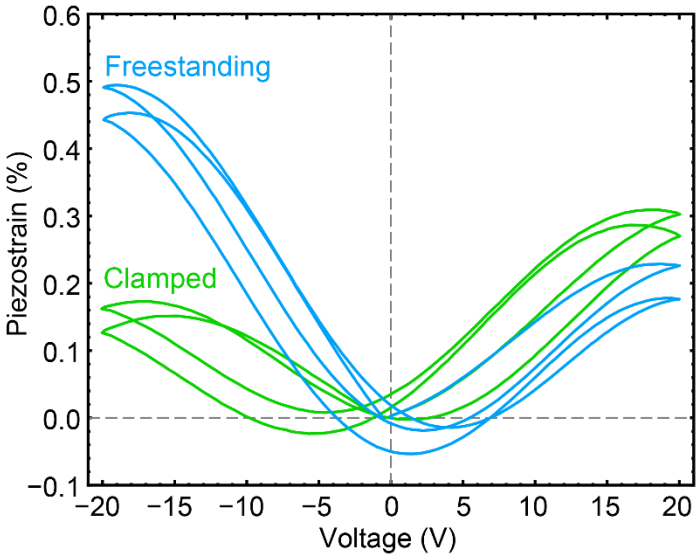

Figure 8.11: Piezostrains achieved for clamped and freestanding PMN-0.32PT.

8.7. Conclusions

This work details preliminary investigations into the impact of mechanical clamping to a substrate on the ferroelectric and piezoelectric responses of PMN-PT thin films. The method described here can produce large freestanding membranes with areas of approximate 5-10 mm^2 with a low density of cracks. It was found that significant cracking of films occurs during the etch process, rather than during transfer, and mitigation of cracks could be achieved by performing a post-growth oxygen anneal, which likely reduces defect-induced lattice deformation and additional strains. Freestanding PMN-PT films were found to exhibit reduced remnant polarization and slimmer hysteresis loops relative to clamped counterparts, indicating the release of the mechanical clamping from the substrate results in increase ease of reorientation and relaxation of polar clusters. Moreover, the frequency-dependence of polarization response in freestanding membranes was dramatically reduced. Finally, piezoelectricity was probed in freestanding membranes using laser Doppler vibrometry, illustrating enhanced piezoelectric responses in freestanding membranes compared to clamped films.

Chapter 9:
Summary of findings and suggestions for future work

Here, the main findings of this dissertation are presented and potential future experiments are discussed to extend these findings. The study of the connection between the perovskite lattice and important properties for both oxygen electrocatalysis and relaxor ferroelectrics has revealed both important limitations to performance, and new means for enhancing properties. Extension of this work through novel *in situ* measurement techniques and new thin-film-enabled device heterostructures are suggested.

Chapter 9: Summary of findings and suggestions for future work

9.1. Findings regarding perovskite surfaces for oxygen electrocatalysis

This work leveraged epitaxial thin films of disordered perovskites to provide insight into the chemical and electronic factors that contribute to the catalytic responses of perovskite surfaces and how manipulation of the lattice can impact these factors. First, the impact of crystallographic surface orientation of $La_{0.8}Sr_{0.2}Co_{0.2}Fe_{0.8}O_3$ was examined, to understand how different surface atomic structures can influence surface chemistry and electronic structure to effect different oxygen electrocatalytic rates. First, electrical conductivity relaxation measurements were performed, demonstrating faster reaction rates for (111) surfaces. Then, epitaxial all-perovskite half-cells were developed to serve as a platform for studying the pressure-dependent electrochemical response of perovskite cathodes. These measurements revealed that (001), (110), and (111) surfaces exhibit the same rate-limiting step for oxygen exchange, likely involving charge transfer to adsorbed oxygen molecules. Subsequent DFT and *in situ* ambient-pressure spectroscopic analyses reveal that the local bonding environment at the surface stabilizes distinct (non-bulk-like) surface chemistries. These results highlight the importance of understanding the possible surface reconstructions, and how deviations from bulk stoichiometry at surfaces may hinder otherwise favorable reaction kinetics. Fast reaction kinetics are found at (111) surfaces that exhibit a balance of important factors such as vacancy concentration, favorable adsorption energy, low strontium segregation, and high *B*-site availability.

Next, the impact of epitaxial strain on both $La_{0.8}Sr_{0.2}Co_{0.2}Fe_{0.8}O_3$ and $La_{0.5}Sr_{0.5}CoO_3$ cathodes was examined. Through a combination of thin-film synthesis, high-temperature electrochemical measurements, and synchrotron-based X-ray linear dichroism experiments, a strong correlation was discovered between the orbital structure and oxygen electrocatalysis rates. Electrochemical studies on epitaxially strained LSCO and LSCF thin films confirm an activity trend previously reported by several groups, namely that biaxial tensile strain enhances oxygen reactivity, while biaxial compressive strain suppresses oxygen reactivity. X-ray linear dichroism measurements found tensile strain reduces the number of empty electron states along the out-of-plane oriented orbitals, which corresponds to a reduction in occupancy of the d_z^2 orbitals. Through correlation to the electrochemical studies, and with an understanding of the rate-limiting step established in the study of orientation dependence, it was proposed that the d_z^2 orbital occupancy can be an important descriptor for oxygen electrocatalysis on perovskite surfaces. Finally, this work also demonstrates that epitaxial strain can be used as a synthetic tool to modulate the electron occupancy of this orbital and subsequently enhance the reactivity of these perovskite catalysts. Together, these studies both highlight important considerations for electrocatalysis on perovskite surfaces, and suggest new engineering pathways for optimizing electrochemical activity in perovskites beyond chemical optimization. Based on these findings, additional studies examining oxygen electrocatalysis of perovskite surfaces can be envisioned.

Chapter 9: Summary of findings and suggestions for future work

9.1.1. Defect structures at perovskite surfaces

The study of surface orientation resulted in the attribution of electrochemical reaction rate differences to different nonstoichiometric surfaces stabilized by difference surface orientations (Chapter 4). In those films, the nonstoichiometry could be so dramatic that, for example, the 110-oriented film was measured to be completely *AO* terminated, which is not a termination expected from a simple picture of cutting the crystal lattice. This is strongly suggestive of a spontaneous surface reconstruction that favors *AO* termination. A deeper study of surface reconstructions on these different perovskite surfaces, involving additional LEIS measurements with depth-profiling, and complementary depth-resolved XPS measurements could provide additional insight as to the defect surfaces that form when films are synthesized with nonstandard surface orientations. Furthermore, studying the connection between PLD synthesis parameters, including, for example, parameters like cooling pressure and laser fluence which are known to impact the defect chemistry of films, and surface reconstructions can reveal methods for engineering favorable surfaces.

Additionally, examination of local defects on these perovskite surfaces can further highlight important considerations for stabilizing favorable surface structures, particularly in these disorder multicomponent perovskite systems. The observation of fast kinetics on (111) surfaces was ultimately attributed to high concentrations of near-surface *B*-site cations, with LEIS experiments showing the presence of some surface-terminating *B* sites. Scanning tunneling microscopy can be used to probe the local density of states around specific *B* sites, as well as specific defect structures, including surface-segregated strontium, oxygen vacancies to understand how these sites contribute to the total electronic structure of the surface. Such measurements have been used to examine oxygen and cation vacancy sites and defect clusters on TiO_2 and Fe_3O_4 surfaces,[332] as well as site-specific density of states. Such measurements could further elucidate different oxygen-vacancy structures stabilized by the different surface orientations, as well as cation-specific electronic structure changes driven by, for example, epitaxial strain. While such studies are typically performed in ultra-high vacuum, combining these studies with thin film samples cooled in different oxygen environments can develop a picture of the evolution of defective perovskite surfaces.

9.1.2. In situ experiments

The work in this dissertation aimed to expand the range of experimental techniques applied to the study of oxygen electrocatalysis in perovskite. One can envision a host of further measurements that could be applied to similar films and heterostructures to advance the findings presented here. The use of ambient-pressure X-ray spectroscopies discussed in this dissertation was predominantly focused on the electronic and chemical structures of the surface in different pure oxygen environments. In some systems, however, it has been discovered that the presence of water, or other chemical species on perovskite surfaces can dramatically change the propensity for electrocatalytic oxygen incorporation.[333] Studying the impact of moisture on the dynamic changes to charge transport, electrochemical impedance spectroscopy, and surface chemistry would

provide further insight into the mechanisms of oxygen reduction on different surface orientations by enabling additional reaction pathways.

Finally, combining the understanding developed from ambient pressure experiments and dichroism measurements, one can envision an all-encompassing measurement, in which the linear dichroism and orbital occupation are measured for an epitaxial electrochemical half-cell under application of electric field and in ambient gas environments. As yet, such an experiment has only been performed in parts, with some *in situ* ambient-pressure field-dependent measurements,[334] and some dichroism measurements,[83,335] but not simultaneously. In such an experiment, one could measure the binding energy shifts of relevant XPS peaks, like the valence band and oxygen 1*s* excitations while driving oxygen in and out of the film with an applied field, but also probe the element-specific orbital occupation around transition metal centers in different atmospheres and while driving with a field. This would allow one to "watch" the oxygenation of the film occur, including which orbitals are impacted most dramatically, and what oxygen species are involved in this reaction.

9.1.3. Novel heterostructures

Considering the results from the dependence of oxygen electrocatalysis on strain, one can envision novel heterostructures that make use of coherently grown epitaxial films that combine favorable characteristics of different materials. One particularly intriguing possibility is that of synthesizing controlled chemical gradients in the cathode to combine desired surface and bulk properties. For example, exploiting the high reactivities of cobalt-based cathodes has been limited by the poor thermomechanical stability and large thermal expansion mismatch with high-performance electrolytes.[114] In other systems, however, stabilization of large epitaxial strain has been demonstrated in compositionally-graded heterostructures, where the composition of the film is smoothly changing from the bottom of the film to the top of the film.[336] In those compositionally-graded films, the top surface of the film was coherently strained with a lattice mismatch of +3.5%, while single-layers of the same composition on the same substrate experienced significant strain relaxation.

A proposed heterostructure based on the strain-dependent oxygen electrocatalysis studied in this work consists of a smooth compositional gradient from LSCF at the substrate/film interface to LSCO at the film surface. In such a heterostructure, the more favorable stability of the LSCF could aid in stabilizing the LSCO surface, while also inducing a tensile strain in the LSCO layer, enhancing the oxygen electrocatalysis at the surface as demonstrated in this work. Such a heterostructure has the added characteristic of a large strontium gradient, with strontium-concentration increasing nearer the surface. Such a gradient may also decrease the propensity for large scale segregation of lattice strontium to the surface, as the chemical gradient promotes strontium diffusion away from the surface. Finally, such a heterostructure provides a means for employing strain-induced enhancement of electrocatalysis in more industry-amenable processes, as the application of epitaxial strain with a substrate is not necessary, and the strain between LSCO and LSCF structures is similar to that demonstrated for LSCO/$SrTiO_3$ heterostructures examined

in this work. Similar strategies have been employed in core-shell Pt/Cu nanoparticles to enhance ORR catalysis.[337] Within this study, various gradients could be explored, including a linear gradient within films of different thicknesses from relatively thin (25 nm) to relatively thick (>100 nm) as well as nonlinear gradients where the bulk of the film is LSCF, and is rapidly graded to LSCO near the surface, with the extreme case of a LSCO/LSCF bilayer. The electrochemical reaction rates could then be measured over high-repetition redox cycles, and combined with surface characterization to evaluate both thermomechanical stability, chemical stability (with specific consideration for strontium segregation) and electrochemical performance.

9.2. Findings regarding scaling and mechanical constraints in perovskite relaxors

In this dissertation the impact of lattice manipulation on the polar properties of perovskites were also studied in two relaxor systems. First, high-quality $PbSc_{1/2}Ta_{1/2}O_3$ thin films of varying thickness were synthesized and studied to understand finite-size effects in relaxors. The degree of chemical-ordering was first probed to understand the impact of PLD parameters on the local chemical structure, and the resulting phase transition, illustrating that growth conditions can be used to control chemical order in relaxors. Next, a series of $PbSc_{1/2}Ta_{1/2}O_3$ films with thicknesses ranging from 7–70 nm were then synthesized and characterized. The temperature-evolution of polar structure in the films was found to be relatively insensitive to finite-size effects, with only small changes apparent below ≈ 22 nm, whereas the magnitude of polarization response is continually suppressed with decreasing thickness beginning at the largest thicknesses. Between 20 nm and 30 nm, a distinct change in scaling is observed in a variety of measurements that reflects changes in the ability of the material to respond to applied fields. Diffuse-scattering measurements suggested this change in scaling behavior occurs when the film thickness approaches the average correlation length of the polar structures. Together, these observations highlight the importance of interactions between polar clusters and the possible impact of film interfaces in influencing the well-known nonlinear polarization response of relaxors.

Next, PMN-PT thin films were fabricated and studied as freestanding membranes to understand the impact of mechanical clamping of the substrate on the ferroelectric and piezoelectric properties. The method described was shown to produce large freestanding membranes with areas of approximate 5-10 mm^2 with a low density of cracks which can further be fabricated into capacitor structures with diameters of 25-100 μm. It was found that significant cracking of films occurs during the etch process, rather than during transfer, and mitigation of cracks could be achieved by performing a post-growth oxygen anneal, which likely reduces defect-induced lattice deformation and additional strains. Electrical characterization of freestanding PMN-PT films were found to exhibit reduced remnant polarization and slimmer hysteresis loops relative to clamped counterparts, indicating the release of the mechanical constraint from the substrate results in increase ease of reorientation of polar clusters under applied fields, as well as relaxation upon removal of the field. Moreover, the frequency-dependence of polarization response in freestanding membranes was dramatically reduced, suggesting previously reported frequency-dependence of polarization rotation was largely impacted by the elastic cost of large-

scale reorientation of polar clusters. Finally, piezoelectricity was probed in a series of freestanding membranes with varying degrees of clamping using laser Doppler vibrometry, illustrating enhanced piezoelectric responses in freestanding membranes compared to clamped films. Together, these findings highlight the importance of mechanical boundary conditions on the polarization response of relaxors. Ultimately, these results have important implications for understanding relaxor material response in thin-film devices as the large electrical response typically associated with relaxors is greatly suppressed at reduced out-of-plane dimensions, but can also be enhanced by release of in-plane mechanical constraints. Based on these studies, additional studies exploring lattice effects in thin film relaxors can be envisioned.

9.2.1. Lead scandium tantalate and growth-controlled ordering

In this work it was demonstrated that some degree of chemical ordering can be induced by optimization of the PLD growth parameters (Chapter 7). Further work focused on more finely tuned control of the chemical-order parameter in thin films could be used as a means to controllable tune the distribution of polar nanodomains in $PbSc_{1/2}Ta_{1/2}O_3$. Such control over the polar structure, particularly in single-crystalline specimens, has been attempted in $PbMg_{1/3}Nb_{2/3}O_3$ films,[338] yet the instability of the highly polar surface terminations resulted in films of lower crystalline quality. Considering $PbSc_{1/2}Ta_{1/2}O_3$ possesses a thermodynamically stable chemically-ordered phase,[240] it presents a unique opportunity for leveraging atomically-precise PLD to control the degree of ordering, allowing for studies that shed light on the impact of the distribution of polar correlations in relaxors. One particularly intriguing question is that of the evolution of the various critical temperatures denoting the relaxor-phase transition, and how those temperatures evolve as the crystal becomes progressively more ordered until it possesses a single ferroelectric T_c. On one hand, disordered $PbSc_{1/2}Ta_{1/2}O_3$ exhibits and average cubic structure while completely ordered $PbSc_{1/2}Ta_{1/2}O_3$ should possess a rhombohedral structure owing to the development of long-range ordered polarization along the [111] of the crystal. Thus, some morphotropic phase boundary (MPBs) may be expected in between these two phases. Unlike more commonly observed MPBs driven by chemical substitution, however, such an MPB would be driven instead by chemical ordering. Based on the well-known enhanced piezoelectric responses near MPBs in common relaxor systems like PMN-PT and PZN-PT,[100] such a chemical-order-induced MPB may, in turn, produce enhanced response in $PbSc_{1/2}Ta_{1/2}O_3$ thin films.

9.2.2. Freestanding relaxor films

The work presented in Chapter 8 on freestanding PMN-PT thin films represents only a preliminary exploration of the properties of freestanding membranes of relaxors. Further studies on freestanding relaxor membranes and devices fabricated from such membranes stands to provide new insight into the coupling of relaxor properties to the lattice, as well as enable new, large responses in such materials. To begin, the observed change in frequency-dependent polarization response when PMN-PT heterostructures were released from the substrate requires further

understanding. While not immediately surprising that the polarization response is coupled to the elastic properties of the film, the occurrence of such a suppression at relatively low frequencies (20 kHz) compared to the time-scales simulated for lead-lead correlations in relaxors, and domain-wall motion in ferroelectrics (on the order of GHz)[328,329] is more puzzling. Such a slow response that is elastically coupled to the lattice may be suggestive of the collective rotation of polar nanodomains in PMN-PT, with long-range lattice deformation limited by clamping to the substrate. Observations of similar collective responses of polar structures has recently been reported for ferroelectric vortices in $(PbTiO_3)_n/(SrTiO_3)_n$ superlattices, where collective oscillations of ordered vortex arrays occur at frequencies more than an order of magnitude slower than the bulk mode of normal $PbTiO_3$.[330] Unlike these ordered polar vortices, however, performing similar studies on relaxors will be made more difficult due to the lack of well-defined structural signatures of the polar structure. Instead, *in situ* X-ray diffraction measurements that include probing both Bragg diffraction and the diffuse scattering under applied fields in both clamped and freestanding films may be used to examine the evolution of the polar structure with different elastic boundary conditions, illuminating both the average unit cell structure during polarization rotation, and the collective order of polar nanodomains. Yet, such measurements remain somewhat frequency limited. With advances in both spatial and temporal resolution, pushing the limit towards the expected dynamics of such nanodomains could be achieved by examination of the speckle-patterns produced in X-ray photon correlation spectroscopy (XPCS). Such experiments have been used to study spin fluctuations in disordered magnetic systems, but use of synchrotron X-ray sources has limited the speed of such measurements.[339] Novel methods leveraging coherent X-ray pulses of free electron lasers stand to push the time-resolution of such characterization approaches toward MHz regimes, allowing for time resolved measurement of fluctuating polar clusters.[340,341] Combining such experiments with *in situ* electrical testing can highlight high-frequency polar correlations in thin films.

Freestanding membranes also enable access to the expected large piezoelectric responses observed in bulk single crystals of various relaxor compositions. In this dissertation, enhancements in the achievable piezostrain were observed in freestanding membranes, achieving up to 0.5% piezostrain. Further optimization of the device heterostructure can enable further enhancements. For example, despite release from the substrate, the PMN-PT layer is still mechanically constrained by the epitaxial electrodes. Further reducing the volume fraction of electrode layer may further reduce the mechanical restriction of the piezoelectric lattice deformation. More interestingly, however, is the possibility of using the relatively simple expression presented in Chapter 8 to engineer specific strain states in the PMN-PT without the use of a substrate. Such substrate-free strain engineering could be used to simultaneously engineer polar nanodomain structures, for example the mixed-phase domain structures recently reported for PMN-PT under -0.75% epitaxial strain, while also avoiding the mechanical clamping from the substrate, and could be used to create even more susceptible PMN-PT heterostructures where large displacements are achievable with small driving fields. Finally, as both transfer and fabrication of freestanding films advances, the question of lateral scaling of devices can be readdressed in such membranes. In both

the studies of thickness-scaling of $PbSc_{1/2}Ta_{1/2}O_3$ films and PMN-PT membranes, suppressed effects compared to single-crystals have been observed, even in the absence of mechanical clamping of the substrate. As discussed in Chapter 8, the large aspect ratio of thin film samples could be one contributor to these suppressed responses.[102] As techniques for transferring and fabricating freestanding films advanced, one can envision fabrication of freestanding capacitor structures with dimensions on the order of hundreds of nanometers, rather than tens-to-hundreds of microns, reducing the aspect ratio of the device into regimes used for bulk single crystals. Such lateral scaling measurements can provide further routes to studying the impact of lateral clamping and aspect ratio on the ferroelectric and piezoelectric responses of relaxors.

9.3. Conclusions

In conclusion this dissertation aimed to explore the methods and impacts of lattice manipulation in disordered perovskite systems across two distinct technological domains. In these systems, which have been extensively studied to understand the compositional-dependence of their desired properties, it was found that controlling the boundary conditions of the lattice effected large changes in electronic and polar properties. In LSCF and LSCO, which have been proposed as next-generation cathodes for oxygen reduction reaction catalysis, it was found that controlling the surface orientation and strain can impact the chemical and electronic structures of the surface of the perovskite, in turn impacting their electrocatalytic performances. In the relaxor-ferroelectric systems $PbSc_{1/2}Ta_{1/2}O_3$ and $PbMg_{1/3}Nb_{2/3}O_3$-$PbTiO_3$, suppressed responses were measured for films at reduced thicknesses and that remained clamped to a substrate. The implications of these findings and suggestions for future work in these various perovskite systems highlight the importance of the boundary conditions of the lattice in dictating properties which are often desired for their respective applications and suggest new routes for engineering enhanced properties through lattice manipulation.

Appendix A:
X-ray Diffraction

Appendix A: X-ray Diffraction

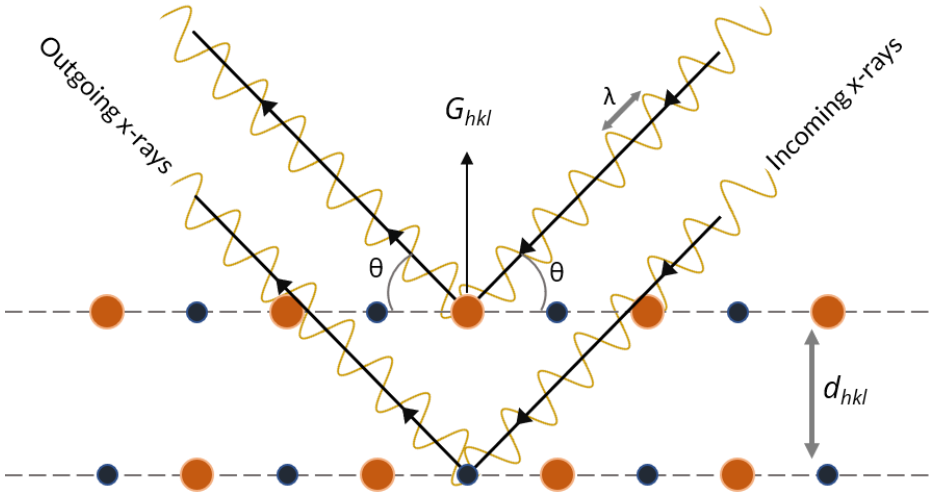

Figure A.1: Schematic depicting Bragg's law for diffraction of x-rays from crystal planes with spacing d_{hkl}.

The predominant method for characterizing the crystal structure of perovskite thin films is X-ray diffraction. There are many approaches for utilizing X-ray diffraction to understand various characteristics of a crystal structure, but almost all are built on the simple Bragg's law (Figure A.1):

$$n\lambda = 2d \sin\theta$$

where, λ is the wavelength of the light source (for this work that is typically copper $K\alpha_1$ X-rays which have a wavelength of 1.5459 Å), θ is the angle of incidence of the X-rays on the sample, n is an integer, and d is the spacing of the atomic planes. Two parallel waves incident on a crystal reflecting off adjacent, parallel atomic planes will constructively interfere only when the additional path travelled for each crystal plane is equal to an integer number of wavelengths. For single crystalline samples, in particular, there is an additional requirement that the scattering vector, G_{hkl}, of the incident X-rays must align with the normal vector of the planes being measured. Typically for thin films, this requires some alignment using a well-known d spacing of the substrate to correct for any sample mounting misalignment. Measurement of the intensity of the diffracted X-ray intensity produces diffraction patterns which can be analyzed to extract structural information.

A variety of structural features of the crystal can be probed using X-ray diffraction.[342] The most basic is a 2θ-omega scan, where the angle between the X-ray source and sample surface, ω, and the diffraction angle, θ, are changed simultaneously such that $\omega = \theta$ (Figure A.2a). This symmetric scan provides a measure of the various lattice d spacings present. For example, in an (001)-oriented thin film, a standard symmetric scan aligned to the 001-diffraction condition probes all lattice spacings parallel with the 00l planes (*e.g.*, 001, 002, 003, etc.). Alignment to alternative substrate peaks can provide access to other diffraction conditions. For example, using the χ-tilting axis, an (001)-oriented film could be tilted back by 54.7° to align to the 111-diffraction condition, and one can subsequently measure the 111, 222, and 333-diffraction conditions (Figure A.2b). Another common measurement is the ω-scan or rocking curve, where 2θ is fixed (*i.e.*, a single d spacing is probed) and the sample is swept in ω. This essentially probes the degree to which all lattice planes with the same d spacing are parallel, and is also called the *mosaicity* of the film. This

Appendix A: X-ray Diffraction

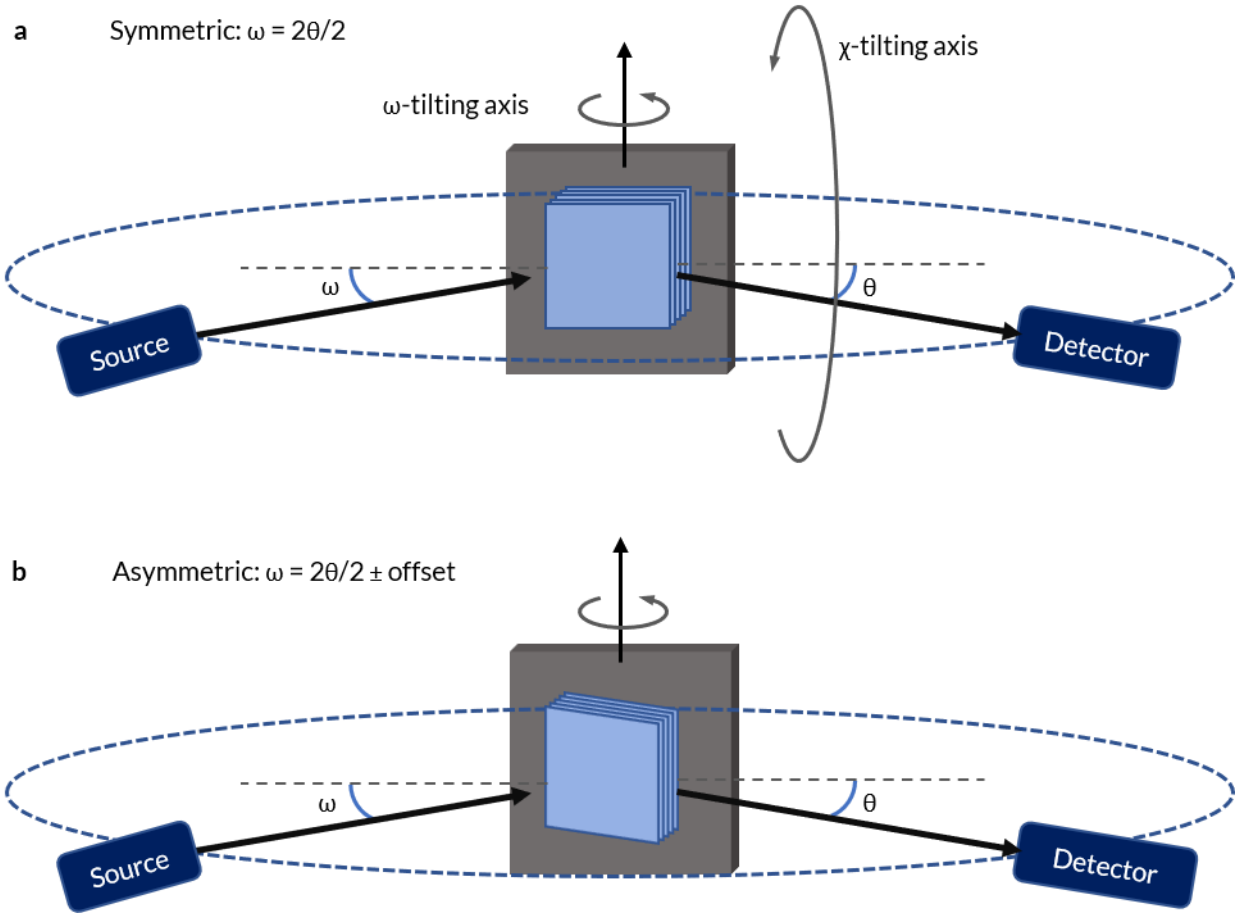

Figure A.2: Illustration of thin film diffraction geometries. a) A symmetric scan for probing lattice planes with scattering vector parallel to the samples surface normal. b) Asymmetric scans allow for probing lattice planes which are not parallel with the sample surface, typically used for measuring reciprocal space maps.

can be used as a measure of crystalline quality of the film. These measurements typically only probe lattice planes parallel with the film surface, but understanding the epitaxial relationship between film and substrate requires measurement of in-plane lattice information. Reciprocal space mapping (RSM) studies measure the intensity while simultaneously sweeping diffraction angles and sample alignment (Figure A.3). Practically, this can be performed by performing repeated 2θ measurements at a variety of ω offsets. Extracting in-plane lattice information requires alignment to a diffraction condition with non-zero *h* or *k* as a well as *l*. For the perovskite structure, the most common diffraction condition for this is the 103-diffraction condition, which is accessible via an asymmetric scan, where $\omega \neq \theta$. For coherently strained films, we expect that the in-plane lattice parameters for the film and substrate will be identical, and will fall on the same Q_x line in reciprocal space. On the other hand, a relaxed film can have different in-plane lattice parameters from the substrate, and will not have the same Q_x in reciprocal space. These are generalized explanations for cube-on-cube epitaxy which is the case for all films discussed in this dissertation, and therefore the 103-diffraction conditions of the film and substrate fall on the same plane in reciprocal space.

Appendix A: X-ray Diffraction

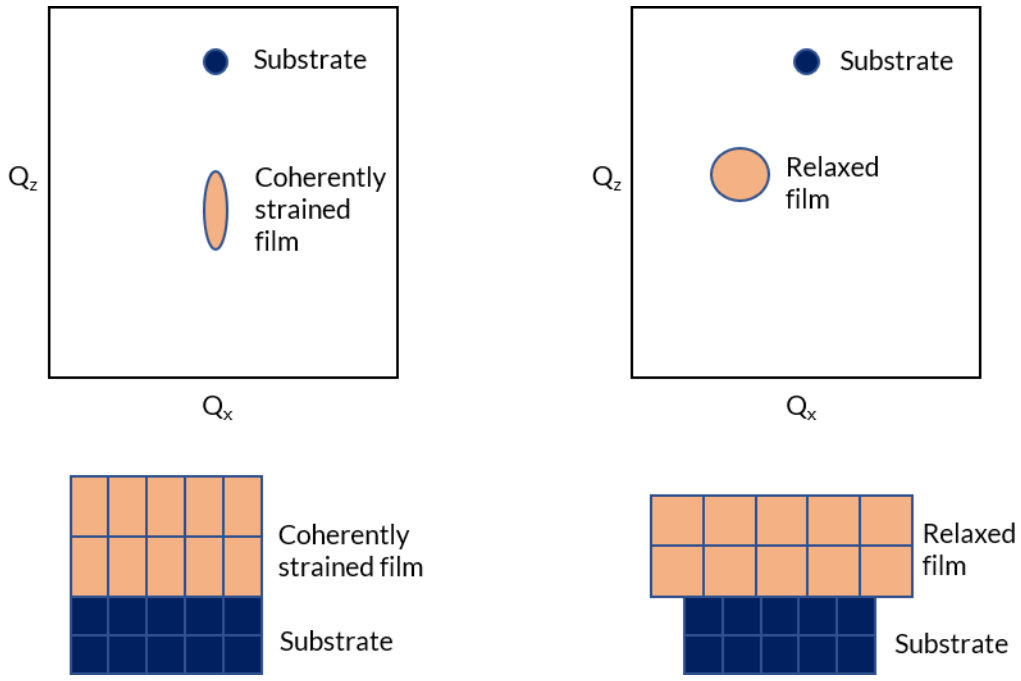

Figure A.3: Schematic depicting expected reciprocal space maps for coherently strained films where substrate and film have the same Q_x compared to relaxed films which have adopt a different lattice parameter and appear with different Q_x in reciprocal space.

Appendix B:
Atomic force microscopy

Appendix B: Atomic force microscopy

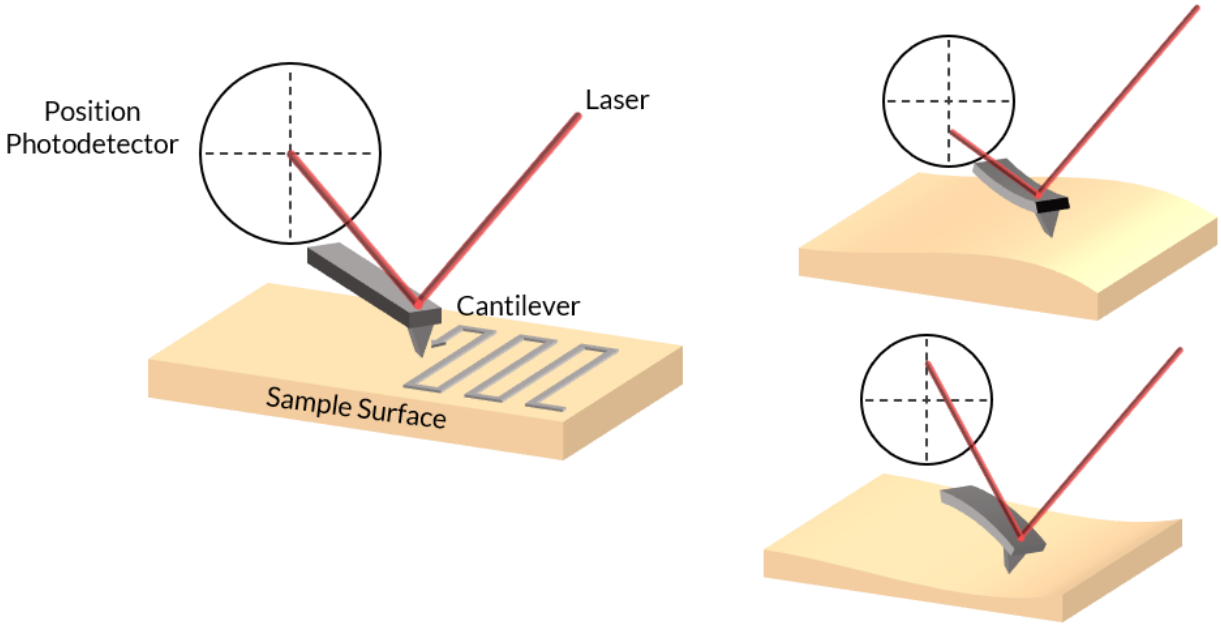

Figure B.1: Schematic of atomic force microscopy illustrating the laser beam reflected off a cantilever. As the surface height changes, bending of the tip is recording as displacement of the beam position on the photodetector.1

One of the most common methods of studying a thin-film surfaces is atomic force microscopy (AFM).[343] Here, a fabricated cantilever with a sharp tip (radius ~10-20 nm) is rastered over the surface of the film. A laser is reflected off the back of the cantilever to a photodetector, and bending/displacement of the cantilever as the tip interacts with the surface topography of the film causes deflection of the laser spot. AFM can be carried out in *contact mode*, where the tip is in physical contact with the film surface (essentially) at all times, but this can cause damage to both the film surface and blunting of the AFM tip. Instead, characterization of a film's topography is typically carried out in *tapping mode*, where the cantilever is excited at a resonant frequency (~300 kHz for the tips used in this work) just above, but not in contact with, the film's surface. As the cantilever is rastered over the surface of the film, changes in surface height are detected as a deflection of the cantilever from the electrostatic interaction of the cantilever tip with the surface of the film. The resulting data provides height information for the surface of the sample over areas on the order of 1-100 μm. AFM characterization is often used to benchmark growth during optimization of deposition parameters, with typical root-mean square surface roughness of 200-400 pm for a "smooth" film. In this work, AFM images were recorded using the MFP-3D (Asylum Research, Inc.) with silicon tips with an aluminum reflex coating on the detector side (Tap300Al-G, BudgetSensors).

Appendix C:
Device Fabrication

Appendix C: Device Fabrication

Study of the electrical properties of thin films requires advanced fabrication techniques to create epitaxial heterostructures in which well-defined stimuli can be applied and responses measured. For the study of dielectric and ferroelectric properties of relaxors, PLD-grown films were fabricated into epitaxial capacitor heterostructures. In this case, the material to be measured is synthesized between two electrically conducting layers. Ideally, an appropriate oxide material is chosen such that the desired epitaxial strain to be applied to the ferroelectric or dielectric layer is also achievable in the electrode layer.

Two primary methods of fabricating capacitor structures can be carried out, utilizing either subtractive methods involving removal of a top electrode deposited *in situ* with the remainder of the heterostructure, or additive methods where the top electrode is deposited into a pattern. Patterning of the film is carried out through standard photolithography techniques. Samples are first cleaned via ultrasonication in acetone for 5 min, before rinsing, drying and subsequent ultrasonication in isopropanol for 5 min. The sample is then dried at 95°C for 5 min before spin-coating. A photoresist (OCG-825) is first spin-coated approximately 1 µm thick onto the cleaned surface of the film. The photoresist is baked at 95°C for a minimum of 5 minutes. A mask consisting of chromium-coated glass with the desired pattern is then placed over the surface of the film before exposing the photoresist with a UV light source. The exposed photoresist is then developed, removing the photoresist that was exposed to UV light. For subtractive methods, the photoresist then serves as a protective layer for subsequent removal of the top electrode. A variety of methods can be used for removal. In this dissertation, two approaches are used to fabricate the top electrode. For $SrRuO_3$ top electrodes, a chemical wet-etch consisting of 0.1 M $NaIO_4$ is used

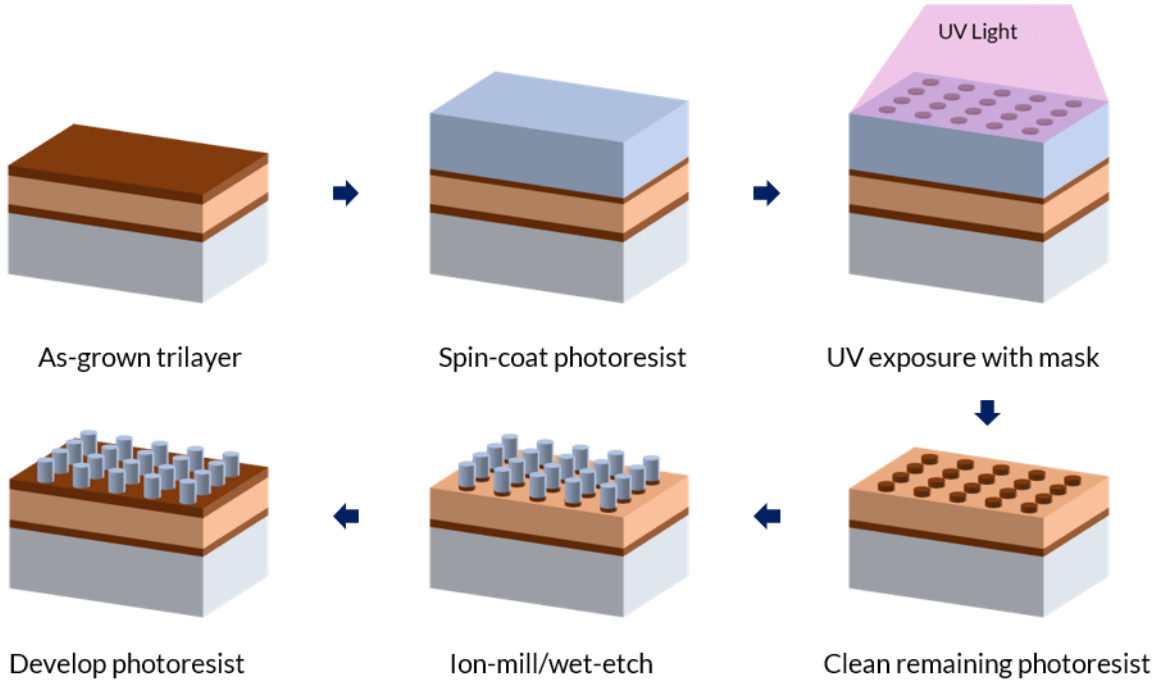

Figure C.1: Schematic of the process for subtractive fabrication of capacitor arrays via ion-milling or chemical-etching.

Appendix C: Device Fabrication

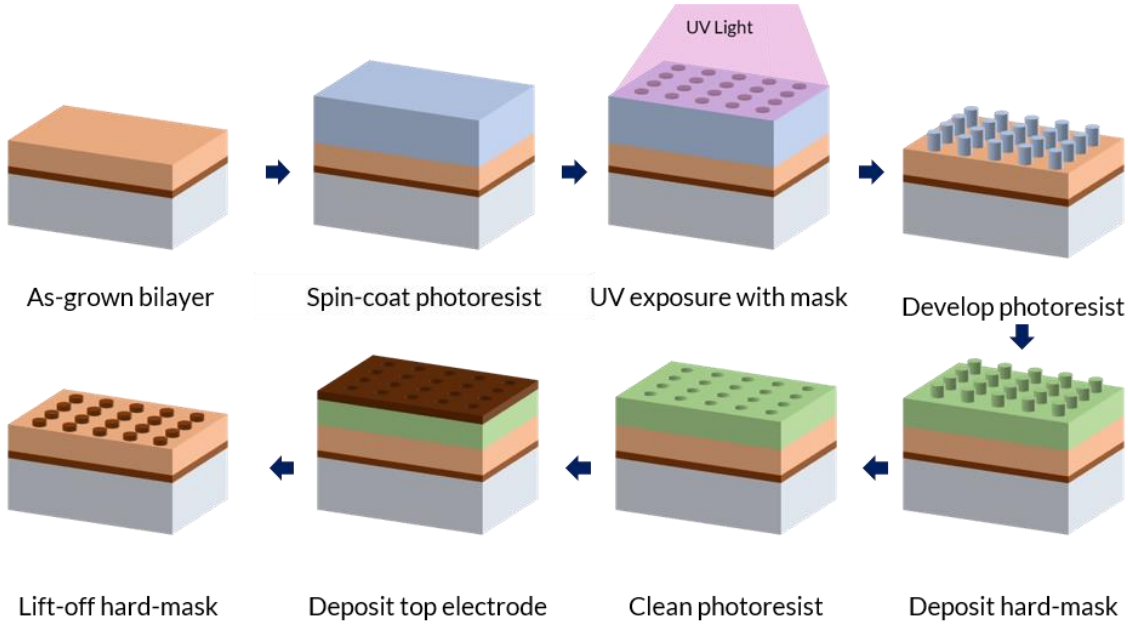

Figure C.2: Schematic depicting the additive fabrication of capacitor arrays using a hard mask.

to preferentially oxidize the ruthenium-site and dissolve $SrRuO_3$. The chemical wet etch must be timed such that the unprotected $SrRuO_3$ is completely etched, but the etchant has not begun to etch underneath the patterned photoresist. For $Ba_{0.5}Sr_{0.5}RuO_3$ top electrodes used in the PMN-PT films studied in Chapter 8, ion-milling was used to define top electrodes as well as the additional variants for study of lateral clamping. The process of ion-milling uses ionized argon gas that is accelerated towards the film, and the resulting bombardment sputters away the surface of the film. With a well-characterized mill rate, the depth of milling can be controlled to remove only the top electrode. After fabrication, the remaining photoresist is washed away, leaving an array of circular top electrodes, with a continuous, shared bottom electrode.

Rather than milling or etching a continuous top electrode layer, fabricated microelectrodes can be made by depositing an oxide thin film directly into a pre-patterned hard mask (Figure C.2).[165] Here, standard photolithography is used to pattern photoresist into the pattern of the final desired devices. The photoresist patterned film is then returned to the deposition chamber, and an amorphous layer of a chemically-etchable oxide layer (e.g., MgO or ZnO) is deposited at room temperature to avoid heating the photoresist. The photoresist is the washed from the heterostructure, leaving a patterned hard-oxide mask. The heterostructure with the patterned hard mask is returned again to the deposition chamber, and the top electrode is deposited at high temperature. Finally, the heterostructure is removed, and the hard mask is chemically etched to lift-off the excess electrode, leaving only the heterostructure with patterned electrodes. In Chapter 7, $PbSc_{1/2}Ta_{1/2}O_3$ both hard-mask and chemical etching were performed to fabricate capacitors, with similar results. Ultimately, wet-etching of top electrodes deposited *in situ* was used for all data presented in Chapter 7.

Additionally, a more complete schematic illustrating the fabrication of the epitaxial half-cells from Chapter 4 is provided (Figure C.3). Initially, a bilayer consisting of the $SrRuO_3$ counter-

electrode layer and the LSGM electrolyte are synthesized in situ. The $SrRuO_3$ bottom electrode layers were deposited from a ceramic target (Praxair) of the same chemistry deposited at a heater temperature of 700°C in a dynamic $\boldsymbol{p_{O_2}}$ of 100 mTorr with a laser fluence of 1.3 J/cm^2 and a repetition rate of 15 Hz. Following the growth of the $SrRuO_3$, the LSGM layers were deposited from a ceramic target of the same chemistry ($La_{0.9}Sr_{0.1}Ga_{0.95}Mg_{0.05}O_3$) at a heater temperature of 800°C in a dynamic $\boldsymbol{p_{O_2}}$ of 40 mTorr with a laser fluence of 1.7 J/cm^2 and repetition rate of 5 Hz. The resulting heterostructures are removed from the deposition chamber and photolithographically

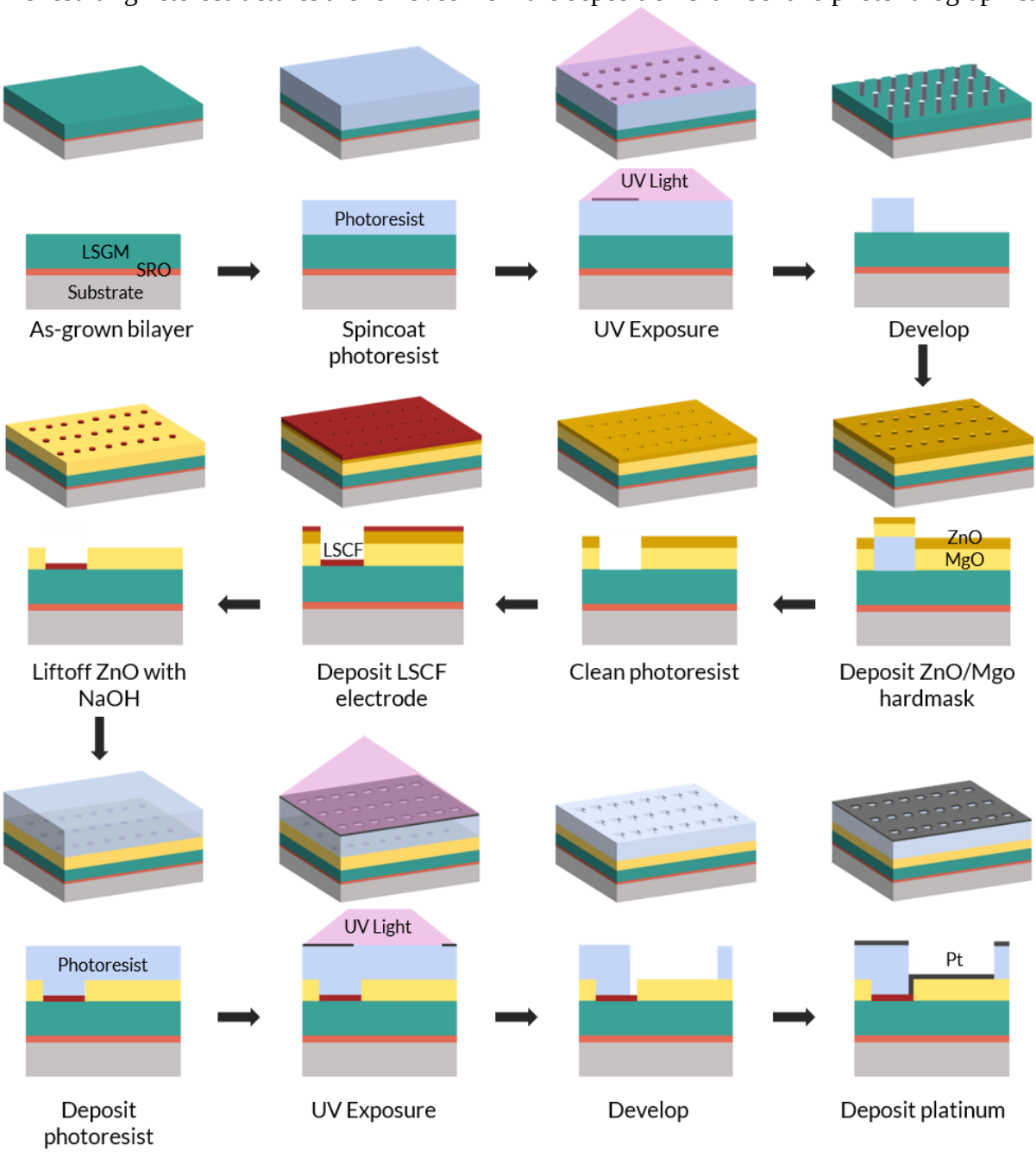

Figure C.40: Schematic illustrating the entire half-cell fabrication process. 3

patterned to define an array of circles that will ultimately define the LSCF active electrode. The patterned sample is then returned to the pulsed-laser deposition chamber, and a room-temperature deposition of 80 nm of MgO followed by 30 nm of ZnO is deposited using a laser fluence of 2.0 J/cm^2 at a repetition rate of 15 Hz and a pressure of 5 mTorr in both cases. Following ZnO/MgO deposition, the photoresist is removed with acetone and isopropanol rinses, removing excess ZnO/MgO, leaving a hard mask with holes to define the LSCF electrodes.[165] The bilayer with patterned hard mask is returned into the pulsed-laser-deposition chamber and subsequent high-temperature deposition is used to grow the LSCF top electrode, using the same conditions as those used for synthesis of single layer films described above. The excess and unwanted LSCF (i.e., that not in the circular capacitor areas) is removed via liftoff of the ZnO layer through a NaOH etch which selectively dissolves the ZnO, leaving behind the MgO-insulating layer, and the circular electrodes of LSCF. A final photolithography step is performed to define the platinum pads which are used for wire-bonded electrical connection to the LSCF electrode. Lift-off of the excess photoresist and platinum leaves the completed half-cell structures.

References:

1. Fernandez, A., Acharya, M., Lee, H., Schimpf, J., Jiang, Y., Lou, D., Tian, Z. & Martin, L. W. Thin-film Ferroelectrics. *Adv Mater* 2108841 (2022)

2. Bednorz, J. G. & Müller, K. A. Perovskite-type oxides—The new approach to high-Tc superconductivity. *Rev Mod Phys* 60, 585–600 (1988).

3. Ramirez, A. P. Colossal magnetoresistance. *J Phys Condens Matter* 9, 8171 (1997).

4. Hwang, J., Rao, R. R., Giordano, L., Katayama, Y., Yu, Y. & Shao-Horn, Y. Perovskites in catalysis and electrocatalysis. *Science* 358, 751–756 (2017).

5. Peña, M. A. & Fierro, J. L. G. Chemical Structures and Performance of Perovskite Oxides. *Chem Rev* 101, 1981–2018 (2001).

6. Imada, M., Fujimori, A. & Tokura, Y. Metal-insulator transitions. *Rev Mod Phys* 70, 1039–1263 (1998).

7. Tokura, Y. & Nagaosa, N. Orbital Physics in Transition-Metal Oxides. *Science* 288, 462–468 (2000).

8. Whatmore, R. Pyroelectric devices and materials. *Reports on Progress in Physics* 49, 1335 (1986).

9. Moya, X., Kar-Narayan, S. & Mathur, N. D. Caloric materials near ferroic phase transitions. *Nat Mater* 13, 439–450 (2014).

10. Muralt, P., Polcawich, R. G. & Trolier-McKinstry, S. Piezoelectric Thin Films for Sensors, Actuators, and Energy Harvesting. *MRS Bull* 34, 658–664 (2009).

11. Noheda, B., Gonzalo, J. A., Cross, L. E., Guo, R., Park, S.-E., Cox, D. E. & Shirane, G. Tetragonal-to-monoclinic phase transition in a ferroelectric perovskite: The structure of PbZr0.52Ti0.48O3. *Phys Rev B* 61, 8687–8695 (2000).

12. Habermeier, H.-U. Thin films of perovskite-type complex oxides. *Mater Today* 10, 34–43 (2007).

13. Damodaran, A. R., Agar, J. C., Pandya, S., Chen, Z., Dedon, L., Xu, R., Apgar, B., Saremi, S. & Martin, L. W. New modalities of strain-control of ferroelectric thin films. *J Phys Condens Matter* 28, 263001 (2016).

14. Hwang, J., Feng, Z., Charles, N., Wang, X. R., Lee, D., Stoerzinger, K. A., Muy, S., Rao, R. R., Lee, D., Jacobs, R., Morgan, D. & Shao-Horn, Y. Tuning perovskite oxides by strain: Electronic structure, properties, and functions in (electro)catalysis and ferroelectricity. *Mater Today* (2019)

15. Zubko, P., Gariglio, S., Gabay, M., Ghosez, P. & Triscone, J.-M. Interface Physics in Complex Oxide Heterostructures. *Annu Rev Conden Ma P* 2, 141–165 (2011).

16. Lee, H. G., Wang, L., Si, L., He, X., Porter, D. G., Kim, J. R., Ko, E. K., Kim, J., Park, S. M., Kim, B., Wee, A. T. S., Bombardi, A., Zhong, Z. & Noh, T. W. Atomic-Scale Metal–Insulator Transition in $SrRuO_3$ Ultrathin Films Triggered by Surface Termination Conversion. *Adv Mater* 32, 1905815 (2020).

17. Fong, D. D., Stephenson, G. B., Streiffer, S. K., Eastman, J. A., Auciello, O., Fuoss, P. H. & Thompson, C. Ferroelectricity in Ultrathin Perovskite Films. *Science* 304, 1650–1653 (2004).

18. Xu, R., Liu, S., Saremi, S., Gao, R., Wang, J. J., Hong, Z., Lu, H., Ghosh, A., Pandya, S., Bonturim, E., Chen, Z. H., Chen, L. Q., Rappe, A. M. & Martin, L. W. Kinetic control of tunable multi-state switching in ferroelectric thin films. *Nat Commun* 10, 1282 (2019).

19. Pesquera, D., Herranz, G., Barla, A., Pellegrin, E., Bondino, F., Magnano, E., Sánchez, F. & Fontcuberta, J. Surface symmetry-breaking and strain effects on orbital occupancy in transition metal perovskite epitaxial films. *Nat Commun* 3, 1189 (2012).

20. Wu, M., Benckiser, E., Haverkort, M. W., Frano, A., Lu, Y., Nwankwo, U., Brück, S., Audehm, P., Goering, E., Macke, S., Hinkov, V., Wochner, P., Christiani, G., Heinze, S., Logvenov, G., Habermeier, H.-U. & Keimer, B. Strain and composition dependence of orbital polarization in nickel oxide superlattices. *Phys Rev B* 88, 125124 (2013).

21. Bera, D., Qian, L., Tseng, T.-K. & Holloway, P. H. Quantum Dots and Their Multimodal Applications: A Review. *Materials* 3, 2260–2345 (2010).

22. Koster, G., Huijben, M. & Rjinders, G. *Epitaxial Growth of Complex Metal Oxides*. (Elsevier, 2015). doi:10.1016/c2013-0-16499-9.

23. Chambers, S. A. Epitaxial Growth and Properties of Doped Transition Metal and Complex Oxide Films. *Adv Mater* 22, 219–248 (2010).

24. Christen, H. & Matter, E.-G. of. Recent advances in pulsed-laser deposition of complex oxides. (2008).

25. Eason, R. Pulsed Laser Deposition of Thin Films. (2018) doi:10.1002/0470052120.

26. Cheung, J. T. & Sankur, H. Growth of thin films by laser-induced evaporation. *Crit Rev Solid State* 15, 63–109 (1988).

27. Cheung, J. & Horwitz, J. Pulsed Laser Deposition History and Laser-Target Interactions. *MRS Bull* 17, 30–36 (1992).

28. Chrisey, D. B. & Hubler, G. K. *Pulsed laser deposition of thin films*. (Wiley-VCH, 2003).

29. Smith, H. M. & Turner, A. F. Vacuum Deposited Thin Films Using a Ruby Laser. *Appl Optics* 4, 147 (1965).

30. Dijkkamp, D., Venkatesan, T., Wu, X. D., Shaheen, S. A., Jisrawi, N., Min-Lee, Y. H., McLean, W. L. & Croft, M. Preparation of Y-Ba-Cu oxide superconductor thin films using pulsed laser evaporation from high T_c bulk material. *Appl Phys Lett* 51, 619–621 (1987).

31. Wu, X. D., Dijkkamp, D., Ogale, S. B., Inam, A., Chase, E. W., Miceli, P. F., Chang, C. C., Tarascon, J. M. & Venkatesan, T. Epitaxial ordering of oxide superconductor thin films on (100) $SrTiO_3$ prepared by pulsed laser evaporation. *Appl Phys Lett* 51, 861–863 (1987).

32. Breckenfeld, E., Wilson, R. & Letters, M.-L. Effect of growth induced (non) stoichiometry on the thermal conductivity, permittivity, and dielectric loss of $LaAlO_3$ films. (2013).

33. Breckenfeld, E., Wilson, R., Karthik, J., Damodaran, A. R., Cahill, D. G. & Martin, L. W. Effect of Growth Induced (Non)Stoichiometry on the Structure, Dielectric Response, and Thermal Conductivity of $SrTiO_3$ Thin Films. *Chem Mater* 24, 331–337 (2012).

34. Damodaran, A. R., Breckenfeld, E., Chen, Z., Lee, S. & Martin, L. W. Enhancement of Ferroelectric Curie Temperature in $BaTiO_3$ Films via Strain-Induced Defect Dipole Alignment. *Adv Mater* 26, 6341–6347 (2014).

35. Dasgupta, A., Saremi, S., Ruijuan, X., Dedon, L. R., Pandya, S., Damodaran, A. R. & Martin, L. W. Nonstoichiometry, structure, and properties of $Ba_{1-x}TiO_y$ thin films. *J Mater Chem C* 6, 10751–10759 (2018).

36. Dedon, L. R., Saremi, S., Chen, Z., Damodaran, A. R., Apgar, B. A., Gao, R. & Martin, L. W. Nonstoichiometry, Structure, and Properties of $BiFeO_3$ Films. *Chemistry of Materials* 28, (2016).

37. Saremi, S., Xu, R., Dedon, L. R. & Advanced …, M.-J. Enhanced electrical resistivity and properties via ion bombardment of ferroelectric thin films. *Advanced Materials* (2016) doi:10.1002/adma.201603968.

38. Saito, K., Kurosawa, T., Akai, T., Oikawa, T. & Funakubo, H. Structural characterization and 90° domain contribution to ferroelectricity of epitaxial $Pb(Zr_{0.35}Ti_{0.65})O_3$ thin films. *J Appl Phys* 93, 545–550 (2003).

39. Xu, R., Liu, S., Grinberg, I., Karthik, J., Damodaran, A. R., Rappe, A. M. & Martin, L. W. Ferroelectric polarization reversal via successive ferroelastic transitions. *Nat Mater* 14, 79–86 (2015).

40. Xu, R., Zhang, J., Chen, Z. & Martin, L. W. Orientation-dependent structural phase diagrams and dielectric properties of $PbZr_{1-x}Ti_xO_3$ polydomain thin films. *Phys Rev B* 91, 144106 (2015).

41. Xu, R., Gao, R., Reyes-Lillo, S. E., Saremi, S., Dong, Y., Lu, H., Chen, Z., Lu, X., Qi, Y., Hsu, S.-L., Damodaran, A. R., Zhou, H., Neaton, J. B. & Martin, L. W. Reducing Coercive-Field Scaling in Ferroelectric Thin Films via Orientation Control. *ACS Nano* 12, (2018).

42. Chu, Y. -H., Cruz, M. P., Yang, C. -H., Martin, L. W., Yang, P. -L., Zhang, J. -X., Lee, K., Yu, P., Chen, L. -Q. & Ramesh, R. Domain Control in Multiferroic BiFeO3 through Substrate Vicinality. *Adv Mater* 19, 2662–2666 (2007).

43. Noguera, C. Polar oxide surfaces. *J Phys Condens Matter* 12, R367–R410 (2000).

44. Tasker, P. W. The stability of ionic crystal surfaces. *J Phys C Solid State Phys* 12, 4977 (2001).

45. Liang, Y. & Bonnell, D. A. Atomic structures of reduced $SrTiO_3$(001) surfaces. *Surf Sci* 285, L510–L516 (1993).

46. Katsube, D. & Abe, M. High-resolution imaging of $LaAlO_3$ (100)–(1 × 4) reconstructed surface using non-contact atomic force microscopy. *Appl Phys Lett* 113, 031601 (2018).

47. Brunen, J. & Zegenhagen, J. Investigation of the $SrTiO_3$ (110) surface by means of LEED, scanning tunneling microscopy and Auger spectroscopy. *Surf Sci* 389, 349–365 (1997).

48. Druce, J., Téllez, H., Burriel, M., Sharp, M. D., Fawcett, L. J., Cook, S. N., McPhail, D. S., Ishihara, T., Brongersma, H. H. & Kilner, J. A. Surface termination and subsurface restructuring of perovskite-based solid oxide electrode materials. *Energy Environ Sci* 7, 3593–3599 (2014).

49. Dulli, H., Dowben, P. A., Liou, S.-H. & Plummer, E. W. Surface segregation and restructuring of colossal-magnetoresistant manganese perovskites $La_{0.65}Sr_{0.35}MnO_3$. *Phys Rev B* 62, R14629–R14632 (2000).

50. Fearn, S., Rossiny, J. C. H., Kilner, J. A. & Evans, J. R. G. Measurement of oxygen transport in $La_{0.8}Sr_{0.2}MnO_3$ perovskite grains. *Solid State Ionics* 211, 51–57 (2012).

51. Kerman, K., Ko, C. & Ramanathan, S. Orientation dependent oxygen exchange kinetics on single crystal $SrTiO_3$ surfaces. *Phys Chem Chem Phys* 14, 11953–11960 (2012).

52. Miyahara, Y., Miyazaki, K., Fukutsuka, T. & Abe, T. Influence of Surface Orientation on the Catalytic Activities of $La_{0.8}Sr_{0.2}CoO_3$ Crystal Electrodes for Oxygen Reduction and Evolution Reactions. *Chemelectrochem* 3, 214–217 (2016).

53. Yan, L., Balasubramaniam, K. R., Wang, S., Du, H. & Salvador, P. A. Effects of crystallographic orientation on the oxygen exchange rate of $La_{0.7}Sr_{0.3}MnO_3$ thin films. *Solid State Ionics* 194, 9–16 (2011).

54. Stoerzinger, K. A., Qiao, L., Biegalski, M. D. & Shao-Horn, Y. Orientation-Dependent Oxygen Evolution Activities of Rutile IrO_2 and RuO_2. *J Phys Chem Lett* 5, 1636–1641 (2014).

55. Stoerzinger, K. A., Diaz-Morales, O., Kolb, M., Rao, R. R., Frydendal, R., Qiao, L., Wang, X. R., Halck, N. B., Rossmeisl, J., Hansen, H. A., Vegge, T., Stephens, I. E. L., Koper, M. T. M. & Shao-Horn, Y. Orientation-Dependent Oxygen Evolution on RuO2 without Lattice Exchange. *ACS Energy Lett* 2, (2017).

56. Schlom, D. G., Chen, L.-Q., Eom, C.-B., Rabe, K. M., Streiffer, S. K. & Triscone, J.-M. Strain Tuning of Ferroelectric Thin Films*. *Annu Rev Mater Res* 37, 589–626 (2007).

57. Damodaran, A. R., Pandya, S., Agar, J. C., Cao, Y., Vasudevan, R. K., Xu, R., Saremi, S., Li, Q., Kim, J., McCarter, M. R., Dedon, L. R., Angsten, T., Balke, N., Jesse, S., Asta, M., Kalinin, S. V. & Martin, L. W. Three-State Ferroelastic Switching and Large Electromechanical Responses in $PbTiO_3$ Thin Films. *Adv Mater* 29, 1702069 (2017).

58. Zeches, R. J., Rossell, M. D., Zhang, J. X., Hatt, A. J., He, Q., Yang, C.-H., Kumar, A., Wang, C. H., Melville, A., Adamo, C., Sheng, G., Chu, Y.-H., Ihlefeld, J. F., Erni, R., Ederer, C., Gopalan, V., Chen, L. Q., Schlom, D. G., Spaldin, N. A., *et al.* A Strain-Driven Morphotropic Phase Boundary in $BiFeO_3$. *Science* 326, 977–980 (2009).

59. Haeni, J. H., Irvin, P., Chang, W., Uecker, R., Reiche, P., Li, Y. L., Choudhury, S., Tian, W., Hawley, M. E., Craigo, B., Tagantsev, A. K., Pan, X. Q., Streiffer, S. K., Chen, L. Q., Kirchoefer, S. W., Levy, J. & Schlom, D. G. Room-temperature ferroelectricity in strained $SrTiO_3$. *Nature* 430, 758–761 (2004).

60. Zhang, J. X., Xiang, B., He, Q., Seidel, J., Zeches, R. J., Yu, P., Yang, S. Y., Wang, C. H., Chu, Y.-H., Martin, L. W., Minor, A. M. & Ramesh, R. Large field-induced strains in a lead-free piezoelectric material. *Nat Nanotechnol* 6, 98 (2011).

61. Takamura, Y., Chopdekar, R. V., Arenholz, E. & Suzuki, Y. Control of the magnetic and magnetotransport properties of $La_{0.67}Sr_{0.33}MnO_3$ thin films through epitaxial strain. *Appl Phys Lett* 92, 162504 (2008).

62. Aruta, C., Ghiringhelli, G., Tebano, A., Boggio, N. G., Brookes, N. B., Medaglia, P. G. & Balestrino, G. Strain induced x-ray absorption linear dichroism in $La_{0.7}Sr_{0.3}MnO_3$ thin films. *Phys Rev B* 73, 235121 (2006).

63. Dho, J., Kim, Y. N., Hwang, Y. S., Kim, J. C. & Hur, N. H. Strain-induced magnetic stripe domains in $La_{0.7}Sr_{0.3}MnO_3$ thin films. *Appl Phys Lett* 82, 1434–1436 (2003).

64. Catalano, S., Gibert, M., Fowlie, J., Íñiguez, J., Triscone, J.-M. & Kreisel, J. Rare-earth nickelates $RNiO_3$: thin films and heterostructures. *Rep Prog Phys* 81, 046501 (2018).

65. Mikheev, E., Hauser, A. J., Himmetoglu, B., Moreno, N. E., Janotti, A., Walle, C. G. V. de & Stemmer, S. Tuning bad metal and non-Fermi liquid behavior in a Mott material: Rare-earth nickelate thin films. *Sci Adv* 1, e1500797 (2015).

66. Guo, E.-J., Desautels, R. D., Keavney, D., Herklotz, A., Ward, T. Z., Fitzsimmons, M. R. & Lee, H. N. Switchable orbital polarization and magnetization in strained $LaCoO_3$ films. *Phys Rev Mater* 3, 014407 (2019).

67. Pinta, C., Fuchs, D., Merz, M., Wissinger, M., Arac, E., Löhneysen, H. v., Samartsev, A., Nagel, P. & Schuppler, S. Suppression of spin-state transition in epitaxially strained $LaCoO_3$. *Phys Rev B* 78, 174402 (2008).

68. Pesquera, D., Barla, A., Wojcik, M., Jedryka, E., Bondino, F., Magnano, E., Nappini, S., Gutiérrez, D., Radaelli, G., Herranz, G., Sánchez, F. & Fontcuberta, J. Strain-Driven Orbital and Magnetic Orders and Phase Separation in Epitaxial Half-Doped Manganite Films for Tunneling Devices. *Phys Rev Appl* 6, 034004 (2016).

69. Rogge, P. C., Chandrasena, R. U., Cammarata, A., Green, R. J., Shafer, P., Lefler, B. M., Huon, A., Arab, A., Arenholz, E., Lee, H. N., Lee, T.-L., Nemšák, S., Rondinelli, J. M., Gray, A. X. & May, S. J. Electronic structure of negative charge transfer $CaFeO_3$ across the metal-insulator transition. *Phys Rev Mater* 2, 015002 (2018).

70. Rogge, P. C., Green, R. J., Shafer, P., Fabbris, G., Barbour, A. M., Lefler, B. M., Arenholz, E., Dean, M. P. M. & May, S. J. Inverted orbital polarization in strained correlated oxide films. *Phys Rev B* 98, 201115 (2018).

71. Cazorla, C. Lattice Effects on the Formation of Oxygen Vacancies in Perovskite Thin Films. *Phys Rev Appl* 7, 044025 (2017).

72. Petrie, J. R., Mitra, C., Jeen, H., Choi, W. S., Meyer, T. L., Reboredo, F. A., Freeland, J. W., Eres, G. & Lee, H. N. Strain Control of Oxygen Vacancies in Epitaxial Strontium Cobaltite Films. *Adv Funct Mater* 26, 1564–1570 (2016).

73. Herklotz, A., Lee, D., Guo, E.-J., Meyer, T. L., Petrie, J. R. & Lee, H. N. Strain coupling of oxygen non-stoichiometry in perovskite thin films. *J Phys Condens Matter* 29, 493001 (2017).

74. Lan, Q. Q., Shen, X., Yang, H. W., Zhang, H. R., Zhang, J., Guan, X. X., Yao, Y., Wang, Y. G., Yu, R. C., Peng, Y. & Sun, J. R. Correlation between magnetism and "dark stripes" in strained $La_{1-x}Sr_xCoO_3$ epitaxial films ($0 \leq x \leq 0.1$). *Appl Phys Lett* 107, 242404 (2015).

75. Gu, Y., Song, C., Zhang, H., Wang, Z., Cui, B., Li, F., Peng, J., Saleem, M. S., Wang, G., Zhong, X., Wang, F., Ma, S., Sun, J., Liu, W., Pan, F. & Zhang, Z. Controllable oxygen

vacancies, orbital occupancy and magnetic ordering in $SrCoO_{3-\delta}$ films. *J Magn Magn Mater* 454, 228–236 (2018).

76. Walter, J., Bose, S., Cabero, M., Yu, G., Greven, M., Varela, M. & Leighton, C. Perpendicular magnetic anisotropy via strain-engineered oxygen vacancy ordering in epitaxial $La_{1-x}Sr_xCoO_{3-\delta}$. *Phys Rev Mater* 2, 111404 (2018).

77. Choi, W. S., Kwon, J.-H., Jeen, H., Hamann-Borrero, J. E., Radi, A., Macke, S., Sutarto, R., He, F., Sawatzky, G. A., Hinkov, V., Kim, M. & Lee, H. N. Strain-Induced Spin States in Atomically Ordered Cobaltites. *Nano Lett* 12, 4966–4970 (2012).

78. Lee, D., Jacobs, R., Jee, Y., Seo, A., Sohn, C., Ievlev, A. V., Ovchinnikova, O. S., Huang, K., Morgan, D. & Lee, H. N. Stretching Epitaxial $La_{0.6}Sr_{0.4}CoO_{3-\delta}$ for Fast Oxygen Reduction. *J Phys Chem C* 121, 25651–25658 (2017).

79. Petrie, J. R., Jeen, H., Barron, S. C., Meyer, T. L. & Lee, H. N. Enhancing Perovskite Electrocatalysis through Strain Tuning of the Oxygen Deficiency. *J Am Chem Soc* 138, 7252–7255 (2016).

80. Stoerzinger, K. A., Choi, W. S., Jeen, H., Lee, H. N. & Shao-Horn, Y. Role of Strain and Conductivity in Oxygen Electrocatalysis on $LaCoO_3$ Thin Films. *J Phys Chem Lett* 6, 487–492 (2015).

81. Kubicek, M., Cai, Z., Ma, W., Yildiz, B., Hutter, H. & Fleig, J. Tensile Lattice Strain Accelerates Oxygen Surface Exchange and Diffusion in $La_{1-x}Sr_xCoO_{3-\delta}$ Thin Films. *Acs Nano* 7, 3276–3286 (2013).

82. Koo, B., Kwon, H., Kim, Y., Seo, H. G., Han, J. W. & Jung, W. Enhanced oxygen exchange of perovskite oxide surfaces through strain-driven chemical stabilization. *Energ Environ Sci* 11, 71–77 (2017).

83. Petrie, J. R., Cooper, V. R., Freeland, J. W., Meyer, T. L., Zhang, Z., Lutterman, D. A. & Lee, H. N. Enhanced Bifunctional Oxygen Catalysis in Strained $LaNiO_3$ Perovskites. *J Am Chem Soc* 138, 2488–2491 (2016).

84. Wang, L., Stoerzinger, K. A., Chang, L., Yin, X., Li, Y., Tang, C. S., Jia, E., Bowden, M. E., Yang, Z., Abdelsamie, A., You, L., Guo, R., Chen, J., Rusydi, A., Wang, J., Chambers, S. A. & Du, Y. Strain Effect on Oxygen Evolution Reaction Activity of Epitaxial $NdNiO_3$ Thin Films. *Acs Appl Mater Inter* 11, 12941–12947 (2019).

85. Ajayan, P., Kim, P. & Banerjee, K. Two-dimensional van der Waals materials. *Phys Today* 69, 38–44 (2016).

86. Yoshimatsu, K., Okabe, T., Kumigashira, H., Okamoto, S., Aizaki, S., Fujimori, A. & Oshima, M. Dimensional-Crossover-Driven Metal-Insulator Transition in $SrVO_3$ Ultrathin Films. *Phys Rev Lett* 104, 147601 (2010).

87. Scherwitzl, R., Gariglio, S., Gabay, M., Zubko, P., Gibert, M. & Triscone, J.-M. Metal-Insulator Transition in Ultrathin $LaNiO_3$ Films. *Phys Rev Lett* 106, 246403 (2011).

88. Liao, Z., Li, F., Gao, P., Li, L., Guo, J., Pan, X., Jin, R., Plummer, E. W. & Zhang, J. Origin of the metal-insulator transition in ultrathin films of $La_{2/3}Sr_{1/3}MnO_3$. *Phys Rev B* 92, 125123 (2015).

89. Lee, H. N., Nakhmanson, S. M., Chisholm, M. F., Christen, H. M., Rabe, K. M. & Vanderbilt, D. Suppressed Dependence of Polarization on Epitaxial Strain in Highly Polar Ferroelectrics. *Phys Rev Lett* 98, 217602 (2006).

90. Catalan, G., Béa, H., Fusil, S., Bibes, M., Paruch, P., Barthélémy, A. & Scott, J. F. Fractal Dimension and Size Scaling of Domains in Thin Films of Multiferroic $BiFeO_3$. *Phys Rev Lett* 100, 027602 (2008).

91. Junquera, J. & Ghosez, P. Critical thickness for ferroelectricity in perovskite ultrathin films. *Nature* 422, nature01501 (2003).

92. Lee, D., Lu, H., Gu, Y., Choi, S.-Y., Li, S.-D., Ryu, S., Paudel, T. R., Song, K., Mikheev, E., Lee, S., Stemmer, S., Tenne, D. A., Oh, S. H., Tsymbal, E. Y., Wu, X., Chen, L.-Q., Gruverman, A. & Eom, C. B. Emergence of room-temperature ferroelectricity at reduced dimensions. *Science* 349, 1314–1317 (2015).

93. Takenaka, H., Grinberg, I., Liu, S. & Rappe, A. M. Slush-like polar structures in single-crystal relaxors. *Nature* 546, 391–395 (2017).

94. Fu, H. & Cohen, R. E. Polarization rotation mechanism for ultrahigh electromechanical response in single-crystal piezoelectrics. *Nature* 403, 281-283 (2000).

95. Phelan, D., Stock, C., Rodriguez-Rivera, J. A., Chi, S., Leão, J., Long, X., Xie, Y., Bokov, A. A., Ye, Z.-G., Ganesh, P. & Gehring, P. M. Role of random electric fields in relaxors. *Proc National Acad Sci* 111, 1754–1759 (2014).

96. Carreaud, J., Gemeiner, P., Kiat, J. M., Dkhil, B., Bogicevic, C., Rojac, T. & Malic, B. Size-driven relaxation and polar states in $PbMg_{1/3}Nb_{2/3}O_3$-based system. *Phys Rev B* 72, 174115 (2005).

97. Randall, C. A., Hilton, A. D., Barber, D. J. & Shrout, T. R. Extrinsic contributions to the grain size dependence of relaxor ferroelectric $Pb(Mg_{1/3}Nb_{2/3})O_3$: $PbTiO_3$ ceramics. *J Mater Res* 8, 880–884 (1993).

98. Papet, P., Dougherty, J. P. & Shrout, T. R. Particle and grain size effects on the dielectric behavior of the relaxor ferroelectric $Pb(Mg_{1/3}Nb_{2/3})O_3$. *J Mater Res* 5, 2902–2909 (1990).

99. Ihlefeld, J. F., Harris, D. T., Keech, R., Jones, J. L., Maria, J. & Trolier-McKinstry, S. Scaling Effects in Perovskite Ferroelectrics: Fundamental Limits and Process-Structure-Property Relations. *J Am Ceram Soc* 99, 2537–2557 (2016).

100. Park, S.-E. & Shrout, T. R. Ultrahigh strain and piezoelectric behavior in relaxor based ferroelectric single crystals. *J Appl Phys* 82, 1804–1811 (1997).

101. Baek, S. H., Park, J., Kim, D. M., Aksyuk, V. A., Das, R. R., Bu, S. D., Felker, D. A., Lettieri, J., Vaithyanathan, V., Bharadwaja, S. S. N., Bassiri-Gharb, N., Chen, Y. B., Sun, H. P., Folkman, C. M., Jang, H. W., Kreft, D. J., Streiffer, S. K., Ramesh, R., Pan, X. Q., *et al.* Giant Piezoelectricity on Si for Hyperactive MEMS. *Science* 334, 958–961 (2011).

102. Keech, R., Shetty, S., Kuroda, M. A., Liu, X. H., Martyna, G. J., Newns, D. M. & Trolier-McKinstry, S. Lateral scaling of $Pb(Mg_{1/3}Nb_{2/3})O_3$-$PbTiO_3$ thin films for piezoelectric logic applications. *J Appl Phys* 115, 234106 (2014).

103. Nagarajan, V., Roytburd, A., Stanishevsky, A., Prasertchoung, S., Zhao, T., Chen, L., Melngailis, J., Auciello, O. & Ramesh, R. Dynamics of ferroelastic domains in ferroelectric thin films. *Nat Mater* 2, 43–47 (2002).

104. Pesquera, D., Parsonnet, E., Qualls, A., Xu, R., Gubser, A. J., Kim, J., Jiang, Y., Velarde, G., Huang, Y., Hwang, H. Y., Ramesh, R. & Martin, L. W. Beyond Substrates: Strain Engineering of Ferroelectric Membranes. *Adv Mater* 32, 2003780 (2020).

105. Lu, D., Baek, D. J., Hong, S. S., Kourkoutis, L. F., Hikita, Y. & Hwang, H. Y. Synthesis of freestanding single-crystal perovskite films and heterostructures by etching of sacrificial water-soluble layers. *Nat Mater* 15, 1255–1260 (2016).

106. Hong, S. S., Gu, M., Verma, M., Harbola, V., Wang, B. Y., Lu, D., Vailionis, A., Hikita, Y., Pentcheva, R., Rondinelli, J. M. & Hwang, H. Y. Extreme tensile strain states in $La_{0.7}Ca_{0.3}MnO_3$ membranes. *Science* 368, 71–76 (2020).

107. Peng, B., Peng, R.-C., Zhang, Y.-Q., Dong, G., Zhou, Z., Zhou, Y., Li, T., Liu, Z., Luo, Z., Wang, S., Xia, Y., Qiu, R., Cheng, X., Xue, F., Hu, Z., Ren, W., Ye, Z.-G., Chen, L.-Q., Shan, Z., *et al.* Phase transition enhanced superior elasticity in freestanding single-crystalline multiferroic $BiFeO_3$ membranes. *Sci Adv* 6, eaba5847 (2020).

108. Harbola, V., Crossley, S., Hong, S. S., Lu, D., Birkhölzer, Y. A., Hikita, Y. & Hwang, H. Y. Strain Gradient Elasticity in $SrTiO_3$ Membranes: Bending versus Stretching. *Nano Lett* 21, 2470–2475 (2021).

109. Shi, Q., Parsonnet, E., Cheng, X., Fedorova, N., Peng, R.-C., Fernandez, A., Qualls, A., Huang, X., Chang, X., Zhang, H., Pesquera, D., Das, S., Nikonov, D., Young, I., Chen, L.-Q., Martin, L. W., Huang, Y.-L., Íñiguez, J. & Ramesh, R. The role of lattice dynamics in ferroelectric switching. *Nat Commun* 13, 1110 (2022).

110. Wachsman, E. D., Marlowe, C. A. & Lee, K. T. Role of solid oxidefuel cells in a balanced energy strategy. *Energy Environ Sci* 5, 5498–5509 (2012).

111. Brett, D. J. L., Atkinson, A., Brandon, N. P. & Skinner, S. J. Intermediate temperature solid oxide fuel cells. *Chem Soc Rev* 37, 1568–1578 (2008).

112. Ruiz-Morales, J. C., Marrero-López, D., Canales-Vázquez, J. & Irvine, J. T. S. Symmetric and reversible solid oxide fuel cells. *Rsc Adv* 1, 1403–1414 (2011).

113. Graves, C., Ebbesen, S. D., Jensen, S. H., Simonsen, S. B. & Mogensen, M. B. Eliminating degradation in solid oxide electrochemical cells by reversible operation. *Nat Mater* 14, 239–244 (2015).

114. Kilner, J. A. & Burriel, M. Materials for Intermediate-Temperature Solid-Oxide Fuel Cells. *Mater Res* 44, 365–393 (2014).

115. Wachsman, E. D. & Lee, K. T. Lowering the Temperature of Solid Oxide Fuel Cells. *Science* 334, 935–939 (2011).

116. Adler, S. B. Factors Governing Oxygen Reduction in Solid Oxide Fuel Cell Cathodes†. *Chem Rev* 104, 4791–4844 (2004).

117. Aguadero, A., Fawcett, L., Taub, S., Woolley, R., Wu, K.-T., Xu, N., Kilner, J. A. & Skinner, S. J. Materials development for intermediate-temperature solid oxide electrochemical devices. *J Mater Sci* 47, 3925–3948 (2012).

118. Adler, S. B. Mechanism and kinetics of oxygen reduction on porous $La_{1-x}Sr_xCoO_3$ electrodes. *Solid State Ionics* 111, 125–134 (1998).

119. Gellings, P. J. & Bouwmeester, H. J. M. Solid state aspects of oxidation catalysis. *Catal Today* 58, 1–53 (2000).

120. Fleig, J. SOLID OXIDE FUEL CELL CATHODES: Polarization Mechanisms and Modeling of the Electrochemical Performance. *Annu Rev Mater Res* 33, 361–382 (2003).

121. Staykov, A., Téllez, H., Akbay, T., Druce, J., Ishihara, T. & Kilner, J. Oxygen Activation and Dissociation on Transition Metal Free Perovskite Surfaces. *Chem Mater* 27, 8273–8281 (2015).

122. Cao, Y., Gadre, M. J., Ngo, A. T., Adler, S. B. & Morgan, D. D. Factors controlling surface oxygen exchange in oxides. *Nat Commun* 10, 1346 (2019).

123. Manthiram, A., Kim, J.-H., Kim, Y. N. & Lee, K.-T. Crystal chemistry and properties of mixed ionic-electronic conductors. *J Electroceram* 27, 93–107 (2011).

124. Anderson, H. U. Review of p-type doped perovskite materials for SOFC and other applications. *Solid State Ionics* 52, 33–41 (1992).

125. Lane, J. A., Benson, S. J., Waller, D. & Kilner, J. A. Oxygen transport in $La_{0.6}Sr_{0.4}Co_{0.2}Fe_{0.8}O_{3-\delta}$. *Solid State Ionics* 121, 201–208 (1999).

126. Sun, C., Hui, R. & Roller, J. Cathode materials for solid oxide fuel cells: a review. *J Solid State Electr* 14, 1125–1144 (2010).

127. Ormerod, R. M. Solid oxide fuel cells. *Chem Soc Rev* 32, 17–28 (2002).

128. Jørgensen, M. J. & Mogensen, M. Impedance of Solid Oxide Fuel Cell LSM/YSZ Composite Cathodes. *J Electrochem Soc* 148, A433–A442 (2001).

129. Teraoka, Y., Nobunaga, T., Okamoto, K., Miura, N. & Yamazoe, N. Influence of constituent metal cations in substituted $LaCoO_3$ on mixed conductivity and oxygen permeability. *Solid State Ionics* 48, 207–212 (1991).

130. Skinner, S. J. Recent advances in Perovskite-type materials for solid oxide fuel cell cathodes. *Int J Inorg Mater* 3, 113–121 (2001).

131. Teraoka, Y., Zhang, H. M., Okamoto, K. & Yamazoe, N. Mixed ionic-electronic conductivity of $La_{1-x}Sr_xCo_{1-y}Fe_yO_{3-\delta}$ perovskite-type oxides. *Mater Res Bull* 23, 51–58 (1988).

132. Waller, D., Lane, J. A., Kilner, J. A. & Steele, B. C. H. The structure of and reaction of A-site deficient $La_{0.6}Sr_{0.4-x}Co_{0.2}Fe_{0.8}O_{3-\delta}$ perovskites. *Mater Lett* 27, 225–228 (1996).

133. Marinha, D., Hayd, J., Dessemond, L., Ivers-Tiffée, E. & Djurado, E. Performance of $(La,Sr)(Co,Fe)O_{3-x}$ double-layer cathode films for intermediate temperature solid oxide fuel cell. *J Power Sources* 196, 5084–5090 (2011).

134. Lee, Y.-L., Kleis, J., Rossmeisl, J., Shao-Horn, Y. & Morgan, D. Prediction of solid oxide fuel cell cathode activity with first-principles descriptors. *Energ Environ Sci* 4, 3966–3970 (2011).

135. Hong, W. T., Risch, M., Stoerzinger, K. A., Grimaud, A., Suntivich, J. & Shao-Horn, Y. Toward the rational design of non-precious transition metal oxides for oxygen electrocatalysis. *Energ Environ Sci* 8, 1404–1427 (2015).

136. Suntivich, J., Gasteiger, H. A., Yabuuchi, N., Nakanishi, H., Goodenough, J. B. & Shao-Horn, Y. Design principles for oxygen-reduction activity on perovskite oxide catalysts for fuel cells and metal–air batteries. *Nat Chem* 3, 546 (2011).

137. Mayeshiba, T. T. & Morgan, D. D. Factors controlling oxygen migration barriers in perovskites. *Solid State Ionics* 296, 71–77 (2016).

138. Lee, Y.-L., Kleis, J., Rossmeisl, J. & Morgan, D. Ab initio energetics of $LaBO_3$ (001) (B=Mn, Fe, Co, and Ni) for solid oxide fuel cell cathodes. *Phys Rev B* 80, 224101 (2009).

139. Grimaud, A., May, K. J., Carlton, C. E., Lee, Y.-L., Risch, M., Hong, W. T., Zhou, J. & Shao-Horn, Y. Double perovskites as a family of highly active catalysts for oxygen evolution in alkaline solution. *Nat Commun* 4, 2439 (2013).

140. Hammer, B. & Norskov, J. K. Why gold is the noblest of all the metals. *Nature* 376, 238–240 (1995).

141. Nørskov, J. K., Bligaard, T., Rossmeisl, J. & Christensen, C. H. Towards the computational design of solid catalysts. *Nat Chem* 1, 37–46 (2009).

142. Readman, J. E., Olafsen, A., Larring, Y. & Blom, R. $La_{0.8}Sr_{0.2}Co_{0.2}Fe_{0.8}O_{3-\delta}$ as a potential oxygen carrier in a chemical looping type reactor, an in-situ powder X-ray diffraction study. *J Mater Chem* 15, 1931–1937 (2005).

143. Lane, J. A. & Kilner, J. A. Measuring oxygen diffusion and oxygen surface exchange by conductivity relaxation. *Solid State Ionics* 136–137, 997–1001 (2000).

144. Lai, W. & Haile, S. M. Impedance Spectroscopy as a Tool for Chemical and Electrochemical Analysis of Mixed Conductors: A Case Study of Ceria. *J Am Ceram Soc* 88, 2979–2997 (2005).

145. Baumann, F. S., Fleig, J., Habermeier, H.-U. & Maier, J. Impedance spectroscopic study on well-defined (La,Sr)(Co,Fe)$O_{3-\delta}$ model electrodes. *Solid State Ionics* 177, 1071–1081 (2006).

146. Fleig, J., Merkle, R. & Maier, J. The p(O_2) dependence of oxygen surface coverage and exchange current density of mixed conducting oxide electrodes: model considerations. *Phys Chem Chem Phys* 9, 2713 (2007).

147. Ogletree, D. F., Bluhm, H., Hebenstreit, E. D. & Salmeron, M. Photoelectron spectroscopy under ambient pressure and temperature conditions. *Nucl Instruments Methods Phys Res Sect Accel Spectrometers Detect Assoc Equip* 601, 151–160 (2009).

148. Shao, Z. & Haile, S. M. A high-performance cathode for the next generation of solid-oxide fuel cells. *Nature* 431, 170 (2004).

149. Lee, Y.-L., Gadre, M. J., Shao-Horn, Y. & Morgan, D. Ab initio GGA+U study of oxygen evolution and oxygen reduction electrocatalysis on the (001) surfaces of lanthanum transition metal perovskites $LaBO_3$ (B = Cr, Mn, Fe, Co and Ni). *Phys Chem Chem Phys* 17, 21643–21663 (2015).

150. Mastrikov, Y. A., Merkle, R., Kotomin, E. A., Kuklja, M. M. & Maier, J. Surface termination effects on the oxygen reduction reaction rate at fuel cell cathodes. *J Mater Chem A* 6, 11929–11940 (2018).

151. Eom, C. J., Kuo, D.-Y., Adamo, C., Moon, E. J., May, S. J., Crumlin, E. J., Schlom, D. G. & Suntivich, J. Tailoring manganese oxide with atomic precision to increase surface site availability for oxygen reduction catalysis. *Nat Commun* 9, 4034 (2018).

152. Akbashev, A. R., Zhang, L., Mefford, J. T., Park, J., Butz, B., Luftman, H., Chueh, W. C. & Vojvodic, A. Activation of ultrathin $SrTiO_3$ with subsurface $SrRuO_3$ for the oxygen evolution reaction. *Energ Environ Sci* 11, 1762–1769 (2018).

153. Burriel, M., Peña-Martínez, J., Chater, R. J., Fearn, S., Berenov, A. V., Skinner, S. J. & Kilner, J. A. Anisotropic Oxygen Ion Diffusion in Layered $PrBaCo_2O_{5+\delta}$. *Chem Mater* 24, 613–621 (2012).

154. Baumann, F. S., Fleig, J., Habermeier, H.-U. & Maier, J. $Ba_{0.5}Sr_{0.5}Co_{0.8}Fe_{0.2}O_{3-\delta}$ thin film microelectrodes investigated by impedance spectroscopy. *Solid State Ionics* 177, 3187–3191 (2006).

155. Fleig, J., Baumann, F. S., Brichzin, V., Kim, H. -R., Jamnik, J., Cristiani, G., Habermeier, H. -U. & Maier, J. Thin Film Microelectrodes in SOFC Electrode Research. *Fuel Cells* 6, 284–292 (2006).

156. Fleig, J., Kim, H.-R., Jamnik, J. & Maier, J. Oxygen Reduction Kinetics of Lanthanum Manganite (LSM) Model Cathodes: Partial Pressure Dependence and Rate-Limiting Steps. *Fuel Cells* 8, 330–337 (2008).

157. Téllez, H., Druce, J., Ju, Y.-W., Kilner, J. & Ishihara, T. Surface chemistry evolution in $LnBaCo_2O_{5+}$ double perovskites for oxygen electrodes. *Int J Hydrogen Energ* 39, 20856–20863 (2014).

158. Druce, J., Ishihara, T. & Kilner, J. Surface composition of perovskite-type materials studied by Low Energy Ion Scattering (LEIS). *Solid State Ionics* 262, 893–896 (2014).

159. Burriel, M., Wilkins, S., Hill, J. P., Muñoz-Márquez, M. A., Brongersma, H. H., Kilner, J. A., Ryan, M. P. & Skinner, S. J. Absence of Ni on the outer surface of Sr doped La 2 NiO 4 single crystals. *Energ Environ Sci* 7, 311–316 (2013).

160. Yan, L., Balasubramaniam, K. R., Wang, S., Du, H. & Salvador, P. Electrical Conductivity Relaxation Study of Solid Oxide Fuel Cell Cathodes using Epitaxial (001)-Oriented Strontium-Doped Lanthanum Manganite Thin Films. *Mrs Online Proc Libr* 1255, 1 (2010).

161. Cox-Galhotra, R. A. & McIntosh, S. Unreliability of simultaneously determining kchem and Dchem via conductivity relaxation for surface-modified $La_{0.6}Sr_{0.4}Co_{0.2}Fe_{0.8}O_{3-\delta}$. *Solid State Ionics* 181, 1429–1436 (2010).

162. Merkle, R. & Maier, J. How Is Oxygen Incorporated into Oxides? A Comprehensive Kinetic Study of a Simple Solid-State Reaction with $SrTiO_3$ as a Model Material. *Angewandte Chemie Int Ed* 47, 3874–3894 (2008).

163. Kubicek, M., Huber, T. M., Welzl, A., Penn, A., Rupp, G. M., Bernardi, J., Stöger-Pollach, M., Hutter, H. & Fleig, J. Electrochemical properties of $La_{0.6}Sr_{0.4}CoO_{3-\delta}$ thin films investigated by complementary impedance spectroscopy and isotope exchange depth profiling. *Solid State Ionics* 256, 38–44 (2014).

164. Gao, R., Jain, A. C. P., Pandya, S., Dong, Y., Yuan, Y., Zhou, H., Dedon, L. R., Thoréton, V., Saremi, S., Xu, R., Luo, A., Chen, T., Gopalan, V., Ertekin, E., Kilner, J., Ishihara, T., Perry, N. H., Trinkle, D. R. & Martin, L. W. Designing Optimal Perovskite Structure for High Ionic Conduction. *Adv Mater* 32, 1905178 (2020).

165. Karthik, J., Damodaran, A. R. & Martin, L. W. Epitaxial Ferroelectric Heterostructures Fabricated by Selective Area Epitaxy of $SrRuO_3$ Using an MgO Mask. *Advanced Materials* 24, 1610–1615 (2012).

166. Mutoro, E., Crumlin, E. J., Biegalski, M. D., Christen, H. M. & Shao-Horn, Y. Enhanced oxygen reduction activity on surface-decorated perovskite thin films for solid oxide fuel cells. *Energ Environ Sci* 4, 3689–3696 (2011).

167. Crumlin, E. J., Mutoro, E., Ahn, S.-J., O', G. J. la, Leonard, D. N., Borisevich, A., Biegalski, M. D., Christen, H. M. & Shao-Horn, Y. Oxygen Reduction Kinetics Enhancement on a Heterostructured Oxide Surface for Solid Oxide Fuel Cells. *J Phys Chem Lett* 1, 3149–3155 (2010).

168. Ishihara, T., Matsuda, H. & Takita, Y. Doped $LaGaO_3$ Perovskite Type Oxide as a New Oxide Ionic Conductor. *J Am Chem Soc* 116, 3801–3803 (1994).

169. Wang, H., Yakal-Kremski, K. J., Yeh, T., Rupp, G. M., Limbeck, A., Fleig, J. & Barnett, S. A. Mechanisms of Performance Degradation of $(La,Sr)(Co,Fe)O_{3-\delta}$ Solid Oxide Fuel Cell Cathodes. *J Electrochem Soc* 163, F581–F585 (2016).

170. Crumlin, E. J., Mutoro, E., Liu, Z., Grass, M. E., Biegalski, M. D., Lee, Y.-L., Morgan, D., Christen, H. M., Bluhm, H. & Shao-Horn, Y. Surface strontium enrichment on highly active perovskites for oxygen electrocatalysis in solid oxide fuel cells. *Energ Environ Sci* 5, 6081–6088 (2012).

171. Schmid, A., Rupp, G. M. & Fleig, J. How To Get Mechanistic Information from Partial Pressure-Dependent Current–Voltage Measurements of Oxygen Exchange on Mixed Conducting Electrodes. *Chem Mater* 30, 4242–4252 (2018).

172. Lee, W., Han, J. W., Chen, Y., Cai, Z. & Yildiz, B. Cation Size Mismatch and Charge Interactions Drive Dopant Segregation at the Surfaces of Manganite Perovskites. *J Am Chem Soc* 135, 7909–7925 (2013).

173. Grass, M. E., Karlsson, P. G., Aksoy, F., Lundqvist, M., Wannberg, B., Mun, B. S., Hussain, Z. & Liu, Z. New ambient pressure photoemission endstation at Advanced Light Source beamline 9.3.2. *Rev Sci Instrum* 81, 053106 (2010).

174. Abbate, M., Groot, F. M. F. de, Fuggle, J. C., Fujimori, A., Strebel, O., Lopez, F., Domke, M., Kaindl, G., Sawatzky, G. A., Takano, M., Takeda, Y., Eisaki, H. & Uchida, S. Controlled-valence properties of $La_{1-x}Sr_xFeO_3$ and $La_{1-x}Sr_xMnO_3$ studied by soft-x-ray absorption spectroscopy. *Phys Rev B* 46, 4511–4519 (1992).

175. Abbate, M., Fuggle, J. C., Fujimori, A., Tjeng, L. H., Chen, C. T., Potze, R., Sawatzky, G. A., Eisaki, H. & Uchida, S. Electronic structure and spin-state transition of $LaCoO_3$. *Phys Rev B* 47, 16124–16130 (1992).

176. Merz, M., Nagel, P., Pinta, C., Samartsev, A., Löhneysen, H. v., Wissinger, M., Uebe, S., Assmann, A., Fuchs, D. & Schuppler, S. X-ray absorption and magnetic circular dichroism of $LaCoO_3$, $La_{0.7}Ce_{0.3}CoO_3$, and $La_{0.7}Sr_{0.3}CoO_3$ films: Evidence for cobalt-valence-dependent magnetism. *Phys Rev B* 82, 174416 (2010).

177. Orikasa, Y., Ina, T., Nakao, T., Mineshige, A., Amezawa, K., Oishi, M., Arai, H., Ogumi, Z. & Uchimoto, Y. An X-ray absorption spectroscopic study on mixed conductive $La_{0.6}Sr_{0.4}Co_{0.8}Fe_{0.2}O_{3-\delta}$ cathodes. I. Electrical conductivity and electronic structure. *Phys Chem Chem Phys* 13, 16637–16643 (2011).

178. Mueller, D. N., Machala, M. L., Bluhm, H. & Chueh, W. C. Redox activity of surface oxygen anions in oxygen-deficient perovskite oxides during electrochemical reactions. *Nat Commun* 6, 6097 (2015).

179. Tsvetkov, N., Lu, Q., Sun, L., Crumlin, E. J. & Yildiz, B. Improved chemical and electrochemical stability of perovskite oxides with less reducible cations at the surface. *Nat Mater* 15, 1010–1016 (2016).

180. Powell, C. J. & Jablonksi, A. *NIST Electron Inelastic-Mean-Free-Path Database - Version 1.2*. (National Institute of Standards and Technology, Gaithersburg, MD, 2010). doi:http://dx.doi.org/10.18434/T48C78.

181. Sunding, M. F., Hadidi, K., Diplas, S., Løvvik, O. M., Norby, T. E. & Gunnæs, A. E. XPS characterisation of in situ treated lanthanum oxide and hydroxide using tailored charge referencing and peak fitting procedures. *J Electron Spectrosc* 184, 399–409 (2011).

182. Li, J. P. H., Zhou, X., Pang, Y., Zhu, L., Vovk, E. I., Cong, L., Bavel, A. P. van, Li, S. & Yang, Y. Understanding of binding energy calibration in XPS of lanthanum oxide by in situ treatment. *Phys Chem Chem Phys* 21, 22351–22358 (2019).

183. Crumlin, E. J., Mutoro, E., Hong, W. T., Biegalski, M. D., Christen, H. M., Liu, Z., Bluhm, H. & Shao-Horn, Y. In Situ Ambient Pressure X-ray Photoelectron Spectroscopy of Cobalt

Perovskite Surfaces under Cathodic Polarization at High Temperatures. *J Phys Chem C* 117, 16087–16094 (2013).

184. Chen, Y., Téllez, H., Burriel, M., Yang, F., Tsvetkov, N., Cai, Z., McComb, D. W., Kilner, J. A. & Yildiz, B. Segregated Chemistry and Structure on (001) and (100) Surfaces of $(La_{1-x}Sr_x)_2CoO_4$ Override the Crystal Anisotropy in Oxygen Exchange Kinetics. *Chem Mater* 27, 5436–5450 (2015).

185. Nemšák, S., Conti, G., Palsson, G. K., Conlon, C., Cho, S., Rault, J. E., Avila, J., Asensio, M.-C., Jackson, C. A., Moetakef, P., Janotti, A., Bjaalie, L., Himmetoglu, B., Walle, C. G. V. de, Balents, L., Schneider, C. M., Stemmer, S. & Fadley, C. S. Observation by resonant angle-resolved photoemission of a critical thickness for 2-dimensional electron gas formation in $SrTiO_3$ embedded in $GdTiO_3$. *Appl Phys Lett* 107, 231602 (2015).

186. Cai, Z., Kubicek, M., Fleig, J. & Yildiz, B. Chemical Heterogeneities on $La_{0.6}Sr_{0.4}CoO_{3-\delta}$ Thin Films—Correlations to Cathode Surface Activity and Stability. *Chem Mater* 24, 1116–1127 (2012).

187. Opitz, A. K., Rameshan, C., Kubicek, M., Rupp, G. M., Nenning, A., Götsch, T., Blume, R., Hävecker, M., Knop-Gericke, A., Rupprechter, G., Klötzer, B. & Fleig, J. The Chemical Evolution of the $La_{0.6}Sr_{0.4}CoO_{3-\delta}$ Surface Under SOFC Operating Conditions and Its Implications for Electrochemical Oxygen Exchange Activity. *Top Catal* 61, 2129–2141 (2018).

188. Pişkin, F., Bliem, R. & Yildiz, B. Effect of crystal orientation on the segregation of aliovalent dopants at the surface of $La_{0.6}Sr_{0.4}CoO_3$. *J Mater Chem A* 6, 14136–14145 (2018).

189. Grosvenor, A. P., Kobe, B. A., Biesinger, M. C. & McIntyre, N. S. Investigation of multiplet splitting of Fe 2p XPS spectra and bonding in iron compounds. *Surf Interface Anal* 36, 1564–1574 (2004).

190. Biesinger, M. C., Payne, B. P., Grosvenor, A. P., Lau, L. W. M., Gerson, A. R. & Smart, R. St. C. Resolving surface chemical states in XPS analysis of first row transition metals, oxides and hydroxides: Cr, Mn, Fe, Co and Ni. *Appl Surf Sci* 257, 2717–2730 (2011).

191. Hong, W. T., Welsch, R. E. & Shao-Horn, Y. Descriptors of Oxygen-Evolution Activity for Oxides: A Statistical Evaluation. *J Phys Chem C* 120, 78–86 (2015).

192. Suntivich, J., Hong, W. T., Lee, Y.-L., Rondinelli, J. M., Yang, W., Goodenough, J. B., Dabrowski, B., Freeland, J. W. & Shao-Horn, Y. Estimating Hybridization of Transition Metal and Oxygen States in Perovskites from O K-edge X-ray Absorption Spectroscopy. *J Phys Chem C* 118, 1856–1863 (2014).

193. Suntivich, J., May, K. J., Gasteiger, H. A., Goodenough, J. B. & Shao-Horn, Y. A Perovskite Oxide Optimized for Oxygen Evolution Catalysis from Molecular Orbital Principles. *Science* 334, 1383–1385 (2011).

194. Jalili, H., Han, J. W., Kuru, Y., Cai, Z. & Yildiz, B. New Insights into the Strain Coupling to Surface Chemistry, Electronic Structure, and Reactivity of $La_{0.7}Sr_{0.3}MnO_3$. *J Phys Chem Lett* 2, 801–807 (2011).

195. Akhade, S. A. & Kitchin, J. R. Effects of strain, d -band filling, and oxidation state on the surface electronic structure and reactivity of 3 d perovskite surfaces. *J Chem Phys* 137, 084703 (2012).

196. Gao, R., Fernandez, A., Chakraborty, T., Luo, A., Pesquera, D., Das, S., Velarde, G., Thoréton, V., Kilner, J., Ishihara, T., Nemšák, S., Crumlin, E. J., Ertekin, E. & Martin, L. W. Correlating Surface Crystal Orientation and Gas Kinetics in Perovskite Oxide Electrodes. *Adv Mater* 2100977 (2021).

197. Yeh, J. J. & Lindau, I. Atomic subshell photoionization cross sections and asymmetry parameters: $1 \leqslant Z \leqslant 103$. *Atom Data Nucl Data* 32, 1–155 (1985).

198. Haverkort, M. W., Hu, Z., Cezar, J. C., Burnus, T., Hartmann, H., Reuther, M., Zobel, C., Lorenz, T., Tanaka, A., Brookes, N. B., Hsieh, H. H., Lin, H.-J., Chen, C. T. & Tjeng, L. H. Spin State Transition in $LaCoO_3$ Studied Using Soft X-ray Absorption Spectroscopy and Magnetic Circular Dichroism. *Phys Rev Lett* 97, 176405 (2006).

199. Hueso, J. L., Holgado, J. P., Pereñíguez, R., Mun, S., Salmeron, M. & Caballero, A. Chemical and electronic characterization of cobalt in a lanthanum perovskite. Effects of strontium substitution. *J Solid State Chem* 183, 27–32 (2010).

200. Uecker, R., Velickov, B., Klimm, D., Bertram, R., Bernhagen, M., Rabe, M., Albrecht, M., Fornari, R. & Schlom, D. G. Properties of rare-earth scandate single crystals (Re=Nd−Dy). *J Cryst Growth* 310, 2649–2658 (2008).

201. Freeland, J. W., Liu, J., Kareev, M., Gray, B., Kim, J. W., Ryan, P., Pentcheva, R. & Chakhalian, J. Orbital control in strained ultra-thin $LaNiO_3/LaAlO_3$ superlattices. *Epl-europhys Lett* 96, 57004 (2011).

202. Disa, A. S., Walker, F. J., Ismail-Beigi, S. & Ahn, C. H. Research Update: Orbital polarization in $LaNiO_3$-based heterostructures. *APL Mater* 3, 062303 (2015).

203. Laan, G. van der. Sum Rules and Fundamental Spectra of Magnetic X-Ray Dichroism in Crystal Field Symmetry. *J Phys Soc Jpn* 63, 2393–2400 (1994).

204. Thole, B. T. & Laan, G. van der. Sum rules for magnetic dichroism in rare earth 4f photoemission. *Phys Rev Lett* 70, 2499–2502 (1992).

205. Cross, L. E. Relaxor ferroelectrics. *Ferroelectrics*, 76, 241-267 (1987).

206. Cross, L. E. Relaxor ferroelectrics: An overview. *Ferroelectrics* 151, 305–320 (1994).

207. Samara, G. A. The relaxational properties of compositionally disordered ABO_3 perovskites. *J Phys Condens Matter* 15, R367 (2003).

208. Smolenskii, G. A. & Agranovskaya, A. I. Dielectric Polarization And Losses Of Some Complex Compounds. *Zhurnal Tekhniceskoj Fiziki [Journal of Technical Physics]* 28, (1958).

209. Pirc, R. & Blinc, R. Vogel-Fulcher freezing in relaxor ferroelectrics. *Phys Rev B* 76, 020101 (2007).

210. Tagantsev, A. K. Vogel-Fulcher relationship for the dielectric permittivity of relaxor ferroelectrics. *Phys Rev Lett* 72, 1100–1103 (1994).

211. Viehland, D., Jang, S., Cross, L. E. & Wuttig, M. The dielectric relaxation of lead magnesium niobate relaxor ferroelectrics. *Philosophical Mag Part B* 64, 335–344 (1991).

212. Fu, D., Taniguchi, H., Itoh, M., Koshihara, S., Yamamoto, N. & Mori, S. Relaxor $Pb(Mg_{1/3}Nb_{2/3})O_3$: A Ferroelectric with Multiple Inhomogeneities. *Phys Rev Lett* 103, 207601 (2009).

213. Levstik, A., Kutnjak, Z., Filipič, C. & Pirc, R. Glassy freezing in relaxor ferroelectric lead magnesium niobate. *Phys Rev B* 57, 11204–11211 (1998).

214. Viehland, Li, Jang, Cross & Wuttig. Glassy polarization behavior of relaxor ferroelectrics. *Phys Rev B Condens Matter* 46, 8013–8017 (1992).

215. Ji, Y., Wang, D., Wang, Y., Zhou, Y., Xue, D., Otsuka, K., Wang, Y. & Ren, X. Ferroic glasses. *Npj Comput Mater* 3, 43 (2017).

216. Kimura, T., Tomioka, Y., Kumai, R., Okimoto, Y. & Tokura, Y. Diffuse Phase Transition and Phase Separation in Cr-Doped Nd1/2Ca1/2MnO3: A Relaxor Ferromagnet. *Phys Rev Lett* 83, 3940–3943 (1999).

217. Chen, L., Bokov, A. A., Zhu, W., Wu, H., Zhuang, J., Zhang, N., Tailor, H. N., Ren, W. & Ye, Z.-G. Magnetoelectric relaxor and reentrant behaviours in multiferroic $Pb(Fe_{2/3}W_{1/3})O_3$ crystal. *Sci Reports* 6, 22327 (2016).

218. Eom, C.-B. & Trolier-McKinstry, S. Thin-film piezoelectric MEMS. *MRS Bull* 37, 1007–1017 (2012).

219. Pandya, S., Wilbur, J., Kim, J., Gao, R., Dasgupta, A., Dames, C. & Martin, L. W. Pyroelectric energy conversion with large energy and power density in relaxor ferroelectric thin films. *Nat Mater* 17, 1–7 (2018).

220. Kim, J., Saremi, S., Acharya, M., Velarde, G., Parsonnet, E., Donahue, P., Qualls, A., Garcia, D. & Martin, L. W. Ultrahigh capacitive energy density in ion-bombarded relaxor ferroelectric films. *Science* 369, 81–84 (2020).

221. Hlinka, J. DO WE NEED THE ETHER OF POLAR NANOREGIONS? *J Adv Dielectr* 02, 1241006 (2012).

222. Davis, M. Picturing the elephant: Giant piezoelectric activity and the monoclinic phases of relaxor-ferroelectric single crystals. *J Electroceram* 19, 25–47 (2007).

223. Bobnar, V. & Kutnjak, Z. Does Burns Temperature Exist in Ferroelectric Relaxors? *Ferroelectrics* 415, 14–19 (2011).

224. Burns, G. & Dacol, F. H. Glassy polarization behavior in ferroelectric compounds $Pb(Mg_{1/3}Nb_{2/3})O_3$ and $Pb(Zn_{1/3}Nb_{2/3})O_3$. *Solid State Commun* 48, 853–856 (1983).

225. Burns, G. & Dacol, F. H. Crystalline Ferroelectrics with a Glassy Polarization Phase. *Jpn J Appl Phys* 24, 85 (1985).

226. Dkhil, B., Gemeiner, P., Al-Barakaty, A., Bellaiche, L., Dul'kin, E., Mojaev, E. & Roth, M. Intermediate temperature scale $T*$ in lead-based relaxor systems. *Phys Rev B* 80, 064103 (2009).

227. Toulouse, J. The Three Characteristic Temperatures of Relaxor Dynamics and Their Meaning. *Ferroelectrics* 369, 203–213 (2008).

228. Cohen, R. E. Origin of ferroelectricity in perovskite oxides. *Nature* 358, 358136a0 (1992).

229. Westphal, V., Kleemann, W. & Glinchuk, M. D. Diffuse phase transitions and random-field-induced domain states of the '"relaxor"' ferroelectric $PbMg_{1/3}Nb_{2/3}O_3$. *Phys Rev Lett* 68, 847–850 (1992).

230. Takenaka, H., Grinberg, I. & Rappe, A. M. Anisotropic Local Correlations and Dynamics in a Relaxor Ferroelectric. *Phys Rev Lett* 110, 147602 (2013).

231. Hiraka, H., Lee, S.-H., Gehring, P. M., Xu, G. & Shirane, G. Cold neutron study on the diffuse scattering and phonon excitations in the relaxor $Pb(Mg_{1/3}Nb_{2/3})O_3$. *Phys Rev B* 70, 184105 (2004).

232. La-Orauttapong, D., Toulouse, J., Robertson, J. L. & Ye, Z.-G. Diffuse neutron scattering study of a disordered complex perovskite $Pb(Zn_{1/3}Nb_{2/3})O_3$ crystal. *Phys Rev B* 64, 212101 (2001).

233. Akbarzadeh, A. R., Prosandeev, S., Walter, E. J., Al-Barakaty, A. & Bellaiche, L. Finite-Temperature Properties of $Ba(Zr,Ti)O_3$ Relaxors from First Principles. *Phys Rev Lett* 108, 257601 (2012).

234. Prosandeev, S., Wang, D., Akbarzadeh, A. R. & Bellaiche, L. First-principles-based effective Hamiltonian simulations of bulks and films made of lead-free $Ba(Zr,Ti)O_3$ relaxor ferroelectrics. *J Phys Condens Matter* 27, 223202 (2015).

235. Tian, Z., Kim, J., Fernandez, A., Huang, X. & Martin, L. W. Effect of substrate clamping on evolution of properties in homovalent and heterovalent relaxor thin films. *Phys Rev B* 105, 094107 (2022).

236. Jaffe, B., Roth, R. S. & Marzullo, S. Piezoelectric Properties of Lead Zirconate-Lead Titanate Solid-Solution Ceramics. *J Appl Phys* 25, 809–810 (1954).

237. Zhili, C., Setter, N. & Cross, L. E. Diffuse ferroelectric phase transition and cation order in the solid solution system $Pb(Sc_{1/2}Nb_{1/2})O_3$:$Pb(Sc_{1/2}Ta_{1/2})O_3$. *Ferroelectrics* 37, 619–622 (1981).

238. Chu, F., Reaney, I. M. & Setter, N. Spontaneous (zero-field) relaxor–to–ferroelectric-phase transition in disordered $Pb(Sc_{1/2}Nb_{1/2})O_3$. *J Appl Phys* 77, 1671–1676 (1995).

239. Setter, N. & Cross, L. E. The contribution of structural disorder to diffuse phase transitions in ferroelectrics. *J Mater Sci* 15, 2478–2482 (1980).

240. Setter, N. & Cross, L. E. The role of B-site cation disorder in diffuse phase transition behavior of perovskite ferroelectrics. *J Appl Phys* 51, 4356–4360 (1980).

241. Chu, F., Setter, N. & Tagantsev, A. K. The spontaneous relaxor-ferroelectric transition of $Pb(Sc_{0.5}Ta_{0.5})O_3$. *J Appl Phys* 74, 5129–5134 (1993).

242. Gehring, P. M., Wakimoto, S., Ye, Z.-G. & Shirane, G. Soft Mode Dynamics above and below the Burns Temperature in the Relaxor $Pb(Mg_{1/3}Nb_{2/3})O_3$. *Phys Rev Lett* 87, 277601 (2001).

243. Kim, J., Takenaka, H., Qi, Y., Damodaran, A. R., Fernandez, A., Gao, R., McCarter, M. R., Saremi, S., Chung, L., Rappe, A. M. & Martin, L. W. Epitaxial Strain Control of Relaxor Ferroelectric Phase Evolution. *Adv Mater* 31, 1901060 (2019).

244. Kumar, A., Baker, J. N., Bowes, P. C., Cabral, M. J., Zhang, S., Dickey, E. C., Irving, D. L. & LeBeau, J. M. Atomic-resolution electron microscopy of nanoscale local structure in lead-based relaxor ferroelectrics. *Nat Mater* 20, 1–6 (2021).

245. Kim, J., Meyers, D. J., Kumar, A., Fernandez, A., Velarde, G. A. P., Tian, Z., Kim, J.-W., LeBeau, J. M., Ryan, P. J. & Martin, L. W. Frequency-dependent suppression of field-induced polarization rotation in relaxor ferroelectric thin films. *Matter* 4, (2021).

246. Kutnjak, Z., Petzelt, J. & Blinc, R. The giant electromechanical response in ferroelectric relaxors as a critical phenomenon. *Nature* 441, nature04854 (2006).

247. Kim, J. Structure-Property Relationships in Relaxor Ferroelectric Thin Films. (2021).

248. Li, F., Cabral, M. J., Xu, B., Cheng, Z., Dickey, E. C., LeBeau, J. M., Wang, J., Luo, J., Taylor, S., Hackenberger, W., Bellaiche, L., Xu, Z., Chen, L.-Q., Shrout, T. R. & Zhang, S. Giant piezoelectricity of Sm-doped $Pb(Mg_{1/3}Nb_{2/3})O_3$-$PbTiO_3$ single crystals. *Sci New York N Y* 364, 264–268 (2019).

249. Li, F., Zhang, S., Yang, T., Xu, Z., Zhang, N., Liu, G., Wang, J., Wang, J., Cheng, Z., Ye, Z.-G., Luo, J., Shrout, T. R. & Chen, L.-Q. The origin of ultrahigh piezoelectricity in relaxor-ferroelectric solid solution crystals. *Nat Commun* 7, 13807 (2016).

250. Li, F., Lin, D., Chen, Z., Cheng, Z., Wang, J., Li, C., Xu, Z., Huang, Q., Liao, X., Chen, L.-Q., Shrout, T. R. & Zhang, S. Ultrahigh piezoelectricity in ferroelectric ceramics by design. *Nat Mater* 17, 349–354 (2018).

251. Pan, H., Ma, J., Ma, J., Zhang, Q., Liu, X., Guan, B., Gu, L., Zhang, X., Zhang, Y.-J., Li, L., Shen, Y., Lin, Y.-H. & Nan, C.-W. Giant energy density and high efficiency achieved in bismuth ferrite-based film capacitors via domain engineering. *Nat Commun* 9, 1813 (2018).

252. Pan, H., Li, F., Liu, Y., Zhang, Q., Wang, M., Lan, S., Zheng, Y., Ma, J., Gu, L., Shen, Y., Yu, P., Zhang, S., Chen, L.-Q., Lin, Y.-H. & Nan, C.-W. Ultrahigh–energy density lead-free dielectric films via polymorphic nanodomain design. *Science* 365, 578–582 (2019).

253. Xu, G., Zhong, Z., Bing, Y., Ye, Z.-G. & Shirane, G. Electric-field-induced redistribution of polar nano-regions in a relaxor ferroelectric. *Nat Mater* 5, nmat1560 (2006).

254. Wen, J., Xu, G., Stock, C. & Gehring, P. M. Response of polar nanoregions in $68\%Pb(Mg_{1/3}Nb_{2/3})O_3$-$32\%PbTiO_3$ to a [001] electric field. *Appl Phys Lett* 93, 082901 (2008).

255. Saremi, S., Kim, J., Ghosh, A., Meyers, D. & Martin, L. W. Defect-Induced (Dis)Order in Relaxor Ferroelectric Thin Films. *Phys Rev Lett* 123, 207602 (2019).

256. Nagarajan, V., Junquera, J., He, J. Q., Jia, C. L., Waser, R., Lee, K., Kim, Y. K., Baik, S., Zhao, T., Ramesh, R., Ghosez, P. & Rabe, K. M. Scaling of structure and electrical properties in ultrathin epitaxial ferroelectric heterostructures. *J Appl Phys* 100, 051609 (2006).

257. Welberry, T. R. & Goossens, D. J. Diffuse scattering and partial disorder in complex structures. *IUCrJ* 1, 550–562 (2014).

258. Xu, G., Shirane, G., Copley, J. R. D. & Gehring, P. M. Neutron elastic diffuse scattering study of $Pb(Mg_{1/3}Nb_{2/3})O_3$. *Phys Rev B* 69, 064112 (2004).

259. Krogstad, M. J., Gehring, P. M., Rosenkranz, S., Osborn, R., Ye, F., Liu, Y., Ruff, J. P. C., Chen, W., Wozniak, J. M., Luo, H., Chmaissem, O., Ye, Z.-G. & Phelan, D. The relation of local order to material properties in relaxor ferroelectrics. *Nat Mater* 1–7 (2018)

260. Hashemizadeh, S. & Damjanovic, D. Nonlinear dynamics of polar regions in paraelectric phase of $(Ba_{1-x}Sr_x)TiO_3$ ceramics. *Appl Phys Lett* 110, 192905 (2017).

261. Damjanovic, D. & Demartin, M. The Rayleigh law in piezoelectric ceramics. *J Phys D Appl Phys* 29, 2057 (1996).

262. Kholkin, A. L., Wütchrich, C., Taylor, D. V. & Setter, N. Interferometric measurements of electric field-induced displacements in piezoelectric thin films. *Rev Sci Instrum* 67, 1935–1941 (1996).

263. Park, Y., Knowles, K. M. & Cho, K. Particle-size effect on the ferroelectric phase transition in $PbSc_{1/2}Ta_{1/2}O_3$ ceramics. *J Appl Phys* 83, 5702–5708 (1998).

264. Tan, Q. & Viehland, D. Grain size dependence of relaxor characteristics in La-modified lead zirconate titanate. *Ferroelectrics* 193, 157–165 (1997).

265. Stenger, C. G. F., Scholten, F. L. & Burggraaf, A. J. Ordering and diffuse phase transitions in $Pb(Sc_{0.5}Ta_{0.5})O_3$ ceramics. *Solid State Commun* 32, 989–992 (1979).

266. Stenger, C. & Burggraaf, A. J. Order–disorder reactions in the ferroelectric perovskites $Pb(Sc_{1/2}Nb_{1/2})O_3$ and $Pb(Sc_{1/2}Ta_{1/2})O_3$. I. Kinetics of the ordering process. *Phys Status Solidi* 61, 275–285 (1980).

267. Stenger, C. G. F. & Burggraaf, A. J. Order–disorder reactions in the ferroelectric perovskites $Pb(Sc_{1/2}Nb_{1/2})O_3$ and $Pb(Sc_{1/2}Ta_{1/2})O_3$. II. Relation between ordering and properties. *Phys Status Solidi* 61, 653–664 (1980).

268. Brinkman, K., Tagantsev, A., Sherman, V., Su, D. & Setter, N. In-plane versus out-of-plane dielectric response in the thin-film relaxor $Pb(Sc_{1/2}Ta_{1/2})O_3$. *Phys Rev B* 73, (2006).

269. Brinkman, K., Wang, Y., Cantoni, M., Su, D., Setter, N. & Petrov, P. K. Processing and properties of ferroelectric relaxor lead scandium tantalate $Pb(Sc_{1/2}Ta_{1/2})O_3$ thin films. *J Mater Res* 22, 217–232 (2007).

270. Brinkman, K., Wang, Y., Su, D., Tagantsev, A., Muralt, P. & Setter, N. The Impact of chemical ordering on the dielectric properties of lead scandium tantalate $Pb(Sc_{1/2}Ta_{1/2})O_3$ thin films. *J Appl Phys* 102, 044110 (2007).

271. Chopra, A., Birajdar, B. I., Berger, A., Alexe, M. & Hesse, D. Thickness-dependent cation order and disorder in $PbSc_{0.5}Ta_{0.5}O_3$ thin films grown by pulsed laser deposition. *New J Phys* 16, 013059 (2014).

272. Chopra, A., Birajdar, B. I., Kim, Y., Alexe, M. & Hesse, D. Enhanced ferroelectric and dielectric properties of (111)-oriented highly cation-ordered $PbSc_{0.5}Ta_{0.5}O_3$ thin films. *J Appl Phys* 114, 224109 (2013).

273. Chopra, A., Birajdar, B. I., Kim, Y., Vrejoiu, I., Alexe, M. & Hesse, D. Epitaxial, cation-ordered, ferroelectric $PbSc_{0.5}Ta_{0.5}O_3$ thin films prepared by pulsed laser deposition. *Appl Phys Lett* 95, 022907 (2009).

274. Chopra, A., Alexe, M. & Hesse, D. Fabrication and orientation control of highly cation-ordered epitaxial $PbSc_{0.5}Ta_{0.5}O_3$ thin films on Si (100). *J Appl Phys* 117, 044102 (2015).

275. Caranoni, C., Lampin, P. & Boulesteix, C. Identification of two lead perovskites, Pb_2ScTaO_6 and $Pb(Sc_{0.5}Nb_{0.5})O_3$, by X-ray powder diffraction patterns. *Powder Diffr* 8, 191–193 (1993).

276. Gao, R., Reyes-Lillo, S. E., Xu, R., Dasgupta, A., Dong, Y., Dedon, L. R., Kim, J., Saremi, S., Chen, Z., Serrao, C. R., Zhou, H., Neaton, J. B. & Martin, L. W. Ferroelectricity in $Pb_{1+\delta}ZrO_3$ Thin Films. *Chem Mater* 24, 331–337 (2017).

277. Grinberg, I., Juhás, P., Davies, P. K. & Rappe, A. M. Relationship between Local Structure and Relaxor Behavior in Perovskite Oxides. *Phys Rev Lett* 99, 267603 (2006).

278. Malibert, C., Dkhil, B., Kiat, J. M., Durand, D., Bérar, J. F. & Biré, A. S. Order and disorder in the relaxor ferroelectric perovskite (PSN): comparison with simple perovskites and. *J Phys Condens Matter* 9, 7485 (1997).

279. Viehland, D., Jang, S. J., Cross, L. E. & Wuttig, M. Freezing of the polarization fluctuations in lead magnesium niobate relaxors. *J Appl Phys* 68, 2916–2921 (1990).

280. Tagantsev, A. K. & Glazounov, A. E. Mechanism of polarization response and dielectric non-linearity of $PbMg_{1/3}Nb_{2/3}O_3$ relaxor ferroelectric. *Phase Transit* 65, 117–139 (1998).

281. Tagantsev, A. K. & Glazounov, A. E. Mechanism of polarization response in the ergodic phase of a relaxor ferroelectric. *Phys Rev B* 57, 18–21 (1998).

282. Glazounov, A. E., Tagantsev, A. K. & Bell, A. J. Evidence for domain-type dynamics in the ergodic phase of the $PbMg_{1/3}Nb_{2/3}O_3$ relaxor ferroelectric. *Phys Rev B* 53, 11281–11284 (1996).

283. Otoničar, M., Bradeško, A., Fulanović, L., Kos, T., Uršič, H., Benčan, A., Cabral, M. J., Henriques, A., Jones, J. L., Riemer, L., Damjanovic, D., Dražić, G., Malič, B. & Rojac, T. Connecting the Multiscale Structure with Macroscopic Response of Relaxor Ferroelectrics. *Adv Funct Mater* 30, 2006823 (2020).

284. Damjanovic, D. & Taylor, David. V. Contributions to the nonlinear dielectric and piezoelectric response of ferroelectric thin films and ceramics. *Ferroelectrics* 221, 137–146 (1999).

285. Vugmeister, B. E. & Rabitz, H. Dynamics of interacting clusters and dielectric response in relaxor ferroelectrics. *Phys Rev B* 57, 7581–7585 (1998).

286. Vugmeister, B. E. & Glinchuk, M. D. Dipole glass and ferroelectricity in random-site electric dipole systems. *Rev Mod Phys* 62, 993–1026 (1990).

287. Xu, G., Wen, J., Stock, C. & Gehring, P. M. Phase instability induced by polar nanoregions in a relaxor ferroelectric system. *Nat Mater* 7, 562 (2008).

288. Dederichs, P. H. Diffuse Scattering from Defect Clusters near Bragg Reflections. *Phys Rev B* 4, 1041–1050 (1971).

289. Dederichs, P. H. The theory of diffuse X-ray scattering and its application to the study of point defects and their clusters. *J Phys F Metal Phys* 3, 471–496 (1973).

290. Dkhil, B., Kiat, J. M., Calvarin, G., Baldinozzi, G., Vakhrushev, S. B. & Suard, E. Local and long range polar order in the relaxor-ferroelectric compounds $PbMg_{1/3}Nb_{2/3}O_3$ and $PbMg_{0.3}Nb_{0.6}Ti_{0.1}O_3$. *Phys Rev B* 65, 024104 (2002).

291. Kim, Y., Disa, A. S., Babakol, T. E., Fang, X. & Brock, J. D. Strain and oxygen vacancy ordering in $SrTiO_3$: Diffuse x-ray scattering studies. *Phys Rev B* 92, 064105 (2015).

292. Kim, Y., Disa, A. S., Babakol, T. E. & Brock, J. D. Strain screening by mobile oxygen vacancies in $SrTiO_3$. *Appl Phys Lett* 96, 251901 (2010).

293. Guo, Y., Luo, H., Ling, D., Xu, H., He, T. & Yin, Zhiwen. The phase transition sequence and the location of the morphotropic phase boundary region in $(1 - x)[Pb(Mg_{1/3}Nb_{2/3})O_3]–xPbTiO_3$ single crystal. *J Phys Condens Matter* 15, L77 (2003).

294. Park, S.-E. & Shrout, T. R. Characteristics of relaxor-based piezoelectric single crystals for ultrasonic transducers. *IEEE Transactions Ultrasonics Ferroelectr Freq Control* 44, 1140–1147 (1997).

295. Kim, S.-G., Priya, S. & Kanno, I. Piezoelectric MEMS for energy harvesting. *MRS Bull* 37, 1039–1050 (2012).

296. Li, J. Y., Rogan, R. C., Üstündag, E. & Bhattacharya, K. Domain switching in polycrystalline ferroelectric ceramics. *Nat Mater* 4, 776–781 (2005).

297. Ye, Z.-G. High-Performance Piezoelectric Single Crystals of Complex Perovskite Solid Solutions. *MRS Bull* 34, 277–283 (2009).

298. Kuwata, J., Uchino, K. & Nomura, S. Dielectric and Piezoelectric Properties of $0.91Pb(Zn_{1/3}Nb_{2/3})O_3$ -$0.09PbTiO_3$ Single Crystals. *Jpn J Appl Phys* 21, 1298–1302 (1982).

299. Yokoyama, S., Okamoto, S., Funakubo, H., Iijima, T., Saito, K., Okino, H., Yamamoto, T., Nishida, K., Katoda, T. & Sakai, J. Crystal structure, electrical properties, and mechanical response of (100)-/(001)-oriented epitaxial $Pb(Mg_{1/3}Nb_{2/3})O_3–PbTiO_3$ films grown on

(100)cSrRuO$_3$‖(100)SrTiO$_3$ substrates by metal-organic chemical vapor deposition. *J Appl Phys* 100, 054110 (2006).

300. Ouyang, J., Kim, D. M., Eom, C. B., Ramesh, R. & Roytburd, A. L. Orientation dependence of the intrinsic converse longitudinal piezoelectric constant for 0.67Pb($Mg_{1/3}Nb_{2/3}$)O_3–0.33$PbTiO_3$ ferroelectric films with a rhombohedral structure. *Smart Mater Struct* 14, 524 (2005).

301. Chen, L., Li, J. H., Slutsker, J., Ouyang, J. & Roytburd, A. L. Contribution of substrate to converse piezoelectricresponse of constrauned thin films. *J Mater Res* 19, 2853–2858 (2004).

302. Bassiri-Gharb, N., Fujii, I., Hong, E., Trolier-McKinstry, S., Taylor, D. V. & Damjanovic, D. Domain wall contributions to the properties of piezoelectric thin films. *J Electroceram* 19, 49–67 (2007).

303. Xu, F., Chu, F. & Trolier-McKinstry, S. Longitudinal piezoelectric coefficient measurement for bulk ceramics and thin films using pneumatic pressure rig. *J Appl Phys* 86, 588–594 (1999).

304. Griggio, F., Jesse, S., Kumar, A., Ovchinnikov, O., Kim, H., Jackson, T. N., Damjanovic, D., Kalinin, S. V. & Trolier-McKinstry, S. Substrate Clamping Effects on Irreversible Domain Wall Dynamics in Lead Zirconate Titanate Thin Films. *Phys Rev Lett* 108, 157604 (2012).

305. Fernandez, A., Kim, J., Meyers, D., Saremi, S. & Martin, L. W. Finite-size effects in lead scandium tantalate relaxor thin films. *Phys Rev B* 101, 094102 (2020).

306. Zhao, W., Kim, J., Huang, X., Zhang, L., Pesquera, D., Velarde, G. A. P., Gosavi, T., Lin, C., Nikonov, D. E., Li, H., Young, I. A., Ramesh, R. & Martin, L. W. Low-Voltage Magnetoelectric Coupling in $Fe_{0.5}Rh_{0.5}$/0.68$PbMg_{1/3}Nb_{2/3}O_3$-0.32$PbTiO_3$ Thin-Film Heterostructures. *Adv Funct Mater* 31, 2105068 (2021).

307. Pesquera, D., Fernandez, A., Khestanova, E. & Martin, L. W. Ferroic and Correlated Responses in Complex Oxide Membranes. *Journal of Physics: Condensed Matter* (2022).

308. Novoselov, K. S., Jiang, D., Schedin, F., Booth, T. J., Khotkevich, V. V., Morozov, S. V. & Geim, A. K. Two-dimensional atomic crystals. *P Natl Acad Sci Usa* 102, 10451–10453 (2005).

309. Velický, M., Toth, P. S., Rakowski, A. M., Rooney, A. P., Kozikov, A., Woods, C. R., Mishchenko, A., Fumagalli, L., Yin, J., Zólyomi, V., Georgiou, T., Haigh, S. J., Novoselov, K. S. & Dryfe, R. A. W. Exfoliation of natural van der Waals heterostructures to a single unit cell thickness. *Nat Commun* 8, 14410 (2017).

310. Novoselov, K. S., Mishchenko, A., Carvalho, A. & Neto, A. H. C. 2D materials and van der Waals heterostructures. *Science* 353, aac9439 (2016).

311. Elangovan, H., Barzilay, M., Seremi, S., Cohen, N., Jiang, Y., Martin, L. W. & Ivry, Y. Giant Superelastic Piezoelectricity in Flexible Ferroelectric $BaTiO_3$ Membranes. *ACS Nano* 14, 5053–5060 (2020).

312. Han, L., Fang, Y., Zhao, Y., Zang, Y., Gu, Z., Nie, Y. & Pan, X. Giant Uniaxial Strain Ferroelectric Domain Tuning in Freestanding $PbTiO_3$ Films. *Adv Mater Interfaces* 7, 1901604 (2020).

313. Xu, R., Huang, J., Barnard, E. S., Hong, S. S., Singh, P., Wong, E. K., Jansen, T., Harbola, V., Xiao, J., Wang, B. Y., Crossley, S., Lu, D., Liu, S. & Hwang, H. Y. Strain-induced room-temperature ferroelectricity in $SrTiO_3$ membranes. *Nat Commun* 11, 3141 (2020).

314. Kum, H. S., Lee, H., Kim, S., Lindemann, S., Kong, W., Qiao, K., Chen, P., Irwin, J., Lee, J. H., Xie, S., Subramanian, S., Shim, J., Bae, S.-H., Choi, C., Ranno, L., Seo, S., Lee, S., Bauer, J., Li, H., *et al.* Heterogeneous integration of single-crystalline complex-oxide membranes. *Nature* 578, 75–81 (2020).

315. Lee, D. K., Park, Y., Sim, H., Park, J., Kim, Y., Kim, G.-Y., Eom, C.-B., Choi, S.-Y. & Son, J. Heterogeneous integration of single-crystalline rutile nanomembranes with steep phase transition on silicon substrates. *Nat Commun* 12, 5019 (2021).

316. Singh, P., Swartz, A., Lu, D., Hong, S. S., Lee, K., Marshall, A. F., Nishio, K., Hikita, Y. & Hwang, H. Y. Large-Area Crystalline $BaSnO_3$ Membranes with High Electron Mobilities. *Acs Appl Electron Mater* 1, 1269–1274 (2019).

317. Ito, A., Masumoto, H. & Goto, T. Effect of Ba substitution on the microstructure and electrical conductivity of $Ba_xSr_{1-x}RuO_3$ thin films prepared by laser ablation. *J Ceram Soc Jpn* 116, 441–444 (2008).

318. Khakpash, N., Khassaf, H., Rossetti, G. A. & Alpay, S. P. Misfit strain phase diagrams of epitaxial PMN–PT films. *Appl Phys Lett* 106, 082905 (2015).

319. Cao, H., Schmidt, V. H., Zhang, R., Cao, W. & Luo, H. Elastic, piezoelectric, and dielectric properties of $0.58Pb(Mg_{1/3}Nb_{2/3})O_3$-$0.42PbTiO_3$ single crystal. *J Appl Phys* 96, 549–554 (2004).

320. Parsonnet, E., Huang, Y.-L., Gosavi, T., Qualls, A., Nikonov, D., Lin, C.-C., Young, I., Bokor, J., Martin, L. W. & Ramesh, R. Toward Intrinsic Ferroelectric Switching in Multiferroic $BiFeO_3$. *Phys Rev Lett* 125, 067601 (2020).

321. Kamba, S. Soft-mode spectroscopy of ferroelectrics and multiferroics: A review. *APL Mater* 9, 020704 (2021).

322. Cohen, R. E. & Krakauer, H. Lattice dynamics and origin of ferroelectricity in $BaTiO_3$: Linearized-augmented-plane-wave total-energy calculations. *Phys Rev B* 42, 6416–6423 (1990).

323. Li, J., Nagaraj, B., Liang, H., Cao, W., Lee, Chi. H. & Ramesh, R. Ultrafast polarization switching in thin-film ferroelectrics. *Appl Phys Lett* 84, 1174–1176 (2004).

324. Boddu, V., Endres, F. & Steinmann, P. Molecular dynamics study of ferroelectric domain nucleation and domain switching dynamics. *Sci Rep-uk* 7, 806 (2017).

325. Bhattacharjee, S., Rahmedov, D., Wang, D., Íñiguez, J. & Bellaiche, L. Ultrafast Switching of the Electric Polarization and Magnetic Chirality in $BiFeO_3$ by an Electric Field. *Phys Rev Lett* 112, 147601 (2014).

326. Liu, S., Grinberg, I. & Rappe, A. M. Exploration of the intrinsic inertial response of ferroelectric domain walls via molecular dynamics simulations. *Appl Phys Lett* 103, 232907 (2013).

327. Liu, S., Grinberg, I. & Rappe, A. M. Intrinsic ferroelectric switching from first principles. *Nature* 534, 360 (2016).

328. Shin, Y.-H., Grinberg, I., Chen, I.-W. & Rappe, A. M. Nucleation and growth mechanism of ferroelectric domain-wall motion. *Nature* 449, 881–884 (2007).

329. Grinberg, I., Shin, Y.-H. & Rappe, A. M. Molecular Dynamics Study of Dielectric Response in a Relaxor Ferroelectric. *Phys Rev Lett* 103, 197601 (2009).

330. Li, Q., Stoica, V. A., Paściak, M., Zhu, Y., Yuan, Y., Yang, T., McCarter, M. R., Das, S., Yadav, A. K., Park, S., Dai, C., Lee, H. J., Ahn, Y., Marks, S. D., Yu, S., Kadlec, C., Sato, T., Hoffmann, M. C., Chollet, M., *et al.* Subterahertz collective dynamics of polar vortices. *Nature* 592, 376–380 (2021).

331. Roytburd, A. L., Alpay, S. P., Nagarajan, V., Ganpule, C. S., Aggarwal, S., Williams, E. D. & Ramesh, R. Measurement of Internal Stresses via the Polarization in Epitaxial Ferroelectric Films. *Phys Rev Lett* 85, 190–193 (2000).

332. Setvín, M., Wagner, M., Schmid, M., Parkinson, G. S. & Diebold, U. Surface point defects on bulk oxides: atomically-resolved scanning probe microscopy. *Chem Soc Rev* 46, 1772–1784 (2017).

333. Kuo, D.-Y., Eom, C. J., Kawasaki, J. K., Petretto, G., Nelson, J. N., Hautier, G., Crumlin, E. J., Shen, K. M., Schlom, D. G. & Suntivich, J. Influence of Strain on the Surface–Oxygen Interaction and the Oxygen Evolution Reaction of $SrIrO_3$. *J Phys Chem C* 122, 4359–4364 (2018).

334. Chueh, W. C., Hao, Y., Jung, W. & Haile, S. M. High electrochemical activity of the oxide phase in model ceria–Pt and ceria–Ni composite anodes. *Nat Mater* 11, 155 (2012).

335. Fernandez, A., Caretta, L., Das, S., Klewe, C., Lou, D., Parsonnet, E., Gao, R., Luo, A., Shafer, P. & Martin, L. W. Strain-Induced Orbital Contributions to Oxygen Electrocatalysis in Transition-Metal Perovskites. *Adv Energy Mater* 2102175 (2021).

336. Mangalam, R .V. K., Damodaran, A., Agar, J. & Advanced, M.-L. Unexpected Crystal and Domain Structures and Properties in Compositionally Graded $PbZr_{1-x}Ti_xO_3$ Thin Films. (2013).

337. Strasser, P., Koh, S., Anniyev, T., Greeley, J., More, K., Yu, C., Liu, Z., Kaya, S., Nordlund, D., Ogasawara, H., Toney, M. F. & Nilsson, A. Lattice-strain control of the activity in dealloyed core–shell fuel cell catalysts. *Nat Chem* 2, 454–460 (2010).

338. Shetty, S., Damodaran, A., Wang, K., Yuan, Y., Gopalan, V., Martin, L. & Trolier-McKinstry, S. Relaxor Behavior in Ordered Lead Magnesium Niobate ($PbMg_{1/3}Nb_{2/3}O_3$) Thin Films. *Adv Funct Mater* 29, 1804258 (2019).

339. Sinha, S. K., Jiang, Z. & Lurio, L. B. X-ray Photon Correlation Spectroscopy Studies of Surfaces and Thin Films. *Adv Mater* 26, 7764–7785 (2014).

340. Roseker, W., Hruszkewycz, S. O., Lehmkühler, F., Walther, M., Schulte-Schrepping, H., Lee, S., Osaka, T., Strüder, L., Hartmann, R., Sikorski, M., Song, S., Robert, A., Fuoss, P. H., Sutton, M., Stephenson, G. B. & Grübel, G. Towards ultrafast dynamics with split-pulse X-ray photon correlation spectroscopy at free electron laser sources. *Nat Commun* 9, 1704 (2018).

341. Cao, Y., Sheyfer, D., Jiang, Z., Maddali, S., You, H., Wang, B.-X., Ye, Z.-G., Dufresne, E. M., Zhou, H., Stephenson, G. B. & Hruszkewycz, S. O. The Effect of Intensity Fluctuations on Sequential X-ray Photon Correlation Spectroscopy at the X-ray Free Electron Laser Facilities. *Crystals* 10, 1109 (2020).

342. Konya, T. X-ray thin-film measurement techniques III. High resolution x-ray diffractometry. *Rigaku J* (2018).

343. Geisse, N. A. AFM and combined optical techniques. *Mater Today* 12, 40–45 (2009).